

MATERIALS PHYSICS AND MECHANICS

Vol. 53, No. 2, 2025

MATERIALS PHYSICS AND MECHANICS

Principal Editors:

Alexander Belyaev

Institute for Problems in Mechanical Engineering of the Russian Academy of Science (RAS), Russia

Andrei Rudskoi

Peter the Great St. Petersburg Polytechnic University, Russia

Founder and Honorary Editor: Ilya Ovid'ko (1961-2017)

Institute for Problems in Mechanical Engineering of the Russian Academy of Sciences (RAS), Russia

Associate Editor:

Anna Kolesnikova

Institute for Problems in Mechanical Engineering of the Russian Academy of Sciences (RAS), Russia

Artem Semenov

Peter the Great St. Petersburg Polytechnic University, Russia

Editorial Board:

S.V. Bobylev

Institute for Problems in Mechanical Engineering (RAS), Russia
A.B. Freidin

Institute for Problems in Mechanical Engineering (RAS), Russia D.M. Klimov

Institute of Problems of Mechanics (RAS), Russia

S.A. Kukushkin

Institute for Problems in Mechanical Engineering (RAS), Russia

A.I. Melker

Peter the Great St. Petersburg Polytechnic University, Russia

R.R. Mulyukov

Institute for Metals Superplasticity Problems (RAS), Russia

A.E. Romanov

Ioffe Institute (RAS), Russia

A.G. Sheinerman

Institute for Problems in Mechanical Engineering (RAS), Russia

E.C. Aifantis

Aristotle University of Thessaloniki, Greece

U. Balachandran

Argonne National Laboratory, USA

G.-M. Chow

National University of Singapore, Singapore

G. Kiriakidis

IESL/FORTH, Greece

N.M. Pugno

Politecnico di Torino, Italy

A.M. Sastry

University of Michigan, Ann Arbor, USA

K. Zhou

Nanyang Technological University, Singapore

A.I. Borovkov

Peter the Great St.Petersburg Polytechnic University, Russia

I.G. Goryacheva

Institute of Problems of Mechanics (RAS), Russia

G.E. Kodzhaspirov

Peter the Great St. Petersburg Polytechnic University, Russia

V.P. Matveenko

Institute of Continuous Media Mechanics (RAS), Russia

Yu.I. Meshcheryakov

Institute for Problems in Mechanical Engineering (RAS), Russia

Yu.V. Petrov

St. Petersburg State University, Russia

N.V. Skiba

Institute for Problems in Mechanical Engineering (RAS), Russia

R.Z. Valiev

Ufa State Aviation Technical University, Russia

K.E. Aifantis

University of Florida, USA

A. Bellosi

Research Institute for Ceramics Technology, Italy

D. Hui

University of New Orleans, USA

T.G. Langdon

University of Southampton, U.K.

B.B. Rath

Naval Research Laboratory, USA

B.A. Schrefler

University of Padua, Italy

"Materials Physics and Mechanics" Editorial Office:

Phone: +7(812)552 77 78, ext. 224 E-mail: mpmjournal@spbstu.ru Web-site: http://www.mpm.spbstu.ru

International scientific journal "Materials Physics and Mechanics" is published by Peter the Great St. Petersburg Polytechnic University in collaboration with Institute for Problems for Mechanical Engineering in the Russian Academy of Sciences in both hard copy and electronic versions. The journal provides an international medium for the publication of reviews and original research papers written in English and focused on the following topics:

- Mechanics of composite and nanostructured materials.
- Physics of strength and plasticity of composite and nanostructured materials.
- Mechanics of deformation and fracture processes in conventional materials (solids).
- Physics of strength and plasticity of conventional materials (solids).
- Physics and mechanics of defects in composite, nanostructured, and conventional materials.
- Mechanics and physics of materials in coupled fields.

Owner organizations: Peter the Great St. Petersburg Polytechnic University; Institute of Problems of Mechanical Engineering RAS.

Materials Physics and Mechanics is indexed in Chemical Abstracts, Cambridge Scientific Abstracts, Web of Science Emerging Sources Citation Index (ESCI) and Elsevier Bibliographic Databases (in particular, SCOPUS).

© 2025, Peter the Great St. Petersburg Polytechnic University © 2025, Institute for Problems in Mechanical Engineering RAS



МЕХАНИКА И ФИЗИКА МАТЕРИАЛОВ

Materials Physics and Mechanics

Том 53, номер 2, 2025 год

Учредители:

Редакционная коллегия журнала

Главный редактор

д.т.н., академик РАН А.И. Рудской

Санкт-Петербургский политехнический университет Петра Великого

Главный научный редактор

д.ф.-м.н., чл.-корр. РАН А.К. Беляев

Институт проблем машиноведения Российской академии наук (РАН)

Основатель и почетный редактор

д.ф.-м.н. И.А. Овидько (1961-2017)

Институт проблем машиноведения Российской академии наук (РАН)

Ответственные редакторы

д.ф.-м.н. А.Л. Колесникова

Институт проблем машиноведения

Российской академии наук (РАН)

д.ф.-м.н. А.С. Семенов

Санкт-Петербургский политехнический университет Петра Великого

Международная редакционная коллегия:

д.ф.-м.н. С.В. Бобылев

Институт проблем машиноведения РАН, Россия д.ф.-м.н., проф. Р.З. Валиев

Уфимский государственный технический университет, Россия

д.ф.-м.н., академик РАН Д.М. Климов

Институт проблем механики РАН, Россия

д.ф.-м.н., проф. С.А. Кукушкин

Институт проблем машиноведения РАН, Россия

д.ф.-м.н., проф. А.И. Мелькер

Санкт-Петербургский политехнический ун-т Петра Великого, Россия д.ф.-м.н., чл.-корр. РАН Р.Р. Мулюков

Институт проблем сверхпластичности металлов РАН, Россия

д.ф.-м.н., проф. А.Е. Романов

Физико-технический институт им. А.Ф. Иоффе РАН, Россия

д.ф.-м.н., проф. А.Б. Фрейдин

Институт проблем машиноведения РАН, Россия

Prof., Dr. E.C. Aifantis

Aristotle University of Thessaloniki, Greece

Dr. U. Balachandran

Argonne National Laboratory, USA

Prof., Dr. G.-M. Chow

National University of Singapore, Singapore

Prof., Dr. G. Kiriakidis

IESL/FORTH, Greece Prof., Dr. N.M. Pugno

Politecnico di Torino, Italy

Prof., Dr. A.M. Sastry

University of Michigan, Ann Arbor, USA

Prof., Dr. K. Zhou

Nanyang Technological University, Singapore

к.т.н., проф. А.И. Боровков

Санкт-Петербургский политехнический ун-т Петра Великого, Россия

д.ф.-м.н., академик РАН И.Г. Горячева

Институт проблем механики РАН, Россия

л.т.н., проф. Г.Е. Коджаспиров

Санкт-Петербургский политехнический ун-т Петра Великого, Россия

д.ф.-м.н., академик РАН В.П. Матвеенко

Институт механики сплошных сред РАН, Россия

д.ф.-м.н., проф. Ю.И. Мещеряков

Институт проблем машиноведения РАН, Россия

д.ф.-м.н., академик РАН Ю.В. Петров

Санкт-Петербургский государственный университет, Россия

д.ф.-м.н. Н.В. Скиба

Институт проблем машиноведения РАН, Россия

д.ф.-м.н. **А.Г. Шейнерман**

Институт проблем машиноведения РАН, Россия

Dr. K.E. Aifantis

University of Florida, USA

Dr. A. Bellosi

Research Institute for Ceramics Technology, Italy

Prof., Dr. D. Hui

University of New Orleans, USA

Prof., Dr. T.G. Langdon

University of Southampton, UK

Dr. B.B. Rath

Naval Research Laboratory, USA

Prof., Dr. B.A. Schrefler

University of Padua, Italy

Тел.: +7(812)552 77 78, доб. 224 E-mail: mpmjournal@spbstu.ru Web-site: http://www.mpm.spbstu.ru

Тематика журнала

Международный научный журнал "Materials Physics and Mechanics" издается Санкт-Петербургским политехническим университетом Петра Великого в сотрудничестве с Институтом проблем машиноведения Российской академии наук в печатном виде и электронной форме. Журнал публикует обзорные и оригинальные научные статьи на английском языке по следующим тематикам:

- Механика композиционных и наноструктурированных материалов.
- Физика прочности и пластичности композиционных и наноструктурированных материалов.
- Механика процессов деформации и разрушения в традиционных материалах (твердых телах).
- Физика прочности и пластичности традиционных материалов (твердых тел).
- Физика и механика дефектов в композиционных, наноструктурированных и традиционных материалах.
- Механика и физика материалов в связанных полях.

Редколлегия принимает статьи, которые нигде ранее не опубликованы и не направлены для опубликования в другие научные издания. Все представляемые в редакцию журнала "Механика и физика материалов" статьи рецензируются. Статьи могут отправляться авторам на доработку. Не принятые к опубликованию статьи авторам не возвращаются.

Журнал "Механика и физика материалов" ("Materials Physics and Mechanics") включен в систему цитирования Web of Science Emerging Sources Citation Index (ESCI), SCOPUS u РИНЦ.

Contents

United model for low-cycle, high and giga-cycle fatigue life prediction N.S. Selyutina, Yu.V. Petrov	1-12
Influence of grain size of nanocrystalline titanium on its dissolution intensity in aluminum G.M. Poletaev, Y.V. Bebikhov, A.S. Semenov	13-24
Electromagnetically cast Al-0.5 wt. % Fe alloy as a core material for the co-extruded copper-clad aluminium wire A.E. Medvedev, O.O. Zhukova, A.F. Shaikhulova, E.B. Medvedev, M.M. Motkov, M.Yu.	25–39 Murashkin
S ₁₁ and S ₂₁ characteristics of carbon fiber fabric fixed in the polyurethane based matrixes O.V. Boiprav, E.S. Belousova, V.S. Mokerov	40-47
Conductive and mechanical properties of graphene-filled polymer composites D.N. Tonkov, M.I. Kobylyatskaya, E.S. Vasilyeva, V.E. Gasumyants	48-54
Effects of post-annealing duration on the properties of β-Ga ₂ O ₃ thin films prepared by spray pyrolysis X. Zhang, D.I. Panov, V.A. Spiridonov, N.K. Kuzmenko, N.D. Prasolov, A.Yu. Ivanov, M.V. Dorogov, H.M. Wei, D.Y. Jiang, D.A. Bauman, A.E. Romanov	55-63
Fundamental theorems and variational criterion in modified couple stress under multi-phase-lags and rotation S. Sharma, S. Devi, R. Kumar	64-82
Modelling forced convection and magneto-elastic interactions in a downward conduit using ferrofluid H. Derraz, M. Bouzit, A. Bencherif	83-103
Effect of loading on tribotechnical characteristics of antifriction diamond-bearing mineral ceramics A.N. Bolotov, O.O. Novikova, V.V. Novikov	104-112
Elastic-plastic deformation when bending rotating workpieces T.V. Brovman	113-122
Al-driven modeling and prediction of mechanical properties of additively manufactured Al-6061/B ₄ C composite D. Kumar, S. Singh, P.K. Karsh, A. Chauhan, G. Saini, A. Chouksey, P. Kumar	123-141

Electrochemical crystallization and functional properties of nickel-based composite coatings	142-148
V.N. Tseluikin, A.S. Dzhumieva, A.I. Tribis, D.A. Tikhonov	
The effect of the magnetron discharge power on the deposition rate of chrome coating obtained by spattering an uncooled extended target G.V. Kachalin, K.S. Medvedev, A.B. Tkhabisimov, D.I. Iliukhin	149-156
Gradient energy-absorbing nature-like metamaterial based on the "Schwarz Primitive"	157-167
S.V. Balabanov, A.M. Kuropiatnik, M.M. Sychov, E.A. Pavlova, S.V. Diachenko	

Submitted: February 10, 2025 Revised: March 17, 2025 Accepted: April 28, 2025

United model for low-cycle, high-cycle and giga-cycle fatigue life prediction

N.S. Selyutina 1,2 10, Yu.V. Petrov 1,2 10

ABSTRACT

The methods for determining the cyclic strengths of metals under low-cycle and high-cycle fatigue are different, since the mechanisms of failure and the extent of the presence or absence of plastic deformation differ for each type of fatigue. The aim of this study is to develop united models for both low-cycle and high-cycle fatigue life prediction. We propose that the relevant relaxation and damage processes are considered and it on different types of metals is tested. In this paper, the cyclic deformation of materials is considered using the proposed model with regard to two processes: stress relaxation and damage accumulation kinetics. Proposed approach allows us to study the united fatigue curves of materials regardless of the chosen type of fatigue (low-cycle fatigue, high-cycle fatigue, giga-cycle fatigue). Fatigue life curves under staircase strain loading and symmetrical sinusoidal strain/stress loading are predicted in this study. A simple numerical scheme for the model is successfully applied to various materials under various types of loading, since the relaxation–kinetic model is phenomenological in nature.

KEYWORDS

fatigue strength • metals • inelastic adaptability • fatigue life curve • short-term strength • long-term strength

Funding. This study was supported by the Russian Science Foundation, project no. 23–71–01059.

Citation: Selyutina NS, Petrov YuV. United model for low-cycle, high-cycle and giga-cycle fatigue life prediction. *Materials Physics and Mechanics*. 2025;53(2): 1–12.

http://dx.doi.org/10.18149/MPM.5322025_1

Introduction

The appearance and propagation of fatigue cracks in materials often cause disasters, and to prevent fatigue failure, it is necessary to evaluate fatigue life of materials. The Wöhler curve is a graphical representation illustrating the relationship between cyclic stress amplitude and the number of cycles to failure (N) for a material that fails as a result of mechanical cycling. This curve is critical to understanding the fatigue behaviours of materials, especially metals. It helps engineers and materials scientists to develop components and structures that can withstand cyclic loads over long periods of time. The fatigue life curve usually includes three characteristic zones: low-cycle, high-cycle and giga-cycle fatigue (Fig. 1). Past research shows that for low-cycle fatigue, the dominant mechanism is associated with plastic deformation and the initiation of various defects, including crack-like defects. The stresses are fairly high level in nature, and the macroscopic fracture of the material occurs after a relatively small number of cycles. In this case, fracture is often accompanied by both the accumulation of plastic deformation and the growth of cracks. For high-cycle fatigue, the initiation and cumulative growth of damage, including crack-like defects, become more significant. This process occurs at



¹ St. Petersburg State University, St. Petersburg, Russia

² Institute for Problems in Mechanical Engineering of the Russian Academy of Science, St. Petersburg, Russia

[™] nina.selutina@gmail.com

N.S. Selyutina, Yu.V. Petrov

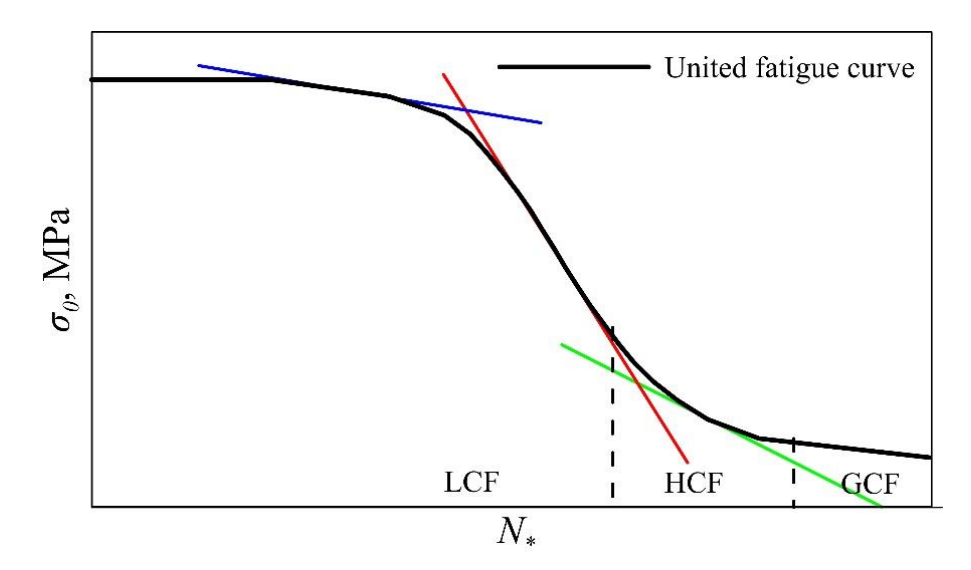


Fig. 1. The dependence of cyclic strength on the number of cycles before failure and its conditional sections within the following zones: LCF is low-cycle fatigue; HCF is high-cycle fatigue; GCF is giga-cycle fatigue

medium-level stress amplitudes, with a moderate number of cycles occurring until the macro-fracture of the material. Both plastic deformation and defect growth contribute to failure. In ultra-high-cycle fatigue, visible damage and cracks are usually caused by internal defects in the material and surface peculiarities. The stress level is of low amplitude, and the rupture of the medium mainly occurs due to the sudden growth of small cracks after a large number of cycles. Studies reviewing past work on low-cycle [1,2] and high-cycle [3–5] fatigue highlighted the diversity of existing approaches and the lack of a unified approach for calculating fatigue life.

For each section of the curves of low-cycle, high-cycle and giga-cycle fatigue, various models have been formulated, including empirical models [6–10], residual stress relaxation models [11–14] and kinetic equations [15–18]. The latter are usually associated with predicting the crack propagation process related to the intermediate stage of fatigue failure between crack initiation, which is invisible to the observer, and final fracture due to the rapid acceleration of crack growth. As noted in [11,12,19], in addition to the processes of fatigue failure, there are relaxation processes associated with the accumulation of plastic deformation in the material. In this case, models are usually formulated separately, and these models take into account the initiation and growth of cracks and other models associated with the relaxation processes of plastic deformation. This study proposes combining the stress relaxation process and the evolution of damage accumulation to predict the complete Wöhler fatique curve.

A relaxation model of cyclic deformation has been formulated previously [20,21], explicitly taking into account the ongoing relaxation processes in the material by introducing a characteristic relaxation time and a stress relaxation function. In previous studies, the proposed model was verified to predict the effects of low-cycle deformation. It was shown that this model is particularly capable of simultaneously predicting the effects of the stabilisation of plastic deformation and the full deformation response of the material across the entire cyclic loading regime. In conventional approaches [1–5], the effect of the deformation amplitude on the deformation response of the material is taken into account

by the linear movement of the hysteresis curve, in contrast to the proposed model, where the deformation response is obtained automatically.

In this paper, based on the relaxation model of cyclic deformation, a fatigue life model of relaxation and damage (FLMRD) is formulated to predict the effects of cyclic deformation for a wide range of cycle numbers, ranging from low-cycle to giga-cycle fatigue. To verify the Wöhler curve, the model is supplemented with the Kachanov–Rabotnov damage equation [15,17], which improves the performance of the original model beyond the stabilising cycle. Theoretical fatigue dependencies for steels are plotted using experimental data derived from the literature as an example.

Fatigue life model of relaxation and damage

Experiments on low-cycle and high-cycle fatigue show the different dependences of the ultimate stress (cyclic strength σ_0) on the cycle number before failure: the so-called fatigue life curve. Existing models used in engineering practice for determining the fatigue life curve are often empirical in nature [9,10]. In this paper, we propose a fatigue life model combining relaxation and damage (FLMRD) that can automatically and simultaneously calculate the short-term and long-term strengths of the material.

To predict the cumulative plastic deformation in a material, we propose using a relaxation model modified for a cyclic process [20,21] with an additional fracture condition. The purpose of the combined FLMRD model in the proposed work is to explicitly take into account the relaxation processes of the force field during cyclic deformation, as well as consider the process of damage accumulation. The combined model assumes that there are three possible cases of cyclic deformation of the material. In the first case, the material undergoes elastic-plastic deformation and there is no stabilisation of plastic deformation, since there is a consistent accumulation of plastic deformation cycle after cycle until the deformation of the material occurs. In the second case—low-cycle fatigue up to $\sim 5.10^4$ cycles the material undergoes elastic-plastic deformation until plastic deformation is stabilised occurs and the material collapses, accumulating critical damage in the material cycle after cycle. In the third case, giga-cycle fatigue, first, the material deforms almost elastically, and then deforms after achieving a stabilisation effect, as in the second case. In the proposed combined model, elastoplastic deformation is predicted using a relaxation model for cyclic deformation [20,21], and the damage accumulation process is predicted using the Kachanov-Rabotnov-type equation [15,17]. The transition point between the two models is taken to be a non-zero initial condition for the damage parameter ω_0 , calculated using the relaxation model of cyclic deformation when the material reaches the stabilising cycle of plastic deformation N_{stab} . Thus, in the first case, the calculation is carried out using only the relaxation model for cyclic deformation [20,21], whereas in the second and third cases, it is carried out using both models. Let us consider in more detail the calculation scheme before $(N < N_{stab})$ and after $(N > N_{stab})$ the beginning of the stabilising cycle of plastic deformation.

Relaxation model of plasticity

In the relaxation model of plastic deformation [22,23], the specimen is deformed to $\varepsilon(t) = \varphi(t) \; H(t)$, where H(t) is the Heaviside function, and $\varphi(t)$ is the strain-time function. The dimensionless function of relaxation $0 < \gamma(t) \le 1$ is introduced:

4 N.S. Selyutina, Yu.V. Petrov

$$\gamma(t) = \begin{cases} 1, & \frac{1}{\tau} \int_{t-\tau}^{t} \left(\frac{\Sigma(s)}{\sigma_{y}}\right)^{\alpha} ds \leq 1, \\ \left(\frac{1}{\tau} \int_{t-\tau}^{t} \left(\frac{\Sigma(s)}{\sigma_{y}}\right)^{\alpha} ds\right)^{-1/\alpha}, & \frac{1}{\tau} \int_{t-\tau}^{t} \left(\frac{\Sigma(s)}{\sigma_{y}}\right)^{\alpha} ds > 1, \end{cases}$$

$$(1)$$

where τ is the incubation time, α is the sensitivity factor of the material to the load amplitude, $\Sigma(t) = E\varepsilon(t)$ is the stress-time function, σ_v is the static yield stress, and t is time.

The equality $\gamma(t)$ in Eq. (1) is related to inelastic strain accumulation prior to macroscopic yield at t., determined from the condition of equality to one integral condition in Eq. (1). A decrease in the relaxation function in the range $0 < \gamma(t) < 1$ corresponds to the transition of the material to the plastic deformation stage. During plastic deformation $t \ge t$., the condition is met for $\gamma(t)$:

$$\frac{1}{\tau} \int_{t-\tau}^{t} \left(\frac{\gamma(t)\Sigma(s)}{\sigma_{y}} \right)^{\alpha} ds = 1.$$
 (2)

Equality (2) is retained due to fixing state at the initial yield t = t. The calculation scheme for t, is given in [11], and subsequent relaxation of elastic stresses are accumulated in the material (0 < $\gamma(t)$ < 1). We determine the true stresses in the deformed specimen at $t \ge t$, in the following form:

$$\sigma(t) = \begin{cases} E\varepsilon(t), & t < t_*, \\ E\varepsilon(t)\gamma(t)^{1-\beta}, & t \ge t_*. \end{cases}$$
 (3)

where E is Young's modulus, and β is the dimensionless scalar parameter ($0 \le \beta < 1$), which describes the degree of material hardening. For $\beta = 0$, no hardening occurs. Young's modulus is determined from static experiments. We propose that Young's modulus is an invariant to loading history. A whole series of monotonic and monotonous deformation dependencies is predicted [22,23].

Relaxation model of cyclic deformation ($N < N_{stab}$)

To predict the cumulative plastic deformation in a material, we propose using a relaxation model of plastic deformation [22,23], modified for a cyclic process [20,21]. The main essence of the proposed relaxation model of cyclic deformation (CRM) is to explicitly take into account the relaxation process in the material.

The equation of the true stresses of the material using the model in [20,21] for the j-th cycle up to $N < N_{stab}$ is presented in the following form:

$$\sigma_{j}\left(\varepsilon_{j}(t)\right)\Big|_{N < N_{stab}; W < W_{*}} = \begin{cases} \sigma\left(\varepsilon_{j}(t)\right), \ t < t_{j}^{unl}, \\ E\left(\varepsilon_{j}(t) - \varepsilon_{j}^{unl}\right) H\left(\varepsilon_{j}(t) - \varepsilon_{j}^{unl}\right), \ t \geq t_{j}^{unl}. \end{cases}$$
(4)

where $\sigma_j(\varepsilon_j(t))$ is the stress time dependence, $\varepsilon_j(t)$ is the current strain time dependence, t_j^{unl} is the unloading time, $\varepsilon_j^{\text{unl}}$ is the strain at t_j^{unl} , N_{stab} is the number of stabilising cycles in the material, and t is the fracture time. The stress-strain relationship in true coordinates $\sigma(\varepsilon_j(t))$ at each j cycle is determined using the relaxation plasticity model [20,21].

$$\sigma\left(\varepsilon_{j}(t)\right) = \begin{cases} E\varepsilon_{j}(t), \ t < t_{y}^{j}, \\ E\left[\gamma_{j}(t)\right]^{1-\beta}\varepsilon_{j}(t), \ t \geq t_{y}^{j}, \end{cases}$$
(5)

with the stress relaxation function on the *j*-th cycle:

$$\gamma_{j}(t) = \begin{cases} 1, \ \frac{1}{\tau} \int_{t-\tau}^{t} \left(\frac{\Sigma(s)}{\sigma_{y}^{j}}\right)^{\alpha} ds \leq 1, \\ \left(\frac{1}{\tau} \int_{t-\tau}^{t} \left(\frac{\Sigma(s)}{\sigma_{y}^{j}}\right)^{\alpha} ds \right)^{-1/\alpha}, \frac{1}{\tau} \int_{t-\tau}^{t} \left(\frac{\Sigma(s)}{\sigma_{y}^{j}}\right)^{\alpha} ds > 1. \end{cases}$$

$$(6)$$

As noted in [22,23], the cyclic yield strength is less than the static yield strength; therefore, in the calculation scheme, we consider σ_y^j to be the static yield strength for samples subjected to cyclic loads.

The yield condition at the *j*-th cycle is determined by the following yield criterion [24]:

$$\frac{1}{\tau} \int_{t_y^j - \tau}^{t_y^j} \left(\frac{\Sigma(s)}{\sigma_y^j} \right)^{\alpha} ds = 1. \tag{7}$$

At the (j+1)-th cycle, the static yield strength is determined by the following condition:

$$\sigma_y^{j+1} + \sigma_y^j = 2 \left| \sigma_j \left(\varepsilon_j(t_j^{unl}) \right) \right|, \tag{8}$$

where $\sigma_y^0 = \sigma_y$. We assume that the time and cycle number are related by the ratio t = N/v, where v is the loading frequency [16].

Using the relaxation model of cyclic deformation (CRM) (4)–(7), with explicit consideration of the ongoing relaxation processes, makes it possible to predict the cumulative plastic strain and volumetric strain energy density in the current cycle. When the plastic deformation is stabilised, the model allows us to evaluate the cyclic strength of the material as the maximum stress of the material on the hysteresis loop, and the corresponding cycle number is N_{stab} .

To calculate the fracture moment when a material reaches cyclic strength σ_0 , we propose to use the condition of equality in the following energy criterion (fracture criterion):

$$W(t) \le W_*,\tag{9}$$

where W is the volumetric strain energy density, and W is the strain energy density under quasi-static loads. The parameter W is defined as the area of the subgraph of the resulting deformation response of the material, calculated using the relaxation model of cyclic deformation (Eqs. (4)–(7)):

$$W_j = \int \sigma_j(\varepsilon_j) d\varepsilon_j. \tag{10}$$

At each cycling step, the change in the cumulative damage parameter is calculated through the cumulative volumetric deformation energy density W_j at the j-th cycle of the material:

$$\omega_j = \frac{\sum_{k=1}^{j} W_k}{W_*}.\tag{11}$$

Kinetic damage equation $(N > N_{stab})$

In order to determine the number of the cycle before the fracture of the material (N-) with a steady-stabilising cycle of plastic deformation ($N > N_{stab}$), it is necessary to use the generalised damage equation [17] of the Kachanov-Rabotnov type [15] with the damage parameter $0 \le \omega \le 1$, defined as follows:

$$\frac{d\omega}{dN} = \frac{A(\sigma_0)^a}{v} \frac{\omega^b}{(1-\omega)^a},\tag{12}$$

6 N.S. Selyutina, Yu.V. Petrov

 σ_0 is the given time stress function, a, b and A are constants. At the beginning of the stabilisation mode N_{stab} , damage ω_0 accumulates in the material. The damage parameter ω_0 is determined by $\omega_0 = W_{stab}/W_*$, being the ratio of the volumetric strain energy density W_{stab} cumulating in a stable cycle N_{stab} to the volumetric strain energy density under quasistatic loads W^* . The volumetric strain energy density per cycle is defined as the area of the subgraph of the deformation diagram calculated using the relaxation model for cyclic deformation. We assume that σ_0 = const is a constant value, determined, using the relaxation model of plasticity in the stabilising cycle, to be the maximum stress of the material on the hysteresis loop.

To solve Eq. (12), a non-zero initial condition ω_0 is assumed, as was the case in the article of [25]:

$$\omega|_{N=N_{stab}} = \omega_0, \tag{13}$$

where $\omega = 1$ at the moment of fracture $N = N^*$ and the damage parameter is equal to 1. Separating the variables, we integrate Eq. (6) over time from N_{stab} to N. as follows:

$$N_* = N_{stab}(\sigma_0) + \frac{1}{A\sigma_0} \left(1 - \frac{1}{\omega_0^2}\right) \frac{\Gamma(a+1)\Gamma(1-b)}{\Gamma(a-b+2)},\tag{14}$$

where $\Gamma(x)$ is the gamma function, defined at x > 0 as:

$$\Gamma(x) = \int_0^\infty s^{x-1} e^{-s} ds. \tag{15}$$

Then, using Eqs. (4)–(15), it is possible to costruct the dependence of the critical stress before failure σ_0 on the cycle number N^* (or the fatigue S-N dependence).

General purpose of the FLMRD model

The main benefit of using the FLMRD model is its simultaneous consideration of two competing processes of plastic deformation and fracture. Its explicit representation of the relaxation function (6) makes it possible to predict the process of plastic deformation. A non-zero initial condition for the damage parameter allows us to estimate the history of the accumulated level of damage (12) in the material when there is no influence of plastic deformation.

Figure 2(a) shows a united fatigue curve for a hypothetical material in logarithmic coordinates under the staircase loading method. By drawing two tangent lines to the inclined portion of the fatigue curve, as shown in Fig. 1, it is possible to identify the stages of low-cycle fatigue (up to $2\cdot10^4$ cycles), high-cycle fatigue (from $2\cdot10^4$ to $3\cdot10^7$ cycles) and ultra-high-cycle fatigue (after $3\cdot10^7$ cycles). These three stages are plotted using the FLMRD model with a fixed set of parameters. Figure 2(b) plots the dependence of the cycle number at which new plastic deformations do not accumulate, N_{stab} , on the number of cycles before failure, N, for a hypothetical material, for which the united fatigue curve is shown in Fig. 2(a).

Each cyclic strength σ_0 corresponds to a cycle number N_{stab} . As shown in Fig. 2(a), with a decrease in the cyclic strength, the cycle number N_{stab} decreases, but the number of cycles before failure N increases. At $N \sim 4.10^7$ cycles, the material deforms elastically, since $N_{stab} = 1$. At $N < 4.10^7$, the material undergoes elastic-plastic deformation. The application of the evolutionary damage equation (7) allows us to "shift" the results on cyclic strength and N_{stab} obtained from the relaxation plasticity model (1)–(6) to the right and obtain the final united fatigue curve. In other words, using a combination of methods

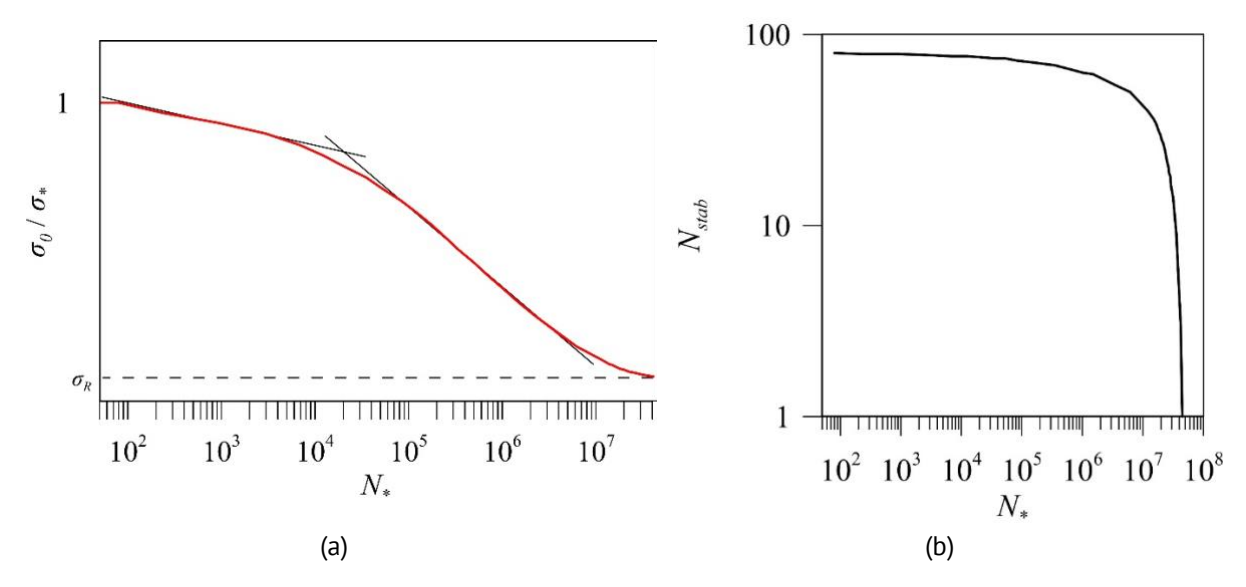


Fig. 2. (a) Dependence of the cyclic strength, normalised to the static strength of the hypothetical material, on the number of cycles for the hypothetical material. (b) The dependence of the cycle number at which new plastic deformations do not accumulate, N_{stab} , on the number of cycles before failure N for a hypothetical material

and obtain the final united fatigue curve. In other words, using a combination of methods to explicitly take into account relaxation processes and the process of damage accumulation, it becomes possible to construct united fatigue curve, including a continuous inclined section of a united fatigue curve that is important for engineering practice.

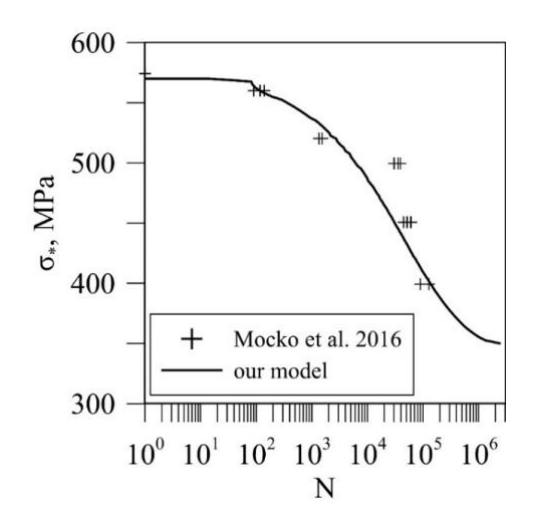
Prediction of cyclic strength of metals before ~106 cycle

In this section, the proposed model is used to predict the cyclic strength under low-cycle and high-cycle fatigue. Let us assess the performance of the proposed combined model with experimental data on soft loading for the two-phase steel DP500 [26], where σ_y^0 =350 MPa and σ^* =570 MPa, and X65 steel [27], where σ_y^0 =420 MPa and σ^* =620 MPa. The cyclic deformation in [26] was carried out based on the sinusoidal tensile load at a frequency of 10 Hz under the following conditions: the minimum stress was 0 and the average stress was half the maximum stress. Previously, based on the same experimental data, it was predicted that plastic deformation would be stabilised [20]. The evaluated parameters of the model were obtained as α = 1, τ = 0.67 ms, β = 0.067, α = 1 and β = 1 for DP500 steel and α = 1, α = 1 ms, α = 0.05, α = 1 and α = 1 for X65 steel (Table 1). For the selected set of parameters of the combined model, we can calculate the dependence of the fracture time on the stabilisation time by integrating Eq. (12):

$$N_* = t_{stab}(N_*) + \frac{1}{A\sigma_0}(\omega_0 - 1 - \ln \omega_0). \tag{16}$$

Figure 3 and 4 show the theoretical fatigue relationship for DP600 dual-phase steel and X65 steel, which is in good agreement with the experimental data. Figure 3 and 4 show that the combined model can predict the complete dependence of the ultimate stress before failure based on the number of cycles, both for low-cycle and high-cycle

8 N.S. Selyutina, Yu.V. Petrov



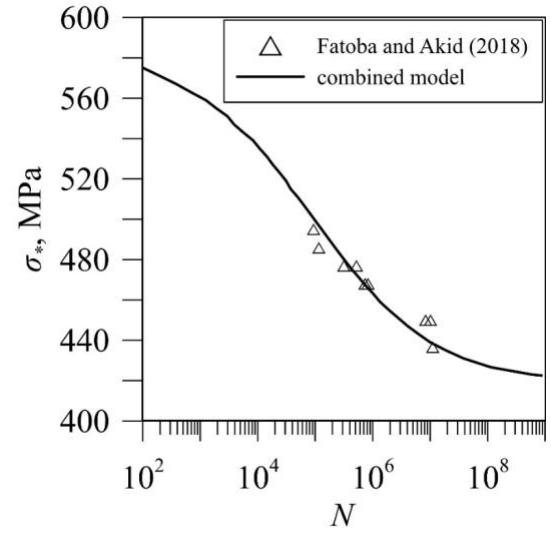


Fig. 3. A prediction of the united fatigue curve of DP500 steel based on the relaxation model of irreversible deformation during cyclic deformation, and experimental data [26]

Fig. 4. A prediction of the united fatigue curve of X65 steel based on the relaxation model of irreversible deformation during cyclic deformation and experimental data [27]

Table 1. The parameters of DP500 and X65 steel for the calculation of the fatigue curve

	α	τ	β	W	Α	а	b	$\sigma_{\!y}^0$	σ*
	-	Ms	ı	J	1/(MPa·s)	-	ı	MPa	MPa
DP500 steel	1	0.67	0.067	2.495	0.01	1	1	350	570
X65 steel	1	1	0.05	2.494	0.01	1	1	420	620

deformation. It is commonly believed that the boundary between low-cycle and high-cycle fatigue occurs at $\sim 5\cdot 10^4$ cycles. Within the framework of the combined model, there is no need for a clear division of cases into low-cycle and high-cycle fatigue, since a united fatigue dependence is predicted for the material.

Let us consider the possibility of predicting the number of cycles before failure depending on the deformation amplitude using 34CrNiMo6 [28–31]. The loading mode used in [28–31] is strain control at the symmetrical cycle. The best agreement with experimental data is achieved using the following parameters: E = 209 GPa, $\alpha = 1$, $\beta = 0.23$, $\sigma_y^0 = 600$ MPa, $\sigma_f = 1180$ MPa, A = 14, $W_0 = 440$, a = 1.2 and b = 1.68 (Table 2). The proposed model successfully predicts the number of cycles until fatigue failure at a given strain amplitude in the low-cycle and high-cycle fatigue ranges (Fig. 5). Note that the predicted united fatigue curve is based on experimental data covering a range of cycles to failure.

Table 2. The parameters of 34CrNiMo6 steel for the calculation of the fatigue curve

	α	τ	β	W	Α	а	b	σ_y^0	σ*
	-	Ms	-	J	1/(MPa·s)	-	-	MPa	MPa
34CrNiMo6	1	0.23	0.067	440	14	1.2	1.68	600	1180

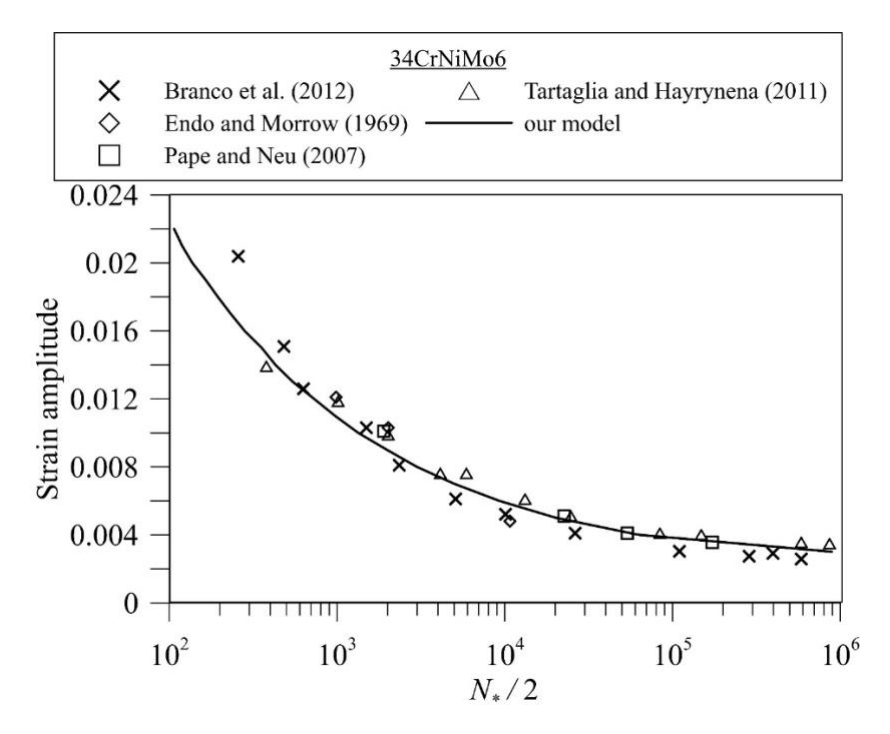


Fig. 5. A prediction of the fatigue curve (Wöhler diagram) of 34CrNiMo6 based on the relaxation model of irreversible deformation during cyclic deformation, and experimental data [28–31]

Prediction of united fatigue life curve based on FLMRD model

In this section, we consider the action of the FLMRD model with fatigue life curves, introduced in the "Fatigue life model of relaxation and damage" section. Examples of the low-cycle, high-cycle and giga-cycle fatigue life prediction for A2017-T4 aluminium alloy, 7075-T651 aluminium alloy, Ti-6Al-4V titanium alloy are shown in Figs. 6–9. Experimental data for A2017-T4 aluminium alloy [32], 7075 aluminium alloy [33,34], Ti-6Al-4V [35,36] and 300M steel [34] have been received in symmetrical compression/tension cyclic mode (R = -1). Parameters α , τ and β were obtained based on the assessment of deformation responses under both quasi-static and cyclic loading, presented in the corresponding experimental works [32–36]. The remaining parameters of the KDE model were selected based on the united fatigue life curves of the materials [32-36]. The best agreement with experimental data is achieved using the parameters, presented in Table 3. Significant differences in the parameters of the KDE model W and A are observed. The theoretical curves in Figs. 6-9 match both sections of the experimental curve well for short-term and long-term strengths within the framework of the FLMRD model, without focusing on the type of cyclic strength with a greater or lesser amount of plastic deformation. The theoretical unite fatigue curve is plotted up to 108 for aluminium alloys and up to 109 cycles for Ti-6Al-4V titanium alloy. Calculation of the deformation energy from the deformation response made it possible to set the initial condition for the kinetic equation of the model and simultaneously calculate both the short-term and long-term strength of metals. The presented kinetic-relaxation model can be applied to other materials and cyclic loading modes.

10 N.S. Selyutina, Yu.V. Petrov

						-				
Loading type	α	τ	Ε	β	W	Α	а	b	σ_y^0	σ*
	1	ms	GPa	_	J	(MPa·s)⁻¹	ı	ı	MPa	MPa
A2017	1	0.5	72	0.13	23	0.1	1.2	2.2	107	440
Ti-6Al-4V	1	0.3	127	0.15	190	150	1.4	2	170	1100
AA7075	1	0.5	72	0.15	18	0.3	1.25	2	131	632
M300 steel	1	0.7	210	0.15	190	40	1.4	2	680	1600

Table 3. The parameters of materials for the fatique life prediction based on FLMRD model

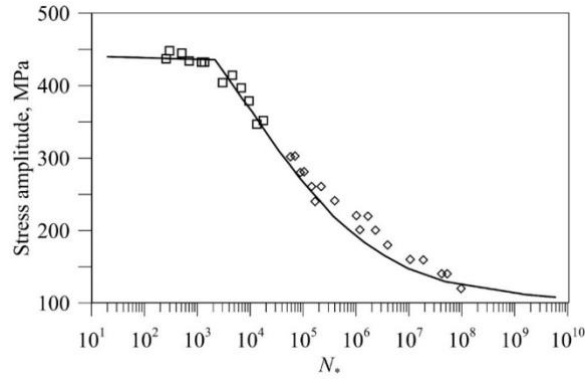


Fig. 6. A prediction of the fatigue life curve of A2017-T4 aluminium alloy based on FLMRD model and experimental data [32]

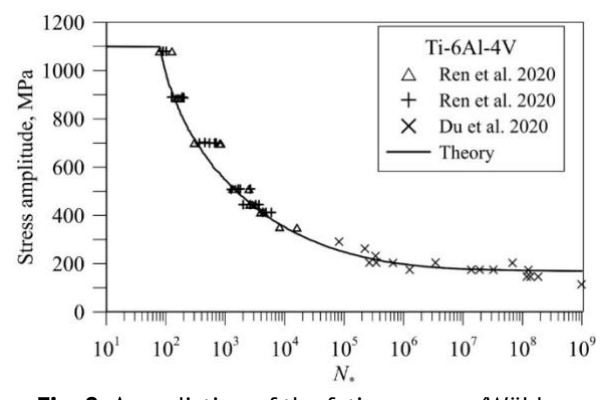


Fig. 8. A prediction of the fatigue curve (Wöhler diagram) of Ti-6Al-4V titanium alloy based on the relaxation model of irreversible deformation during cyclic deformation, and experimental data [35,36]

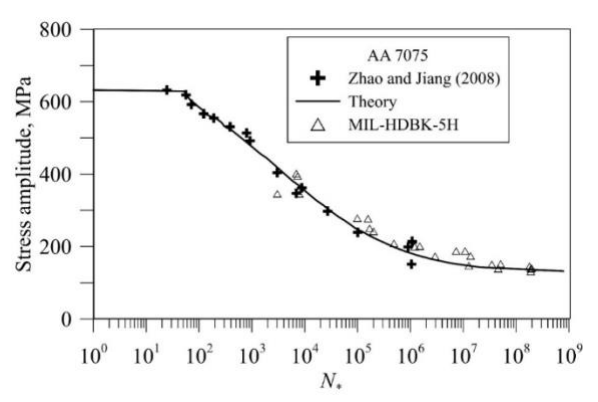


Fig. 7. A prediction of the fatigue life curve of 7075-T651 aluminium alloy based on FLMRD model and experimental data [33,34]

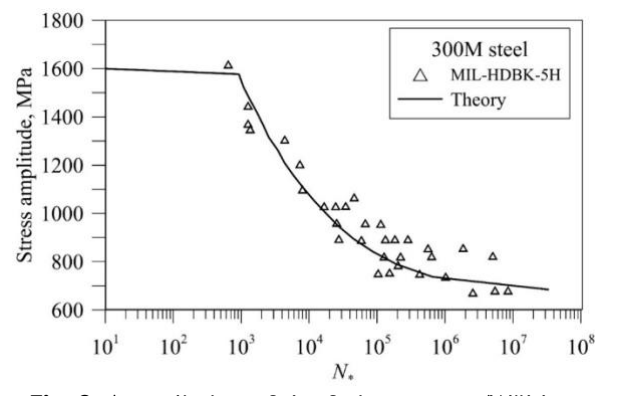


Fig. 9. A prediction of the fatigue curve (Wöhler diagram) of 300M steel based on the relaxation model of irreversible deformation during cyclic deformation, and experimental data [34]

Conclusions

An analysis of two fatigue dependencies was carried out: the short-term and long-term strengths of steels and the amplitude of deformations, both depending on the number of cycles before failure.

A predictive FLMRD model was established to estimate the united fatigue curve. The united theoretical fatigue curves of steel 45, DP 500 steel, X65 steel, 34CrNiMo6 steel, A2017-T4 aluminium alloy, 7075 aluminium alloy, Ti-6Al-4V and 300M steel show that the developed FLMRD model can serve as a convenient tool for modelling short-term and long-term strengths.

The FLMRD model can be used for the calculation of the number of cycles before fracture, cyclic strength, irreversible energy deformation (current, at the moment of the

completion of plastic deformation and at the moment of final brittle failure), accumulated irreversible deformation and the amount of cumulative damage.

The necessity of simultaneous consideration of the damage accumulation process under cyclic loads and the relaxation processes of plastic deformation is highlighted, and this can be carried out by considering the characteristic relaxation times of a given material.

CRediT authorship contribution statement

Nina S. Selyutina "Sce": writing – review & editing, writing – original draft, conceptualization, analysis of the result, investigation; **Yuri V. Petrov** "Sce": writing – original draft, the main idea, state of the problem, conceptualization, combining model, analysis of the result, supervision.

Conflict of interest

The authors declare that they have no conflict of interest.

References

- 1. Lakshmi S, Prabha DC. A Review on Low Cycle Fatigue Failure. *International Journal of Science Technology and Engineering*. 2017;3(11): 77 80.
- 2. Xu Y, Li X, Zhang Y, Yang J. Ultra-Low Cycle Fatigue Life Prediction Model A Review. *Metals.* 2023;13(6): 1142. 3. Jeddi D, Palin-Luc T. A review about the effects of structural and operational factors on the gigacycle fatigue of steels. *Fatigue and Fracture of Engineering Materials and Structures.* 2018;41(5): 969–990.
- 4. Sakai T. Historical review and future prospect for researcher on very high cycle fatigue of metallic materials. *Fatigue and Fracture of Engineering Materials and Structures*. 2023;46(4) 1217–1255.
- 5. Hectors K, Waele WD. Cumulative Damage and Life Prediction Models for High-Cycle Fatigue of Metals: A Review. *Metals*. 2021;11(2): 204.
- 6. Basquin OH. The exponential law of endurance tests. *Proceedings-American Society for Testing and Materials*. 1910;10: 625–630.
- 7. Arutyunyan AR. Influence of aging on fatigue strength of carbon fiber reinforced plastics. *Materials Physics and Mechanics*. 2024;52(1): 118-125.
- 8. Arutyunyan AR, Arutyunyan RA. Damage and fracture of viscous-plastic compressible materials. *Materials Physics and Mechanics*. 2020;44(2): 250-255.
- 9. Murakami Y, Takagi T, Wada K, Matsunaga H. Essential structure of S-N curve: Prediction of fatigue life and fatigue limit of defective materials and nature of scatter. *International Journal of Fatigue*. 2021;146: 106138.
- 10. Klemenc J, Fajdiga M. Joint estimation of E-N curves and their scatter using evolutionary algorithms. *International Journal of Fatigue*. 2013;56: 42-53.
- 11. Benedetti M, Fontanari V, Scardi P, Ricardo CLA, Bandini M. Reverse bending fatigue of shot peened 7075–T651 aluminium alloy: The role of residual stress relaxation. *International Journal of Fatigue*. 2009;31(8–9): 1225–1236.
- 12. Zhuang WZ, Halford GR. Investigation of residual stress relaxation under cyclic load. *International Journal of Fatique*. 2001;23: S31 37.
- 13. Jhansale HR, Topper TH. Engineering analysis of the inelastic stress response of a structural metal under variable cyclic strains. *Cyclic stress–strain behavior–analysis, experimentation, and failure prediction.* American Society for Testing and Materials ASTM; 1973. p.246–270.
- 14. Kodama S. The behavior of residual stress during fatigue stress cycles. In: *Proceedings of the international conference on mechanical behavior of metals II*. Kyoto (Japan); 1972. p.111–118.
- 15. Rabotnov YuN. *Problems of Strength of Materials and Structures*. Moscow: Izd. Akad. Nauk SSSR: 1959. (In Russian)

12 N.S. Selyutina, Yu.V. Petrov

16. Arutyunyan AR. Formulation of the fatigue fracture criterion of composite materials. *Vestnik of Saint Petersburg University. Mathematics. Mechanics. Astronomy.* 2020;7(3): 511–517 [in Russian].

- 17. Stepanova LV, Igonin SA. Rabotnov damage parameter and description of delayed fracture: Results, current status, application to fracture mechanics, and prospects. *Journal of Applied Mechanics and Technical Physics*. 2015;56: 282–292.
- 18. Tanaka K, Akiniwa Y. Fatigue crack propagation behaviour derived from S-N data in very high cycle regime. *Fatigue and Fracture of Engineering Materials and Structures*. 2002;25(8-9): 775-784.
- 19. Avilés R, Albizuri J, Rodríguez A. López de Lacalle LN. Influence of low-plasticity ball burnishing on the high-cycle fatigue strength of medium carbon AISI 1045 steel. *International Journal of Fatigue*. 2013;55: 230–244.
- 20. Selyutina NS, Petrov YV. Effect of plastic strain stabilisation under low-cycle deformation. *Physical Mesomechanics*. 2020;23: 384–389.
- 21. Selyutina NS, Smirnov IV, Petrov YuV. Stabilisation effect of strain hysteresis loop for steel 45. *International Journal of Fatigue*. 2021;145: 106133.
- 22. Selyutina N, Petrov YV. Instabilities of dynamic strain diagrams predicted by the relaxation model of plasticity. *Journal of Dynamic Behavior of Materials*. 2022;8: 304–315.
- 23. Petrov YV, Borodin EN. Relaxation Mechanism of Plastic Deformation and Its Justification Using the Example of the Sharp Yield Point Phenomenon in Whiskers. *Physics of the Solid State*. 2015;57(2): 353–359.
- 24. Selyutina NS, Petrov YuV. Prediction of the dynamic yield strength of metals using two structural-temporal parameters. *Physics of the Solid State*. 2018;60(2): 244–249.
- 25. Kashtanov AV, Petrov YuV. Energy Approach to Determination of the Instantaneous Damage Level. *Technical Physics*. 2006;51(5): 604–608.
- 26. Moćko W, Brodecki A, Kruszka L. Mechanical response of dual phase steel at quasi-static and dynamic tensile loadings after initial fatigue loading. *Mechanics of Materials*. 2016;92: 18–27.
- 27. Fatoba O, Akid R. Uniaxial cyclic elasto-plastic deformation and fatigue failure of API-5L X65 steel under various loading conditions. *Theoretical and Applied Fracture Mechanics*. 2018;94: 147–159.
- 28. Branco R, Costa JD, Antunes FV. Low-cycle fatigue behavior of 34CrNiMo6 high strength steel. *Theoretical and Applied Fracture Mechanics*. 2012;58(1): 28–34.
- 29. Endo T, Morrow J. Cyclic stress-strain and fatigue behavior of representative aircraft metals. *Journal of Materials*. 1969;4: 159–175.
- 30. Pape JA, Neu RW. A comparative study of the fretting fatigue behavior of 4340 steel and PH 13-8 Mo stainless steel. *International Journal of Fatigue*. 2007;29(12): 2219–2229.
- 31. Tartaglia J, Hayrynena KL. Comparison of fatigue properties of austempered vs quenched and tempered 4340 steel. *Journal of Materials Engineering and Performance*. 2011;21: 1008–1024.
- 32. Furuya Y, Nishikawa H, Hirukawa H, Nagashima N, Takeuchi E. NIMS fatigue data sheet on low- and high-cycle fatigue properties of A2017-T4 (Al-4.0Cu-0.6Mg) aluminium alloy. *Science and Technology of Advanced Materials: Methods*. 2023;3(1): 2234272.
- 33. Zhao T, Jiang Y. Fatique of 7075-T651 aluminum alloy. International Journal of Fatique. 2008;30(5): 834-849.
- 34. Military Handbook: Metallic materials and elements for aerospace vehicle structures. Department of Defense USA; 1998.
- 35. Du L, Qian G, Zheng L, Hong Y. Influence of processing parameters of selective laser melting on high-cycle and very-high-cycle fatigue behaviour of Ti-6Al-4V. *Fatigue and Fracture of Engineering Materials and Structures*. 2020;44(1): 240–256.
- 36. Ren YM, Lin X, Guo PF, Yang HO, Tan H, Chen J, Li J, Zhang YY, Huang WD. Low cycle fatigue properties of Ti-6Al-4V alloy fabricated by high-power laser directed energy deposition: Experimental and prediction. *International Journal of Fatigue*. 2019;127: 58–73.

Submitted: February 10, 2025 Revised: April 22, 2025 Accepted: May 12, 2025

Influence of grain size of nanocrystalline titanium on its dissolution intensity in aluminum

G.M. Poletaev ^{1 12}, Y.V. Bebikhov ², A.S. Semenov ²

ABSTRACT

Using molecular dynamics simulations, this study investigates the influence of grain size of nanocrystalline titanium on its dissolution intensity in aluminum at various temperatures, compared to the dissolution of monocrystalline titanium. It is shown that the grain size in nanocrystalline titanium significantly affects the intensity of mutual dissolution of the components. This is explained by the fact that grain boundaries act as channels for accelerated diffusion, and as the average grain size decreases, the density of grain boundaries increases. In the case of grains on the order of several nanometers, the density of grain boundaries and the contribution of grain boundary diffusion are relatively high. For example, at a temperature of 800 K, which is significantly below the melting point of aluminum, dissolution in the model occurred more intensely for grain sizes smaller than 9 nm than for monocrystalline titanium at 1100 K — this temperature is not only 300 K higher but also corresponds to liquid aluminum. Thus, the nanocrystalline structure and high density of grain boundaries in titanium may be one of the reasons, alongside the energy stored in defects due to deformation, for the reduction in activation energy for the synthesis reaction in the Ti–Al system following mechanical processing of the initial mixture.

KEYWORDS

molecular dynamics • titanium • intermetallide • diffusion • grain boundary

Funding. The study was funded by the Russian Science Foundation (project No. 24-22-00092, https://rscf.ru/project/24-22-00092/).

Citation: Poletaev GM, Bebikhov YV, Semenov AS. Influence of grain size of nanocrystalline titanium on its dissolution intensity in aluminum. Materials Physics and Mechanics. 2025;53(2): 13-24. http://dx.doi.org/10.18149/MPM.5322025_2

Introduction

Intermetallic compounds of the Ti–Al system and their alloys possess a combination of properties such as high yield strength at elevated temperatures and good oxidation and corrosion resistance, along with relatively low density, making them promising for use as high-temperature structural materials, particularly in the aerospace and automotive industries [1–5]. It is known that non-equilibrium processing methods, including intensive deformation, mechanical alloying, rapid quenching, etc., allow for the creation of various unique non-equilibrium microstructures capable of enhancing the mechanical properties of intermetallic alloys [6–9]. One promising method for producing intermetallics, including those in the Ti-Al system, is pre-treatment before the high-temperature synthesis reaction stage through mechanical processing of the initial metal powders, such as by milling in planetary ball mills [10–16]. During this mechanochemical activation process, so-called mechanocomposites are formed, consisting of a matrix made from a more ductile component (in this case, aluminum), within which nanosized particles



¹ Polzunov Altai State Technical University, Barnaul, Russia

² Polytechnic Institute of North-Eastern Federal University, Mirny, Russia

[™] qmpoletaev@mail.ru

of a more brittle component (titanium) are located [15,16]. Mechanical milling of the initial powders and the resulting nanocomposites are used, in particular, in the rapidly developing field of additive manufacturing [15,17]. This system is characterized by a high degree of non-equilibrium due to the high concentration of defects, interfaces, and internal stresses. One of the most interesting properties of such non-equilibrium systems consisting of nanocomposites is a significantly lower effective activation energy for the synthesis reaction compared to conventional powders: the synthesis reaction (ignition) begins at a temperature substantially lower than the melting point of aluminum [10–16].

Currently, the question remains open regarding what exactly is the main factor in the reduction of ignition temperature in mechanically activated mixtures. Among the reasons typically considered are the following: 1) preliminary mixing of components and a significant increase in their contact area; 2) accumulation of excess energy due to deformation in the form of various structural defects, which can be released as additional heat during structural relaxation; 3) a decrease in the melting point of aluminum due to the presence of a high concentration of defects or even an amorphous phase; 4) more intense mutual diffusion due to the presence of a high density of diffusion channels in the form of grain boundaries, predominantly in titanium.

The first reason mentioned, namely the increase in the contact area of the components, is sometimes cited as the main reason for the decrease in the activation energy of the synthesis reaction, often in combination with the second one, i.e. the accumulation of excess energy in the form of defects, as, for example, in [18,19], where molecular dynamics simulation of the deformation of round metal particles, their subsequent deformation and the initial stage of mutual diffusion was carried out. However, strictly speaking, an increase in only the contact area of the components cannot lead to a decrease in the activation energy of the synthesis reaction and, accordingly, the ignition temperature. This only leads to an increase in the intensity of dissolution, which, in particular, was shown by us in the study of the dissolution of a round titanium particle in aluminum [20], as well as in the simulation of mutual diffusion in the case of a flat interphase boundary [21].

The second mentioned reason is the accumulation of excess energy during deformation in the form of non-equilibrium defects in the structure of the components, such as grain boundaries, dislocations, disclinations, point defects, and their complexes. This cause for the reduction of activation energy for the synthesis reaction is identified as a primary factor in works such as [22–24]. Indeed, excess or accumulated potential energy can be released upon heating due to partial healing of the structure and a reduction in defect density. For instance, in [25,26], we demonstrated that during the recrystallization of metals with a nanocrystalline structure, characterized by a very high density of grain boundaries compared to conventional polycrystals, the release of energy and temperature increase can be significant and substantially influence diffusion processes.

Sometimes, another reason for the reduction of ignition temperature in mechanically activated powders is considered to be the possible decrease in the melting point of nanocrystalline aluminum compared to conventional coarse-grained aluminum. It is known that the onset temperature for the high-temperature synthesis reaction in systems such as Ti–Al and Ni–Al, in the case of conventional powders, coincides with the

melting point of aluminum. Numerous studies, primarily conducted through simulations, have indeed shown that nanomaterials exhibit what is known as the "size-dependent melting point depression phenomenon", meaning that the melting temperature of nanomaterials depends on their effective size: grain size, film thickness, and nanoparticle diameter. Regarding materials with a nanocrystalline structure, works [27-32] have demonstrated through molecular dynamics simulations that melting in these materials is not a homogeneous process; it typically begins at free surfaces and grain boundaries. A reduction in average grain size led to a decrease in the melting point of nanocrystalline Ag [28,29] and Al [30,31]. In [25,26], we also observed a decrease in the melting point for Ni nanoparticles with a nanocrystalline structure compared to monocrystalline particles. However, in another of our studies [20], dedicated to investigating the dissolution of a titanium nanoparticle in aluminum, it was shown that the structural state of titanium has a much greater influence on the intensity of mutual diffusion than the structural state of aluminum. Therefore, the reason related to a possible decrease in the melting point of aluminum does not seem to be primary in the case of reducing the onset temperature for the synthesis reaction in powders subjected to mechanical activation.

The fourth possible reason, which this work addresses, is the formation of a high concentration of accelerated diffusion channels in titanium due to intensive deformation, manifested as grain boundaries, dislocations, and pores. The role of these additional channels (primarily grain boundaries) is seen as one of the main factors, alongside the energy accumulated in defects. It is known that diffusion along grain boundaries is orders of magnitude more intense than diffusion in the bulk involving conventional point defects, and the presence of a high density of grain boundaries can lead to a sufficiently high rate of mutual diffusion, comparable to diffusion at the onset temperature of the reaction. This work aims to test this hypothesis and is dedicated to investigating, using molecular dynamics methods, the influence of grain size of nanocrystalline titanium on its dissolution intensity in aluminum at various temperatures compared to the dissolution of monocrystalline titanium.

Description of the model

To describe the interatomic interactions in the Ti–Al system, EAM potentials from [33] were used, which were derived based on comparisons with experimental data and *ab initio* calculations for various properties and structures of the metals Ti, Al, and the intermetallic compounds Ti₃Al and TiAl. These potentials have proven effective in various studies and have undergone successful validation across a wide range of mechanical and structural-energy properties of Ti-Al alloy systems [33−36].

The interphase boundary between Ti and Al was created at the center of the simulated computational cell along the XY plane, as shown in Fig. 1(a). The number of Ti atoms was approximately equal to the number of Al atoms. Periodic boundary conditions were applied along all axes. A vacuum layer was created along the Z-axis, parallel to the interphase boundary (Fig. 1(a)), allowing the bimetal to freely change volume during the simulation of mutual diffusion. When varying the temperature, thermal expansion of the metals was taken into account, and the dimensions of the computational cell were adjusted accordingly. The dimensions along the X and Y axes were chosen to be

multiples, with minimal possible deviation, of the periodicity of both Ti and Al crystal lattices. Additionally, the unequal thermal expansion of metals was also considered for each specific temperature at which the simulation was conducted. The dimensions of the cell along all axes were approximately 20–25 nm, and the total number of atoms was around 300 thousand. Thus, an NPT canonical ensemble was used in the model. To maintain a constant temperature, a Nose-Hoover thermostat was applied. The time integration step in the molecular dynamics method was set to 2 fs.

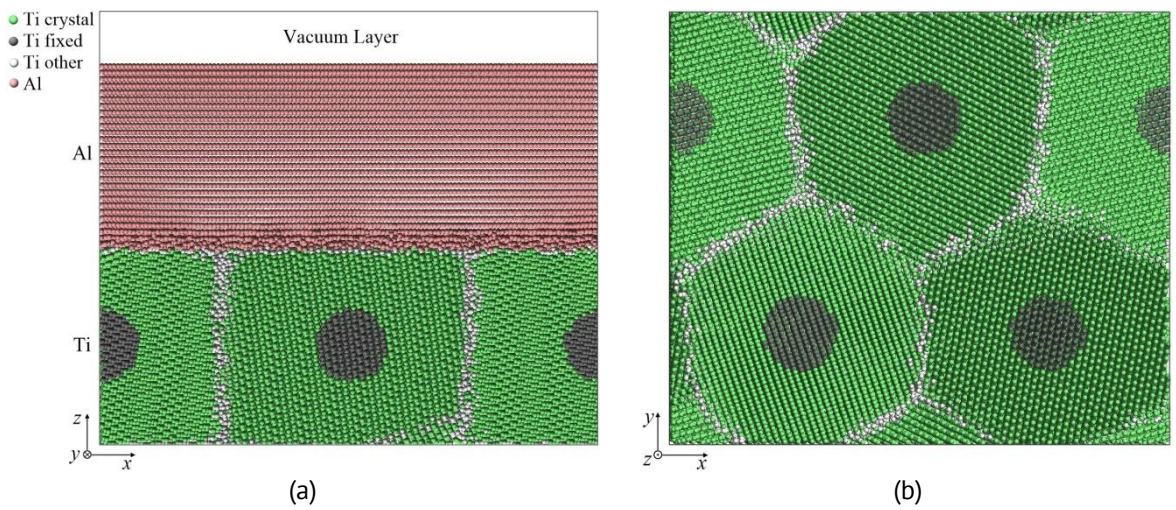


Fig. 1. Example of a computational cell containing the interface between aluminum and nanocrystalline titanium with an average grain size of 8.8 nm: (a) section in the XZ plane; (b) section of titanium in the XY plane

In works [20,21], we previously established that the intensity of mutual diffusion at the Ti–Al interface is primarily influenced by the structure of titanium: the presence of defects, the orientation of the interphase boundary relative to the titanium lattice, etc. The structure of aluminum is much more easily transformed and tends to adapt to the orientation of the titanium lattice near the interphase boundary [21]. When aluminum has a nanocrystalline or amorphous structure, rapid recrystallization or crystallization (in the case of an initially amorphous structure) would occur at temperatures close to its melting point (which are considered in this work). Therefore, creating a nanocrystalline structure not only in titanium but also in aluminum does not make sense.

The nanocrystalline structure of titanium with initially uniform grain sizes was created as follows. In the ideal titanium crystal, prior to the stage of bonding with aluminum, the centers of future grains were determined based on the specified average grain size. These centers were located in the computational cell at the nodes of a superlattice with hexagonal packing in the XY plane, parallel to the interphase boundary (Fig. 1(b)). The structure around each center was rotated in space at random angles within spheres with a diameter of 0.8 times the specified grain size (the nearest distance between centers). With the structure inside the spheres fixed, the remaining structure was melted and then subjected to crystallization simulation by holding it for 500 ps at a temperature of 1500 K. In the final stage, the structure was cooled to 0 K. The rotation of grains when creating their arbitrary orientation in space was performed around two axes

by random angles. In this regard, the boundaries were generally of a mixed type and mostly high-angle. Boundaries of a special type were not observed in the model.

To prevent the influence on the results of recrystallization and grain growth during the simulation, especially for small grains, the structure at the centers of the grains within spheres with a diameter of 0.3 times the average grain size remained fixed throughout the simulation. The fixed regions at the centers of the grains are highlighted in dark gray in Fig. 1(b). This was done to conduct the study of mutual diffusion under conditions of unchanged grain size.

The average grain size varied from 2.7 to 8.8 nm. In Fig. 1(b), sections of the computational cells with grains sized 8.8 nm are shown using a crystal phase visualizer based on the Common Neighbor Analysis (CNA) method [37]. Green Ti atoms are those whose nearest environment corresponds to the HCP crystal structure, white atoms indicate that the crystal lattice is either undefined or corresponds to an amorphous structure, and dark gray atoms are those that remained stationary during the simulation. The grains in the model had a shape close to that of an icosahedron. In most cases, the grain boundaries were of a mixed type.

After the stage of creating the nanocrystalline titanium structure, the next step was to create a layer of aluminum with approximately the same number of atoms as that of titanium and to bond it with titanium. Following this, the structure was relaxed once more, but at a low starting temperature, with subsequent cooling to a temperature close to 0 K.

In addition to the interfaces between nanocrystalline titanium and aluminum, the boundaries between monocrystalline titanium and aluminum were also considered for comparison. Two orientations of the boundary relative to the crystal lattices of Ti (HCP) and Al (FCC) were examined: (0001):(111) and (0011):(001).

Results and Discussion

For a quantitative assessment of mutual diffusion at the interphase boundary, we found the use of a traditional diffusion coefficient, derived from real experiments, to be inconvenient and fraught with several drawbacks, primarily related to the necessity and complexity of isolating only the mutual component of diffusion alongside, for example, self-diffusion and other possible atomic movements in the model. In a computer model, it is possible to utilize more precise and specific characteristics. In our case, to evaluate the dissolution of atoms of one metal in another, a special characteristic was used — the specific number of dissolved atoms $\Delta N/S$, where ΔN is the difference in the number of dissolved atoms of the metal in question at the current and initial time points, and S is the area of the interphase boundary. An atom of the metal in question was considered dissolved if the number of atoms of the other metal in its immediate vicinity exceeded 50 %. The immediate vicinity was defined as a volume within a radius of 0.37 nm, which includes only the first coordination sphere. At the initial stage of mutual diffusion, that is, when one of the metals contains a relatively low concentration of the second metal, which is considered in the present work, the mutual diffusion coefficient of titanium atoms is linearly proportional to the specific number of dissolved atoms.

Figure 2 shows examples of the dependence of the quantity $\Delta N/S$ on the time of computer simulation for cases with average grain sizes in titanium of 3 and 7.4 nm at

constant temperatures below and above the melting point of aluminum: 800 K (Fig. 2(a)) and 1100 K (Fig. 2(b)). In all cases, as seen in the figures, dissolution initially occurred rapidly, then the rate decreased and subsequently remained approximately constant. A similar dissolution behavior was observed by other researchers, for example in [38,39], as well as by us in [20] during the investigation of the dissolution of titanium nanoparticles in aluminum. This behavior is explained by the formation of a diffusion zone saturated with atoms of both components during the initial stage.

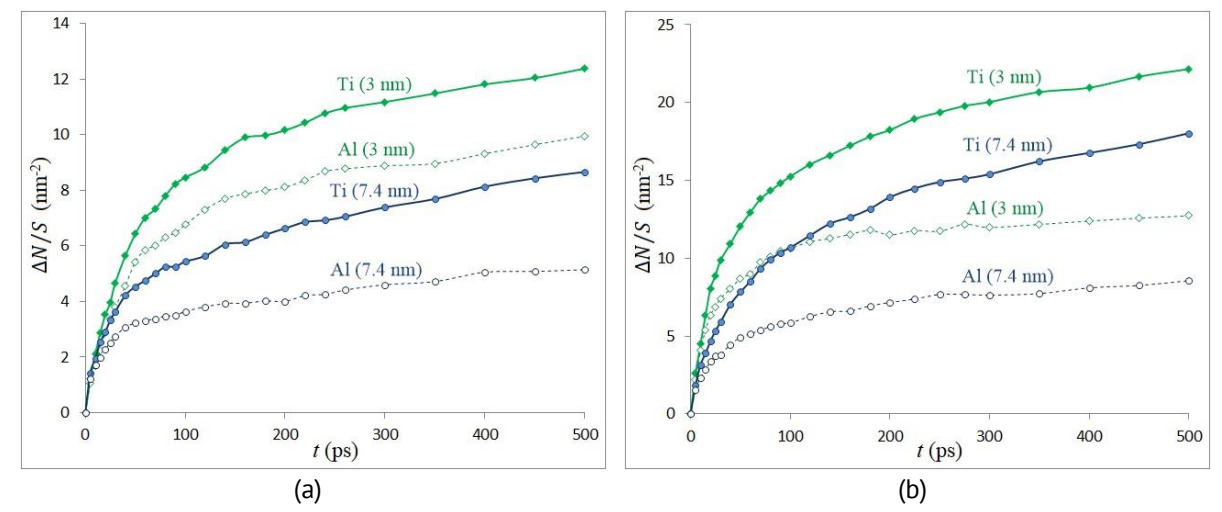


Fig. 2. Dependencies of the specific number of dissolved atoms $\Delta N/S$ on the time of computer simulation for average grain sizes in titanium of 3 and 7.4 nm at constant temperatures: (a) 800 K, (b) 1100 K

As can be seen from the provided dependencies, titanium diffuses into aluminum significantly more intensively than aluminum diffuses into titanium. With increasing temperature, and especially after the melting of aluminum (Fig. 2(b)), this difference only increases. This is a well-known phenomenon that, in the case of solid-state contact, is explained by the relatively lower mobility of atoms in the titanium lattice, primarily due to the greater depth of the potential wells in which titanium atoms are located. Upon melting aluminum, both self-diffusion in aluminum and the diffusion of titanium atoms in liquid aluminum significantly increase, while titanium remains in a crystalline state.

The graphs presented in Fig. 2 also show that the diffusion of both titanium atoms into aluminum and aluminum atoms into titanium occurs significantly more intensively for a grain size of 3 nm compared to a grain size of 7.4 nm. This already serves as qualitative evidence that grain size, or more precisely, the density of grain boundaries in titanium, affects the intensity of mutual diffusion.

To investigate this issue in more detail, we obtained the dependencies of the specific number of dissolved atoms $\Delta N/S$ on temperature after computer simulations lasting 300 ps for all considered grain sizes in titanium (Fig. 3). The temperature was maintained constant during the simulation, with values ranging from 500 to 1200 K. For comparison, similar dependencies were also obtained for the cases of the interphase boundary between monocrystalline titanium and aluminum with boundary orientations relative to the crystal lattices of Ti and Al (0001):(111) and (0011):(001) (the lower graphs in Fig. 3, highlighted in red).

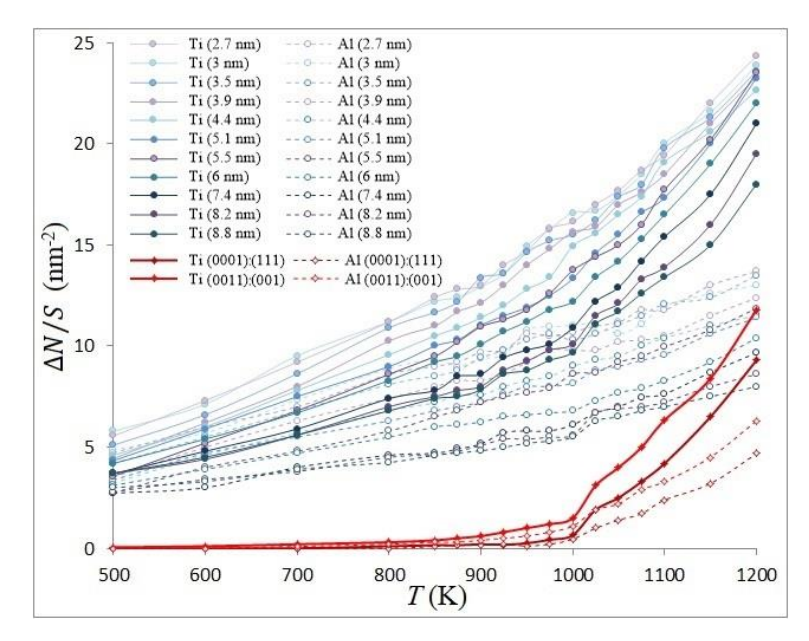


Fig. 3. Dependencies of the specific number of dissolved atoms $\Delta N/S$ on temperature after computer simulation for 300 ps for various grain sizes in titanium. Solid curves represent the dissolution of titanium in aluminum, while dashed curves represent the dissolution of aluminum in titanium

As the temperature increases, the intensity of diffusion also increases, which is consistent with the classical Arrhenius equation for diffusion, according to which the probability of elementary diffusion events exponentially rises with temperature. However, it should be understood that the classical Arrhenius equation is intended to describe steady-state diffusion, meaning that the diffusion flux and diffusion coefficient remain constant over the time interval considered. In our case, however, the diffusion process is more complex: as shown above (Fig. 2), it involves at least two stages characterized by different diffusion rates of the components. A third stage is also to be expected — gradual slowing of diffusion due to the equalization of component concentrations in the mixture.

As seen in Fig. 3, with increasing temperature, the intensity of titanium dissolution in aluminum increases faster than that of aluminum in titanium, especially after the melting of aluminum. Titanium remained in a solid state throughout the entire temperature range considered – the mobility of atoms in titanium was significantly lower than that of atoms in aluminum.

After the melting of aluminum (in the model, the melting temperature of aluminum was approximately 1015 K), a noticeable jump can be observed in the graphs, which became more pronounced with increasing average grain size. The most significant step was observed in the case of monocrystalline titanium (the lower graphs in Fig. 3). This clearly demonstrates the influence of the aggregate state of aluminum on the diffusion rate: in the case of monocrystalline titanium, this influence is decisive; however, in the case of a nanocrystalline structure with grain sizes on the order of several nanometers, this influence is significantly weaker, and for grain sizes less than approximately 6 nm, it is almost negligible.

It should be noted that the authors of the potential for Al obtained a melting temperature value of 1042 K [40]. However, this value was found in [40] for

computational cells that contained no defects, including surfaces. In [32], we demonstrated that in the presence of grain boundaries or free surfaces, melting occurs heterogeneously and begins at these locations, resulting in a lower melting temperature in the model compared to that calculated by the authors of the potential for a defect-free crystal. For example, it was shown in [32] that the melting temperature depends on the crystallographic orientation of the surface. The following values were obtained for aluminum in [32]: (110) - 990 K, (100) - 1004 K, (111) - 1016 K.

In [21], we previously demonstrated that the orientation of the interphase boundary relative to the titanium lattice (and to a significantly lesser extent, relative to the aluminum lattice) affects the intensity of mutual diffusion. For the orientations considered in this work, diffusion is more intense for the orientation (0011):(001) and less intense for the orientation (0001):(111), as clearly seen in the graphs in Fig. 3 (lower graphs). This is explained by the density of atoms in the near-surface layer of titanium, specifically by the difference in depths of the potential wells in which they are located. Different energies are required to detach them from the plane and draw them into the aluminum phase for different orientations.

The main conclusion that can be drawn from the graphs in Fig. 3 is the critical influence of grain size in titanium on the intensity of mutual dissolution of the components. Indeed, as seen in Fig. 3, as the average grain size decreases, and consequently the density of grain boundaries in titanium increases, the specific number of dissolved atoms $\Delta N/S$ significantly increases. This is particularly evident when comparing the values of $\Delta N/S$ obtained for monocrystalline titanium (the lower red graphs in Fig. 3) and for the nanocrystalline structure (the upper graphs). It is well known that grain boundaries act as channels for accelerated diffusion, with diffusion along grain boundaries occurring orders of magnitude faster than in the bulk of the grains [41]. As the average grain size decreases, the density of grain boundaries increases. In our case, with grains only a few nanometers in size, the density of grain boundaries and the contribution of grain boundary diffusion are relatively very high.

For clarity, to demonstrate that a sufficiently high density of grain boundaries in titanium can significantly reduce the activation energy of the synthesis reaction, Fig. 4 presents the dependencies of $\Delta N/S$ on the average grain size d in titanium. Three pairs of graphs are shown for the dissolution of titanium and aluminum: at temperatures of 800 and 1100 K. For comparison, the values of $\Delta N/S$ for the case of monocrystalline titanium with the initial orientation of the interphase boundary (0011):(001) at 1100 K are indicated by dashed lines (at this temperature, aluminum is liquid, so its initial orientation is irrelevant). In the case of the (0011) orientation, dissolution occurs faster than with the (0001) boundary orientation; therefore, the first option was chosen for comparison.

As the average grain size d decreases, the specific number of dissolved atoms $\Delta N/S$ for both titanium and aluminum increases, which clearly illustrates the influence of grain boundary density in titanium on the intensity of mutual diffusion. Figure 4 also clearly shows that even at a temperature of 800 K, which is significantly below the melting point of aluminum, dissolution is more intense for grain sizes less than 9 nm than for the case of monocrystalline titanium at 1100 K. This latter temperature is not only 300 K higher but also corresponds to aluminum that is already in a liquid state.

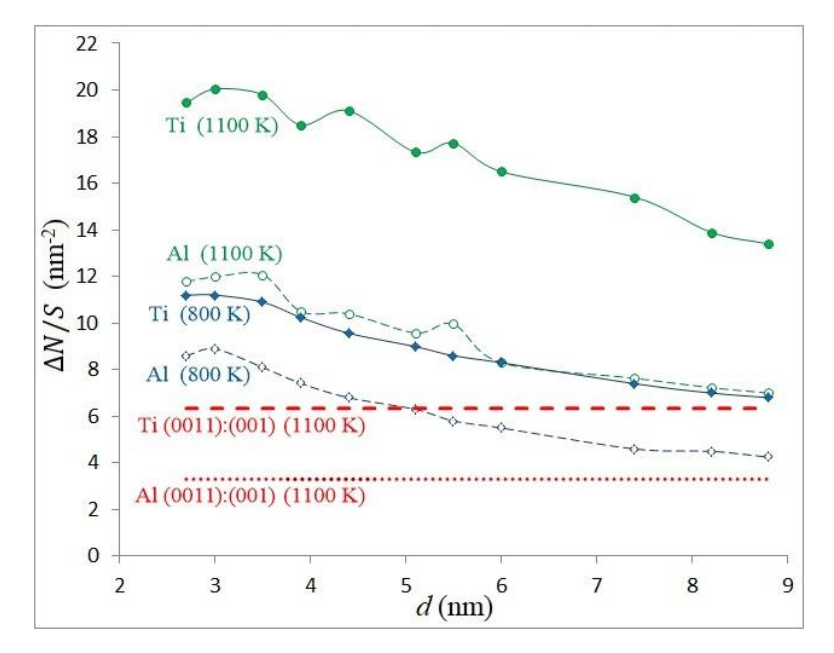


Fig. 4. Dependencies of the specific number of dissolved atoms $\Delta N/S$ on the average grain size d in titanium during simulation for 300 ps at temperatures of 800 K and 1100 K. For comparison, the values of $\Delta N/S$ for the case of monocrystalline titanium with the initial orientation of the interphase boundary (0011):(001) at 1100 K are also shown as dashed lines

To demonstrate that the grain boundaries in the model indeed served as channels for facilitated diffusion for both aluminum atoms diffusing into the titanium phase and titanium atoms migrating more intensively into aluminum from the grain boundaries, Fig. 5 presents an example of the distribution of titanium atoms (Fig. 5(a)) and aluminum atoms (Fig. 5(b)) in a layer of the other metal near the interphase boundary. These images were obtained for an average grain size of 7.4 nm and after 500 ps of simulation at a temperature of 900 K, which is below the melting point of aluminum.

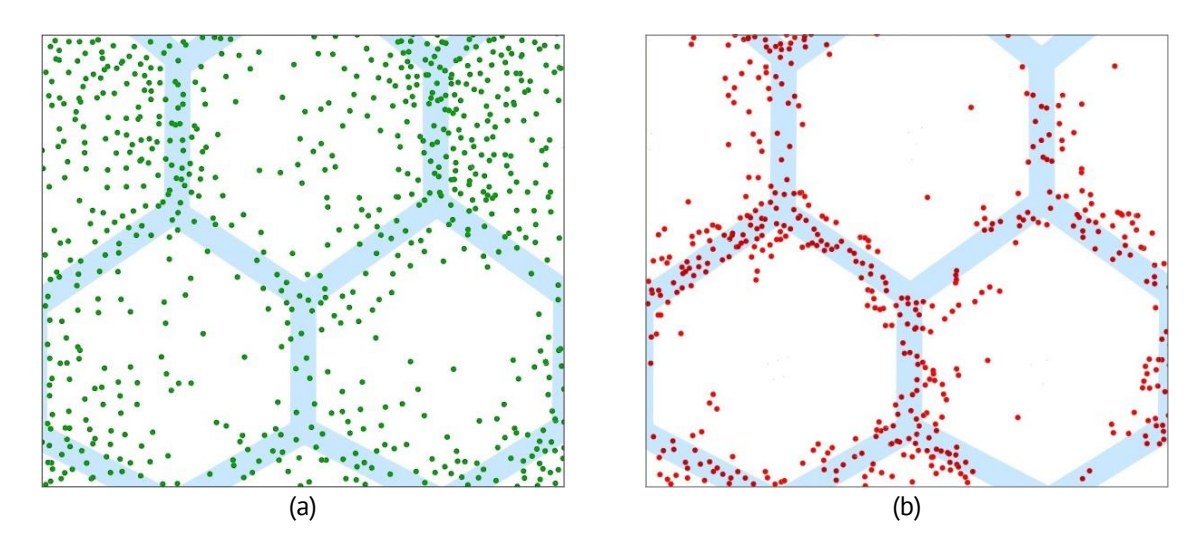


Fig. 5. Distributions of titanium (*a*) and aluminum atoms (*b*) in a layer of the other metal near the interphase boundary after simulation at a temperature of 900 K for 500 ps. Average grain size is 7.4 nm. Atoms of the second metal, into which the atoms have diffused, are not shown. The positions of the grain boundaries in titanium are indicated by wide blue lines

In the figures, especially in the case of aluminum diffusion into titanium (Fig. 5(b)), it is clearly visible that diffusion predominantly occurs along the grain boundaries (the positions of the boundaries are indicated by wide blue lines in the images). The intensity of diffusion along different boundaries, as can be observed, varied. This is evidently related to the characteristics of the boundaries that affect diffusion permeability, particularly their energy and specific free volume [41].

In the case of titanium atoms diffusing into the aluminum phase (Fig. 5(a)), a greater blurring is observed compared to the diffusion of aluminum atoms into titanium. This is apparently related to the relatively "looser" structure of aluminum and the comparatively greater mobility of titanium atoms in aluminum than vice versa.

Thus, based on the results obtained in this study, as well as on the findings of our previous works [20,21,25] and works of other authors [22–24], we can conclude that among the four potential factors mentioned in the introduction that may influence the reduction of the activation energy of the synthesis reaction in the Ti–Al system after mechanical treatment of the initial mixture, two factors make the primary contribution: the energy stored in defects and the high density of grain boundaries in titanium. In the first case, as a result of structural transformations, part of the energy stored in defects created during intense deformation is released upon heating and "healing" of the structure. This additional energy reduces the amount of energy required to initiate the synthesis reaction. In the second case, grain boundaries in titanium serve as channels for accelerated or facilitated diffusion. As their density increases, the intensity of mutual diffusion also increases proportionally, while the activation energy for diffusion and, consequently, the activation energy for the synthesis reaction also decrease.

Conclusions

Using molecular dynamics simulations, this study investigates the influence of grain size of nanocrystalline titanium on its dissolution intensity in aluminum at various temperatures, compared to the dissolution of monocrystalline titanium.

In the modeling of mutual diffusion, it was shown that, regardless of the grain size in titanium, the diffusion process involved two stages. Initially, the dissolution of the components occurred intensely, then the dissolution rate decreased and subsequently remained approximately constant. This pattern of dissolution is explained by the formation of a diffusion zone saturated with atoms of both components during the first stage. A third stage is also to be expected, which lies beyond the time frame of the model — gradual slowing of diffusion due to the equalization of component concentrations in the mixture.

In our work, it has been shown that the grain size in nanocrystalline titanium significantly affects the intensity of mutual dissolution of the components. This is explained by the fact that grain boundaries act as channels for accelerated diffusion, with diffusion along grain boundaries occurring orders of magnitude faster than in the bulk of the grains. As the average grain size decreases, the density of grain boundaries increases. In the case of grains on the order of several nanometers, the density of grain boundaries and the contribution of grain boundary diffusion are relatively very high. For example, at a temperature of 800 K, which is significantly below the melting point of aluminum, dissolution in the model was more intense for grain sizes less than 9 nm than for the case

of monocrystalline titanium at 1100 K, which is not only 300 K higher but also corresponds to aluminum that is already in a liquid state.

Thus, the nanocrystalline structure and high density of grain boundaries in titanium may be one of the reasons, alongside the energy stored in defects due to deformation, for the reduction in activation energy for the synthesis reaction in the Ti–Al system following mechanical processing of the initial mixture.

CRediT authorship contribution statement

Gennady M. Poletaev Sce: conceptualization, writing – review & editing, writing – original draft; Yuriy V. Bebikhov Sce: investigation, data curation; Alexander S. Semenov Sce: investigation, data curation.

Conflict of interest

The authors declare that they have no conflict of interest.

References

- 1. Kim YW. Ordered intermetallic alloys, part III: gamma titanium aluminides. *The Journal of The Minerals, Metals & Materials Society.* 1994;46: 30–39.
- 2. Appel F, Beaven PA, Wagner R. Deformation processes related to interfacial boundaries in two-phase γ-titanium aluminides. *Acta Metallurgica et Materialia*. 1993;41(6): 1721–1732.
- 3. Lapin J. TiAl-based alloys: Present status and future perspectives. In: *Proceedings of the Metal; Tanger: Ostrava, Czech Republic.* 2009;19(21.5): 2019–2031.
- 4. Tetsui T. Manufacturing technology for gamma-TiAl alloy in current and future applications. *Rare Metals*. 2011;30: 294–299.
- 5. Voisin T, Monchoux J-P, Couret A. Near-net shaping of titanium-aluminum jet engine turbine blades by SPS. In: *Spark Plasma Sintering of Materials*. Cham: Springer; 2019. p.713–737.
- 6. Morris MA, Leboeuf M. Grain-size refinement of γ -Ti-Al alloys: effect on mechanical properties. *Materials Science and Engineering: A.* 1997;224(1–2): 1–11.
- 7. Bohn R, Klassen T, Bormann R. Mechanical behavior of submicron-grained γ-TiAl-based alloys at elevated temperatures. *Intermetallics*. 2001;9(7): 559–569.
- 8. Kambara M, Uenishi K, Kobayashi KF. Nano-structured intermetallic compound TiAl obtained by crystallization of mechanically alloyed amorphous TiAl, and its subsequent grain growth. *Journal of Materials Science*. 2000;35: 2897–2905.
- 9. Kimura H. High-strength intermetallic TiAl synthesized via high-temperature crystallization of the amorphous alloy. *Philosophical Magazine A.* 1996;73(3): 723–737.
- 10. Boldyrev VV, Tkacova K. Mechanochemistry of Solids: Past, Present, and Prospects. *Journal of Materials Synthesis and Processing*. 2000;8: 121–132.
- 11. Rogachev AS, Shkodich NF, Vadchenko SG, Baras F, Chassagnon R, Sachkova NV, Boyarchenko OD. *International Journal of Self-Propagating High-Temperature Synthesis*. 2013;22: 210–216.
- 12. Rogachev AS, Shkodich NF, Vadchenko SG, Baras F, Kovalev DY, Rouvimov S, Napapushev AA, Mukasyan AS. Influence of the high-energy ball milling on structure and reactivity of the Ni+Al powder mixture. *Journal of Alloys and Compounds*. 2013;577: 600–605.
- 13. Shuck CE, Mukasyan AS. Reactive Ni/Al Nanocomposites: Structural Characteristics and Activation Energy. *The Journal of Physical Chemistry A*. 2017;121(6): 1175–1181.
- 14. Rogachev AS. Mechanical activation of heterogeneous exothermic reactions in powder mixtures. *Russian Chemical Reviews*. 2019;88(9): 875–900.
- 15. Nepapushev AA, Moskovskikh DO, Buinevich VS, Vadchenko SG, Rogachev AS. Production of rounded reactive composite Ti/Al powders for selective laser melting by high-energy ball milling. *Metallurgical and Materials Transactions B.* 2019;50: 1241–1247.

- 16. Filimonov VYu, Loginova MV, Ivanov SG, Sitnikov AA, Yakovlev VI, Sobachkin AV, Negodyaev AZ, Myasnikov AYu. Peculiarities of phase formation processes in activated Ti+Al powder mixture during transition from combustion synthesis to high-temperature annealing. *Combustion Science and Technology*. 2019;192(3): 457 470.
- 17. Nguyen Q, Huang C, Schoenitz M, Sullivan KT, Dreizin EL. Nanocomposite thermite powders with improved flowability prepared by mechanical milling. *Powder Technology*. 2018;327: 368–380.
- 18. Fourmont A, Politano O, Le Gallet S, Desgranges C, Baras F. Reactivity of Ni-Al nanocomposites prepared by mechanical activation: a molecular dynamics study. *Journal of Applied Physics*. 2021;129(6): 065301.
- 19. Baras F, Bizot Q, Fourmont A, Le Gallet S, Politano O. Mechanical activation of metallic powders and reactivity of activated nanocomposites: a molecular dynamics approach. *Applied Physics A*. 2021;127: 555.
- 20. Poletaev GM, Bebikhov YV, Semenov AS, Sitnikov AA, Yakovlev VI. Molecular dynamics study of the dissolution of titanium nanoparticles in aluminum. *Materials Physics and Mechanics*. 2023;51(5): 9–15.
- 21. Poletaev GM, Bebikhov YuV, Semenov AS, Sitnikov AA. Molecular dynamics investigation of the effect of the interface orientation on the intensity of titanium dissolution in crystalline and amorphous aluminum. *Journal of Experimental and Theoretical Physics.* 2023;136(4): 477–483.
- 22. Hoffmann U, Horst C, Kunz E. Reactive Comminution. In: Sundmacher K, Keinle A, Seidel-Morgenstern A. (eds.) *Integrated Chemical Processes*. Wiley; 2005. p.407 436.
- 23. Khina BB. Effect of mechanical activation on SHS: Physicochemical mechanism. *International Journal of Self-Propagating High-Temperature Synthesis*. 2008;17: 211–217.
- 24. Mukasyan AS, Khina BB, Reeves RV, Son SF. Mechanical activation and gasless explosion: nanostructural aspects. *Chemical Engineering Journal*. 2011;174(2–3): 677–686.
- 25. Poletaev GM, Bebikhov YV, Semenov AS. Molecular dynamics study of the formation of the nanocrystalline structure in nickel nanoparticles during rapid cooling from the melt. *Materials Chemistry and Physics*. 2023;309:128358. 26. Poletaev GM, Gafner YY, Gafner SL. Molecular dynamics study of melting, crystallization and devitrification of nickel nanoparticles. *Letters on Materials*. 2023;13(4): 298–303.
- 27.Phillpot SR, Lutsko JF, Wolf D, Yip S. Molecular-dynamics study of lattice-defect-nucleated melting in silicon. *Physical Review B.* 1989;40: 2831.
- 28. Xiao S, Hu W, Yang J. Melting behaviors of nanocrystalline Ag. *The Journal of Physical Chemistry B*. 2005;109(43): 20339–20342.
- 29. Xiao S, Hu W, Yang J. Melting temperature: from nanocrystalline to amorphous phase. *Journal of Chemical Physics*. 2006;125(18): 184504.
- 30. Wejrzanowski T, Lewandowska M, Sikorski K, Kurzydlowski KJ. Effect of grain size on the melting point of confined thin aluminum films. *Journal of Applied Physics*. 2014;116(16): 164302.
- 31. Noori Z, Panjepour M, Ahmadian M. Study of the effect of grain size on melting temperature of Al nanocrystals by molecular dynamics simulation. *Journal of Materials Research*. 2015;30: 1648–1660.
- 32. Poletaev G, Rakitin R, Bebikhov Y, Semenov A. Molecular dynamics study of melting initiation at tilt grain boundaries depending on their misorientation angle in aluminum. *Physica Scripta*. 2025;100(1): 015988.
- 33. Zope RR, Mishin Y. Interatomic potentials for atomistic simulations of the Ti-Al system. *Physical Review B.* 2003;68: 024102. 34. Kim Y-K, Kim H-K, Jung W-S, Lee B-J. Atomistic modeling of the Ti-Al binary system. *Computational Materials Science*. 2016;119: 1–8.
- 35. Pei Q-X, Jhon MH, Quek SS, Wu Z. A systematic study of interatomic potentials for mechanical behaviours of Ti-Al alloys. *Computational Materials Science*. 2021;188: 110239.
- 36. Poletaev GM, Bebikhov YuV, Semenov AS, Starostenkov MD. Self-diffusion in melts of Ni-Al and Ti-Al systems: molecular dynamics study. *Letters on Materials*. 2021;11(4): 438–441.
- 37. Tsuzuki H, Branicio PS, Rino JP. Structural characterization of deformed crystals by analysis of common atomic neighborhood. *Computer Physics Communications*. 2007;177(6): 518–523.
- 38. Levchenko EV, Evteev AV, Lorscheider T, Belova IV, Murch GE. Molecular dynamics simulation of alloying in an Al-coated Ti nanoparticle. *Computational Materials Science*. 2013;79: 316–325.
- 39. Cherukara MJ, Weihs TP, Strachan A. Molecular dynamics simulations of the reaction mechanism in Ni/Al reactive intermetallics. *Acta Materialia*. 2015;96: 1–9.
- 40. Mishin Y, Farkas D, Mehl MJ, Papaconstantopoulos DA. Interatomic potentials for monoatomic metals from experimental data and ab initio calculations. *Physical Review B*. 1999;59(5): 3393–3407.
- 41. Bokstein B., Rodin A. Grain boundary diffusion and grain boundary segregation in metals and alloys. *Diffusion Foundations*. 2014;1: 99–122.

Submitted: March 02, 2025 Revised: March 19, 2025 Accepted: April 8, 2025

Electromagnetically cast Al-0.5 wt. % Fe alloy as a core material for the co-extruded copper-clad aluminium wire

A.E. Medvedev ^{1 ©} D, O.O. Zhukova ¹, A.F. Shaikhulova ¹ D, E.B. Medvedev ¹,

M.M. Motkov 20, M.Yu. Murashkin 10

ABSTRACT

In this study, the electromagnetically cast Al-0.5 wt. % Fe alloy was used as a core material for the copper-clad aluminium wire with the copper grade M2 outer sleeve. The choice of core material decreased the risk of premature copper-clad aluminium wire failure due to higher, compared to pure Al, mechanical strength and thermal stability. The mechanical bonding of the bimetallic wire was conducted via joint cold drawing. The produced copper-clad aluminium wire with the 37 % copper fraction in the cross-section is characterized by good adhesion of the Al and Cu layers. No intermetallic particles were observed on the Al-Cu interface in neither hard-drawn nor annealed state. Hard-drawn copper-clad aluminium wire is characterized by high mechanical strength and electrical conductivity while possessing an acceptable level of ductility. Subsequent to cold drawing annealing at 300 °C for 1h led to decrease of yield strength and ultimate tensile strength, as well as to increase in ductility and electrical conductivity. However, in both hard-drawn and annealed states copper-clad aluminium wire is characterized by the properties that lay within and even exceed the values recommended by international standards. Evaluation of the copper-clad aluminium wire ultimate tensile strength according to the rule of mixtures showed the importance of surface preparation on all the stages of the wire production.

KEYWORDS

copper-clad aluminium • hybrid materials • CCAW • electromagnetic crystallization • mechanical strength electrical conductivity • ductility • rule of mixtures

Funding. This work has been supported by the grant of the Russian Science Foundation, 20-79-10133.

Acknowledgements. The research was carried out using the equipment of the Core Facility Centre "Nanotech" of Ufa University of Science and Technology.

Citation: Medvedev AE, Zhukova OO, Shaikhulova AF, Medvedev EB, Motkov MM, Murashkin MYu. Electromagnetically cast Al-0.5 wt. % Fe alloy as a core material for the co-extruded copper-clad aluminium wire. *Materials Physics and Mechanics*. 2025;53(2): 25–39.

http://dx.doi.org/10.18149/MPM.5322025_3

Introduction

Copper and its alloys are mainly used as a material for the electrical conductors – wires, cables, busbars etc. due to their high electrical conductivity [1,2]. Since copper and its alloys are relatively expensive material, and its use is limited for economic reasons, the search for more affordable and available alternatives to copper is an urgent task for the modern electrical industry. Conventionally, aluminum and its alloys are the materials of choice for copper substitution due to the relatively low density and low cost. Since modern metallurgy and materials science have effectively reached the limits of further



¹ Ufa University of Science and Technology, Ufa, Russia

² Siberian Federal University, Krasnoyarsk, Russia

[™] medvedevandreyrf@gmail.com

improving the properties of metals and alloys, it is nearly impossible to replace copper and copper materials with other metals and alloys, at least within reasonable prices.

Instead of pushing the limits of single materials, such as metals and alloys, another approach can be taken. Two different metals or alloys can be physically bonded into one hybrid material [3–5]. The variety of materials that this hybrid product may consist of, along with the number of ways of joining them together, provides a wide range of metallic composites [4]. Competently picked materials can supply the combination of desired properties (such as high ductility, high mechanical strength, electrical conductivity etc.) without inheriting undesirable properties (brittleness, low corrosion resistance, low mechanical strength etc.). Since two-component composite already gives a lot of potential with the reaching of desired properties, simultaneously providing challenges of technological nature, usually multi-metal composite only consists of two metals/alloys, on rare occasion – of three or more [6,7]. Thus, the most balanced in terms of profits and complexity are bimetallic materials – a composite material consisting of two different metals or their alloys [4,8–10].

In the electrical industry the most common type of bimetallic conductor is a copper-clad aluminium wire (CCAW) – a composite with an aluminum core and a copper sleeve. Basically, the CCAW is a copper wire, in which the core part of it is substituted with aluminium. Since mechanical properties (especially bending resistance) are mostly determined by the outer part of cylindrical rods and wires, from the mechanical point of view CCAW is virtually a full-copper wire. In case of low-frequency currents the electrical conductivity of CCAW is calculated by the rule of mixture [11,12], but in case of high-frequency currents the electrical current will run along the surface of the conductor. So, in certain applications CCAW will have all the advantages of a full-copper wire, while also having lower density, weight and cost. Thus, CCAW are mostly used in high-frequency applications – audio equipment, high-frequency electrical conductors, and high-precision equipment etc. [13,14].

There are different ways of producing CCAW, although the most simple and widespread is the mechanical cladding, or joint cold drawing, in which copper tape is wound onto aluminum wire, followed by drawing [15]. In some cases, use of combined casting and subsequent drawing/rolling [16,17] is preferable.

The production of bimetallic materials has complications of the technological nature. The most notable effect of the joint cold drawing is the severe drop in the ductility of the CCAW – ductility of less than 1 % in hard-drawn state is considered acceptable according to the international standards [18,19]. The most straightforward way of increasing the CCAW ductility is post-deformation annealing aimed at ant recovery and, sometimes, recrystallization of the aluminium and copper layers [20,21]. Since copper has a notably higher melting point compared to aluminium, thus it requires an annealing temperature of at least 300 °C to initiate recovery, preferably higher [22]. Annealing of the CCAW at this temperature leads to the following complications: (i) severe softening of the aluminium core and (ii) initiation and growth of Al-Cu intermetallic on the Al-Cu interface.

Softening of the aluminium core leads to the overall decrease of the CCAW mechanical strength with the risk of falling out of recommended by the standards interval. While not being the major issue (since mechanical properties of the CCAW are

mostly determined by the properties of the Cu layer), this still could affect the performance of the composite wire.

The initiation and growth of intermetallic Al_xCu_y particles on the Al-Cu interface possesses higher risks for the CCAW performance [23]. These particles can form even at room temperature, but temperature increase significantly accelerates these processes. Intermetallic Al_xCu_y particles are brittle in nature and may severely decrease the ductility of the CCAW. Thus, annealing, aimed at ductility increase, may result in opposite result. The issue of the intermetallic particles' presence is even more prominent in CCAW produced via hot deformation or using the liquid phase.

Softening of the aluminium core (and increase of the difference in mechanical strength of the Al and Cu layers) may be avoided by introducing thermally stable aluminium alloys. Conventionally, technically pure aluminium is used as a core material for the CCAW, since core material is usually not expected to demonstrate any performance except for the low density and low cost [24]. Using aluminium alloys, especially thermally stable high-strength aluminium alloys may improve the properties of the CCAW. Alloys of Al-Zr [25], Al-RE (rare earth) [26], Al-Mg-Si [27] systems usually fall into this category, but their price is rather high, and in case of high completion this could be the resulting factor. Recently studied Al-Fe alloys, besides being highly common and inexpensive, also demonstrated the tendency to sustain their mechanical properties at elevated temperatures [28–30]. Thus, using Al-Fe alloys instead of technically pure aluminium may improve the CCAW performance during the annealing without significant increase in cost [31–33].

The issue of the intermetallic particles' presence on the Al-Cu interface can be avoided by choosing the correct temperature and duration of the annealing. Previously it was demonstrated that the temperature interval of 250 °C to 350 °C and duration interval of 30 to 90 min is enough to notably increase the ductility of the CCAW without causing the undesired intermetallic initiation and growth [20,34].

In this study, a potential method of obtaining the bimetallic wire with a copper sleeve and a core made of an aluminum alloy was demonstrated. The core material used was a conductive heat-resistant Al-0.5 wt. % Fe alloy, obtained by casting in electromagnetic crystallizer, due to its increased mechanical characteristics and heat resistance [35,36]. Wires made of such an alloy are characterized by increased strength and thermal stability, while maintaining a relatively high level of electrical conductivity. The presence in the composition of a small amount of accessible material – iron – ensures the low cost of this alloy [37]. In previous study the CCAW with a similar core, made of Al-0.5Fe alloy, was produced via copper electrodeposition [38,39]. This method, while having some advantages, demonstrated its overall ineffectiveness in terms of reaching the desired level of properties. In this study another approach was taken – mechanical bonding of the Al and Cu alloys by cold deformation [9,10].

Material and Methods

The bimetallic wires were fabricated by co-extrusion. Initial rods with a diameter of 11 mm and a length of more than 2 m made from Al-0.5 wt. % Fe alloy were manufactured by continuous casting into an electromagnetic crystallizer (EMC) [36].

The aluminium wire rod was then cold drawn (CD) to diameter of 7 mm and put into hollow tube made of copper grade M2 alloy with the inner diameter of 8 mm and outer diameter of 10 mm. The chemical composition of the alloys is presented in Table 1. Before inserting the aluminium rod into copper tube, the contact surfaces were mechanically cleaned and degreased. The formed billet was then drawn to 3 mm diameter on a laboratory drawing machine with a reduction of $\sim 90\%$ in 10 passes.

Table 1. Chemical composition of the initial materials

Alloy	Cu	Al	Fe	Σ Zn, Si, etc
Al-0.5Fe	≤ 0.04	99.37 min	0.51	≤ 0.13
Cu grade M2	99.87 min	≤ 0.05	≤ 0.05	≤ 0.03

Macrostructure studies were performed on an Olympus Q15OR optical microscope. Scanning electron microscopy (SEM) was performed on a Tescan MIRA microscope. Annealing was performed in an atmosphere furnace Nabertherm B180 at 300 °C for 1 h. Annealing temperature and time were chosen based on the results of study [3]. Samples upon annealing were cooled into water to remove the dross from the surface. The electrical resistivity of the studied material was measured in accordance with the IEC 60468:1974 standard [40]. Straightened samples of at least 1 m long part were taken. Microhardness (HV) was measured using the Vickers method on a Buehler MicroMet 5101 device under a load of 1 N and a holding time under load of 10 s. At least 10 points were made for each composite wire constituent to ensure minimal measuring error. Microhardness was measured on a cross-section of the samples, prior used for the SEM.

To obtain statistically reliable results, tensile tests were carried out on three samples for each state on a universal tensile testing machine Instron 5982 at room temperature and at a speed of 100 mm/min in accordance with government standard GoSt No. 10446-80 "Wires. Tensile testing methods". Based on the test results, the values of the yield strength ($\sigma_{0.2}$), ultimate tensile strength (σ_{UTS}) and elongation to failure (δ) were determined.

Results and Discussion

Choice of the core material

The produced CCAW consists of two notably different materials, with different levels of mechanical strength and ductility. In order to ensure the uniformity and repeatability of the mechanical and functional properties in CCAW it is important to diminish the aforementioned differences. One of the ways to do that is to use aluminium alloys with the level of mechanical strength, as close to that of copper as possible. Since CCAW is also a subject for the annealing at relatively high (for the aluminium) temperature (300 °C) it is also important that the chosen aluminium alloy is characterized by thermal stability.

Both these requirements are met by Al-0.5Fe alloy, cast into electromagnetic mold (Al-0.5Fe EMC). High crystallization rate along with constant stirring provide structural features that in turn ensure increased mechanical strength and thermal stability.

Table 2 contains the results of microhardness tests conducted at the core material and sleeve material of the samples studied after cold drawing and after subsequent

annealing at 300 °C for 1 h. The samples designation goes as follows: CCAW MC (copper-clad aluminium wire, mechanical cladding) and CCAW-A MC (copper-clad aluminium wire, mechanical cladding, annealed). Table also contains microhardness data for the aluminium alloy with the similar to Al-0.5Fe chemical composition but produced by continuous casting and rolling (Al-0.5Fe CCR). Samples of the Al-0.5Fe CCR were cold-drawn to the same deformation value as Al-0.5Fe EMC alloy and were subjected to the identical heat treatment. Also, for comparison reasons, the microhardness of the Al-0.4 wt. % Zr alloy is presented, as was used in the similar study [38].

Table 2	CCAW MC	and CCAW-A MC	microhardness data
Table 2.	LLAVV MIL	and CLAVV-A MC	micronardness dara

	Microhardness, HV						
Alloy	Hard-drawn state	Annealed state					
Cu grade M2 (sleeve)	135 ± 2	130 ± 2					
	Core material						
Al-0.5Fe EMC	56 ± 2	45 ± 1					
Al-0.5Fe CCR	57 ± 2	34 ± 1					
Al-Zr CCR	53 ± 3	53 ± 2					

Microhardness of the copper layer is seemingly unaffected by the annealing – the temperature is too low to initiate notable recovery process. The Al-0.5Fe EMC alloy undergoes recovery, resulting in the drop of the microhardness from 56 to 45 HV. Samples of the Al-0.5Fe CCR alloy, while having the same level of microhardness in the cold-drawn state (57 HV), demonstrate lower level of microhardness after annealing (34 HV), thus lower thermal stability. Interestingly, Al-Zr alloy is also unaffected by the annealing. However, Al-Zr alloy is more expensive and requires more complex technological treatment, in order to achieve such properties.

While the difference in microhardness of copper and aluminium alloys in CCAW is very significant, it is possible to reduce it both in hard-drawn and annealed states by choosing the right chemical composition and casting conditions of the aluminium alloy. Thus, Al-0.5Fe EMC is a reasonable alternative to similar alloys, produced by the conventional methods, at the same time being cheaper alternative to another Al-based thermally stable alloys.

CCAW structural assessment

Figure 1 shows the results of the optical metallography of CCAW MC and CCAW-A MC samples. According to it the adjacent copper to aluminium appears to be full along the interface (Fig. 1(a)). The Cu-Al interface has small voids about 4 μ m width and 10 μ m in length (Fig. 1(b)). These voids are formed due to incomplete deformation of the aluminium core surface, that was not polished or prepared in any way specifically after cold drawing. Nevertheless, the number of these voids is small, and they are placed within the interface discontinuously.

Annealing at 300 °C for 1 h seemingly doesn't affect the thickness of the copper layer (Fig. 1(c)), as was the case in CCAW obtained by electrodeposition [39]. Copper layer has notable change in thickness in the lower half of the sample studied, but it is most probably

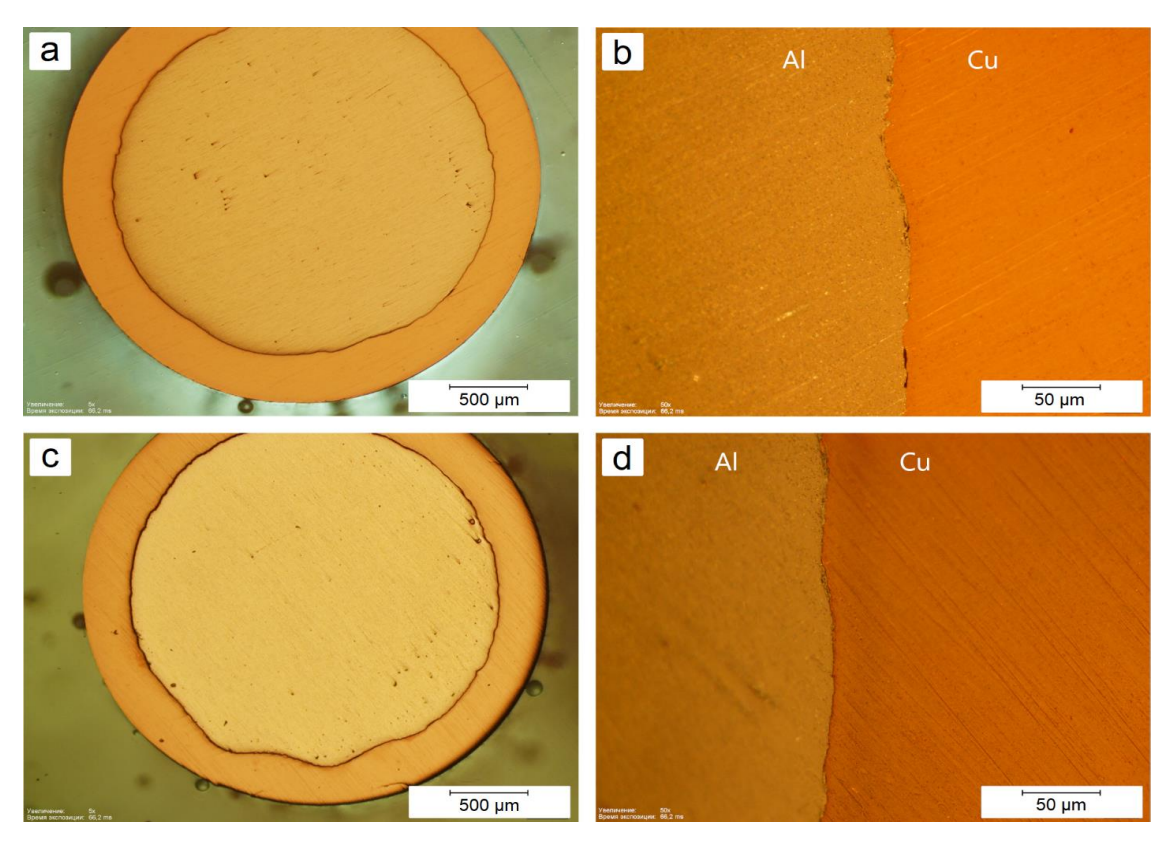


Fig. 1. Optical metallography of the cross section of a CCAW MC (a,b) and CCAW-A MC (c,d). The images show the aluminum core (grey) and copper sleeve (orange)

caused by the uneven surface of the initial Al alloy rod. This suggestion is supported by the smooth and even outer surface of the Cu sleeve. Cu-Al interface in the annealed state demonstrates changes – the voids, presented in the initial sample, were not observed.

The thickness of the copper layer is $308 \pm 20 \, \mu m$ in CCAW MC sample and $313 \pm 22 \, \mu m$ in CCAW-A MC, which corresponds to $36.2 \pm 6 \, \%$ and $37.6 \pm 7 \, \%$ fraction of the cross-section, respectively (Table 3). The thickness of the copper layer is unaffected by the annealing, no visible evidence of the interdiffusion is presented. The difference in Al layer thickness before and after annealing is minor and most likely caused by the fluctuations of the initial Al-Fe rod diameter, considering the measurements of it were taken from two different samples.

Table 3. Changes in the Cu layer thickness during the annealing

State	Layer thi	ckness, µm	Fraction in the cross-section, %		
State	Al	Cu	Al	Cu	
CCAW MC	1123 ± 20	308 ± 20	63.8 ± 6.0	36.2 ± 6.0	
CCAW-A MC	1177 ± 22	313 ± 22	62.4 ± 7.0	37.6 ± 7.0	

Figure 2 shows the cross-section of the CCAW MC and CCAW-A MC samples. Aluminium and copper have a significantly different atomic number so the contrast of these elements in the SEM pictures (especially in backscattered electrons mode) is clearly seen. The Al-Cu interface is continuous, not containing any visible defects. The interdiffusion layers in Al-Cu interfaces have distinct contrasts from both Al and Cu [41], which is not observed in the presented samples, so no Al-Cu interdiffusion evidence was found.

Figure 2(a) shows the interface in CCAW MC sample. The element contrast is clearly distinct, no other than Al or Cu phase particles are observed. The interface in CCAW-A MC sample is wider and contains gaps with the width of up to 10 µm (Fig. 2(b)). The smoothened surface of the Al-Cu interface (Fig. 2(b)), most likely, is due to the heating of the air, remaining in the "pocket" between the copper and aluminum alloy at the Al-Cu. As a result, existing voids could have arisen or developed, initially formed due to incomplete contact between the copper and aluminum layers. In any case, the effect described is local in nature, since these "pockets" or discontinuities have a discrete distribution along contact between the layers.

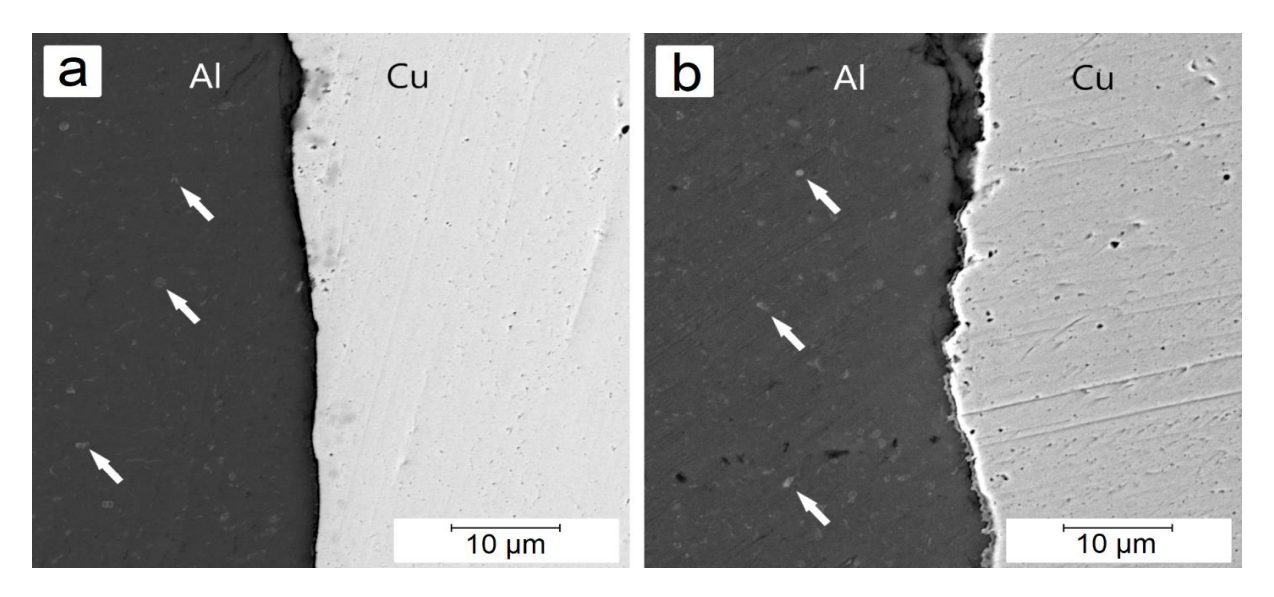


Fig. 2. Microstructure of the CCAW MC (a) and CCAW-A MC (b), cross-section, SEM. The images show the aluminum core (dark gray) and copper outer sleeve (bright gray). White arrows indicate the intermetallic Al_xFe_y particles within the Al-Fe alloy

Figure 3 presents the results of the EDXS analysis of the CCAW MC and CCAW-A MC samples. Line scan across the Cu-Al interface shows no increase of the Al and Cu signals overlap after annealing, once again proving the absence of the Cu-Al interdiffusion.

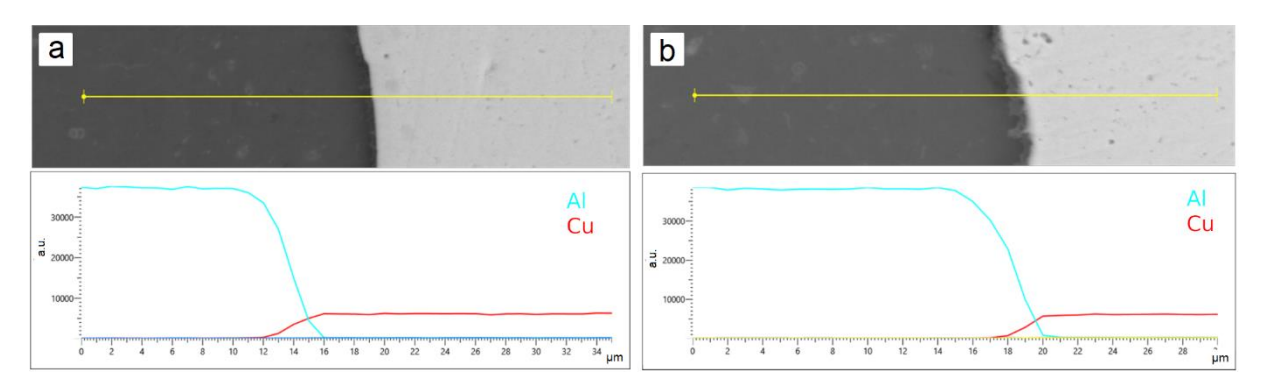


Fig. 3. EDXS results for CCAW MC (a) and CCAW-A MC (b), cross-section, SEM. The direction of line scanning is from left to right

CCAW physical and mechanical properties

Table 4 shows the properties of Al-0.5Fe alloy wire samples without copper cladding – aluminium wire (AW), and with cladding (CCAW MC, CCAW-A MC states). The initial EMC Al-0.5Fe alloy is relatively soft (σ_{UTS} of 90 MPa) alloy, with high value of elongation to failure (32.5 %) and level of electrical conductivity (57.8 % IACS) close to that of pure aluminium (62.0 % IACS) [22]. Cold drawing of the initial AW rod reduces the elongation to failure sixfold, increases the ultimate tensile strength twofold and seemingly has no effect on the electrical conductivity.

Table 4. Physical and	mechanical	nronarties of	M-Fe and	CCA wires
Table 4. Physical and	IIIECHAHICAL I	Di Obei ties oi	AL-FE allu	CCA WILES

5. .	Electrical properties		Mechanical properties		
State	ω, MS/m	IACS, %	$\sigma_{0.2}$, MPa	$\sigma_{ t UTS}$, MPa,	δ, %
Al-0.5Fe as-cast [43]	29.83 ± 0.1	57.8 ± 0.5	35 ± 3	90 ± 7	32.5 ± 3.4
Al-0.5Fe hard-drawn (AW) [43]	29.54 ± 0.1	58.4 ± 0.4	170 ± 12	204 ± 14	5.3 ± 0.2
CCAW MC	34.72 ± 1.1	67.2 ± 0.4	260 ± 11	316 ± 16	2.1 ± 0.3
CCAW-A MC	35.12 ± 0.9	68.0 ± 0.4	197 ± 8	225 ± 9	8.0 ± 0.7
Al-10%Cu hard-drawn [18,19]	-	62.9 % min	-	110 - 205	1 % min
Al-10%Cu annealed [18,19]	-	62.9 % min	_	135 - 170	5 – 15 % min
Al-15%Cu hard-drawn [18,19]	-	64.4 % min	-	110 - 205	1 % min
Al-15%Cu annealed [18,19]	-	64.4 % min	-	135 - 170	5 – 15 % min
CCAW ED [39]	29.68 ± 0.9	57.5 ± 0.5	185 ±6	187 ± 7	1.5 ± 0.1
CCAW-A ED [39]	31.43 ± 0.8	60.9 ± 0.3	135 ± 5	184 ± 6	4.3 ± 0.6

The CCAW MC wire with the same 3 mm diameter as AW has both exceeding ultimate strength (316 MPa) and electrical conductivity (67.2 % IACS). Unfortunately, the elongation to failure of CCAW MC is 2.1 %, which is borderline insufficient for the commercial use [42]. As was mentioned in the introduction, the low ductility of copper-clad aluminium wires is improved by annealing. Annealed at 300 °C for 1 h CCAW MC sample demonstrates increased elongation to failure (8.1 %) and electrical conductivity (68.0 % IACS) as well as decreased, but still high for annealed aluminium alloy level of ultimate tensile strength of 225 MPa.

CCAW MC and CCAW-A MC samples notably exceed the commercially available copper-clad samples in terms of mechanical and physical strength in both cold-worked and annealed states (Table 4). It is important to note, however, that the maximum amount of copper in commercial samples is 15 %, while in the samples studied this value is about 35–37 %. Increased amount of copper contributes to high strength and high electrical conductivity in CCAW MC and CCAW-A MC samples.

Table 4 also contains the results of similar tests for the copper-clad Al-Fe wire, obtained by the electrodeposition method (CCAW ED and CCAW-A ED samples, respectively) [39]. Electrical conductivity and mechanical properties are higher for the CCAW MC samples in both deformed and annealed states. Partially this could be attributed to the higher fraction of the copper (there is an average 8 % of copper in CCAW ED samples), and partially to the presence of Ni interlayer in CCAW ED samples.

The engineering stress-strain curves of the CCAW MC and CCAW-A MC samples, as well as CCAW ED and CCAW-A ED samples, are presented in Fig. 4. While the curve for the AW has regular for Al-0.5Fe alloy shape, the curves for the CCAW MC and CCAW-A MC are two-staged having sudden drop of strength with subsequent partial recovery and eventual failure. This drop corresponds to the failure of aluminium alloy core, that fractured first. The rest of the curve corresponds to the failure of the copper sleeve. Similar behavior was demonstrated by CCAW ED and CCAW-A ED samples, although the drop is not so strongly expressed, and the overall fracture of the sample has a more uniform character. Despite having a two-stage stress-strain curve, the CCAW MC and CCAW-A MC samples have uniform plastic deformation stage up until the copper sleeve fracture occurs.

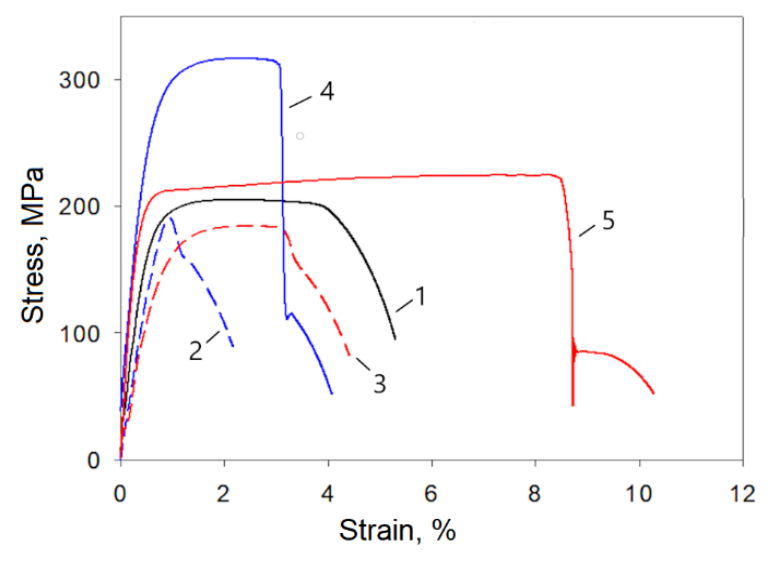


Fig. 4. Engineering stress-strain curves for aluminum wire (1) [43]; copper-clad via electrodeposition aluminum wire in the initial (2) and annealed (3) states [39]; mechanically copper-clad aluminum wire in the hard-drawn (4) and annealed (5) states

Compared to the ED samples, MC samples have significantly higher ductility and ultimate tensile strength for both deformed and annealed states. The character of the two-stage fracture also different – ED samples have smoothed transition between stages, while transition on MC samples, especially in the annealed state, has more abrupt character.

CCAW fracture analysis

The cross-sections of CCAW MC and CCAW-A MC after tensile tests are presented in Fig. 5. CCAW MC and CCAW-A MC samples demonstrate the non-simultaneous fracture of the aluminium alloy core and copper sleeve. The relative narrowing of the aluminium alloy core in CCAW-A MC sample is higher than that of CCAW MC (Fig. 5), correlating to the higher elongation to failure values of this sample (Table 4).

Figure 6 demonstrates the central part of the aluminium alloy core fracture surface in CCAW MC (Fig. 6(a,b)) and CCAW-A MC (Fig. 6(c,d)). Both samples demonstrate a dimpled character of the fracture surface, with dimples being larger in CCAW-A MC sample, which correlates with the four times elongation to failure increase during the annealing.

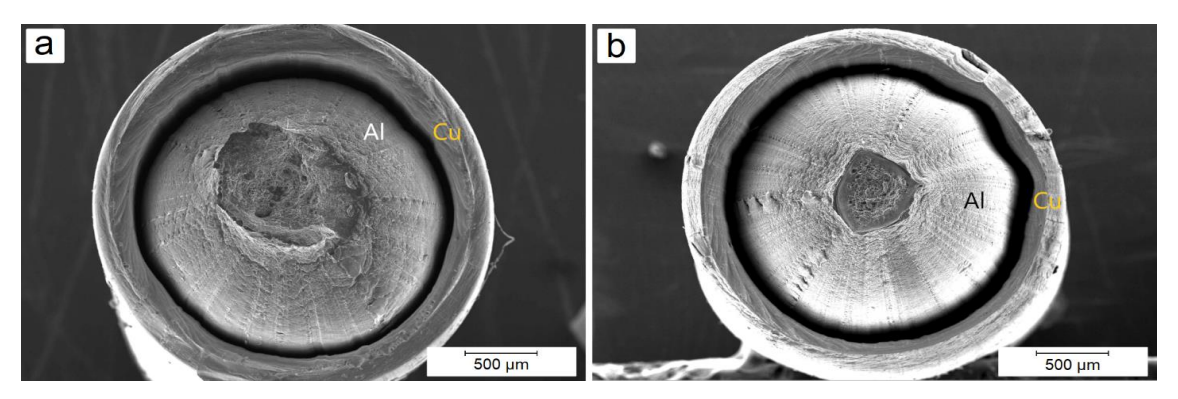


Fig. 5. Results of fractographic analysis of CCAW MC (a) and CCAW-A MC (b) samples, SEM

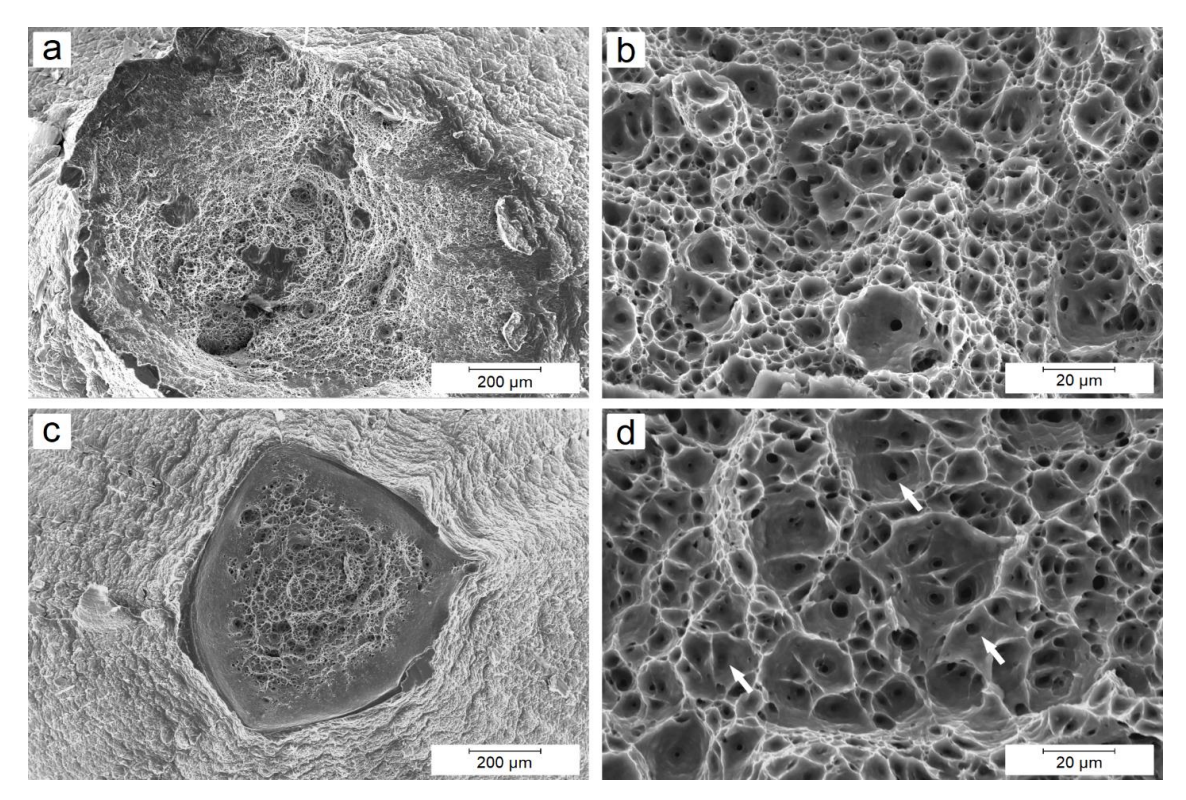


Fig. 6. Results of fractographic analysis of Al-0.5Fe alloy wire core of samples: (a,b) CCAW MC, (c,d) CCAW-A MC, SEM

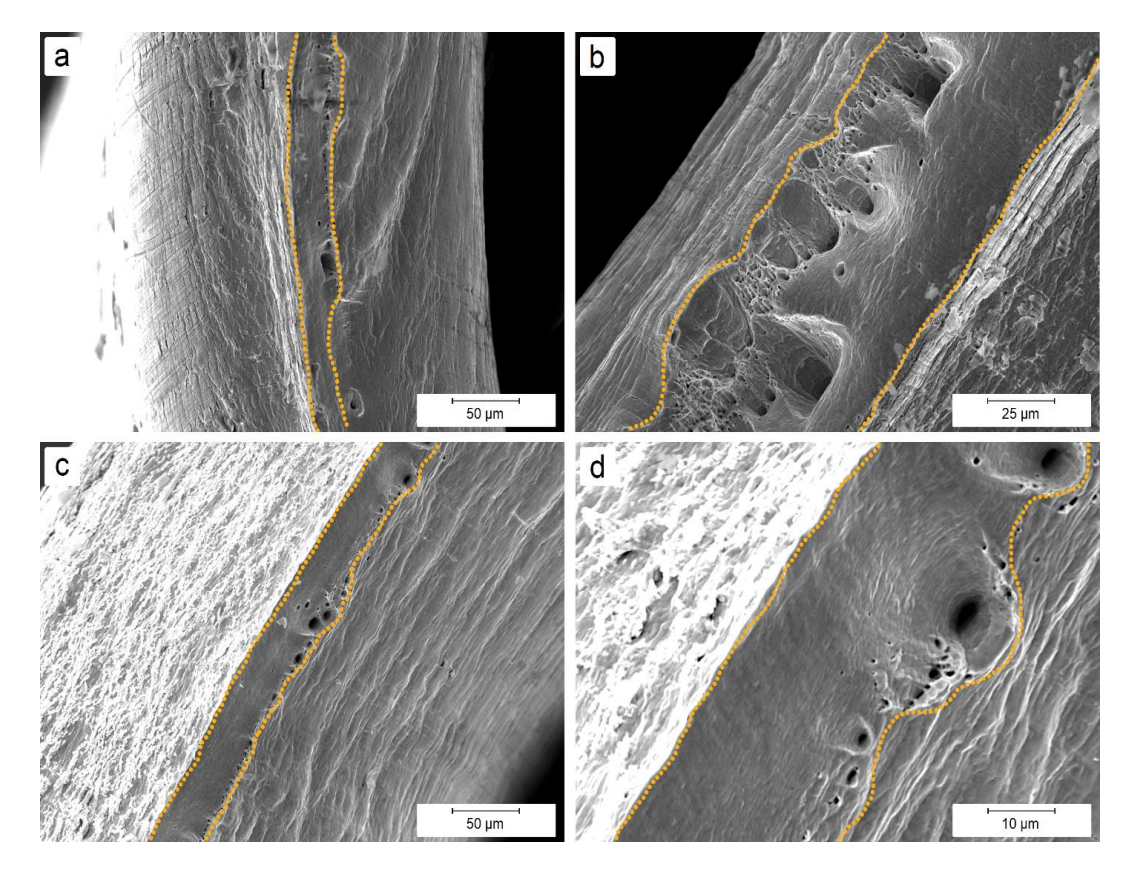


Fig. 7. Results of fractographic analysis of copper sleeve samples: (a,b) CCAW MC, (c,d) CCAW-A MC, SEM.

Orange dotted lines outline the borders of the fracture surface

Figure 7 demonstrates the fracture surface of the copper sleeve in CCAW MC (Fig. 7(a,b)) and CCAW-A MC (Fig. 7(c,d)). The fracture has similar character in both states and could be considered semi-brittle, since it has both dimples, typical for the ductile fracture, and so-called "river patterns", typical for the brittle fracture [44]. Annealing at 300 °C for 1 h has seemingly no effect on the character of the copper sleeve fracture.

Discussion

The stress-strain curves analysis (Fig. 4), as well as fracture analysis of the CCAW demonstrated the complex nature of the fracturing behavior. CCAW doesn't behave like a single metal or alloy, and the prediction of the mechanical properties is further complicated by difference in mechanical properties of the constituents, presence of the interface of the core and the sleeve and potential presence of intermetallic particles, oxides and transition layers on it. In the absence of the factors contributing to the premature failure of the bimetallic sample the tensile strength can be evaluated quite accurately.

Generally, tensile strength of the bimetallic metal-metal hybrid materials can be calculated using the rule of mixture with high precision. The rule of mixtures (ROM) [11] is expressed by:

$$\sigma_{\rm c} = \sigma_1 \times V_1 + \sigma_2 \times V_2,\tag{1}$$

where σ_c is the ultimate tensile strength (σ_{UTS}) of the composite; σ_1 (V_2) and σ_2 (V_2) are the σ_{UTS} and volume fractions of the constituents, respectively. Using the data from Table 2 in Eq. (1), Table 5 can be formed.

State	Material	σ _{υτs} , MPa		
		Experimental	Calculated (ROM)	
	Al-0.5Fe core	215 ± 10	-	
Hard-drawn	Grade M2 Cu sleeve	470 ± 22	-	
	CCAW	316 ± 16	307	
	Al-0.5Fe core	176 ± 8	-	
Annealed	Grade M2 Cu sleeve	451 ± 28	-	
	CCAW	225 ± 9	279	

Table 5. Experimental and calculated values of σ_{UTS} for CCAW

The calculations of σ_{UTS} presented in Table 5 are made with the assumption that the bimetallic wire is ideal, has no voids or embrittling particles on the constituent's interface. In the hard-drawn state calculated σ_{UTS} is equal to the experimental one, down to the error value, proving relevancy of the ROM implementation concept. Despite the presence of the voids on the Cu-Al interface (Fig. 1(b), Fig. 2(a)), the absence of the coarse third-phase particles allows to predict the ultimate tensile strength level of the hard-drawn CCAW with high accuracy.

In the CCAW-A sample, however, the difference in experimental and calculated σ_{UTS} is relatively high (50 MPa) up to a degree when it cannot be considered as a measuring or calculation error. The evaluated σ_{UTS} in the CCAW-A sample is higher, representing the occurrence of the factors, responsible for the premature failure of the bimetallic wire. Researchers also point out that ROM is very sensitive to the interface [3]. The annealing could affect the surface of the Cu layer, although this effect could be neglected since annealing temperature of 300 °C is not high enough to cause any significant changes (Fig. 1). Most probable cause of the σ_{UTS} difference is the formation of particles, or the growth of the existed ones, on the Cu-Al interface. On Fig. 1(d) the presence of certain formations between Cu and Al layers is clearly visible. As for the nature of these formations, two suggestions can be made. First, these are aluminium oxide particles, formed or grown during the annealing. The annealing was performed in the atmospheric oven, and the interface voids, clearly observed in hard-drawn wire (Fig. 1(b)), could form channels transferring oxygen into the gap between Cu and Al. These interface formations can also be, judging by their smooth appearance, melted Cu-Al particles. Similar effect was observed in [3]. In this study, the melted particles were also observed on the Cu-Al interface in bimetallic strips after annealing, although at notably higher temperatures (350 °C and higher). The SEM and EDXS data, however, testify against this suggestion, since no irregularities were found on the Cu-Al interface, making the oxide presence suggestion the most probable one.

Conclusions

This paper presents the results of the production of the copper-clad aluminium wire (CCAW) in both hard-drawn and annealed states. The core of the bimetallic wire consists of the electromagnetically cast thermally stable Al-0.5 wt. % Fe alloy, and the sleeve is made of grade M2 copper alloy. The following conclusions were drawn:

1. For the first time samples of a bimetallic wire based on electromagnetically cast Al-0.5 wt. % Fe alloy wire with grade M2 copper were obtained by cold co-extrusion. The fraction of copper

in the cross-section is about 37 %, no visible defects or intermetallic particles are observed at the Al-Cu interface. The production method resulted in a strong mechanical bond between aluminium and copper layers both in hard-drawn and annealed states.

- 2. The ultimate tensile strength (316 MPa), electrical conductivity (67.2 % IACS) and ductility (2.1 %) of produced CCAW notably exceeds those of commercially produced CCAW with the core made of technically pure aluminium. Annealing of the CCAW at 300 °C for 1 hour led to an increase in electrical conductivity to 68.0 % IACS and ductility to 8.0 %, while maintaining high level of ultimate tensile strength (225 MPa).
- 3. Produced CCAW, both in hard-drawn and annealed states, satisfies and exceeds the requirements for the CCAW according to ASTM B566. "Standard Specification for Copper-Clad Aluminium Wire, 2002" and SJ/T 11223-2000. "Copper-clad aluminum wire, 2000" commercial standards for CCAW.
- 4. It was demonstrated that implementation of different Al-based alloys as a core material for the CCAW has potential to not only improve the physical and mechanical properties of these products, but also potentially their functional properties, widening the area of their application. The thermal stability of the electromagnetically cast Al-0.5 Fe alloy, diminishing the difference in core's and sleeve's strength of the CCAW, contributed to the high mechanical properties and overall performance of the annealed CCAW.
- 5. The calculated with the rule of mixtures level of ultimate tensile strength is in good accordance with the experimental results for hard-drawn CCAW and higher for the annealed CCAW, signifying the occurrence of the processes on the Cu-Al, leading to a decrease in UTS of the annealed wire. Improved surface quality control on all stages of CCAW production is a mean of improving the mechanical properties of the product.

CRediT authorship contribution statement

Andrey E. Medvedev (DSC): writing – original draft; Olga O. Zhukova SC: data curation; Aygul F. Shaikhulova (DSC): investigation; Evgenii B. Medvedev SC: conceptualization; Mikhail M. Motkov (DSC): writing – review & editing; Maxim Yu. Murashkin (DSC): supervision.

Conflict of interest

The authors declare that they have no conflict of interest.

References

- 1. An Z, Yan J, An H, Tan J, Han Y, Li H, et al. Resource, environmental and economics research for primary and secondary copper: A bibliometric and systematic review. *Journal of Cleaner Production*. 2023;425: 138671.
- 2. Huang W, Yu H, Wang L, Wu X, Ouyang C, Zhang Y, He J. State of the art and prospects in sliver- and copper-matrix composite electrical contact materials. *Materials Today Communications*. 2023;37: 107256.
- 3. Fu X, Wang R, Zhu Q, Wang P, Zuo Y. Effect of Annealing on the Interface and Mechanical Properties of Cu-Al-Cu Laminated Composite Prepared with Cold Rolling. *Materials*. 2020;13(2): 369.
- 4. Pambhar AC, Valaki JB. Experimental studies of formability in single point incremental forming of Cu-Al bimetallic sheets. *Materials Today: Proceedings*. 2023.
- 5. Pawlicki M, Drenger T, Pieszak M, Borowski J. Cold upset forging joining of ultra-fine-grained aluminium and copper. *Journal of Materials Processing Technology*. 2015;223: 193–202.

- 6. Lapovok R, Ng HP, Tomus D, Estrin Y. Bimetallic copper-aluminium tube by severe plastic deformation. *Scripta Materialia*. 2012;66: 1081–1084.
- 7. Qi Y, Lapovok R, Estrin Y. Microstructure and electrical conductivity of aluminium/steel bimetallic rods processed by severe plastic deformation. *Journal of Materials Science*. 2016;51: 6860–6875.
- 8. Kocich R. Effects of twist channel angular pressing on structure and properties of bimetallic Al/Cu clad composites. *Materials & Design*. 2020;196:109255.
- 9. Zhukova OO, Medvedev AE, Shaykhulova AF, Medvedev EB, Murashkin MY, Motkov MM. Production of bimetallic wire with a core of Al-1.7 wt. % Fe alloy obtained by electromagnetic crystallization and a shell of copper alloy grade M2. *Materials. Technologies. Design.* 2024;6(4(19)): 5–12.
- 10. Zhukova OO, Medvedev AE, Kiryanova KE, Medvedev EB, Motkov MM. Properties of bimetallic wire with copper sheath and Al-0.5Fe-0.3Cu alloy core obtained by casting in an electromagnetic crystallizer. *Materials. Technologies. Design.* 2024;6(3(18)): 27–33.
- 11. Feng B, Xin Y, Sun Z, Yu H, Wang J, Liu Q. On the rule of mixtures for bimetal composites. *Materials Science and Engineering A-structural Materials Properties Microstructure and Processing*. 2017;704: 173–180.
- 12. Tian L, Anderson I, Riedemann T, Russell A. Modeling the electrical resistivity of deformation processed metal-metal composites. *Acta Materialia*. 2014;77: 151–161.
- 13. Barrett C, Tetelman A, Nix W. The Principles of Engineering Materials. Hoboken, NJ, USA: Prentice-Hall; 1973.
- 14. Dowling M, Al-Hamaoy AR, A. Obeidi M. Laser surface cladding of metal parts. *Results in Surfaces and Interfaces*. 2023;12: 100142.
- 15. Gueydan A, Hug E. Secondary creep stage behavior of copper-clad aluminum thin wires submitted to a moderate temperature level. *Materials Science and Engineering: A.* 2018;709: 134–138.
- 16. Li K, Liu X, Zhao Y. Research status and prospect of friction stir processing technology. *Coatings*. 2019;9(2), 129.
- 17. Chen Y, Wang A, Tian H, Xie J, Wang X. Study on optimization of nozzle for copper-aluminium clad plate twin-roll cast-rolling. *Journal of Materials Research and Technology*. 2021;10: 1075–1085.
- 18. ASTM B566-93. Standard Specification for Copper-Clad Aluminium Wire. 2002.
- 19. SJ/T 11223-2000. *Copper-clad aluminum wire*. 2000.
- 20. Song JW, Hong JP, An YJ, Son SH, Park JS, Kim SH, Kang SH, Kang JH. Evaluation of the Mechanical and Electrical Properties of Multistage Drawn Copper-Clad Aluminum Wire After Annealing Process. *Metals*. 2024;14(2): 1386.
- 21. Sharifian Amiri F, Hosseinipour SJ, Jamshidi Aval H, Jamaati R. Evaluation of strength and electrical conductivity of copper clad-AA6063 bimetallic composite wire after annealing treatment. *Materials Chemistry and Physics.* 2024;312:128660.
- 22. Mondolfo LF. *Aluminum Alloys: Structure and Properties*. London: Butterworths; 1976.
- 23. Lee JE, Bae DH, Chung WS, Kim KH, Lee JH, Cho YR. Effects of annealing on the mechanical and interface properties of stainless steel/aluminum/copper clad-metal sheets. *Journal of Materials Processing Technology*. 2007;187–188: 546–549.
- 24. Cho Y-R. Clad Metals: Fabrication, Properties, and Applications. Metals. 2021;11(8): 1186.
- 25. International Electrotechnical Commission. IEC 62004:2007. *Thermal-resistant aluminium alloy wire for overhead line conductor*. 2007.
- 26. Medvedev AE, Murashkin MY, Enikeev NA, Valiev RZ, Hodgson PD, Lapovok R. Enhancement of mechanical and electrical properties of Al-RE alloys by optimizing rare-earth concentration and thermomechanical treatment. *Journal of Alloys and Compounds*. 2018;745: 696–704.
- 27. EN 50183:2002. Conductors for overhead lines Aluminium-magnesium-silicon alloy wires. 2002.
- 28. Tcherdyntsev VV, Kaloshkin SD, Afonina EA, Tomilin IA, Baldokhin Y V, Shelekhov E V, et al. Effect of Deformation by High Pressure Torsion on the Phase Composition and Microhardness of Mechanically Alloyed and Rapidly Quenched Al-Fe alloys. *Defect and Diffusion Forum.* 2003;216–217: 313–322.
- 29. Sasaki TT, Ohkubo T, Hono K. Microstructure and mechanical properties of bulk nanocrystalline Al-Fe alloy processed by mechanical alloying and spark plasma sintering. *Acta Materialia*. 2009;57: 3529–3538.
- 30. Nayak SS, Pabi SK. Structure of nanocomposites of Al-Fe alloys prepared by mechanical alloying and rapid solidification processing. *Bulletin of Materials Science*. 2008;31: 449–454.
- 31. Bian Z, Dai S, Wu L, Chen Z, Wang M, Chen D, et al. Thermal stability of Al-Fe-Ni alloy at high temperatures. *Journal of Materials Research and Technology*. 2019;8(3): 2538–2548.
- 32. Chen JK, Hung HY, Wang CF, Tang NK. Thermal and electrical conductivity in Al-Si/Cu/Fe/Mg binary and ternary Al alloys. *Journal of Materials Science*. 2015;50: 5630–5639.

- 33. Medvedev A, Zhukova O, Enikeev N, Kazykhanov V, Timofeev V, Murashkin M. The Effect of Casting Technique and Severe Straining on the Microstructure, Electrical Conductivity, Mechanical Properties and Thermal Stability of the Al-1.7 wt. % Fe Alloy. *Materials*. 2023;16(8): 3067.
- 34. Amiri FS, Hosseinipour SJ, Aval HJ, Jamaati R. Fabrication of a novel high-strength and high-conductivity copper-clad aluminum composite wire. *CIRP Journal of Manufacturing Science and Technology*. 2023;41: 144–159.
- 35. Belov N, Murashkin M, Korotkova N, Akopyan T, Timofeev V. Structure and properties of Al-0.6 wt. % Zr wire alloy manufactured by direct drawing of electromagnetically cast wire rod. *Metals*. 2020;10(6): 769.
- 36. Li J, Nian Y, Liu X, Zong Y, Tang X, Zhang C, Zhang L. Application of electromagnetic metallurgy in continuous casting: A review. *Progress in Natural Science: Materials International*. 2024;34(1): 1–11.
- 37. Zhao Q, Qian Z, Cui X, Wu Y, Liu X. Optimizing microstructures of dilute Al-Fe-Si alloys designed with enhanced electrical conductivity and tensile strength. *Journal of Alloys and Compounds*. 2015;650: 768–776. 38. Medvedev AE, Kiryanova KE, Medvedev EB, Gorbatkov MV, Zhukova OO, Murashkin MYu. Copper-clad thermally stable Al-Zr wire, produced via copper electrodeposition. *Materials Physics and Mechanics*. 2024;52(5): 29–39.
- 39. Medvedev AE, Kiryanova KE, Medvedev EB, Gorbatkov M V, Motkov MM. Microstructure and properties of the Al-0,5 wt.% Fe alloy wire, copper-clad by electrochemical deposition. *International Journal of Lightweight Materials and Manufacture*. 2025;8(1): 28–37.
- 40. IEC 62641:2023. Conductors for overhead lines Aluminium and aluminium alloy wires for concentric lay stranded conductors. 2023.
- 41. Zheng H, Zhang R, Xu Q, Kong X, Sun W, Fu Y, Wu M, Kiu K. Fabrication of Cu/Al/Cu Laminated Composites Reinforced with Graphene by Hot Pressing and Evaluation of Their Electrical Conductivity. *Materials*. 2023;16(2): 622.
- 42. ASTM B800-05. Standard Specification for 8000 Series Aluminum Alloy Wire for Electrical Purposes Annealed and Intermediate Tempers. 2021.
- 43. Medvedev AE, Zhukova OO, Fedotova DD, Murashkin MYu. The mechanical properties, electrical conductivity, and thermal stability of a wire made of Al-Fe alloys produced by casting into an electromagnetic crystallizer. *Frontier Materials & Technologies*. 2022;3(1): 96–105.
- 44. François D. 2.4 Fracture mechanisms of metals. In: Herrmann HJ, Roux S. (eds.) *Random Materials and Processes. Statistical Models for the Fracture of Disordered Media.* North-Holland: Elsevier; 1990. p. 59–65.

Submitted: September 2, 2024 Revised: February 8, 2025 Accepted: March 10, 2025

S_{11} and S_{21} characteristics of carbon fiber fabric fixed in the polyurethane based matrixes

O.V. Boiprav [™] , E.S. Belousova , V.S. Mokerov

Belarusian State University of Informatics and Radioelectronics, Minsk, Republic of Belarus

[™]smu@bsuir.by

ABSTRACT

The aim of the research presented in the paper was the establishment of the regularities of change of electromagnetic radiation reflection (S_{11}) and transmission (S_{21}) characteristics values in the frequency range 2.0 – 17.0 GHz of carbon fiber fabric fixed in the polyurethane mastic based matrices depending on these matrixes composition. Such research is urgent due to the following reasons: (1) carbon fiber materials are characterized low stability of S_{11} and S_{21} characteristics due to their hydroscopicity; (2) to increase stability of S_{11} and S_{21} characteristics and strength of carbon fiber materials it's necessary to perform their additional processing (for example, to fix them in matrices or substrates). It's demonstrated in the paper that values of S_{11} characteristics in the frequency range 2.0 – 17.0 GHz of carbon fiber fabric fixed in the matrix from polyurethane without fillers are from -0.1 till -3.5 dB. S_{11} characteristic values in the frequency range 2.0 – 17.0 GHz of carbon fiber fabric fixed in the matrix from polyurethane with aluminum oxide, titanium oxide and zinc oxide fillers are from -0.1 till -11.0 dB, from -0.1 till -3.0 dB, from -0.1 till -5.0 dB respectively. S_{21} characteristic values in the frequency range 2.0 - 17.0 Hz of the listed materials are from -20.0 till -40.0 dB. The studied materials are suitable for use for making special boxes for storing equipment sensitive to microwave interference.

KEYWORDS

electromagnetic radiation • carbon fiber fabric • microwave absorber • polyurethane matrix • S_{11} characteristic S_{21} characteristic

Citation: Boiprav OV, Belousova ES, Mokerov VS. S_{11} and S_{21} characteristics of carbon fiber fabric fixed in the polyurethane based matrixes. *Materials Physics and Mechanics*. 2025;53(2): 40–47. http://dx.doi.org/10.18149/MPM.5322025 4

Introduction

Carbon fiber materials are currently widely used for the manufacture of microwave absorbers [1-10]. This is due to the following advantages of these materials [11]:

- 1. high electrical conductivity, due to which microwave absorbers based on these materials are characterized by high efficiency;
- 2. the possibility of providing the required electrical conductivity values for these materials by changing the percentage of carbon fibers in their composition (due to the indicated advantage, the required operating frequency range, as well as the S_{11} and S_{21} characteristics values can be provided for electromagnetic radiation absorbers based on the indicated materials);
- 3. flexibility, due to which products of complex shape (special clothing, covers for electronic devices, modules for cladding the walls of shielded rooms) can be manufactured from the microwave absorbers based on the indicated materials;



4. high corrosion resistance compared to metals with comparable values of specific electrical conductivity.

The indicated absorbers are used to solve the following problems [12–17]: protection of electronic devices from electromagnetic interference, protection of humans from electromagnetic radiation; ensuring the security of information processed using computing equipment. Since the introduction of 5G technologies, the urgency of solving the first and the second of the indicated problems has increased significantly [18–22]. However, microwave absorbers based on carbon fiber materials are characterized by such disadvantage as instability of the values of S_{11} and S_{21} characteristics values, due to the fact that:

- 1. carbon fibers are weakly fixed in the volume of the indicated materials and, as a result of mechanical action (bending, stretching, etc.), can change their mutual arrangement;
- 2. carbon fibers are hygroscopic.

To exclude the indicated disadvantage of the microwave absorbers based on carbon fiber materials it's necessary to perform their additional processing by fixing them in the matrices or substrates. The aim of the presented study was to establish the patterns of change of S_{11} and S_{21} characteristics values of carbon fiber fabric depending on the composition of the matrix in which they are fixed. To achieve the stated aim, the following tasks were solved:

- 1. selection and justification of the material for forming the matrix in which it is advisable to fix carbon fiber fabric;
- 2. selection and justification of the types of fillers to be added to the selected material for forming the matrix;
- 3. making of experimental samples using the selected matrix and fillers;
- 4. measurement and analysis of S_{11} and S_{21} characteristics values in the frequency range of 2.0–17.0 GHz of the manufactured experimental samples;
- 5 development of recommendations for the practical application of the studied materials.

Material and Methods

Polyurethane mastic was chosen as the material for forming the matrix in which it is advisable to fix carbon fiber fabric. The choice of such a material is due to the following advantages:

- 1. flexibility, which, together with the flexibility of carbon fiber fabric, allows for providing a similar property for microwave absorbers based on such components;
- 2. availability and low cost (the cost of the selected material in the volume required to form 1.0-3.0 mm thick matrices for the manufacture of 1.0 m^2 of microwave absorbers based on carbon fiber fabric is 10.0-30.0 times lower than the cost of 1.0 m^2 of such fiber material):
- 3. controlled viscosity (the viscosity of the selected material is reduced by adding a petroleum solvent to it [23], which improves the adhesive properties of the matrix formed on the basis of such material, and also reduces the time required to include fillers in it [24-26]).

Finely dispersed materials characterized by dielectric properties were chosen as fillers for addition to the polyurethane mastic. This choice is due to the fact that by adding these materials to the composition of microwave absorbers containing conductive

components, it is possible to reduce their wave resistance, and, as a consequence, reduce their S_{11} characteristics values and increase electromagnetic radiation absorption characteristics values [27,28]. The following finely dispersed materials characterized by dielectric properties were chosen for addition to the polyurethane mastic: aluminum oxide, titanium dioxide; zinc oxide.

The cost of the listed materials in the volume required to form 1.0-3.0 mm thick matrices for the production of $1.0~\text{m}^2$ of microwave absorbers based on carbon fiber fabric is lower than the cost of polyurethane mastic for forming such matrices in the specified volume. The particle size of the listed materials is $0.1-1.0~\mu\text{m}$. It has been experimentally established that the optimal volume ratio of the mixture of polyurethane mastic and aluminum oxide, titanium dioxide or zinc oxide is 70.0:30.0%. Using the selected materials, experimental samples were made for the study. Table 1 presents the characteristics of these samples.

Table 1. The characteristics of the made samples for the study

Sample	The composition of matrix used for the sample preparing
Sample 1	-
Sample 2	Polyurethane mastic
Sample 3	Polyurethane mastic (70.0 vol. %), aluminum oxide (30.0 vol. %)
Sample 4	Polyurethane mastic (70.0 vol. %), titanium oxide (30.0 vol. %)
Sample 5	Polyurethane mastic (70.0 vol. %), zinc oxide (30.0 vol. %)

Sample 1 was a carbon fiber fabric fragment, the length and width of which were not less than the length and width of the antenna aperture included in the setup for measuring S_{11} and S_{21} characteristics values in the frequency range 2.0 – 17.0 GHz. Samples 2–5 were made in the following way:

- 1. cutting off a fragment from a roll of carbon fiber fabric with use of scissors. The length and width of the fragment were not less than the length and width of the antenna aperture included in the setup for measuring S_{11} and S_{21} characteristics values in the frequency range 2.0 17.0 GHz;
- 2. during the manufacture of sample 2, uniform mechanical application of a 2.0 ± 1.0 mm thick layer of polyurethane mastic to both surfaces of the fragment cut as a result of implementing stage 1 with use of spatula;
- 3. during the manufacture of samples 3-5:
- 3.1. uniform mechanical application of a 2.0 ± 1.0 mm thick layer of polyurethane mastic to one surface of the fragment cut off on the stage 1 with use of spatula;
- 3.2. preparation of a mixture of polyurethane mastic and finely dispersed aluminum oxide (when making sample 3), titanium dioxide (when making sample 4), zinc oxide (when making sample 5), taking into account that the volume ratio of the components in such mixture should be 70.0: 30.0%. The building mixer was used in course of the mixture preparation;
- 3.3. uniform mechanical application of a 2.0 ± 1.0 mm thick layer of the mixture prepared on the stage 3.2 to the second surface of the fragment cut off on the stage 1 with use of spatula.

Optic microscopy image of the surface fragment of the carbon fiber fabric used for the sample making is presented on Fig. 1. The carbon material used for the samples making is characterized by the following properties: density is 200.0 g/m²; weave type is twill; equal strength (has the same number of threads in the warp and weft). 70.0: 30.0 % volume ratio of the components of the mixture preparing in stage 3.2 is optimal one. This is because that increasing of the aluminum oxide, titanium dioxide or zinc oxide content in the mixture leads to the decreasing of the mechanical straight of the layers formed on the base of it and applied in the stage 3.3. Decreasing of the aluminum oxide, titanium dioxide or zinc oxide content in the mixture leads to the increasing of the wave resistance of the layers formed on the base of it and applied in the stage 3.3.

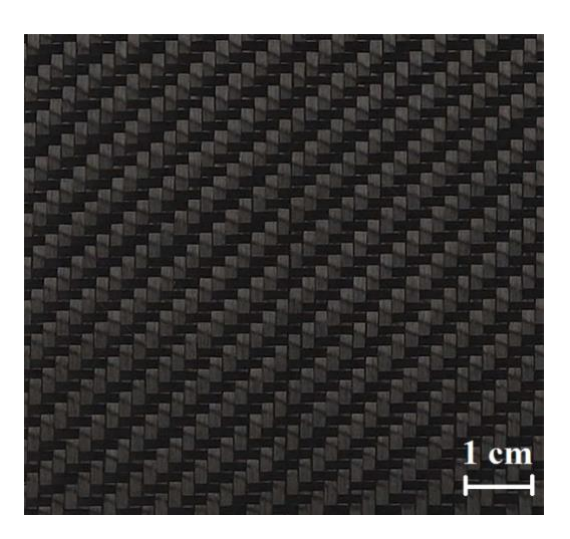


Fig. 1. Optic microscopy image of the surface fragment of the carbon fiber fabric used for the samples making

 2.0 ± 1.0 mm thickness of layer of the mixture prepared on the stage 3.2 is the optimal one. This is because such thickness is minimum possible one which could be applied on the surface of the carbon fiber fabric. The increasing of this thickness leads to the increasing the mass of such fabric and worsens its performance properties. There were made 5 units of every sample. The measurements of S_{11} and S_{21} characteristics values in the frequency range 2.0 - 17.0 GHz were carried out with use of setup included: panoramic meter of transmission and reflection coefficients SNA 0.01-18; two horn antennas P6-23M with aperture size 351.0×265.0 mm.

The measurements of the indicated values were carried out in accordance with method described in [29]. The relative error module of measurements of S_{11} and S_{21} characteristics values using the panoramic meter of transmission and reflection coefficients SNA 0.01-18 doesn't exceed 10.0 %.

Results and Discussion

 S_{11} characteristics in the frequency range 2.0–17.0 GHz of samples 1–5 are presented on Fig. 2. As it seen on Fig. 2, S_{11} characteristic values in the frequency range 2.0–17.0 GHz of the sample 1 vary from –0.1 till –3.0 dB, of the samples 2–5 – from –0.1 till –6.0 dB, from –0.1 till –11.0 dB, from –0.1 till –5.0 dB respectively.

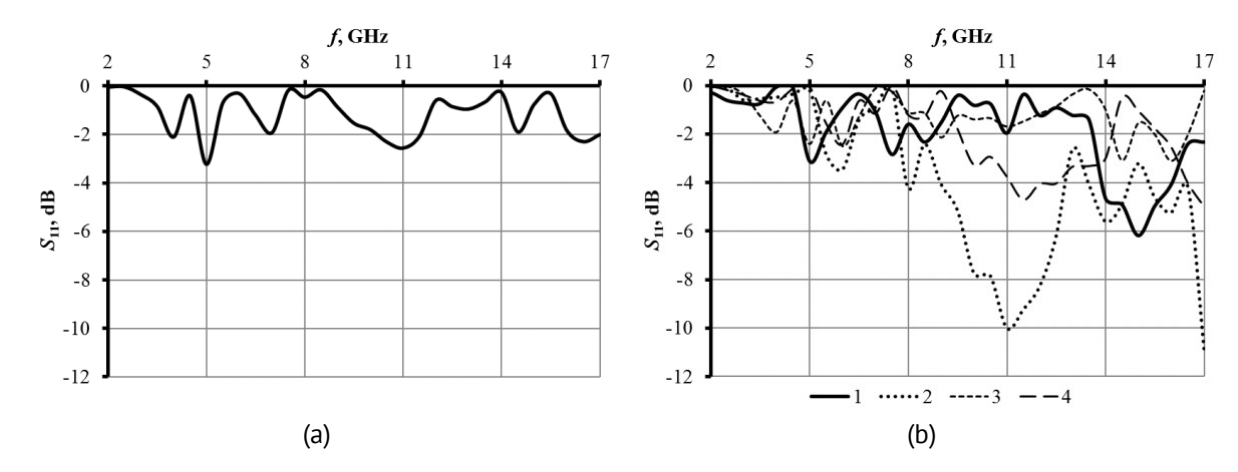


Fig. 2. S_{11} characteristic in the frequency range 2.0–17.0 GHz of samples 1 (a), and 2–5 (b, curves 1–4 respectively)

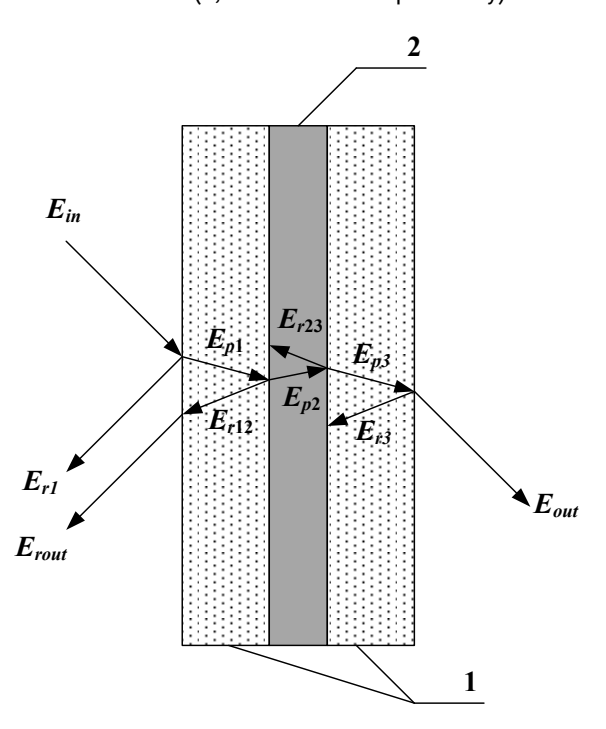


Fig. 3. The scheme of interaction of electromagnetic waves with the samples: 1 - matrix; 2 - carbon fiber fabric; $E_{in} - \text{incident}$ waves; $E_{r.1} - \text{the}$ waves reflected from the surface of matrix part covering carbon fiber fabric outer surface (surface oriented to the electromagnetic waves source); $E_{rout} - \text{the}$ waves reflected from the boundary between surface of matrix part covering carbon fiber fabric outer surface and carbon fiber fabric outer surface and passed through this part of matrix back to the electromagnetic waves source; $E_{\rho 1} - \text{the}$ waves passed through the matrix part covering carbon fiber fabric outer surface; $E_{r12} - \text{the}$ waves reflected from the boundary between surface of matrix part covering carbon fiber fabric; $E_{r23} - \text{the}$ waves reflected from the boundary between surface of matrix part covering carbon fiber fabric inner surface and carbon fiber fabric inner surface; $E_{\rho 2} - \text{the}$ waves passed through the matrix part covering carbon fiber fabric inner surface; $E_{\rho 2} - \text{the}$ waves passed through the matrix part covering carbon fiber fabric inner surface; $E_{\rho 2} - \text{the}$ waves passed through the sample

 S_{11} characteristics in the frequency range 2.0 – 17.0 GHz of the samples 2, 3 and 5 have resonant points. These points are 15.0, 11.0 and 11.5 GHz respectively. These points are the result of antiphase interaction on the listed frequencies of electromagnetic waves

reflected from the matrix surface and electromagnetic waves reflected from the carbon fiber fabric surface [30]. The scheme of such interaction is presented on Fig. 3.

It was established, the studied samples are characterized by the similar S_{21} characteristic in the frequency range 2.0–17.0 GHz. These characteristics are presented on Fig. 4. As it seen from Fig. 4, S_{21} characteristic values in the frequency range 2.0 – 17.0 GHz of the studied samples vary from –20.0 till –40.0 dB. Thus, fixing of the carbon fiber fabric in the polyurethane mastic based matrices doesn't impact on it S_{21} characteristic values in the frequency range 2.0 – 17.0 GHz. This is because the carbon fibers provide significantly greater losses of electromagnetic radiation energy in the indicated frequency range compared with the polyurethane mastic and finely dispersed aluminum oxide, titanium dioxide and zinc oxide [31,32].

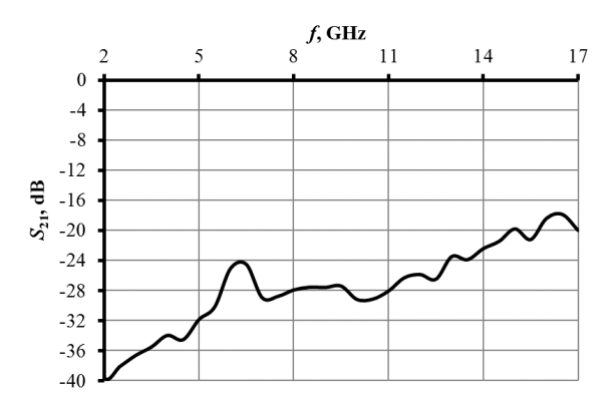


Fig. 4. S_{21} characteristic in the frequency range 2.0–17.0 GHz of samples 1–5

Conclusions

Thus, it's possible to reduce on 0.5 - 3.0 dB S_{11} characteristic values in the frequency range 2.0 - 17.0 GHz of carbon fiber fabric by fixing it in the polyurethane mastic-based matrix. If add to this matrix filler in the form of finely dispersed aluminum oxide or zinc oxide it's possible to increase on 0.5 - 5.0 dB the indicated reduction. In general, S_{11} characteristic values of the carbon fiber fabric are reduced after it fixing in the polyurethane mastic due to reducing of the wave resistance of this fabric surface. S_{21} characteristic values in the frequency range 2.0 - 17.0 GHz carbon fiber fabric vary from -20.0 till -40.0 dB and don't depend significantly form the content of matrix where it's fixed. The studied materials are suitable for use for making special boxes for storing equipment sensitive to microwave interferences.

CRediT authorship contribution statement

Olga V. Boiprav (DSC): supervision, conceptualization, investigation, writing – original draft; **Elena S. Belousova** (DSC): conceptualization, investigation; **Vyacheslav S. Mokerov**: investigation, data curation.

Conflict of interest

The authors declare that they have no conflict of interest.

References

- 1. Méjean C, Pometcu L, Benzerga R, Sharaiha A, Paven-Thivet CL, Badard M, Pouliguen P. Electromagnetic Absorber Composite Made of Carbon Fibers Loaded Epoxy Foam for Anechoic Chamber Application. *Materials Science and Engineering: B.* 2017;220: 59–65.
- 2. Li Z, Haigh A, Soutis C, Gibson A. X-Band Microwave Characterisation and Analysis of Carbon Fibre-Reinforced Polymer Composites. *Composite Structures*. 2019;208: 224–232.
- 3. Zhou W, Long L, Xiao P, Jia C-k, Li Y. Comparison in Dielectric and Microwave Absorption Properties of SiC Coated Carbon Fibers With PyC and BN Interphases. *Surface and Coatings Technology*. 2019;359: 272–277.
- 4. Zhang X, Qi S, Zhao Y, Wang L, Fu J, Yu M. Synthesis and Microwave Absorption Properties of Fe@Carbon Fibers. *RSC Advances*. 2020;10(54): 32561–32568.
- 5. Breiss H, El Assal A, Benzerga R, Méjean C, Sharaiha A. Long Carbon Fibers for Microwave Absorption: Effect of Fiber Length on Absorption Frequency Band. *Micromachines*. 2020;11(12): 1081.
- 6. Chen J, Zheng J, Huang Q, Wang F, Ji G. Enhanced Microwave Absorbing Ability of Carbon Fibers with Embedded FeCo/CoFe2O4 Nanoparticles. *ACS Applied Materials & Interfaces*. 2021;13(30): 36182–36189.
- 7. Gunwant D, Vedrtnam A. Microwave Absorbing Properties of Carbon Fiber Based Materials: A Review and Prospective. *Journal of Alloys and Compounds*. 2021;881:160572.
- 8. Guo S, Zhang Y, Chen J, Wu Y, Cao J, Tang S, Ji G. The Excellent Electromagnetic Wave Absorbing Properties of Carbon Fiber Composites: the Effect of Metal Content. *Inorganic Chemistry Frontiers*. 2022;9: 3244–3250.
- 9. Huang L, Duan Y, Pang H. Thin Layers of Microwave Absorbing Metamaterials with Carbon Fibers and FeSi Alloy Ribbons to Enhance the Absorption Properties. *EPJ Applied Metamaterials*. 2023;10(3).
- 10. Liu Y, Huang X, Yan X, Xia L, Zhang T, Sun J, Liu Y, Zhou Y. Pushing the Limits of Microwave Absorption Capability of Carbon Fiber in Fabric Design Based on Genetic Algorithm. *Journal of Advanced Ceramics*. 2023;12(2): 329–340.
- 11. Bhatt P, Goe A. Carbon Fibres: Production, Properties and Potential Use. Materials Science Research India. 2023;14(1).
- 12. Wu T-L, Buesink F, Canavero F. Overview of Signal Integrity and EMC Design Technologies on PCB: Fundamentals and Latest Progress. *IEEE Transactions on Electromagnetic Compatibility*. 2013;55(4):624–638.
- 13. Damatopoulou T, Lazaris V, Kladas A, Mamalis AG. Electromagnetic Compatibility Issues in Electric Vehicle Applications. *Materials Science Forum.* 2018;915: 71–76.
- 14. Delfini A, Albano M, Vricella A, Santoni F, Rubini G, Pastore R, Marchetti M. Advanced Radar Absorbing Ceramic-Based Materials for Multifunctional Applications in Space Environment. *Materials*. 2018;11(9): 1730.
- 15. Deutschmann B, Winkler G, Kastner P. Impact of Electromagnetic Interference on the Functional Safety of Smart Power Devices for Automotive Applications. *Elektrotechnik und Informationstechnik*. 2018;135: 352–359.
- 16. Zhukov PA, Kirillov VY. The Application of Radar Absorbing Materials to Reduce Interference Emissions from Instruments and Devices of Spacecraft Electrical Systems. *IOP Conference. Series: Materials Science and Engineering.* 2019;868: 012009.
- 17. Frah MAA, Pavlushkina T, Babinova A, Belyaev V, Makeev M, Osipkov A, Konopleva E, Zhachkin V, Usachev V. Protection from Electromagnetic Pollution by Using Metal Based Shielding Materials. *Journal of Physics Conference Series*. 2021;2056(1): 012058.
- 18. Elzanaty A, Chiaraviglio L, Alouini M-S. 5G and EMF Exposure: Misinformation, Open Questions, and Potential Solutions. *Frontiers in Communications and Networks*. 2021;2.
- 19. Matthew UO, Kazaure JS. Chemical Polarization Effects of Electromagnetic Field Radiation from the Novel 5G Network Deployment at Ultra High Frequency. *Health and Technology*. 2021;11(2): 305–317.
- 20. Baqir MA, Latif H, Altintas O, Akhtar MN, Karaaslan M, Server H, Hameed M, Idrees NM. Fractal Metamaterial Based Multiband Absorber Operating in 5G Regime. *Optik*. 2022;266: 169626.
- 21. Mohammed SA, Albadri RAK, Al-Badri KSL. Simulation of the Microwave Five-Band a Perfect Metamaterial Absorber for the 5G Communication. *Heliyon*. 2023;9(9): e19466.
- 22. Ruan JF, Meng ZF, Zou RZ, Pan SM, Ji SW. Ultra-Wideband Metamaterial Absorber Based on Frequency Selective Resistive Film for 5G Spectrum. *Microwave and Optical Technology Letters*. 2023;65(1): 20–27.
- 23. Janardhan R, Ramamurthy K, Anand JS. Solution Properties of Polyurethane. Polymer Testing. 1994;13(5): 397 404.
- 24. Dillard DA. Physical Properties of Adhesives. In: da Silva LFM, Öchsner A, Adams RD (eds). *Handbook of Adhesion Technology*. Berlin: Springer; 2011. p.391–414.
- 25. Qian J, Lin J, Shi M. Combined Dry and Wet Adhesion Between a Particle and an Elastic Substrate. *Journal of Colloid and Interface Science*. 2016;483: 321–333.

- 26. Wang Y, Feng Z, Frechette J. Dynamic Adhesion due to Fluid Infusion. *Current Opinion in Colloid & Interface Science*. 2020;50: 101397.
- 27. An YJ, Nishida K, Yamamoto T, Ueda S, Deguchi T. Microwave Absorber Properties of Magnetic and Dielectric Composite Materials. *Electronics and Communications in Japan*. 2010;93(4): 18–26.
- 28. Elmahaishi MF, Azis RS, Ismail I, Muhammad FD. A Review on Electromagnetic Microwave Absorption Properties: Their Materials and Performance. *Journal of Materials Research and Technology*. 2022;20: 2188–2220.
- 29. Boiprav O, Ayad H, Abdaljlil SA, Lynkou L, Abdulmawlay M. Charcoal- and Foil-Containing Materials for Radio Electronic Control Systems Protection from Electromagnetic Interferences. In: 2022 IEEE 21st international Conference on Sciences and Techniques of Automatic Control and Computer Engineering (STA). 2022. p.299–304.
- 30. Sun J, Wang W, Yue Q. Review on Microwave-Matter Interaction Fundamentals and Efficient Microwave-Associated Heating Strategies. *Materials*. 2016;9(4): 231.
- 31. Nefedov IS. Effects of Electromagnetic Interaction in Periodic Arrays of Single-Wall Metallic Carbon Nanotubes. *Materials Physics and Mechanics*. 2012;13(1): 1–8.
- 32. Winarno N, Firdaus RA, Afifah RMA. The Effect of Conductivity and Permittivity on Propagation and Attenuation of Waves using FDTD. *Materials Physics and Mechanics*. 2019;42: 617–624.

Submitted: March 25, 2025 Revised: April 18, 2025 Accepted: May 20, 2025

Conductive and mechanical properties of graphene-filled polymer composites

D.N. Tonkov 🖾 🗓, M.I. Kobylyatskaya 🗓, E.S. Vasilyeva, V.E. Gasumyants 🗓

Peter the Great St. Petersburg Polytechnic University, St. Petersburg, Russia

™wtk dima@mail.ru

ABSTRACT

The conductive and mechanical properties of polymer composites based on styrene-butadiene rubber with different concentrations of graphene as a filler are studied. Based on the dependence of the resistivity of composites on the graphene content, the range of its values corresponding to the hopping conductivity mechanism was determined. For composites of compositions from this range, the sensitivity of the resistance to the degree of uniaxial stretching, as well as mechanical properties were investigated. The values of the gauge factor were determined, and it was found that with an increase in graphene content in the composite, its value first increases and then decreases. It is found that even under minimal stresses in composites, along with elastic deformations, plastic deformations also develop, and the proportion of the latter increases with the filler concentration. As a result, complete mechanical relaxation of the composites does not occur after the applied stress is removed.

KEYWORDS

polymer composite materials • styrene-butadiene rubber • graphene • resistivity • gauge factor • deformations **Citation:** Tonkov DN, Kobylyatskaya MI, Vasilyeva ES, Gasumyants VE. Conductive and mechanical properties of graphene-filled polymer composites. *Materials Physics and Mechanics*. 2025;53(2): 48–54. http://dx.doi.org/10.18149/MPM.5322025_5

Introduction

In recent years, there has been a significant increase in the number of studies devoted to polymer conductive composite materials with graphene-based fillers, as well as other structures in which graphene is used as one of the materials [1-7]. This is due to the unique physical and chemical characteristics of graphene-containing materials and the prospects for their application in various fields of science and technology. Polymer nanocomposite films represent a promising basis for developing sensor devices for use as elements of wearable electronics [8-10]. These materials are characterized by unique structural and mechanical properties, which makes it possible to achieve such important characteristics of composites from a practical point of view as lightness, flexibility, wear resistance and corrosion resistance, as well as the ability to form products in various configurations. Devices based on polymer nanocomposites are distinguished by their miniature size, making them nearly invisible to users when worn continuously. The development and application of new sensor materials contribute to progress in various fields such as medicine [11–14], the sports industry [15], professional activities in hazardous conditions where health monitoring is necessary [16], as well as in game design and fashion [17]. In addition, polymer nanocomposites are actively used as triboelectric generators [18].



One of the promising areas for the use of flexible conductive polymer composites is their use for the creation of strain sensors [19,20], for which a conductive filler is introduced into the polymer matrix. The conductive network formed by the filler particles (e.g., metallic micro- or nanoparticles) is partially destroyed during deformation, which leads to an increase in the resistance of the composite. However, traditional composites based on metallic fillers have low flexibility and elasticity, as well as sensitivity to stretching in a very limited range [21]. In this sense, polymer composites with carbon-based fillers exhibit better characteristics, which is why composites based on various polymers with fillers such as graphite [22], graphene [23] or carbon nanotubes [24] have been actively studied in recent years. However, the properties of the resulting composites with these fillers depend significantly on the synthesis method, the type of polymer matrix and filler, as well as the filler content, which initiates further research. It should be noted that graphene is an excellent choice as a filler material for such composites due to its conductivity, thermal conductivity, and mechanical properties [25].

This study presents an experimental investigation of the conductive and mechanical properties of flexible polymer composites based on styrene-butadiene rubber (SBR) as the matrix and graphene as the filler. The aim of the study was to determine the dependence of the strain sensitivity of the obtained composites, their elongation under uniaxial static tension, ultimate strength and relaxation properties on the graphene content.

Materials and Methods

Styrene-butadiene rubber (SBR) from Sigma-Aldrich was used as the non-conductive polymer matrix, and powdered graphene was used as the filler.

The process of forming the composite film involved the preliminary dispersion of the graphene powder in the CCl₄ solvent using magnetic stirring in a sealed flask to prevent the solvent from evaporating and air from entering the system. SBR granules were then added to the obtained dispersion in an amount of 5.9 wt. % relative to the mass of the solvent, after which mixing was continued until the polymer was completely dissolved. The resulting solution was poured into a PTFE mold and dried in an exhaust system for 1 h until the solvent was completely removed.

Samples with graphene content ranging from 13 to 33 wt. % relative to the total composite mass were synthesized. The resistivity ρ of the obtained films was measured using the Van der Pauw method. To determine the ρ dependence on the degree of mechanical stretching, the samples were fixed in a measurement cell with a movable part, and electrical contacts were connected to them. After this, step-by-step stretching was carried out by registering the resistivity values at each stage.

The mechanical properties of the composite films were analyzed using the same setup without connecting electrical contacts. The strength and relaxation properties were studied by repeatedly stretching the samples in 10 mm steps. At the end of each cycle, the sample was held in a stretched state for 5 sec, after which the load was removed, and after 25 sec the residual length of the sample was measured. The relaxation time was determined by stretching the sample to 400 % of its initial length and then recording the change in length every 20 sec until the relaxation process was complete.

Results and Discussion

To analyze the change in the conductive properties of the composites under deformation, it is necessary to take into account the percolation threshold for the conductive filler particles introduced into the dielectric polymer matrix. The main parameter that determines the properties of the resulting composite is the degree of particle overlap [26]. At high particle concentrations, a continuous conductive cluster is formed, where the particles directly contact with each other. As the particle concentration decreases, their arrangement becomes sparser, and the conduction mechanism changes to a hopping form. With a further decrease in the particle concentration, taking into account their average size, the probability of such "jumps" significantly reduced resulting in a sharp decrease in the conductivity of the composite to nearly zero levels. It is the samples with filler concentrations at which hopping conductivity is realized that are the most promising for use as active elements in sensor devices. The probability of "jumping" (and, consequently, the conductivity value) depends exponentially on the distance between the conductive particles, which makes such composites the most sensitive to stretching.

Thus, to obtain samples with high sensitivity to deformation, it was necessary to determine the range of graphene concentrations corresponding to the hopping conduction mechanism. Figure 1 shows the dependence of the resistivity of the investigated samples at room temperature on the filler mass fraction. From the data presented it is evident that at graphene concentrations below 33 wt. % a sharp increase in the resistivity of the samples is observed. This indicates the destruction of the continuous conductive cluster and the transition to hopping conductivity. For this reason, samples with graphene concentrations of 30, 24, and 16 % were selected for further measurements.

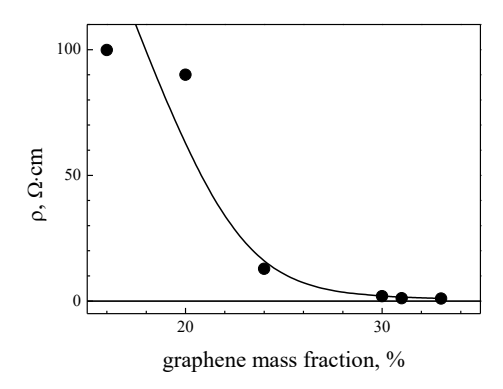


Fig. 1. The dependence of the resistivity of composites at T = 300 K on the graphene content

Fig. 2. Changes in the resistivity of composites under their stretching

For the three composites of the above compositions, Fig. 2 shows the dependence of the resistivity, normalized to its value in the absence of applied stress, ρ_0 , on the relative elongation of the sample under the influence of uniaxial stress, $\Delta L/L_0 \cdot 100\%$, where L_0 is the initial length of the sample, ΔL is the change in its length under stretching. For the composites of each composition, the data are provided for the stress ranges in which they exhibit conductivity.

As expected, an increase in graphene concentration leads to an expansion of the applied stress range in which the composite retains its resistivity. A noticeable change in the resistivity of the composite at the minimum graphene concentration (16 %) occurred at a stretch of 12 %, while at its maximum concentration (30 %), it occurred at a stretch of 24–30 %. At the same time, the composite with the highest graphene content among those studied has lower sensitivity to stretching: to noticeably change the resistivity, it had to be stretched over a significantly greater length. This effect of filler concentration on stretch sensitivity can be explained by the fact that stretching increases the distance between particles, which, from the perspective of conductivity values, is equivalent to a decrease in the filler concentration. Additionally, as noted by the authors of [27], strong stretching of graphene-containing composites leads to a change in the dimensionality of the filler particles (transition from a three-dimensional to a two-dimensional case), which should lead to an increase in the values of the percolation threshold and, consequently, to a decrease in the effect of stretching on the resistivity value.

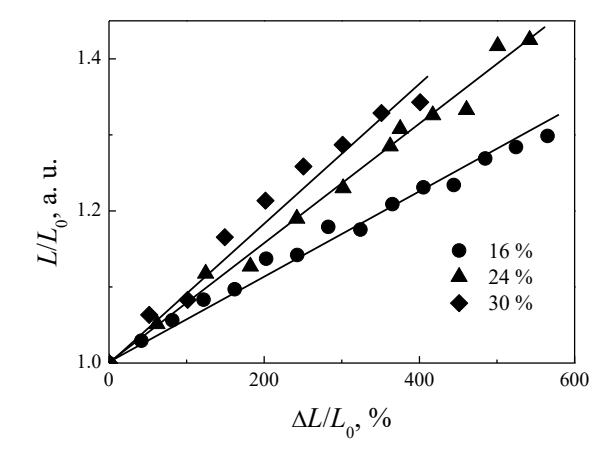
For composites of different compositions, the values of the gauge factor were calculated using the equation:

$$GF = (\Delta \rho_{\text{max}}/\rho_0)/(\Delta L_{\text{max}}/L_0), \tag{1}$$

where Δp_{max} and ΔL_{max} are the maximum changes in resistivity and length, respectively. This coefficient characterizes the sensitivity of the resistivity of composites to stretching and can be used to compare data obtained for different composites [28–33]. As the filler concentration increases, the gauge factor first rises and then decreases. For the sample with 16 % graphene content, the gauge factor is GF = 534.7, for the sample with 24 % content – GF = 2661, and for the sample with 30% content – GF = 340.4. This can be explained by the fact that increasing the filler concentration leads to two different effects. The first of these is due to the fact that the range of stress in which the composite retains its conductive properties increases (see Fig. 2), which should lead to a decrease in the GF value. The opposite effect on the GF value is caused by the decrease in the resistivity of the composite in the absence of stress that occurs with an increase in the graphene concentration (see Fig. 1).

To initially estimate the mechanical properties of the synthesized composites, an assessment of their tensile strength, an analysis of the nature of the deformations developing in them under uniaxial static tension, and a study of their relaxation properties were carried out. The samples were repeatedly stretched with a successive increase in their extension in 10 mm increments until they failed. After each stretching step, the sample length L was measured 25 sec after the stress was removed. The obtained results are presented in Fig. 3 as the dependence of the ratio of the sample length L to its initial length L0 on its relative elongation under stretching.

As seen from the presented data, the tensile strength decreases with an increase in filler content and is 565, 542, and 401 % for composites with graphene contents of 16, 24, and 30 %, respectively. Additionally, it is evident that none of the synthesized composite samples retain their initial length even under minimal applied stress, which indicates the occurrence the irreversible plastic deformations in them, along with elastic ones. The slope of the dependences shown in Fig. 3 increases consistently with increasing filler concentration, which suggests an increase in the proportion of irreversible deformations, i.e., the occurrence of the effect of their accumulation under repeated stretching of the sample.



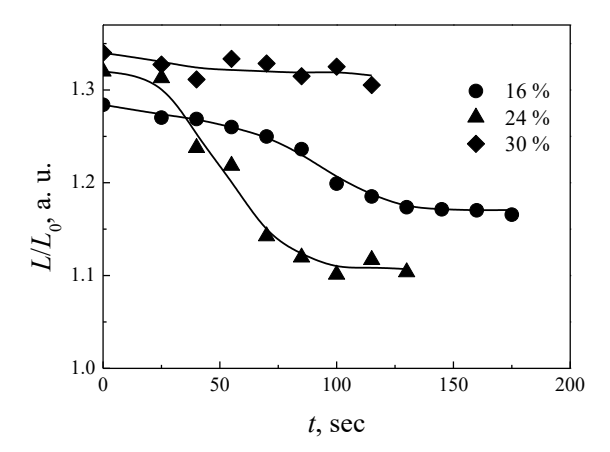


Fig. 3. The dependence of relative elongation of composite samples after stress removal on the degree of their stretching

Fig. 4. The dependence of the relative change in the length of composites after stress removal on time

The results of the study of the relaxation properties of the synthesized composites after stress of 400 % are presented in Fig. 4. Composites of all studied compositions do not return to their original length even 2-3 min after the stress is removed. This can be due to the formation of jams of flat filler particles inside the polymer matrices during stretching [34–36]. The sample with 30 % graphene content practically does not relax at all, and the sample with 16 % graphene content relaxes, but rather weakly. The composite with 24 % graphene content demonstrates the best relaxation properties, both in terms of time and degree of relaxation. Thus, a filler concentration of 24 % is close to the critical point for the studied composites, above which the improvement of the mechanical properties is replaced by their deterioration. It should be noted that this result indirectly corresponds to the data obtained in [37] when analyzing the properties of composites based on polyvinyl acetate with graphene filler. The authors of [37] studied samples in a lower range of graphene concentration range than in our study (below its possible critical value), but found that a consistent increase in the graphene content in composites initially leads to a significant improvement in their mechanical properties, but then this improvement slows down.

Thus, the graphene content of 24 % is optimal for the studied SBR-based polymer composites, as it corresponds to both the maximum strain sensitivity and the best relaxation properties.

Conclusions

In this study, we investigated the electrical and mechanical properties of polymer composites based on styrene-butadiene rubber with variable content of graphene as a conductive filler. It was found that increasing the graphene concentration in the SBR matrix leads to an increase in the range of value of applied uniaxial stress in which the composite slightly changes its resistivity. A gradual increase in graphene concentration first leads to an increase in the sensitivity of composite resistivity to stretching, and then to a decrease. At the same time, the tensile strength of the composites decreases slightly, and repeated uniaxial stretching leads to the accumulation of plastic deformations preventing complete relaxation of the samples after deformation.

The maximum change in the resistivity under deformation was observed in the composite with a graphene concentration of 24 %, for which the value of the gauge factor reaches GF = 2661. This graphene concentration also corresponds to the best relaxation properties. The obtained data indicate the potential of using the synthesized composites for the development of sensor devices for flexible wearable electronics.

Conflict of interest

The authors declare that they have no conflict of interest.

References

- 1. Skiba NV. Deformation mechanism of bimodal metal-graphene composites with nanotwinned structure. *Materials Physics and Mechanics*. 2021;47(5): 676–680.
- 2. Zhang B, Sun F, Li Y, Wu D, Yang C, Wang Z, Gao J, Zhao G, Sun S. Changing the potassium-based activation path to prepare coal-based porous carbon with more graphitic or graphene structures for high-performance organic supercapacitors. *Carbon*. 2024;219: 118812.
- 3. Li W, Liu M, Cheng S, Zhang H, Yang W, Yi Z, Zeng Q, Tang B, Ahmad S, Sun T. Polarization independent tunable bandwidth absorber based on single-layer graphene. *Diamond and Related Materials*. 2024;142: 110793.
- 4. Kopac T. Evaluation of recent studies on electrochemical hydrogen storage by graphene-based materials: Impact of modification on overall effectiveness. *International Journal of Hydrogen Energy*. 2024;69: 777–803. 5. Fan X, He C, Ding J, Gao Q, Ma H, Lemme MC, Zhang W. Graphene MEMS and NEMS. *Microsystems &*
- Nanoengineering. 2024;10(1): 154.
 6. Tonkov DN, Kobylyatskaya MI, Vasilyeva ES, Semencha AV, Gasumyants VE. Conductive properties of flexible polymer composites with different carbon-based fillers. *Journal of Physics: Conference Series*.
- 2022;2227(1): 012022.

 7. Tonkov D, Vasilyeva E, Tolochko O, Gasumyants V. Conductive and tensoresistive properties of flexible polymer composites: Experimental study and modeling. In: 2024 International Conference on Electrical
- Engineering and Photonics (EExPolytech). Saint Petersburg: Russian Federation; 2024. pp. 410–413 8. Khayal A, Nami SAA. Next-generation wearable technologies: The rise of multifunctional hydrogels in smart electronics. Journal of Cleaner Production. 2025: 145265.
- 9. Li J, Zhao Y, Fan Y, Chen J, Gong J, Li WJ. Flexible wearable electronics for enhanced human-computer interaction and virtual reality applications. *Nano Energy*. 2025;138: 110821.
- 10. Li Y, Li Q, Yin H, Jiang C, Chen Y, Jiang L, Guo Y. Super P carbon nanoparticles activated hydrogel sensors for developing fully integrated wearable electronics via an in-situ writing strategy. *Chemical Engineering Journal*. 2025;508: 161060.
- 11. Bonato P. Advances in wearable technology and applications in physical medicine and rehabilitation. *Journal of NeuroEngineering and Rehabilitation*. 2002;2: 2.
- 12. Avcu E, Bastan FE, Guney M, Yildiran Avcu Y, Ur Rehman MA, Boccaccini AR. Biodegradable polymer matrix composites containing graphene-related materials for antibacterial applications: A critical review. *Acta Biomaterialia*. 2022;151:1–44.
- 13. Das TK, Prusty S. Graphene-based polymer composites and their applications. *Polymer-Plastics Technology and Engineering*. 2013;52(4): 319–331.
- 14. Mousavi SM, Hashemi SA, Kalashgrani MY, Omidifar N, Bahrani S, Vijayakameswara Rao N, Babapoor A, Gholami A, Chiang W-H. Bioactive graphene quantum dots based polymer composite for biomedical applications. *Polymers*. 2022;14(3): 617.
- 15. Aroganam G, Manivannan N, Harrison D. Review on wearable technology sensors used in consumer sport applications. *Sensors*. 2019;19(9): 1983.
- 16. Chutturi M, Kelkar BU, Yadav SM, Wibowo ES, Bhuyar P, Naik BP, Sinha A, Lee SH. Exploring nanolignin as a sustainable biomacromolecule in polymer composites: Synthesis, characterization, and applications: A review. *International Journal of Biological Macromolecules*. 2025;304(2): 140881.

- 17. Wilson S, Laing R. (2018). Wearable technology: Present and future. In: *Proceedings of the 91st Textile Institute World Conference, Vol. 1.* Leeds: United Kingdom; 2018. p. 272–286.
- 18. Yang S, Larionova T, Kobykhno I, Klinkov V, Shalnova S, Tolochko O. Graphene-doped thermoplastic polyurethane nanocomposite film-based triboelectric nanogenerator for self-powered sport sensor. *Nanomaterials.* 2024;14(19): 1549.
- 19. Ma L, Lu W. Carbon nanotube film based flexible bi-directional strain sensor for large deformation. *Materials Letters*. 2020;260: 126959.
- 20. Ren J, Wang C, Zhang X, Carey T, Chen K, Yin Y, Torrisi F. Environmentally-friendly conductive cotton fabric as flexible strain sensor based on hot press reduced graphene oxide. *Carbon*. 2017;111: 622–630.
- 21. Trivedi DN, Rachchh NV. Graphene and its application in thermoplastic polymers as nano-filler A review. *Polymer*. 2022;240: 124486.
- 22. Takei K, Takahashi T, Ho JC, Ko H, Gillies AG, Lew PW, Fearing RS, Javey A. Nanowire active-matrix circuitry for low-voltage macroscale artificial skin. *Nature Materials*. 2010;9: 821–826.
- 23. Xia Y, Zhang Q, Wu XE, Kirk TV, Chen XD. Practical and durable flexible strain sensors based on conductive carbon black and silicone blends for large scale motion monitoring applications. *Sensors*. 2019;19(20): 4553.
- 24. Shi G, Zhao Z, Pai J-H, Lee I, Zhan, L, Stevenson C, Ishara K, Zhang R, Zhu H, Ma J. Highly Sensitive, Wearable, Durable Strain Sensors and Stretchable Conductors Using Graphene/Silicon Rubber Composites. *Advanced Functional Materials*. 2016;26(42): 7614–7625.
- 25. Dalmas F, Dendievel R, Chazeau L, Cavaille J-Y, Gauthier C. Carbon nanotube-filled polymer composites. Numerical simulation of electrical conductivity in three-dimensional entangled fibrous networks. *Acta Materialia*. 2006;54(11): 2923–2931.
- 26. Phiri J, Gane P, Maloney TC. General overview of graphene: Production, properties and application in polymer composites. *Materials Science and Engineering: B.* 2017;215: 9–28.
- 27. Hu N, Karube Y, Arai M, Watanabe T, Yan C, Li Y, Liu Y, Fukunaga H. Investigation on sensitivity of a polymer/carbon nanotube composite strain sensor. *Carbon*. 2010;48(3): 680–687.
- 28. Chen Y, Li Y, Xu D, Zhai W. Fabrication of stretchable, flexible conductive thermoplastic polyurethane/graphene composites via foaming. *RSC Advances*. 2015;5(100): 82034–82041.
- 29. Shchegolkov AV, Shchegolkov AV, Kaminskii VV, Chumak MA. Polymer composites with nanomaterials for strain gauging: A review. *Journal of Composites Science*. 2025;9(1): 8.
- 30. Zhang W, Piao S, Lin L, Yin Y, Guo J, Jiang Z, Cho Y, Li R, Gao J, Pang H, Piao Y. Wearable and antibacterial HPMC-anchored conductive polymer composite strain sensor with high gauge factors under small strains. *Chemical Engineering Journal*. 2022;435(2): 135068.
- 31. Zhang Y, Zhang Y, Deng W, Li Q, Guo M, Chen G. Skin-like soft thermoelectric composites with a "J-shaped" stress-strain behavior for self-powered strain sensing. *Advanced Functional Materials*. 2025;35(14): 2420644.
- 32. Costa P, Nunes-Pereira J, Oliveira J, Silva J, Moreira JA, Carabineiro SAC, Buijnsters JG, Lanceros-Mendez S. High-performance graphene-based carbon nanofiller/polymer composites for piezoresistive sensor applications. *Composites Science and Technology*. 2017;153: 241–252.
- 33. Yang H, Yao X, Zheng Z, Gong L, Yuan L, Yuan Y, Liu Y. Highly sensitive and stretchable graphene-silicone rubber composites for strain sensing. *Composites Science and Technology*. 2018;167: 371–378.
- 34. Ader F, Sharifzadeh E, Azimi N. Unveiling the impact of percolation phenomenon on the microstructure of polymer nanocomposites based on the combination of scaling and percolation theories. *Polymer Composites*. 2024;45(17): 16280–16292.
- 35. Yusuf J, Sapuan SM, Rashid U, Ilyas RA, Hassan MR. Thermal, mechanical, thermo-mechanical and morphological properties of graphene nanoplatelets reinforced green epoxy nanocomposites. *Polymer Composites*. 2024;45(3): 1998–2011.
- 36. Lee SJ, Yoon SJ, Jeon I-Y. Graphene/polymer nanocomposites: Preparation, mechanical properties, and application. *Polymers*. 2022;14(21): 4733.
- 37. Zhang Q, Chen D. Enhanced mechanical properties of graphene-based poly(vinyl alcohol) composites. *Macromolecules*. 2010;43(5): 2357–2363.

Submitted: November 24, 2024 Revised: April 4, 2025 Accepted: May 12, 2025

Effects of post-annealing duration on the properties of β -Ga₂O₃ thin films prepared by spray pyrolysis

X. Zhang ^{1 \subseteq (1)}, D.I. Panov ¹ (1), V.A. Spiridonov ¹ (1), N.K. Kuzmenko ¹, N.D. Prasolov ² (1),

A.Yu. Ivanov ¹, M.V. Dorogov ¹, H.M. Wei ³, D.Y. Jiang ³, D.A. Bauman ¹,

A.E. Romanov 1,2,4

ABSTRACT

The post-annealing duration dependence of structural and optical properties of polycrystalline β -Ga₂O₃ thin films fabricated on sapphire (Al₂O₃) substrate via the spray pyrolysis method are presented. Extending the annealing time for fixed temperature 900 °C from 1 to 2 h improves crystallinity of the films, as evidenced by an increase in the average grain size approximately from 8 to 14 nm, a reduction in the full width at half maximum of the $\bar{2}02$ β -Ga₂O₃ diffraction peak from 0.43 to 0.29°. However, extending the post-annealing duration to 3 h induces excessive grain coarsening into island-like crystalline domains. These findings demonstrate that for the chosen experimental conditions, a 2-hour annealing at 900 °C represents an optimum for achieving relatively smooth and solid β -Ga₂O₃ films while balancing crystallinity and film homogeneity.

KEYWORDS

Ga₂O₃ film • spray pyrolysis • sol-qel • post-anneal • duration

Funding. This work was supported by the Ministry of Science and Higher Education of the Russian Federation, project no. FSER-2025-0005. X. Zhang was supported by the China Scholarship Council. A.E. Romanov was also supported by Foreign Experts Key Support Project (Northeast Special Project), Grant No. D20240015 for his work in China on theoretical analysis of the obtained results.

Citation: Zhang X, Panov DI, Spiridonov VA, Kuzmenko NK, Prasolov ND, Ivanov AYu, Dorogov MV, Wei HM, Jiang DY, Bauman DA, Romanov AE. Effects of post-annealing duration on the properties of β-Ga₂O₃ thin films prepared by spray pyrolysis. *Materials Physics and Mechanics*. 2025;53(2): 55–63. http://dx.doi.org/10.18149/MPM.5322025_6

Introduction

Gallium oxide (Ga₂O₃), particularly its thermodynamically stable monoclinic β-phase, emerged as a promising ultra-wide bandgap semiconductor for next-generation power electronics and deep-ultraviolet (UV) optoelectronic devices [1]. With a bandgap of ~ 4.9eV, β-Ga₂O₃ exhibits exceptional properties, including a high breakdown electric field (8 MV/cm), Baliga's figure of merit (BFOM = $\varepsilon \cdot \mu \cdot E_c^3$, where ε is relative dielectric constant, μ is electron mobility and E_c is critical electric field) (3444), and thermal stability up to its melting point (~1795 °C) [2–4]. These characteristics position Ga₂O₃ as a superior alternative to the conventional semiconductors like SiC and GaN in high-voltage, high-



¹ ITMO University, St. Petersburg, Russia

² Ioffe Institute, St. Petersburg, Russia

³ School of Materials Science and Engineering, Changchun University of Science and Technology, Changchun, China

⁴ ITMO/CUST Joint Institute of Mechanics and Optics, Changchun, China

[™] 314519083@qq.com

temperature applications such as solar-blind photodetectors, Schottky diodes, and MOSFETs [1,2]. However, the performance of β -Ga₂O₃ thin films is critically dependent on their crystallinity, stoichiometry, and defect density, which are strongly influenced by synthesis methods and post-processing.

Thin-film fabrication techniques for β -Ga₂O₃ include molecular beam epitaxy (MBE) [5], pulsed laser deposition (PLD) [6], chemical vapor deposition (CVD) [7], metalorganic vapor-phase epitaxy (MOVPE) [8], halide vapor phase epitaxy (HVPE) [9], and radio frequency magnetron sputtering (RFMS) [10,11]. While these methods yield high-quality epitaxial layers, they suffer from limitations such as high equipment costs, complex vacuum requirements, and limited scalability. In contrast, sol-gel methods [12,13] like spray pyrolysis [14,15] offer cost-effective, scalable alternatives. The sol-gel technique excels in molecular-level homogeneity and precise doping control, enabling uniform incorporation of dopants such as Al [16] or Sn [17] to tailor optical and electrical properties. Spray pyrolysis, on the other hand, combines simplicity with industrial scalability, allowing large-area deposition at atmospheric pressure.

Post-annealing is a critical step in optimizing the structural and functional properties of solution-processed Ga_2O_3 films [18,19]. Thermal treatment facilitates the decomposition of organic residues, enhances crystallinity by promoting phase transitions, and mitigates defects such as oxygen vacancies [20,21]. This work investigates the effects of post-annealing duration on the properties of β - Ga_2O_3 thin films fabricated via spray pyrolysis method on sapphire substrate. By correlating annealing time with structural evolution, surface morphology, and optoelectronic performance, we aim to establish optimal processing parameters for high-performance devices.

Materials and Methods

β-Ga $_2O_3$ thin films were synthesized on (0001)-oriented sapphire (Al $_2O_3$) substrate via a particular variant of sol-gel technique, namely, spray pyrolysis method. The precursor solution was formulated using gallium nitrate hydrate [Ga(NO $_3$) $_3$ ·8H $_2$ O, 99.9 %, Lankhit] dissolved in 2-methoxyethanol [C $_3$ H $_8$ O $_2$, 99.5 %, Leap Chem], serving as the solvent. Monoethanolamine (MEA) [C $_2$ H $_7$ NO, 99.5 %, Vekton] was introduced as a stabilizer to ensure solution homogeneity and prevent premature precipitation. The molar concentrations of both gallium nitrate and 2-methoxyethanol were maintained at 0.25 mol/L, with a 3:1 molar ratio of gallium nitrate to MEA. The mixture was magnetically stirred at 60 °C for 1 h to achieve a pale yellow, transparent and stable sol. Prior to deposition, the (0001) sapphire substrate underwent ultrasonic cleaning in sequential baths of isopropanol and deionized water (10 min each) to remove organic contaminants and particulate matter.

The spray pyrolysis setup for Ga_2O_3 thin film fabrication has been described in detail in our previous work [14]. Figure 1 illustrates the preparation workflow. The sol was sprayed onto substrates mounted on a heating stage maintained at 140 °C. Following solvent evaporation, the samples were transferred to a preheated muffle furnace and pre-annealed at 500 °C for 10 min under ambient air atmosphere. This deposition-pre-annealing cycle was repeated 30 times to achieve the desired film thickness. After fabrication, the samples were subjected to post-annealing in the same muffle furnace

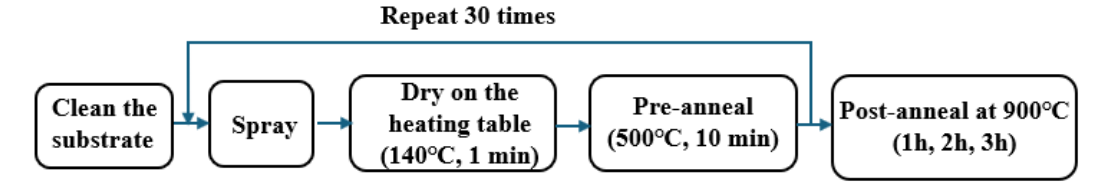


Fig. 1. The workflow of Ga₂O₃ films fabricated by spray pyrolysis

at 900 °C (this temperature corresponds to experimental results published in [21,22]) in air with varying durations of 1, 2, and 3 h.

The crystal structure of the samples was characterized using a Rigaku Ultima IV X-ray diffractometer (XRD) with Cu-K α radiation (λ = 0.15418 nm). XRD patterns were acquired in the 2ϑ angular range of 25 to 70° at a scanning rate of 0.5°/min.

The average crystallite size, representing the coherent scattering domain, was determined through Halder-Wagner analysis [23,24] of the XRD data using the following relation:

$$\left(\frac{\beta^*}{d^*}\right)^2 = \frac{1}{t} \times \left(\frac{\beta^*}{d^{*2}}\right) + \left(\frac{\varepsilon}{2}\right)^2,\tag{1}$$

 $(\frac{\beta^*}{d^*})^2 = \frac{1}{t} \times \left(\frac{\beta^*}{d^{*2}}\right) + \left(\frac{\varepsilon}{2}\right)^2,$ (1) where $\beta^* = \frac{\beta cos\theta}{\lambda}$, $d^* = \frac{2sin\theta}{\lambda}$, β denotes the experimental FWHM (in radians), $\lambda = 0.15418 \text{ nm}$ (Cu-K α radiation wavelength), ε quantifies the micro-strain within crystallites, t corresponds to the average crystallite size.

The surface morphology of the films was characterized using a TESCAN Mira 3 scanning electron microscope (SEM). For quantitative surface roughness analysis, a Veeco Dimension 3100 atomic force microscope (AFM) was employed to measure the rootmean-square (RMS) roughness and map nanoscale topographic features.

The optical properties of the β-Ga₂O₃ thin films were investigated through transmittance spectroscopy and Tauc plot analysis [25]. Optical transmission spectra were acquired in the 200-850 nm wavelength range using a PerkinElmer Lambda 950 UV-Vis-NIR spectrophotometer, with (0001)-oriented sapphire substrates serving as optical windows. Film thickness was determined via cross-sectional SEM imaging. The optical bandgap (E_q) was calculated using the Tauc relation [25]:

$$(\alpha h \nu)^2 = A(h \nu - E_a), \tag{2}$$

where α is the absorption coefficient, hv represents photon energy, and A is a proportionality constant.

The influence of post-annealing temperature on surface morphology and optoelectronic properties was systematically evaluated through comparative analysis of structural and optical data.

Results and Discussion

Figure 2 shows the XRD spectra of β -Ga₂O₃ films post-annealed at 900 °C for 1, 2, and 3 h. Four significant reflection peaks are observed at 30.2, 31.6, 59.3, and 64.7°, corresponding to the (400), ($\bar{2}02$), ($\bar{6}03$), and ($\bar{7}12$) crystallographic planes of crystallites in β -Ga₂O₃ polycrystalline film, respectively. With the increase of post-annealing duration, the intensity of the $\bar{2}02$ peak is significantly enhanced and its FWHM decreases, while the other main peaks do not change significantly. This selective enhancement of the

contribution of $(\bar{2}02)$ orientation can be attributed to the synergistic effect between substrate-induced epitaxial orientation and thermally activated grain reorganization. The (0001) surface of sapphire substrate has a hexagonal close-packed structure and has a template effect, which is conducive to the growth of β -Ga₂O₃ grains along a specific crystallographic direction. The $(\bar{2}02)$ facet of β -Ga₂O₃ may show good lattice matching with the substrate, thus minimizing the interface energy and promoting the preferred orientation during post-annealing.

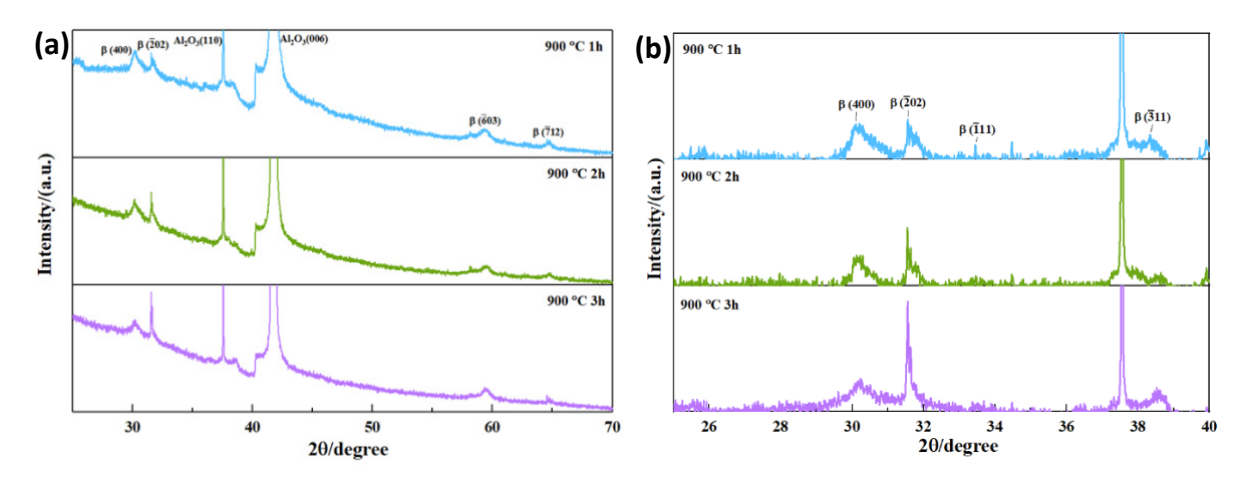


Fig. 2. XRD patterns of β-Ga₂O₃ thin films post-annealed at 900 °C for durations of 1, 2, and 3 h (a), detailed patterns (b), compared with ICDD reference data (PDF 00-041-1103)

Table 1 summarizes the analysis of diffraction peaks for β-Ga₂O₃ thin films postannealed at 900 °C for 1, 2, and 3 h. Initially, increasing the annealing duration from 1 to 2 h resulted in a reduction of the full width at half maximum (FWHM) for $\overline{2}02$ peak from 0.43 to 0.29°, accompanied by an increase in average crystallite size from 8.15 to 14.06 nm. This behavior is consistent with enhanced crystallinity and grain coarsening, aligning with classical Ostwald ripening [26], where smaller grains dissolve to supply larger ones, thereby reducing lattice defects and micro-strains. However, extending the annealing time to 3 h further reduces the full width at half maximum (FWHM) to 0.13°, while decreasing the average crystallite size to 11.44 nm. This behavior of the average grain size contradicts the traditional mechanism of nucleation during film crystallization from the amorphous state. Similar effects were observed in other studies [21,27]. In part, this behavior of the grain size can be explained by processes similar to sintering, when additional formation of small grains occurs in the pores between large grains. This can lead to a decrease in the average grain size at a certain stage. Another reason may be the diffusion of aluminum from the substrate, which is observed at temperatures of 900–1000 °C [27,28]. Due to diffusion, a double solid solution (Al_xGa_{1-x})₂O₃ can form in the region close to the substrate, which can also lead to a decrease in the average grain size [29]. However, these hypotheses require verification and confirmation by independent experiments, as well as the dependence of the grain size on the annealing time.

Figure 3 shows top-view SEM images of β -Ga₂O₃ films post-annealed at 900 °C for 1, 2, and 3 h, showing the evolution of the film surface morphology and grain structure under different heat treatment durations. For the sample post-annealed for 1 h (Fig. 3(a)), the film surface is relatively smooth and uniform, and the grains are small and

Table 1. Diffraction peak analysis of β -Ga₂O₃ films with post-annealing temperature of 900 °C and time of 1, 2, and 3 h

Duration, h	FWHM of $\overline{2}02$ peak, $^{\circ}$	Average crystallite size, nm
1	0.43	8.15
2	0.29	14.06
3	0.13	11.44

loosely distributed. This indicates that the grain growth is limited in the initial stage of post-annealing because the thermal energy is insufficient for significant atomic diffusion. When the time is extended to 2 h (Fig. 3(b)), the grain density and uniformity are significantly improved, and directional texture appears on the surface. This texture may be aligned with the crystal plane orientations, reflecting the enhancement of atomic mobility and stress relaxation during long post-annealing. For the sample post-annealed for 3 h (Fig. 3(c)), the grain clusters are significantly coarsened to form irregularly sized crystal islands, and the directional texture disappears, which is the result of the combined effects of competitive grain growth mechanisms or local strain redistribution.

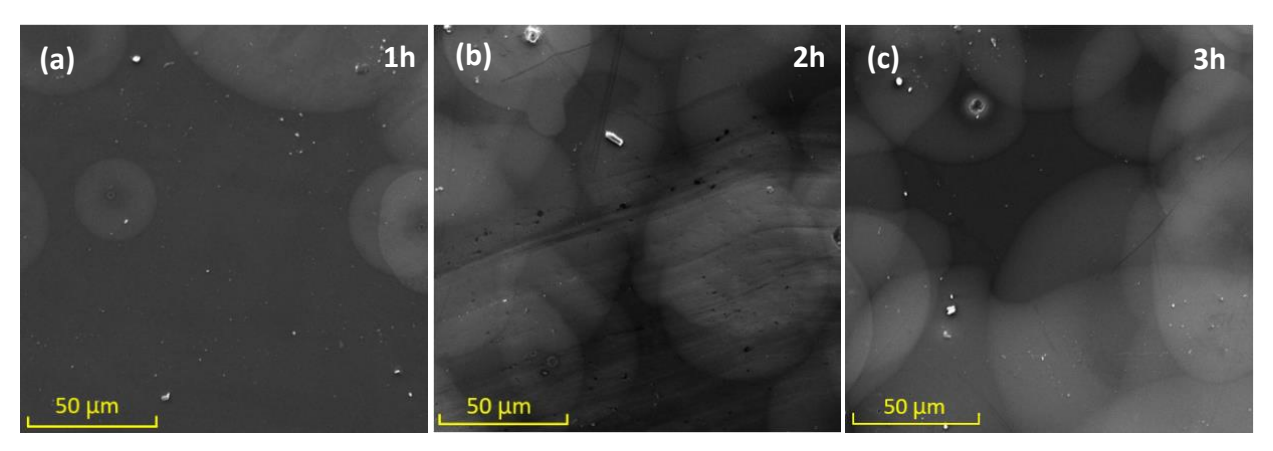


Fig. 3. SEM top-view images of β -Ga₂O₃ films post-annealed at 900 °C for (a) 1, (b) 2, (c) 3 h

Side-view SEM images of β -Ga₂O₃ films post-annealed at 900 °C for 1, 2, and 3 h are shown in Fig. 4. The thickness of all samples is from 1 to 1.1 µm, demonstrating that the annealing time has little effect on the film thickness. For the sample post-annealed for 1 h (Fig. 4(a)), the film exhibits a relatively discontinuous layered structure. The grain boundaries are not resolved and the interface between the film and the substrate is slightly rough, indicating incomplete crystallization and limited atomic mobility in the initial stage of post-annealing. This is because the oxygen vacancy compensation effect is stronger than grain growth in a shorter post-annealing time, and insufficient stored thermal energy will limit the complete densification of the film. When the post-annealing time is increased to 2 h (Fig. 4(b)), a more uniform and continuous film cross section structure is observed, accompanied by neatly arranged columnar grains, indicating that atomic diffusion and micro-stress relaxation are enhanced. For the 3 h post-annealed sample (Fig. 4(c)), the columnar grains evolved into larger irregularly shaped domains. This overgrowth and partial structural degradation indicate that the grain growth mechanism shifted from controlled grain growth to competitive crystallization, and excessive thermal exposure led to local micro-strain accumulation.

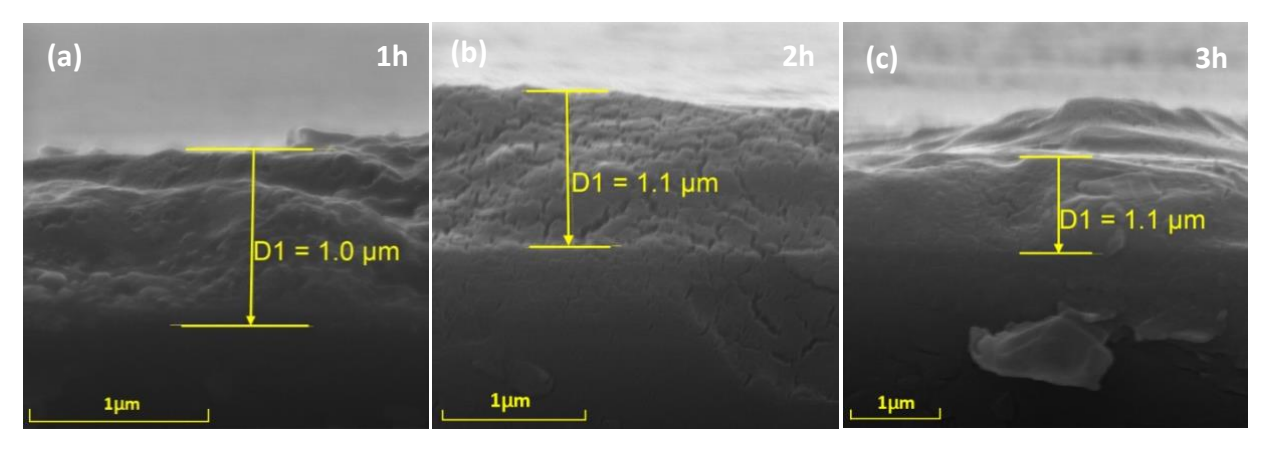


Fig. 4. SEM side-view images of β -Ga₂O₃ films post-annealed at 900°C for (a) 1, (b) 2, (c) 3 h

The two-dimensional AFM images (1 × 1 μ m²) of β -Ga₂O₃ films with different postannealing durations were analyzed using AFM. As shown in Fig. 5, the surface of the film post-annealed for 1 h is smooth and uniform, with sparse grain distribution and the RMS roughness of 0.94 nm. When the post-annealing duration is extended to 2 h, a significant increase in grain density and size is observed, and the closely packed grains coalesce into a continuous and dense film structure. RMS roughness corresponding to this morphological transformation increases to 1.87 nm. This result is consistent with the increase in the average grain size (see Table 1). Further extending the post-annealing duration to 3 h will form heterogeneous crystal islands of various sizes, and the RMS roughness increases significantly to 2.54 nm. This change is due to thermally driven atomic reorganization. Initially, extending the post-annealing duration is beneficial for the migration of gallium and oxygen atoms to energetically favorable lattice positions, thereby enhancing the densification and crystallinity of the film [30]. However, overannealing will destroy this balance. This process leads to non-uniform grain growth and competitive crystallization, which increases surface roughness, size differences, and spatial inhomogeneity of grain distribution. Therefore, prolonged thermal exposure can compromise the homogeneity of the structure.

Figure 6 shows the transmittance and estimated band gap of β -Ga₂O₃ films post-annealed at 900 °C for 1, 2, and 3 h. The transmittance of the samples is about 90 % in the 300–850 nm range and has sharp absorption band edges near 250 nm. As the post-annealing

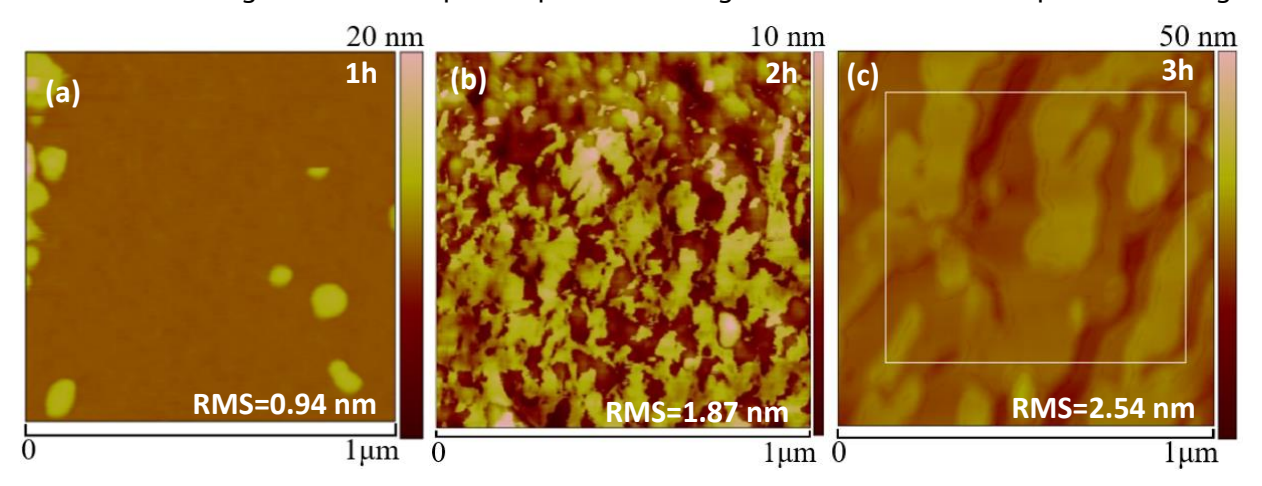


Fig. 5. AFM images of $\beta\text{-}Ga_2O_3$ films post-annealed at 900 °C for (a) 1, (b) 2, (c) 3 h

time increases, the measured optical band gap values are 4.98, 4.93, and 4.95 eV. The change in the band gap width may be associated with the corresponding changes in the micro-stresses in the film, discussed above. Concurrently, the extended post-annealing duration can facilitate diffusion-driven incorporation of Al^{3+} ions from the (0001) Al_2O_3 substrate into Ga^{3+} lattice positions within the β - Ga_2O_3 lattice sites. This may lead to the formation of a double solid solution of ($AlGa)_2O_3$ in the near-substrate region, the band gap width of which is larger than that of gallium oxide, proportional to the aluminum content [31]. However, the observed variations in the band gap width are too small to confidently draw conclusions about any noticeable trend.

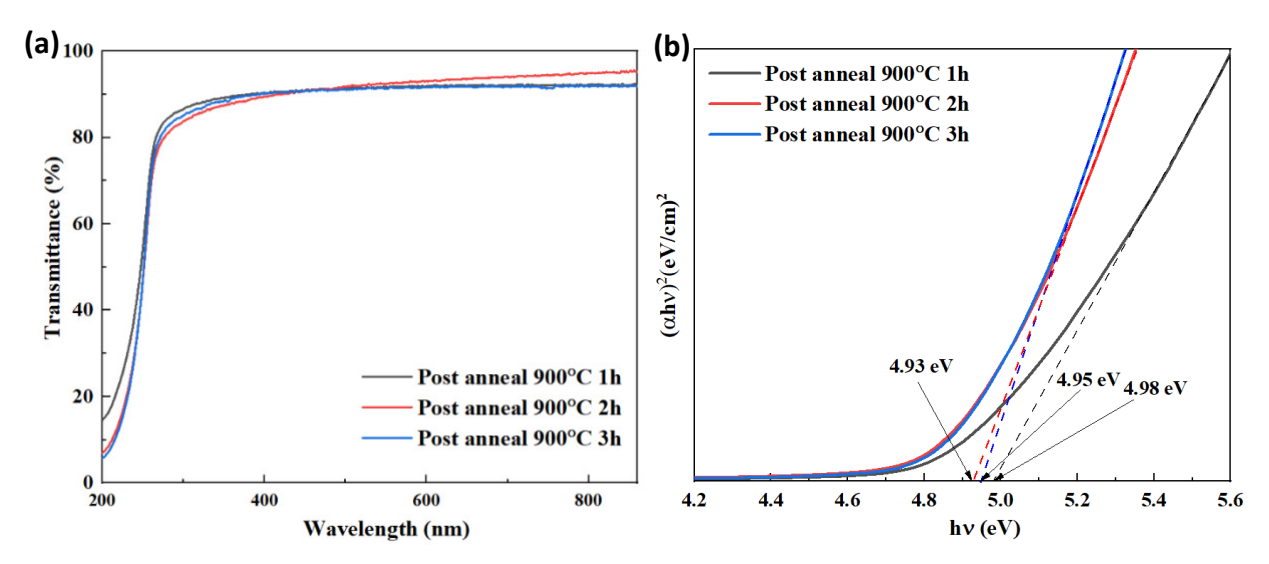


Fig. 6. (a) Optical transmission spectra and (b) bandgap estimation of β-Ga₂O₃ films post-annealed at 900 °C for 1, 2, 3 h

Conclusions

In this study we have systematically investigated the structural evolution and optic properties of spray-pyrolyzed β -Ga $_2$ O $_3$ thin films as function of post-annealing duration (1–3 h at 900 °C). Increasing the post-annealing duration from 1 to 2 h enhances crystallinity, as evidenced by the growth of the average grain size from 8.15 to 14.06 nm, a reduction in the FWHM of the $\overline{2}$ 02 peak from 0.43 to 0.29°, and an increase in the RMS surface roughness from 0.94 to 1.87 nm. Concurrently, stress relaxation mediated by grain boundary migration narrows the optical bandgap from 4.98 to 4.93 eV. However, extending the post-annealing duration to 3 h further reduces the FWHM of the $\overline{2}$ 02 peak to 0.13°, while decreasing the average grain size to 11.44 nm and elevating the RMS surface roughness to 2.54 nm. This suggests that prolonged post-annealing triggers competitive grain growth, leading to heterogeneous coarsening into island-like crystalline domains.

The obtained results underscore that moderate post-annealing duration (2 h) optimizes crystallinity, whereas excessive thermal exposure compromises structural homogeneity. This study establishes that under the chosen experimental conditions, a 2-hour post-annealing at 900 °C represents an optimum for obtaining relatively smooth and solid β -Ga₂O₃ thin films. These findings advance the development of cost-effective,

scalable Ga₂O₃-based technologies, effectively bridging the gap between laboratory-scale synthesis and industrial applications.

CRediT authorship contribution statement

Xi Zhang "SC: writing — original draft, conceptualization, investigation, data curation; Dmitrii I. Panov "SC: data curation; Vladislav A. Spiridonov "SC: data curation; Natalia K. Kuzmenko SC: data curation; Nikita D. Prasolov "SCE: data curation; Andrey Yu. Ivanov "SCE: data curation; Maksim V. Dorogov "SCEE: data curation; Haoming Wei SCEE: investigation; Dmitrii A. Bauman "SCEE: writing — review & editing, supervision; Alexey E. Romanov "SCEE: supervision.

Conflict of interest

The authors declare that they have no conflict of interest.

References

- 1. Pearton SJ, Yang J, Cary PH, Ren F, Kim J, Tadjer MJ, Mastro MA. A review of Ga₂O₃ materials, processing, and devices. *Applied Physics Reviews*. 2018;5(1): 011301.
- 2. Stepanov SI, Nikolaev VI, Bougrov VE, Romanov AE. Gallium oxide: properties and applications a review. *Reviews on Advanced Materials Science*. 2016;44(1): 63–86.
- 3. Liu Z, Li PG, Zhi YS, Wang XL, Chu XL, Tang WH. Review of gallium oxide based field-effect transistors and schottky barrier diodes. *Chinese Physics B.* 2019;28(1): 017105.
- 4. Schneider SJ, Waring JL. Phase equilibrium relations in the Sc_2O_3 - Ga_2O_3 System. *Journal of Research of the National Bureau of Standards-A. Physics and Chemistry.* 1963;67A(1): 19–25.
- 5. Oshima T, Okuno T, Fujita S. Ga_2O_3 thin film growth on c-plane sapphire substrates by molecular beam epitaxy for deep-ultraviolet photodetectors. *Japanese Journal of Applied Physics*. 2007;46(11): 7217–7220.
- 6. Xu C, Shen L, Liu H, Pan X, Ye Z. High-quality β -Ga₂O₃ films with influence of growth temperature by pulsed laser deposition for solar-blind photodetectors. *Journal of Electronic Materials*. 2021;50(4): 2043–2048.
- 7. Rafique S, Han L, Zhao H. Synthesis of wide bandgap Ga_2O_3 ($E_g \sim 4.6$ -4.7 eV) thin films on sapphire by low pressure chemical vapor deposition. *Physica Status Solidi (a)*. 2016;213(4): 1002–1009.
- 8. Tadjer MJ, Mastro MA, Mahadik NA, Currie M, Wheeler VD, Freitas JA, Greenlee JD, Hite JK, Hobart KD, Eddy CR, Kub FJ. Structural, optical, and electrical characterization of monoclinic β -Ga₂O₃ grown by MOVPE on sapphire substrates. *Journal of Electronic Materials*. 2016;45(4), 2031–2037.
- 9. Murakami H, Nomura K, Goto K, Sasaki K, Kawara K, Thieu QT, Togashi R, Kumagai Y, Higashiwaki M, Kuramata A, Yamakoshi S, Monemar B, Koukitu A. Homoepitaxial growth of β -Ga₂O₃ layers by halide vapor phase epitaxy. *Applied Physics Express*. 2015;8(1): 015503.
- 10. Yue W, Yan J, Wu J, Zhang L. Structural and optical properties of Zn-doped β -Ga₂O₃ films. *Journal of Semiconductors*. 2012;33(7): 073003.
- 11. Mohammed AAA, Lim WF. Effects of implementing dual-step nitrogen ambient for growth and post-deposition annealing of Ga₂O₃ films sputtered on silicon. *Journal of Materials Science: Materials in Electronics*. 2024;35: 1763.
- 12. Hench LL, West JK. The sol-gel process. *Chemical Reviews*. 1990;90(1): 33–72.
- 13. Zhu Y, Xiu X, Cheng F, Li Y, Xie Z, Tao T, Chen P, Liu B, Zhang R, Zheng YD. Growth and nitridation of β -Ga₂O₃ thin films by sol-gel spin-coating epitaxy with post-annealing process. *Journal of Sol-Gel Science and Technology*. 2021;100: 183–191.
- 14. Panov DI, Zhang X, Spiridonov VA, Azina LV, Nuryev RK, Prasolov ND, Sokura LA, Bauman DA, Bougrov VE, Romanov AE. Thin films of gallium oxide obtained by spray-pyrolysis: method and properties. *Materials Physics and Mechanics*. 2022;50(1): 107–117.
- 15. Ouadah E, Hamdadou N. Synthesis of WO2.72:Fe thin films via ammonium tungstate precursor by spray pyrolysis technique and annealing. *Materials Physics and Mechanics*. 2024;52(4): 141–151.

- 16. Tang X, Li KH, Liao CH, Vasquez JMT, Wang C, Xiao N, Li X. Chemical solution deposition of epitaxial indium- and aluminum-doped Ga_2O_3 thin films on sapphire with tunable bandgaps. *Journal of the European Ceramic Society*. 2022;42(1): 175–180.
- 17. Li Y, Li Y, Ji Y, Wang H, Zhong D. Sol-gel preparation of Sn doped gallium oxide films for application in solar-blind ultraviolet photodetectors. *Journal of Materials Science*. 2022;57: 1186–1197.
- 18. Kaminskii VV, Panov DYu, Spiridonov VA, Bauman DA, Kalganov DA, Scheglov MP, Romanov AE. Effect of high-temperature annealing on the internal friction and optical transmittance of single crystal gallium oxide. *Materials Physics and Mechanics*. 2024;52(5): 48–54.
- 19. Spiridonov VA, Panov DI, Ivanov AYu, Bauman DA, Romanov AE. The effect of high-temperature annealing on the properties of bulk β -Ga2O3 obtained in different growth atmospheres. *Materials Physics and Mechanics*. 2024;52(3): 80–85.
- 20. Rafique S, Han L, Zhao H. Thermal annealing effect on β -Ga₂O₃ thin film solar blind photodetector hetero epitaxially grown on sapphire substrate. *Physica Status Solidi (a)*. 2017;214(8): 1700063.
- 21. Bae MS, Kim SH, Baek JS, Koh JH. Comparative study of high-temperature annealed and RTA process β -Ga₂O₃ thin film by sol-gel process. *Coatings*. 2021;11(10): 1220.
- 22. Zhang X, Jiang DY, Zhao M, Zhang HX, Li MY, Xing MJ, Han JC, Romanov AE. The effect of annealing temperature on Ga_2O_3 film properties. *Journal of Physics: Conference Series.* 2021;1965: 012066.
- 23. Nath D, Singh F, Das R. X-Ray diffraction analysis by Williamson-Hall, Halder-Wagner and size-strain plot methods of CdSe nanoparticles- a comparative study. *Materials Chemistry and Physics*. 2020;239: 122021.
- 24. Halder NC, Wagner CNJ. Separation of particle size and lattice strain in integral breadth measurements. *Acta Crystallographica*. 1966;20(2): 312–313.
- 25. Sangiorgi N, Aversa L, Tatti R, Verucchi R, Sanson A. Spectrophotometric method for optical band gap and electronic transitions determination of semiconductor materials. *Optical Materials*. 2017;64: 18–25.
- 26. Baldan A. Review progress in Ostwald ripening theories and their applications to nickel-base superalloys Part I: Ostwald ripening theories. *Journal of Materials Science*. 2002;37: 2171–2202.
- 27. Hu H, Liu Y, Han G, Fang C, Zhang Y, Liu H, Wang Y, Liu Y, Ye J, Hao Y. Effects of post annealing on electrical performance of polycrystalline Ga_2O_3 photodetector on sapphire. *Nanoscale Research Letters*. 2020;15(1): 100. 28. Goyal A, Yadav BS, Thakur OP, Kapoor AK, Muralidharan R. Effect of annealing on β - Ga_2O_3 film grown by pulsed laser deposition technique. *Journal of Alloys and Compounds*. 2014; 583: 214–219.
- 29. Rubio EJ, Mates TE, Manandhar S, Nandasiri M, Shutthanandan V, Ramana CV. Tungsten incorporation into gallium oxide: crystal structure, surface and interface chemistry, thermal stability, and interdiffusion. *The Journal of Physical Chemistry C.* 2016;120(47): 26720–26735.
- 30. Dong L, Jia R, Xin B, Zhang Y. Effects of post-annealing temperature and oxygen concentration during sputtering on the structural and optical properties of β -Ga₂O₃ films. *Journal of Vacuum Science & Technology A.* 2016;34(6): 060602. 31. Zakgeim D, Bauman D, Panov D, Spiridonov V, Kremleva A, Smirnov A, Odnoblyudov M, Romanov A, Bougrov V. Growing of bulk β -(Al_xGa_{1-x})₂O₃ crystals from the melt by Czochralski method and investigation of their structural and optical properties. *Applied Physics Express.* 2022;15(2): 025501.

Submitted: March 05, 2024 Revised: September 19, 2024 Accepted: February 17, 2025

Fundamental theorems and variational criterion in modified couple stress under multi-phase-lags and rotation

S. Sharma ¹, S. Devi ², R. Kumar ² ¹⁰

- ¹University of Houston, Houston, Texas, USA
- ² Kurukshetra University, Kurukshetra, Haryana, India

ABSTRACT

Present study involves a new mathematical formulation of modified couple stress thermoelastic diffusion under multi-phase-lags model in rotating frame of reference. The governing equations for multi-phase-lags model in rotating frame of reference are obtained with the aid of modified Fourier's and Fick's laws and used to explore the energy, uniqueness, reciprocity theorems and variational criterion. Instantaneous concentrated body forces, heat and chemical potential sources along with moving heat and chemical potential sources are taken to illustrate the applications of the reciprocity theorem for a specific case. It has been observed that results obtained are dominated by the physical field. Some well-known results are also explored as special cases. The multi-phase-lags and rotation in modified couple stress material makes it more realistic as all the field quantities depend upon information from surrounding at a particular point. Physical views presented in this article may be useful for the design (composition, arrangement, device, etc.) new material, geophysics and other scientific domains. Also, the study has tremendous applications in material science, geomechanics, soil dynamics and electronic industry.

KEYWORDS

modified couple stress • thermoelastic diffusion • multi-phase-lags • rotating frame of reference • energy theorem uniqueness • reciprocity theorem • variation criterion

Citation: Sharma S, Devi S, Kumar R. Fundamental theorems and variational criterion in modified couple stress under multi-phase-lags and rotation. *Materials Physics and Mechanics*. 2025;53(2): 64–82. http://dx.doi.org/10.18149/MPM.5322025_7

Introduction

Over the last four decennary, the generalized theories of thermoelasticity has been established to remove the paradox of uncoupled and coupled theories. Lord and Shulman [1] (LS) proposed generalized thermoelastic model comprising one relaxation time whereas Green and Lindsay [2] (GL) rectified the LS model by involving another relaxation time to the respective equations and developed the new thermoelasticity theory. This modification allows that GL model to be dependent only on the strain-acceleration relation. To analyze the flow of heat without energy dissipation, Green and Naghdi [3] imported thermal displacement gradient to the humanistic Fourier law. Plethora of investigations based on the generalized theories of thermoelasticity have been considered in the work of Hetnarski and Ignaczak [4].

Phase lag with heat flow was first introduced by Tzou [5], who generalized it in the Cattaneo-Vernotte [6,7] (CV) formulation. The single-phase-lag heat transfer hypothesis is the term used most frequently to describe this idea. The dual-phase-lag (DPL) heat transfer theory was established by Tzou [8,9] be accumulating the temperature gradient



[™]rajneesh kuk@rediffmail.com

65 S. Sharma, S. Devi, R. Kumar

and heat flux with two-phase-lag time constants. Roychoudhari [10] introduced a new model which being the extension of DPL theory and named as three-phase-lag thermoelastic model which involves Fourier's law of heat conduction being replaced by an approximation to an alteration to the Fourier's law with the consideration of three distinct phase lags for the heat flux vector, the temperature gradient and the thermal displacement gradient. Comprehensive work on thermal conductivity and phase lags has been given in book by Tzou [11].

In [12–15], Nowacki explored the thermoelastic diffusion model which is based on humanistic thermoelasticity theory. The thermoelastic diffusion theory with one relaxation time and two relaxation times have been proposed by Sherief et al. [16] and Kumar and Kansal [17], respectively.

A modified elasticity theory, such as couple stress theory, has been developed because classical theories of continuum mechanics are inadequate to describe the mechanical nature of micro/nano structures. Couple stress theory being an extended elasticity theory which in extension to the classical force per unit area, also involve the impact of couple per unit area on material volume. As shear stress no more requires to be conjugated in order to retain rational equilibrium, this permits for the probability of the asymmetric stress tensor. One of the non-classical theories as classical couple stress theory was developed by Mindlin and Tiersten [18], Toupin [19] and Koiter [20]. This theory involves extension to the two traditional Lame's constants for isotropic elastic material, the governing equation for isotropic materials also involves higher order material length scale characteristics. Modified couple stress (MCS) theory was formulated from couple stress theory by Yang et al. [21] depicted that couple stress tensor is symmetric, and strain energy is quadratic function of strain and symmetric curvatures MCS theory include single material length scale parameter contrary to two classical substantial constants. In micro/nanosystems, the theory has been broadly applied to examine the vibration, bending, and buckling of structures including beams, plates, and shells. Various investigators have predicted theoretically the size-dependent behavior of microstructures by using the MCS theory. Also, it has been documented by analyzing theoretical and experimental researches by Park and Geo [22]. Aouadi [23] presented reciprocity and uniqueness in anisotropic thermoelastic diffusion materials. Kumar, Kothari and Mukhopadhyay [24] proved a convolutional type variational criterion and reciprocity theorem based on the isotropic thermoelastic diffusion model. Kumar and Gupta [25,26] presented uniqueness reciprocity theorem and wave phenomena in thermoelastic diffusion with fractional derivative and also in different theories of thermoelasticity. Sarkar and Mukhopadhyay [27] presented energy and uniqueness theorem along with the variational criterion in thermoelastic model with three-phaselags and memory dependent derivatives (MDD).

El-Karamany and Ezzat [28] established the uniqueness and reciprocal theorems for a linear anisotropic and inhomogeneous thermoelastic centro-symmetric solid in the frame of two-temperature Green–Naghdi theories. El-Karamany and Ezzat [29] investigated the uniqueness and reciprocal theorems without deploy of Laplace Transforms for the DPL thermoelasticity theory. Bala [30] explored basics theorems (uniqueness, continuous dependence and reciprocity) in relaxed micromorohic thermoelastic material. Al-Lehaibi [31] examined the variational criterion in two

temperature thermoelastic material without energy dissipation. In [32], Paul and Mukhopadhyay presented a novel mathematical model on generalized thermoelastic diffusion theory and presented uniqueness, reciprocity and variational criterion in thermoelastic diffusion model.

Recently, some efforts have been done to modify the humanistic Fourier's law of heat conduction by considering time derivative of higher order by Abouelregal [33–35]. The refined multi-phase-lag (RPL) model finds many advantages in various problems. Zenkour [36–38] presented a distinct form of the RPL model to concern with thermoelastic replies of many various composite materials. Ezzat and Fayik [39] constructed thermoelastic diffusion with fractional order derivatives and proved uniqueness, reciprocity theorems and variational criterion. Kumar and Sharma [40] analysed presented some theorems in piezo-thermoelastic with mass diffusion. Sharma et al. [41] investigated basic theorems and plane waves in the context of thermoelastic diffusion using a multi-phase-lag model with temperature dependence.

Due to the fact that various large body like earth, moon and other planet have an angular velocity as well as earth itself act like a huge magnet, it is convincing to explore the fundamental basic theorems in modified couple stress thermoelastic diffusion medium rotating with angular velocity. Roy Choudhuri [42] examined the plane harmonic waves in an unbounded isotropic electromagnetic thermoelastic medium when the entire medium rotates with a uniform angular velocity. Kumar and Devi [43] presented the effect of hall current and rotation in modified couple stress generalized thermoelastic half-space due to ramp-type heating.

Ezzat [44] investigated fundamental solution in generalized magneto-thermoelasticity with two relaxation times for perfect conductor cylindrical region. Ezzat and Youssef [45] established Stokes' first problem for an electro-conducting micropolar fluid with thermoelectric properties. Sharma et al. [46] established the plane waves and fundamental solution in an electro microstretch of elastic solids. Ezzat et al. [47] examined the equations of generalized thermo-viscoelasticity for an isotropic medium with variable thermal conductivity and fractional-order heat transfer. Sharma and Khator [48,49] examined some problems of power generation due to renewable sources and also explored micro-grid planning in the renewable inclusive prosumer market. Panja et al. [50] investigated a thermoelastic model with higher order time derivatives for a crack in a rotating solid. Bibi et al. [51] established the propagation and refection of thermoelastic wave in a rotating nonlocal fractional order porous medium under Hall current influence. El-Sapa et al. [52] investigated the influence of rotation and viscosity on generalized conformable fractional micropolar thermoelasticity with two temperatures.

In this work, MCS thermoelastic diffusion with multi-phase-lags model along with rotating frame of reference has been presented. This model has been applied to explore fundamental energy theorems, uniqueness and reciprocity and variational criterion. These theorems are impacted by the various physical field variables forming the model. Applications of reciprocity theorem for body forces, heat sources and chemical potential sources are taken for specific case. Some unique cases are deduced and compared with the well-established results.

Governing equations

Consider the domain V of three dimensional space (\mathbb{R}^3) which is bounded by the piecewise smooth surface A in modified couple stress thermoelastic diffusion under multi-phase-lag model in rotating frame of reference. Let $\mathbf{x} = (x_1, x_2, x_3)$ be position of state variables and time variable $t \in \overline{V} \times [0, \infty)$, where, $\overline{V} = V \cup A$.

Then the preliminary equations by following Kumar and Kansal [17], Zenkour [36] given as:

1. stress-strain-temperature-chemical potential relation:

$$t_{ij} = 2\mu e_{ij} - \alpha e_{kij} \chi_{lk,l} + \delta_{ij} (\lambda_0 e_{kk} - \gamma_1 T - \gamma_2 P); \tag{1}$$

2. equation of motion:

$$t_{ij,j} + \rho F_i = \rho \ddot{u}_i + \rho (\mathbf{\Omega} \times (\mathbf{\Omega} \times \mathbf{u}))_i + \rho (2\mathbf{\Omega} \times \dot{\mathbf{u}})_i;$$
(2)

3. displacement-strain relation:

$$e_{ij} = \frac{1}{2} (u_{i,j} + u_{j,i}); \tag{3}$$

4. energy equation:

$$-q_{i,i} + Q = \rho T_0 \dot{S}; \tag{4}$$

5. modified Fourier law:

$$\left(\delta^{0} + \sum_{r=1}^{N^{0}} \frac{\tau_{q}^{r}}{r!} \frac{\partial^{r}}{\partial t^{r}}\right) q_{i} = -K \left(1 + \sum_{r=1}^{M^{0}} \frac{\tau_{T}^{r}}{r!} \frac{\partial^{r}}{\partial t^{r}}\right) T_{,i}; \tag{5}$$

6. entropy-strain-temperature-chemical potential relation:

$$\rho T_0 \dot{S} = l_1 T_0 \dot{T} + \gamma_1 T_0 \dot{e}_{kk} + dT_0 \dot{P}; \tag{6}$$

7. mass concentration law:

$$-\eta_{i,i} + A_0 = \dot{C}; \tag{7}$$

8. equation of chemical potential:

$$\left(\delta^{0} + \sum_{r=1}^{N^{0}} \frac{\tau_{\eta}^{r}}{r!} \frac{\partial^{r}}{\partial t^{r}}\right) \eta_{i} = -D \left(1 + \sum_{r=1}^{M^{0}} \frac{\tau_{P}^{r}}{r!} \frac{\partial^{r}}{\partial t^{r}}\right) P_{,i}; \tag{8}$$

9. mass concentration-chemical potential-strain-temperature relation:

$$C = nP + \gamma_2 e_{kk} + dT, \tag{9}$$

where

$$\lambda_0 = \lambda - \frac{\beta_2^2}{b}, \gamma_1 = \beta_1 + \frac{a}{b}\beta_2, \gamma_2 = \frac{\beta_2}{b}, d = \frac{a}{b}, n = \frac{1}{b}, l_1 = \frac{\rho C_E}{T_0} + \frac{a^2}{b}.$$
 (10)

Here, the medium is rotating with angular velocity $\Omega = \Omega \hat{v}$, where \hat{v} is the unit vector along the axis of rotation and the equations of the motion (2) include two additional terms namely:

- 1. the centripetal acceleration $\Omega \times (\Omega \times u)$ due to time-varying motion;
- 2. the Coriolis acceleration $2\boldsymbol{\Omega} \times \dot{\boldsymbol{u}}$.

In the Eqs. (1)–(10), λ and μ are Lame's constants, ρ is the density, α is couple stress parameter, C_E is the specific heat at the constant strain, q_i are the components of heat flux vector \mathbf{q} , F_i , u_i being the components of body force per unit mass and the components of the displacement vector \mathbf{u} respectively, χ_{ij} is symmetric curvature, K, S, P and D related the thermal conductivity, entropy per unit mass , chemical potential and thermal diffusitivity coefficient respectively, t_{ij} (= t_{ji}), e_{ij} (= e_{ji}) (i, j = 1, 2, 3) being the component of the stress tensor and the component of the strain tensor respectively, e_{kij} is alternate tensor, T (= θ - T_0), where T, θ and T_0 concern to temperature increment, the absolute temperature of medium and the reference temperature of the body respectively chosen such that, $|T/T_0| << 1$, $\beta_1 = (3\lambda + 2\mu)\alpha_t$, $\beta_2 = (3\lambda + 2\mu)\alpha_c$, where α_t , α_c correspond to the

coefficient of thermal linear expansion and diffusion expansion coefficient respectively; δ_{ij} is Kronecker's symbols, Q and A_0 are source of heat and source of chemical potential respectively, a is coefficient which describes measure of thermoelastic diffusion, b is coefficient of mass diffusion, thermal relaxation times with τ_q and $\tau_T \geq 0$ and diffusion relaxation times with τ_η and $\tau_P \geq 0$, δ^0 is constant taking the values 0 or 1, dot(') denotes time differentiation; N^0 and M^0 are finite positive integers.

Energy theorem

Statement

Conservation of energy for every time and every region V of (\mathbb{R}^3) is of the profile [27]:

$$\frac{d}{dt}\left(K^* + W + P^* + M^* + d\int_V TPdV\right) = \tau_1^* \left[\int_A TT_{,i} n_i dA - \int_V T_{,i} T_{,i} dV\right] + \tau_2^* \left[\int_A PP_{,i} n_i dA - \int_V P_{,i} P_{,i} dV\right] + \rho \int_V F_i u_i dV + \int_A h_i u_i dA + \frac{1}{T_0} \int_V QT dV + \int_V A_0 P dV - (11)$$

$$- \rho \int_V (\mathbf{\Omega} \times (\mathbf{\Omega} \times \mathbf{u}))_i \dot{u}_i dV - \rho \int_V (2\mathbf{\Omega} \times \dot{\mathbf{u}})_i \dot{u}_i dV,$$

where K^* , W, P^* and M^* indicates the kinetic energy, the isothermal strain energy, heat potential and mass (diffusion) potential respectively and:

$$\tau_{1}^{*} = \frac{K\tau_{T}^{*}}{T_{0}\tau_{q}^{*}}, \quad \tau_{2}^{*} = \frac{D\tau_{P}^{*}}{\tau_{\eta}^{*}}, \quad \tau_{q}^{*} = \left(\delta^{0} + \sum_{r=1}^{N^{0}} \frac{\tau_{q}^{r}}{r!} \frac{\partial^{r}}{\partial t^{r}}\right), \quad \tau_{T}^{*} = \left(1 + \sum_{r=1}^{M^{0}} \frac{\tau_{T}^{r}}{r!} \frac{\partial^{r}}{\partial t^{r}}\right), \quad \tau_{P}^{*} = \left(1 + \sum_{r=1}^{M^{0}} \frac{\tau_{P}^{r}}{r!} \frac{\partial^{r}}{\partial t^{r}}\right). \tag{12}$$

Proof

Let the Eqs. (1) and (12) required with the subsequent boundary restrictions:

$$t_{ij}n_j = h_i(x, t), T(x, t) = v(x, t), P(x, t) = \omega(x, t), x \in A, t > 0,$$
(13)

where $h_i(x,t)$ is component of surface traction, $\omega(x,t)$ is chemical potential and v(x,t) is heating of the surface to the temperature, n_j is the outward unit normal of A.

Multiplying Eq. (2) by \dot{u}_i and integrating over region V, yields:

$$\int_{V} (t_{ij,j} + \rho F_{i}) \dot{u}_{i} dV = \int_{V} \rho \ddot{u}_{i} \dot{u}_{i} dV + \int_{V} \rho (\boldsymbol{\Omega} \times (\boldsymbol{\Omega} \times \boldsymbol{u}))_{i} \dot{u}_{i} dV + \int_{V} \rho (2\boldsymbol{\Omega} \times \dot{\boldsymbol{u}})_{i} \dot{u}_{i} dV.$$
(14)

In light of the relation $t_{ij,j}\dot{u}_i=(t_{ij}\dot{u}_i)_{,j}-t_{ij}\dot{u}_{i,j}$ and Gauss's divergence theorem, Eq. (14) with the aid of Eq. (3) reduces to:

$$\int_{V} \rho F_{i} \dot{u}_{i} dV + \int_{A} h_{i} \dot{u}_{i} dA = \int_{V} \rho \ddot{u}_{i} \dot{u}_{i} dV + \int_{V} \rho (\boldsymbol{\Omega} \times (\boldsymbol{\Omega} \times \boldsymbol{u}))_{i} \dot{u}_{i} dV + + \int_{V} \rho (2\boldsymbol{\Omega} \times \dot{\boldsymbol{u}})_{i} \dot{u}_{i} dV + \int_{V} t_{ij} \dot{e}_{ij} dV.$$
(15)

Incorporating Eqs. (1) and (15), yields:

$$\rho \int_{V} F_{i} \dot{u}_{i} dV + \int_{A} h_{i} \dot{u}_{i} dA = \rho \int_{V} \ddot{u}_{i} \dot{u}_{i} dV + \rho \int_{V} (\boldsymbol{\Omega} \times (\boldsymbol{\Omega} \times \boldsymbol{u}))_{i} \dot{u}_{i} dV + + \rho \int_{V} (2\boldsymbol{\Omega} \times \dot{\boldsymbol{u}})_{i} \dot{u}_{i} dV + \int_{V} [2\mu e_{ij} - \alpha e_{kij} \chi_{lk,l} + \delta_{ij} (\lambda_{0} e_{kk} - \gamma_{1} T - \gamma_{2} P)] \dot{e}_{ij} dV.$$

$$(16)$$

Introducing the following functions is isothermal strain energy:

$$W = \mu \int_{V} e_{ij} e_{ij} dV + \frac{\lambda_0}{2} \int_{V} e_{kk} e_{kk} dV, \qquad (17)$$

$$K^* = \frac{\rho}{2} \int_V \dot{u}_i \dot{u}_i \, dV. \tag{18}$$

Equation (16) with the aid of Eqs. (17) and (18) reduces:

$$\rho \int_{V} F_{i} \dot{u}_{i} dV + \int_{A} h_{i} \dot{u}_{i} dA = \frac{d}{dt} W + \frac{d}{dt} K^{*} + \rho \int_{V} (\boldsymbol{\Omega} \times (\boldsymbol{\Omega} \times \boldsymbol{u}))_{i} \dot{u}_{i} dV + + \rho \int_{V} (2\boldsymbol{\Omega} \times \dot{\boldsymbol{u}})_{i} \dot{u}_{i} dV - \int_{V} \gamma_{1} T \dot{e}_{kk} dV - \int_{V} \gamma_{2} P \dot{e}_{kk} dV,$$

$$(19)$$

where
$$\int_{V} e_{kij} \chi_{lk,l} \, \dot{e}_{ij} dV = 0$$
, as $\dot{e}_{ij} = \dot{e}_{ji}$ and $e_{ijk} = -e_{ikj}$, $\frac{1}{2} \left(\int_{V} e_{kij} \chi_{lk,l} \, \dot{e}_{ij} dV + \int_{V} e_{kji} \chi_{lk,l} \, \dot{e}_{ji} dV \right) = 0$, $\int_{V} \ddot{u}_{i} \dot{u}_{i} \, dV = \frac{1}{2} \frac{d}{dt} \left(\int_{V} \dot{u}_{i} \dot{u}_{i} \, dV \right)$.

In Eq. (19), the first two integrals on left hand sides encloses the explanation of motion (the body force F_i , surface traction t_i) whereas the last two integrals of right-hand sides of Eq. (19) encloses the explanation such as heat source and mass diffusion source with heating of the body.

Equation (5) with the aid of Eqs. (4) and (6) can be written as:

$$\left(\delta^0 + \sum_{r=1}^{N^0} \frac{\tau_q^r}{r!} \frac{\partial^r}{\partial t^r}\right) (l_1 T_0 \dot{T} + \gamma_1 T_0 \dot{e}_{kk} + dT_0 \dot{P} - Q) = K \left(1 + \sum_{r=1}^{M^0} \frac{\tau_T^r}{r!} \frac{\partial^r}{\partial t^r}\right) T_{,ii}. \tag{20}$$

Multiplying Eq. (20) with T and integrating over the region V, we get:

$$\tau_q^* [\int_V l_1 T_0 \dot{T} T dV + \int_V \gamma_1 T_0 \dot{e}_{kk} T dV + \int_V dT_0 \dot{P} T dV - \int_V Q T dV] = K \tau_T^* \int_V T_{,ii} T dV, \tag{21}$$

where

$$\tau_q^* = \left(\delta^0 + \sum_{r=1}^{N^0} \frac{\tau_q^r}{r!} \frac{\partial^r}{\partial t^r}\right), \, \tau_T^* = \left(1 + \sum_{r=1}^{M^0} \frac{\tau_T^r}{r!} \frac{\partial^r}{\partial t^r}\right). \tag{22}$$

In light of the relation $TT_{,ii} = (TT_{,i})_{,i} - T_{,i}T_{,i}$ and dividing by T_0 , Eq. (21) can be written as:

$$\tau_{q}^{*} \left[l_{1} \int_{V} \dot{T} T dV + \gamma_{1} \int_{V} \dot{e}_{kk} T dV + d \int_{V} \dot{P} T dV - \frac{1}{T_{0}} \int_{V} Q T dV \right] = \frac{K}{T_{0}} \tau_{T}^{*} \int_{V} \left(\left(T T_{,i} \right)_{,i} - T_{,i} T_{,i} \right) dV. \tag{23}$$

Using divergence theorem in Eq. (23), yields:

$$\tau_{q}^{*} \left[l_{1} \int_{V} \dot{T} T dV + \gamma_{1} \int_{V} \dot{e}_{kk} T dV + d \int_{V} \dot{P} T dV - \frac{1}{T_{0}} \int_{V} Q T dV \right] = \frac{K}{T_{0}} \tau_{T}^{*} \int_{A} T T_{,i} n_{i} dA - \frac{K}{T_{0}} \tau_{T}^{*} \int_{V} T_{,i} T_{,i} dV.$$
(24)

Introducing the following function:

$$P^* = \frac{l_1}{2} \int_V T^2 dV. {25}$$

Equation (24) with the help of Eq. (25) takes the form:

$$\tau_{q}^{*} \left[\frac{dP^{*}}{dt} + \gamma_{1} \int_{V} \dot{e}_{kk} T dV + d \int_{V} \dot{P} T dV - \frac{1}{T_{0}} \int_{V} Q T dV \right] = \frac{K}{T_{0}} \tau_{T}^{*} \int_{A} T T_{,i} n_{i} dA - \frac{K}{T_{0}} \tau_{T}^{*} \int_{V} T_{,i} T_{,i} dV.$$
 (26)

Incorporating Eqs. (7) and (8) in Eq. (9) determine:

$$\left(\delta^{0} + \sum_{r=1}^{N^{0}} \frac{\tau_{\eta}^{r}}{r!} \frac{\partial^{r}}{\partial t^{r}}\right) \left(n\dot{P} + \gamma_{2}\dot{e}_{kk} + d\dot{T} - A_{0}\right) = D\left(1 + \sum_{r=1}^{M^{0}} \frac{\tau_{P}^{r}}{r!} \frac{\partial^{r}}{\partial t^{r}}\right) P_{,ii}. \tag{27}$$

Multiplying Eq. (27) by P and integrating over the region V, we obtain:

$$\tau_{\eta}^*[n\int_V \dot{P}PdV + \gamma_2\int_V P\,\dot{e}_{kk}dV + d\int_V \dot{T}PdV - \int_V A_0PdV] = D\tau_P^*\int_V P_{,ii}PdV, \tag{28}$$
 where

$$\tau_{\eta}^* = \left(\delta^0 + \sum_{r=1}^{N^0} \frac{\tau_{\eta}^r}{r!} \frac{\partial^r}{\partial t^r}\right); \tau_P^* = \left(1 + \sum_{r=1}^{M^0} \frac{\tau_P^r}{r!} \frac{\partial^r}{\partial t^r}\right). \tag{29}$$

In light of the relation $PP_{,ii} = (PP_{,i})_{,i} - P_{,i}P_{,i}$ and applying divergence theorem in Eq. (28) can be written as:

$$\tau_{\eta}^{*}[n\int_{V}\dot{P}PdV + \gamma_{2}\int_{V}P\dot{e}_{kk}dV + d\int_{V}\dot{T}PdV - \int_{V}A_{0}PdV] = D\tau_{P}^{*}\int_{A}PP_{,i}n_{i}dA - D\tau_{P}^{*}\int_{V}P_{,i}P_{,i}dV.$$
(30)

Introducing the following function:

$$M^* = \frac{n}{2} \int_V P^2 dV. {31}$$

With the aid of Eq. (31), Eq. (30) can be written as:

$$\tau_{\eta}^{*}[\frac{dM^{*}}{dt} + \gamma_{2} \int_{V} P \,\dot{e}_{kk} dV + d \int_{V} \dot{T} P dV - \int_{V} A_{0} P dV] = D \tau_{P}^{*} \int_{A} P \,P_{,i} n_{i} dA - D \tau_{P}^{*} \int_{V} P_{,i} P_{,i} dV. \tag{32}$$
Equation (19) with the aid of Eqs. (26) and (32) can be written as Eq. (11).

Uniqueness theorem

Theorem

Consider the domain V of three-dimensional space (\mathbb{R}^3) which is bounded by the piecewise smooth surface A in linear modified couple stress isotropic thermoelastic diffusion under multi-phase-lag model in rotating frame of reference. There is only one solution of functions: $u_i(x,t)$, T(x,t), P(x,t) of class $C^{(m)}(m \ge 2)$ and $t_{ij}(x,t)$, $e_{ij}(x,t)$ of class $C^{(l)}$, for $x \in V + A$ possessing coordinates $x = (x_1, x_2, x_3)$ at $t \ge 0$ that satisfy Eqs. (1)–(9) contingent to the border restrictions:

$$u_i(x,t) = U_i(x,t), T(x,t) = v(x,t), P(x,t) = \omega(x,t), x \in A, t > 0,$$
 (33)

and the initial conditions at t=0:

$$u_i(x,0) = u_{0i}(x)$$
, $T(x,0) = T_0(x)$, $P(x,0) = P_0(x)$, for $x \in V$, (34)

$$\frac{\partial^{k} u_{i}(x,0)}{\partial t^{k}} = u_{0i}^{(k)}(x), k = 1, 2, 3, ..., \max\{N^{0}, M^{0}\}, \text{ for } x \in V,$$
(35)

$$\frac{\partial^k T(x,0)}{\partial t^k} = T_0^{(k)}(x), k = 1, 2, 3, ..., \max\{N^0, M^0\}, \text{ for } x \in V,$$
(36)

$$\frac{\partial^{k} P(x,0)}{\partial t^{k}} = P_{0}^{(k)}(x), k = 1, 2, 3, ..., \max\{N^{0}, M^{0}\}, \text{ for } x \in V,$$
(37)

where $u_{0i}(x)$, $u_{0i}^{(k)}(x)$, $T_0(x)$, $T_0^{(k)}(x)$, $P_0(x)$ and $P_0^{(k)}(x)$ are known functions.

Let the Laplace transformation of all field variables exists, and physical parameters fulfill the disparities: $\lambda_0 > 0$, $\mu > 0$, $\rho > 0$, K > 0, $C_E > 0$, $T_0 > 0$, D > 0, d > 0, n > 0, $\tau_T > 0, \tau_q > 0, \tau_P > 0, \tau_\eta > 0.$

Solution

Let $u_i^{(1)}, T^{(1)}, P^{(1)}, \dots$ and $u_i^{(2)}, T^{(2)}, P^{(2)}, \dots$ are two set of solution of Eqs. (1)–(9) with homogeneous border and initial restrictions. Let us take:

$$\Pi^{0} = \{ u_{i} = u_{i}^{(1)} - u_{i}^{(2)}, \ T = T^{(1)} - T^{(2)}, \ P = P^{(1)} - P^{(2)} \}.$$
 (38)

The set Π^0 satisfy the governing Eqs. (1)–(9) without body force, heat source and mass diffusion source and also functions u_i , T and P fulfill the homogeneous border and initial restrictions:

$$u_i(x,t) = 0, T(x,t) = 0, P(x,t) = 0, x \in A, t > 0,$$
 (39)

$$u_i(x,0) = 0, T(x,0) = 0, P(x,0) = 0, \text{ for } x \in V,$$
 (40)

$$\frac{\partial^{k} u_{i}(x,0)}{\partial t^{k}} = 0, k = 1, 2, 3, ..., \max\{N^{0}, M^{0}\}, \text{ for } x \in V,$$
(41)

$$\frac{\partial^{k} u_{i}(x,0)}{\partial t^{k}} = 0, k = 1, 2, 3, ..., \max\{N^{0}, M^{0}\}, \text{ for } \mathbf{x} \in V,
\frac{\partial^{k} T(\mathbf{x},0)}{\partial t^{k}} = 0, k = 1, 2, 3, ..., \max\{N^{0}, M^{0}\}, \text{ for } \mathbf{x} \in V,
\frac{\partial^{k} P(\mathbf{x},0)}{\partial t^{k}} = 0, k = 1, 2, 3, ..., \max\{N^{0}, M^{0}\}, \text{ for } \mathbf{x} \in V.$$
(41)

(42)

$$\frac{\partial^{k} P(x,0)}{\partial t^{k}} = 0, k = 1, 2, 3, ..., \max\{N^{0}, M^{0}\}, \text{ for } x \in V.$$
(43)

Let the Laplace transform be defined as:

$$\overline{f}(\mathbf{x}, s) = L(f(\mathbf{x}, t)) = \int_0^\infty f(\mathbf{x}, t) e^{-st} dt; s > 0.$$
(44)

Applying the Laplace transform on Eqs. (1)–(9), (39) and (40) after removing the body forces, thermal source and chemical potential source and omitting the bar for further simplification yield:

$$t_{ij} = 2\mu e_{ij} - \alpha e_{kij} \chi_{lk,l} + \delta_{ij} (\lambda_0 e_{kk} - \gamma_1 T - \gamma_2 P), \tag{45}$$

$$t_{ij,j} = \rho s^2 u_i, \tag{46}$$

$$e_{ij} = \frac{1}{2} (u_{i,j} + u_{j,i}), \tag{47}$$

$$-q_{i,i} = \rho T_0 s S, \tag{48}$$

$$\left(\delta^{0} + \sum_{r=1}^{N^{0}} \frac{\tau_{q}^{r}}{r!} s^{r}\right) q_{i} = -K \left(1 + \sum_{r=1}^{M^{0}} \frac{\tau_{T}^{r}}{r!} s^{r}\right) T_{,i},\tag{49}$$

$$\rho T_0 sS = l_1 T_0 sT + \gamma_1 T_0 s e_{kk} + dT_0 sP, \tag{50}$$

$$-\eta_{i,i} = sC, \tag{51}$$

$$\left(\delta^{0} + \sum_{r=1}^{N^{0}} \frac{\tau_{\eta}^{r}}{r!} s^{r}\right) \eta_{i} = -D \left(1 + \sum_{r=1}^{M^{0}} \frac{\tau_{r}^{r}}{r!} s^{r}\right) P_{,i}, \tag{52}$$

$$C = nP + \gamma_2 e_{kk} + dT, \tag{53}$$

$$u_i(x,s) = 0, T(x,s) = 0, P(x,s) = 0, x \in A,$$
 (54)

$$u_i(x,0) = 0, T(x,0) = 0, P(x,0) = 0, x \in V.$$
 (55)

Consider the integral:

$$\int_{V} t_{ij} e_{ij} dV = \int_{V} t_{ij} u_{i,j} dV = \int_{V} (t_{ij} u_{i})_{i} dV - \int_{V} t_{ij,j} u_{i} dV.$$
 (56)

With the help of divergence theorem and owing to Eq. (54), yield:

$$\int_{V} \left(t_{ij} u_i \right)_{i} dV = \int_{A} u_i t_{ij} n_j dA = 0.$$

$$(57)$$

Equation (56) with the aid of Eq. (57) takes form:

$$\int_{V} t_{ij} e_{ij} dV + \int_{V} t_{ij,j} u_{ij} dV = 0.$$
 (58)

Equation (58) with the aid of Eqs. (45) and (46) can be expressed in the form:

$$\int_{V} \left[2\mu e_{ij} - \alpha e_{kij} \chi_{lk,l} + \delta_{ij} (\lambda_0 e_{kk} - \gamma_1 T - \gamma_2 P) \right] e_{ij} dV + \int_{V} \rho s^2 u_i^2 dV = 0.$$
 (59)

To determine, $\gamma_1 \int_V Te_{kk} dV$, following Biot [53], let us introduce a vector function ϕ_i connected with entropy through relation:

$$q_i = T_0 \dot{\phi}_i, \ \rho S = -\phi_{i,i}. \tag{60}$$

Invoking Eq. (60) in Eqs. (49) and (50) respectively and assuming that $\phi_i(\mathbf{x}, 0) = \dot{\phi}_i(\mathbf{x}, 0) = 0$, we get respectively:

$$\left(\delta^{0} + \sum_{r=1}^{N^{0}} \frac{\tau_{q}^{r}}{r!} s^{r}\right) s T_{0} \phi_{i} = -K \left(1 + \sum_{r=1}^{M^{0}} \frac{\tau_{r}^{r}}{r!} s^{r}\right) T_{,i}, \tag{61}$$

$$-T_0 s \phi_{i,i} = l_1 T_0 s T + \gamma_1 T_0 s e_{kk} + d T_0 s P. \tag{62}$$

Multiply both sides of Eq. (61) by ϕ_i and integrating over the region V of body, yields:

$$\int_{V} \left(\delta^{0} + \sum_{r=1}^{N^{0}} \frac{\tau_{q}^{r}}{r!} s^{r} \right) s T_{0} \phi_{i}^{2} dV = -K \int_{V} \left(1 + \sum_{r=1}^{M^{0}} \frac{\tau_{r}^{r}}{r!} s^{r} \right) T_{,i} \phi_{i} dV.$$
 (63)

With the help of divergence theorem and owing to Eq. (54), Eq. (63) can be written as:

$$\int_{V} \left(\delta^{0} + \sum_{r=1}^{N^{0}} \frac{\tau_{q}^{r}}{r!} s^{r} \right) s T_{0} \phi_{i}^{2} dV = K \int_{V} \left(1 + \sum_{r=1}^{M^{0}} \frac{\tau_{r}^{r}}{r!} s^{r} \right) T \phi_{i,i} dV.$$
 (64)

Incorporating Eq. (62) in Eq. (64), gives:

$$-\gamma_1 \int_V T e_{kk} dV = \frac{1}{\kappa \left(1 + \sum_{r=1}^{M^0} \frac{\tau_T^r}{r!} s^r\right)} \int_V \left(\delta^0 + \sum_{r=1}^{N^0} \frac{\tau_q^r}{r!} s^r\right) s T_0 \phi_i^2 dV + \int_V l_1 T^2 dV + \int_V P dT dV. \tag{65}$$

To determine $\gamma_2 \int_V Pe_{kk} dV$, let us introduce the vector function N_i defined as:

$$\eta_i = \dot{N}_i, C = -N_{i,i}. \tag{66}$$

Substituting the value of η_i and C from Eq. (66) in Eqs. (52) and (53) respectively and assuming that $N_i(x, 0) = N_i(x, 0) = 0$, we obtain respectively:

$$\left(\delta^{0} + \sum_{r=1}^{N^{0}} \frac{\tau_{\eta}^{r}}{r!} s^{r}\right) s N_{,i} = -D \left(1 + \sum_{r=1}^{M^{0}} \frac{\tau_{r}^{p}}{r!} s^{r}\right) P_{,i}, \tag{67}$$

$$-N_{i,i} = nP + \gamma_2 e_{kk} + dT. \tag{68}$$

Multiplying both sides of Eq. (67) by N_i and integrating over the region of the body, we obtain:

$$\int_{V} \left(\delta^{0} + \sum_{r=1}^{N^{0}} \frac{\tau_{\eta}^{r}}{r!} s^{r} \right) s N_{i}^{2} dV = -D \int_{V} \left(1 + \sum_{r=1}^{M^{0}} \frac{\tau_{p}^{r}}{r!} s^{r} \right) P_{,i} N_{i} dV.$$
 (69)

With the help of divergence theorem and owing to Eq. (54), Eq. (69) can be written as:

$$\int_{V} \left(\delta^{0} + \sum_{r=1}^{N^{0}} \frac{\tau_{\eta}^{r}}{r!} s^{r} \right) s N_{i}^{2} dV = D \int_{V} \left(1 + \sum_{r=1}^{M^{0}} \frac{\tau_{r}^{p}}{r!} s^{r} \right) P N_{i,i} dV.$$
 (70)

Using Eq. (68) in Eq. (70), yields:

$$-\gamma_2 \int_V Pe_{kk} dV = \frac{1}{D\left(1 + \sum_{r=1}^{M^0} \frac{\tau_P^r}{r!} s^r\right)} \int_V \left(\delta^0 + \sum_{r=1}^{N^0} \frac{\tau_\eta^r}{r!} s^r\right) s N_i^2 dV + \int_V nP^2 dV + \int_V PdT dV. \tag{71}$$

Using the value of $\gamma_1 \int_V Te_{kk} dV$ from Eq. (65) and $\gamma_2 \int_V Pe_{kk} dV$ from Eq. (71) in Eq. (59), we get:

$$\int_{V} 2\mu e_{ij} e_{ij} dV + \int_{V} \lambda_{0} e_{kk} e_{kk} dV + \int_{V} \rho s^{2} u_{i}^{2} dV + \frac{1}{K \left(1 + \sum_{r=1}^{M^{0}} \frac{\tau_{r}^{r}}{r!} s^{r}\right)} \int_{V} \left(\delta^{0} + \sum_{r=1}^{N^{0}} \frac{\tau_{q}^{r}}{r!} s^{r}\right) s T_{0} \phi_{i}^{2} dV + \int_{V} l_{1} T^{2} dV + \frac{1}{D \left(1 + \sum_{r=1}^{M^{0}} \frac{\tau_{r}^{r}}{r!} s^{r}\right)} \int_{V} \left(\delta^{0} + \sum_{r=1}^{N^{0}} \frac{\tau_{\eta}^{r}}{r!} s^{r}\right) s N_{i}^{2} dV + \int_{V} n P^{2} dV + 2 \int_{V} P dT dV = 0,$$
(72)

where $\int_V e_{kij} \chi_{lk,l} e_{ij} dV = 0$. As product of alternative tensor (e_{ijk}) with second order tensor (e_{ij}) is always equal to zero.

It is evident that $\int_V (l_1 T^2 + n P^2 + 2P dT) dV$ appearing in Eq. (72) is always positive because of new thermodynamics law [12]:

$$0 < d^2 < l_1 n. (73)$$

Therefore Eq. (72) vanishes at t=0, owing to the homogeneous initial conditions, and it must be always non-positive for t>0.

Since material parameters are positive and the integrand function in Eq. (72) is a sum of squares, thus we conclude that:

$$u_i = T = e_{ij} = t_{ij} = P = 0. (74)$$

That is the Laplace transforms of the difference function (38) are zeros and according to Learch's theorem [54], the inverse Laplace transform of each is unique, consequently:

$$u_i^{(1)} = u_i^{(2)}, T^{(1)} = T^{(2)}, P^{(1)} = P^{(2)}.$$
 (75)

Hence, uniqueness theorem is proved owing to initial and boundary restrictions.

Reciprocity theorem

Let us take a modified couple stress thermoelastic diffusion under multi-phase-lags in rotating frame of reference body occupying the region V and bounded by surface A. We consider the stress t_{ij} and the strains e_{ij} are continuous having the first derivatives whereas the displacement u_i , temperature T and chemical potential P are continuous holding continuous derivatives up to the second order, for $x \in V + A$, t > 0.

Incorporating Eq. (2) in Eq. (1), yields:

$$\left[2\mu e_{ij} - \alpha e_{kij}\chi_{lk,l} + \delta_{ij}(\lambda_0 e_{kk} - \gamma_1 T - \gamma_2 P)\right]_{,j} + \rho F_i = \rho \ddot{u}_i + \rho \left(\mathbf{\Omega} \times (\mathbf{\Omega} \times \mathbf{u})\right)_i + \rho \left(2\mathbf{\Omega} \times \dot{\mathbf{u}}\right)_i.$$
(76)

Equation (4) with the aid of Eqs. (5) and (6) take form:

$$\left(\delta^{0} + \sum_{r=1}^{N^{0}} \frac{\tau_{q}^{r}}{r!} \frac{\partial^{r}}{\partial t^{r}}\right) \left(l_{1}T_{0}\dot{T} + \gamma_{1}T_{0}\dot{e}_{kk} + dT_{0}\dot{P} - Q\right) = K\left(1 + \sum_{r=1}^{M^{0}} \frac{\tau_{T}^{r}}{r!} \frac{\partial^{r}}{\partial t^{r}}\right) T_{,ii}. \tag{77}$$

Equation (7) with the aid of Eqs. (8) and (9) take form:

$$\left(\delta^{0} + \sum_{r=1}^{N^{0}} \frac{\tau_{\eta}^{r}}{r!} \frac{\partial^{r}}{\partial t^{r}}\right) \left(n\dot{P} + \gamma_{2}\dot{e}_{kk} + d\dot{T} - A_{0}\right) = D\left(1 + \sum_{r=1}^{M^{0}} \frac{\tau_{p}^{r}}{r!} \frac{\partial^{r}}{\partial t^{r}}\right) P_{,ii}. \tag{78}$$

We assume that the system of Eqs. (76)–(78) is assist with the boundary condition given by Eq. (13) and homogeneous initial conditions (40)–(43).

To procure dynamic reciprocity relationship for MCMRR owing to the action of body forces $F_i(x, t)$, together with boundary condition (13), the homogeneous initial condition

(40)–(43) surface traction $h_i(x,t)$, chemical potential $\omega(x,t)$ and heating of the surface to the temperature v(x,t).

Exploring Laplace transform defined by Eq. (44) on Eqs. (2), (76)–(78) and (13):

$$t_{ij,j} + \rho F_i = \rho s^2 u_i + \rho (\mathbf{\Omega} \times (\mathbf{\Omega} \times \mathbf{u}))_i + \rho (2\mathbf{\Omega} \times s\mathbf{u})_i, \tag{79}$$

$$[2\mu e_{ij} - \alpha e_{kij}\chi_{lk,l} + \delta_{ij}(\lambda_0 e_{kk} - \gamma_1 T - \gamma_2 P)]_{,j} + \rho F_i = \rho s^2 u_i + \rho (\mathbf{\Omega} \times (\mathbf{\Omega} \times \mathbf{u}))_i + \rho (2\mathbf{\Omega} \times s\mathbf{u})_i,$$
(80)

$$\left(\delta^{0} + \sum_{r=1}^{N^{0}} \frac{\tau_{q}^{r}}{r!} s^{r}\right) \left(l_{1} T_{0} s T + \gamma_{1} T_{0} s e_{kk} + d T_{0} s P - Q\right) = K \left(1 + \sum_{r=1}^{M^{0}} \frac{\tau_{T}^{r}}{r!} s^{r}\right) T_{,ii},\tag{81}$$

$$\left(\delta^{0} + \sum_{r=1}^{N^{0}} \frac{\tau_{\eta}^{r}}{r!} s^{r}\right) (nsP + \gamma_{2} se_{kk} + dTs - A_{0}) = D\left(1 + \sum_{r=1}^{M^{0}} \frac{\tau_{r}^{p}}{r!} s^{r}\right) P_{,ii}, \tag{82}$$

$$t_{ij}n_j = h_i(x,s), T(x,s) = v(x,s), P(x,s) = \omega(x,s), x \in A.$$
 (83)

We know examine two problems where applied body force, surface temperature and chemical potential are specified separately. Let the variable appear in these two problems be characterized by superscript in parentheses. Thus, we take the first problem $u_i^{(1)}, e_{ij}^{(1)}, t_{ij}^{(1)}, T^{(1)}, P^{(1)}, \eta_i^{(1)}, \dots$ whereas for the second problem $u_i^{(2)}, e_{ij}^{(2)}, t_{ij}^{(2)}, T^{(2)}, P^{(2)}, \eta_i^{(2)}, \dots$ Each set of variables satisfies the system of Eqs. (55) and (79)–(83).

Let us consider the integral:

$$\int_{V} t_{ij}^{(1)} e_{ij}^{(2)} dV = \int_{V} t_{ij}^{(1)} u_{i,j}^{(2)} dV = \int_{A} t_{ij}^{(1)} u_{i}^{(2)} dA - \int_{V} t_{ij,j}^{(1)} u_{i}^{(2)} dV.$$
 (84)

Using divergence theorem, symmetry of t_{ij} and incorporating Eqs. (79) and (83) in Eq. (84), determine:

$$\int_{V} t_{ij}^{(1)} e_{ij}^{(2)} dV = \int_{A} h_{i}^{(1)} u_{i}^{(2)} dA - \rho \int_{V} s^{2} u_{i}^{(1)} u_{i}^{(2)} dV + \rho \int_{V} F_{i}^{(1)} u_{i}^{(2)} dV - \rho \int_{V} [(\mathbf{\Omega} \times (\mathbf{\Omega} \times \mathbf{u}))_{i}^{(1)} + (2\mathbf{\Omega} \times s\mathbf{u})_{i}^{(1)}] u_{i}^{(2)} dV.$$
(85)

An analogous to Eq. (85), the integral $\int_V t_{ij}^{(2)} e_{ij}^{(1)} dV$ can be written as:

$$\int_{V} t_{ij}^{(2)} e_{ij}^{(1)} dV = \int_{A} h_{i}^{(2)} u_{i}^{(1)} dA - \rho \int_{V} s^{2} u_{i}^{(2)} u_{i}^{(1)} dV + \rho \int_{V} F_{i}^{(2)} u_{i}^{(1)} dV - \rho \int_{V} [(\mathbf{\Omega} \times (\mathbf{\Omega} \times \mathbf{u}))_{i}^{(2)} + (2\mathbf{\Omega} \times s\mathbf{u})_{i}^{(2)}] u_{i}^{(1)} dV.$$
(86)

Subtracting Eqs. (85) and (86), we get:

$$\int_{V} \left(t_{ij}^{(1)} e_{ij}^{(2)} - t_{ij}^{(2)} e_{ij}^{(1)} \right) dV = \int_{A} \left(h_{i}^{(1)} u_{i}^{(2)} - h_{i}^{(2)} u_{i}^{(1)} \right) dA + \rho \int_{V} \left(F_{i}^{(1)} u_{i}^{(2)} - F_{i}^{(2)} u_{i}^{(1)} \right) dV - \rho \int_{V} \left[\left(\mathbf{\Omega} \times (\mathbf{\Omega} \times \mathbf{u}) \right)_{i}^{(1)} u_{i}^{(2)} - \left(\mathbf{\Omega} \times (\mathbf{\Omega} \times \mathbf{u}) \right)_{i}^{(2)} u_{i}^{(1)} \right] dV - \rho \int_{V} \left[\left(2\mathbf{\Omega} \times s \mathbf{u} \right)_{i}^{(1)} u_{i}^{(2)} - \left(2\mathbf{\Omega} \times s \mathbf{u} \right)_{i}^{(2)} u_{i}^{(1)} \right] dV. \tag{87}$$

Now multiplying Eq. (45) by $e_{ij}^{(2)}$ and $e_{ij}^{(1)}$ for the first and second problem respectively, subtracting and integrating over the region V, gives:

$$\int_{V} \left(t_{ij}^{(1)} e_{ij}^{(2)} - t_{ij}^{(2)} e_{ij}^{(1)} \right) dV = \int_{V} \left[\gamma_{1} \left(T^{(2)} e^{(1)} - T^{(1)} e^{(2)} \right) - \gamma_{2} \left(P^{(1)} e^{(2)} - P^{(2)} e^{(1)} \right) \right] dV, \tag{88}$$
 where $e_{ij} \delta_{ij} = e_{kk} = e$.

Using Eq. (87) in Eq. (88), yields:

$$\int_{A} \left(h_{i}^{(1)} u_{i}^{(2)} - h_{i}^{(2)} u_{i}^{(1)} \right) dA + \rho \int_{V} \left(F_{i}^{(1)} u_{i}^{(2)} - F_{i}^{(2)} u_{i}^{(1)} \right) dV - \\
-\rho \int_{V} \left[\left(\mathbf{\Omega} \times (\mathbf{\Omega} \times \mathbf{u}) \right)_{i}^{(1)} u_{i}^{(2)} - \left(\mathbf{\Omega} \times (\mathbf{\Omega} \times \mathbf{u}) \right)_{i}^{(2)} u_{i}^{(1)} \right] dV - \rho \int_{V} \left[(2\mathbf{\Omega} \times s\mathbf{u})_{i}^{(1)} u_{i}^{(2)} - \\
-(2\mathbf{\Omega} \times s\mathbf{u})_{i}^{(2)} u_{i}^{(1)} \right] dV = \int_{V} \left[\gamma_{1} \left(T^{(2)} e^{(1)} - T^{(1)} e^{(2)} \right) - \gamma_{2} \left(P^{(1)} e^{(2)} - P^{(2)} e^{(1)} \right) \right] dV. \tag{89}$$

To derive second part, multiplying (81) by $T^{(2)}$ and $T^{(1)}$ for the first and second problem respectively, subtract and integrate over the region V:

$$\left(\delta^{0} + \sum_{r=1}^{N^{0}} \frac{\tau_{q}^{r}}{r!} s^{r}\right) \left[\gamma_{1} s T_{0} \int_{V} \left(e^{(1)} T^{(2)} - e^{(2)} T^{(1)}\right) dV + dT_{0} s \int_{V} \left(P^{(1)} T^{(2)} - P^{(2)} T^{(1)}\right) dV - \int_{V} \left(Q^{(1)} T^{(2)} - Q^{(2)} T^{(1)}\right) dV\right] = K \left(1 + \sum_{r=1}^{M^{0}} \frac{\tau_{r}^{r}}{r!} s^{r}\right) \int_{V} \left(T_{ii}^{(1)} T^{(2)} - T_{ii}^{(2)} T^{(1)}\right) dV. \tag{90}$$

Using divergence theorem and with the aid of Eq. (83), Eq. (90) takes the form:

$$\left(\delta^{0} + \sum_{r=1}^{N^{0}} \frac{\tau_{q}^{r}}{r!} s^{r}\right) \left[\gamma_{1} s T_{0} \int_{V} \left(e^{(1)} T^{(2)} - e^{(2)} T^{(1)}\right) + dV \, dT_{0} s \int_{V} \left(P^{(1)} T^{(2)} - P^{(2)} T^{(1)}\right) dV - \int_{V} \left(Q^{(1)} T^{(2)} - Q^{(2)} T^{(1)}\right) dV\right] = K \left(1 + \sum_{r=1}^{M^{0}} \frac{\tau_{r}^{r}}{r!} s^{r}\right) \int_{A} \left(T_{i}^{(1)} v^{(2)} - T_{i}^{(2)} v^{(1)}\right) dA. \tag{91}$$

Equation (91) established the second part of the reciprocity theorem which involves the thermal causes of the motion v: heating of the surface A. To derive third part, multiply Eq. (82) by $P^{(2)}$ and $P^{(1)}$ to the first and second problem respectively, then integrate over the volume V.

$$\left(\delta^{0} + \sum_{r=1}^{N^{0}} \frac{\tau_{\eta}^{r}}{r!} s^{r}\right) \left[\gamma_{2} s \int_{V} \left(e^{(1)} P^{(2)} - e^{(2)} P^{(1)}\right) dV + ds \int_{V} \left(T^{(1)} P^{(2)} - T^{(2)} P^{(1)}\right) dV - \int_{V} \left(A_{0}^{(1)} P^{(2)} - A_{0}^{(2)} P^{(1)}\right) dV\right] = \left(1 + \sum_{r=1}^{M^{0}} \frac{\tau_{r}^{r}}{r!} s^{r}\right) \int_{V} \left(P_{ii}^{(1)} P^{(2)} - P_{ii}^{(2)} P^{(1)}\right) dV. \tag{92}$$

Using divergence theorem and with the aid of Eq. (83), Eq. (92) takes form:

$$\left(\delta^{0} + \sum_{r=1}^{N^{0}} \frac{\tau_{\eta}^{r}}{r!} s^{r}\right) \left[\gamma_{2} s \int_{V} \left(e^{(1)} P^{(2)} - e^{(2)} P^{(1)}\right) dV + s d \int_{V} \left(T^{(1)} P^{(2)} - T^{(2)} P^{(1)}\right) dV - \int_{V} \left(A_{0}^{(1)} P^{(2)} - A_{0}^{(2)} P^{(1)}\right) dV\right] = D \left(1 + \sum_{r=1}^{M^{0}} \frac{\tau_{r}^{r}}{r!} s^{r}\right) \int_{A} \left(P_{i}^{(1)} \omega^{(2)} - P_{i}^{(2)} \omega^{(1)}\right) dA. \tag{93}$$

Equation (93) constitutes the third part of reciprocity theorem with containing the chemical potential causes of motion. Using the integral $\int_V (e^{(1)}T^{(2)}-e^{(2)}T^{(1)})dV$ from Eq. (91) and $\int_V (e^{(1)}P^{(2)}-e^{(2)}P^{(1)})dV$ from Eq. (93) in Eq. (89), we obtain:

$$K\left(1 + \sum_{r=1}^{M^{0}} \frac{\tau_{r}^{r}}{r!} s^{r}\right) R_{2} \int_{A} \left(T_{,i}^{(1)} v^{(2)} - T_{,i}^{(2)} v^{(1)}\right) dA + T_{0} R_{1} D\left(1 + \sum_{r=1}^{M^{0}} \frac{\tau_{r}^{r}}{r!} s^{r}\right) \times \\ \times \int_{A} \left(P_{,i}^{(1)} \omega^{(2)} - P_{,i}^{(2)} \omega^{(1)}\right) dA - R_{1} s T_{0} R_{2} \int_{A} \left(h_{i}^{(1)} u_{i}^{(2)} - h_{i}^{(2)} u_{i}^{(1)}\right) dA - \\ -\rho s T_{0} R_{1} R_{2} \int_{V} \left(F_{i}^{(1)} u_{i}^{(2)} - F_{i}^{(2)} u_{i}^{(1)}\right) dV + \rho s T_{0} R_{1} R_{2} \times \int_{V} \left[\left(\mathbf{\Omega} \times \left(\mathbf{\Omega} \times \mathbf{u}\right)\right)_{i}^{(1)} u_{i}^{(2)} - \\ -\left(\mathbf{\Omega} \times \left(\mathbf{\Omega} \times \mathbf{u}\right)\right)_{i}^{(2)} u_{i}^{(1)}\right] dV \rho s T_{0} R_{1} R_{2} \int_{V} \left[\left(2\mathbf{\Omega} \times s \mathbf{u}\right)_{i}^{(1)} u_{i}^{(2)} - \left(2\mathbf{\Omega} \times s \mathbf{u}\right)_{i}^{(2)} u_{i}^{(1)}\right] dV + \\ + R_{1} R_{2} \int_{V} \left(Q^{(1)} T^{(2)} - Q^{(2)} T^{(1)}\right) dV + T_{0} R_{1} R_{2} \int_{V} \left(A_{0}^{(1)} P^{(2)} - A_{0}^{(2)} P^{(1)}\right) dV = 0,$$

$$(94)$$

where, $\left(\delta^0 + \sum_{r=1}^{N^0} \frac{\tau_q^r}{r!} s^r\right) = R_1$, $\left(\delta^0 + \sum_{r=1}^{N^0} \frac{\tau_\eta^r}{r!} s^r\right) = R_2$. Equation (94) represents the reciprocity theorem (general form) in the transformed domain.

For the implementation of the inverse Laplace transform on Eqs. (89), (91), (93) and (94), we shall use the following convolution theorem and symbolic notations:

$$L^{-1}{F(s)G(s)} = \int_0^t f(t-\zeta)g(\zeta)d\zeta = \int_0^t g(t-\zeta)f(\zeta)d\zeta,$$
(95)

$$\Lambda_1(f(\mathbf{x},\zeta)) = \left(\delta^0 f(\mathbf{x},\zeta) + \sum_{r=1}^{N^0} \frac{\tau_q^r}{r!} \frac{\partial^r f(\mathbf{x},\zeta)}{\partial \zeta^r}\right),\tag{96}$$

$$\Lambda_2(f(\mathbf{x},\zeta)) = \left(\delta^0 f(\mathbf{x},\zeta) + \sum_{r=1}^{N^0} \frac{\tau_\eta^r}{r!} \frac{\partial^r f(\mathbf{x},\zeta)}{\partial \zeta^r}\right),\tag{97}$$

$$\Lambda_3(f(\mathbf{x},\zeta)) = \left(\delta^0 + \sum_{r=1}^{N^0} \frac{\tau_q^r}{r!} \frac{\partial^r}{\partial \zeta^r}\right) \left(\delta^0 f(\mathbf{x},\zeta) + \sum_{r=1}^{N^0} \frac{\tau_\eta^r}{r!} \frac{\partial^r f(\mathbf{x},\zeta)}{\partial \zeta^r}\right). \tag{98}$$

Thus, we get the first, second, third and general forms of the reciprocity theorem in the resulting form:

$$\int_{A} \int_{0}^{t} h_{i}^{(1)}(\mathbf{x}, t - \zeta) u_{i}^{(2)}(\mathbf{x}, \zeta) d\zeta dA + \rho \int_{V} \int_{0}^{t} F_{i}^{(1)}(\mathbf{x}, t - \zeta) u_{i}^{(2)}(\mathbf{x}, \zeta) d\zeta dV + \\
+ \gamma_{1} \int_{V} \int_{0}^{t} T^{(1)}(\mathbf{x}, t - \zeta) e^{(2)}(\mathbf{x}, \zeta) d\zeta dV + \gamma_{2} \int_{V} \int_{0}^{t} P^{(1)}(\mathbf{x}, t - \zeta) e^{(2)}(\mathbf{x}, \zeta) d\zeta dV - \\
- \rho \int_{V} \int_{0}^{t} (\mathbf{\Omega} \times (\mathbf{\Omega} \times \mathbf{u}))_{i}^{(1)}(\mathbf{x}, t - \zeta) u_{i}^{(2)}(\mathbf{x}, \zeta) d\zeta dV - \\
- \rho \int_{V} \int_{0}^{t} (2\mathbf{\Omega} \times \frac{\partial}{\partial \zeta} \mathbf{u})_{i}^{(1)}(\mathbf{x}, t - \zeta) u_{i}^{(2)}(\mathbf{x}, \zeta) d\zeta dV = S_{21}^{12}, \\
K \int_{A} \int_{0}^{t} T_{i}^{(1)}(\mathbf{x}, t - \zeta) v^{(2)}(\mathbf{x}, \zeta) d\zeta dA + \\
+ K \sum_{T=1}^{M^{0}} \frac{\tau_{T}^{T}}{r!} \int_{A} \int_{0}^{t} T_{i}^{(1)}(\mathbf{x}, t - \zeta) \frac{\partial}{\partial \zeta}^{T} v^{(2)}(\mathbf{x}, \zeta) d\zeta dA - \\
- \gamma_{1} T_{0} \int_{V} \int_{0}^{t} e^{(1)}(\mathbf{x}, t - \zeta) \frac{\partial}{\partial \zeta} \Lambda_{1} \left(T^{(2)}(\mathbf{x}, \zeta) \right) d\zeta dV - dT_{0} \int_{V} \int_{0}^{t} P^{(1)}(\mathbf{x}, t - \zeta) \times$$
(100)

$$\begin{split} & \times \frac{\partial}{\partial \zeta} \Lambda_{1} \Big(T^{(2)}(\mathbf{x},\zeta) \Big) \, d\zeta dV + \int_{V} \int_{0}^{t} Q^{(1)}(\mathbf{x},t-\zeta) \Lambda_{1} \Big(T^{(2)}(\mathbf{x},\zeta) \Big) \, d\zeta dV = S_{21}^{12}, \\ & D \int_{A} \int_{0}^{t} P_{i}^{(1)}(\mathbf{x},t-\zeta) \omega^{(2)}(\mathbf{x},\zeta) \, d\zeta dA + \\ & + D \sum_{r=1}^{n-1} \frac{\tau_{r}^{2}}{\tau_{r}^{2}} \int_{A} \int_{0}^{t} P_{i}^{(1)}(\mathbf{x},t-\zeta) \frac{\partial^{r}}{\partial \zeta^{r}} \omega^{(2)}(\mathbf{x},\zeta) \, d\zeta dA - \\ & - \gamma_{2} \int_{V} \int_{0}^{t} e^{(1)}(\mathbf{x},t-\zeta) \frac{\partial}{\partial \zeta} \Lambda_{2} \Big(P^{(2)}(\mathbf{x},\zeta) \Big) \, d\zeta dV - \\ & - d \int_{V} \int_{0}^{t} \Lambda_{0}^{(1)}(\mathbf{x},t-\zeta) \lambda_{2} \frac{\partial}{\partial \zeta} \Lambda_{2} \Big(P^{(2)}(\mathbf{x},\zeta) \Big) \, d\zeta dV \\ & + \int_{V} \int_{0}^{t} \Lambda_{0}^{(1)}(\mathbf{x},t-\zeta) \Lambda_{2} \Big(P^{(2)}(\mathbf{x},\zeta) \Big) \, d\zeta dV + S_{21}^{12}, \\ & K \int_{A} \int_{0}^{t} T_{i}^{(1)}(\mathbf{x},t-\zeta) \Lambda_{2} \Big(V^{(2)}(\mathbf{x},\zeta) \Big) \, d\zeta dA + \\ & + K \sum_{r=1}^{m-1} \frac{\tau_{r}^{r}}{\tau_{r}^{r}} \int_{A} \int_{0}^{t} T_{i}^{(1)}(\mathbf{x},t-\zeta) \frac{\partial^{r}}{\partial \zeta^{r}} \Lambda_{2} \Big(v^{(2)}(\mathbf{x},\zeta) \Big) \, d\zeta dA + \\ & + D T_{0} \int_{A} \int_{0}^{t} P_{i}^{(1)}(\mathbf{x},t-\zeta) \Lambda_{1} \Big(\omega^{(2)}(\mathbf{x},\zeta) \Big) \, d\zeta dA - \\ & - \rho T_{0} \int_{V} \int_{0}^{t} F_{i}^{(1)}(\mathbf{x},t-\zeta) \frac{\partial}{\partial \zeta} \Lambda_{3} \Big(u_{i}^{(2)}(\mathbf{x},\zeta) \Big) \, d\zeta dA - \\ & - T_{0} \int_{A} \int_{0}^{t} h_{i}^{(1)}(\mathbf{x},t-\zeta) \frac{\partial}{\partial \zeta} \Lambda_{3} \Big(u_{i}^{(2)}(\mathbf{x},\zeta) \Big) \, d\zeta dA + \\ & + \rho T_{0} \int_{V} \int_{0}^{t} \left(\Omega \times (\Omega \times \mathbf{u}) \right)_{i}^{(1)}(\mathbf{x},t-\zeta) \frac{\partial}{\partial \zeta} \Lambda_{3} \Big(u_{i}^{(2)}(\mathbf{x},\zeta) \Big) \, d\zeta dV - \\ & + T_{0} \int_{V} \int_{0}^{t} \left(\Omega \times (\Omega \times \mathbf{u}) \right)_{i}^{(1)}(\mathbf{x},t-\zeta) \frac{\partial}{\partial \zeta} \Lambda_{3} \Big(u_{i}^{(2)}(\mathbf{x},\zeta) \Big) \, d\zeta dV + \\ & + \int_{V} \int_{0}^{t} Q^{(1)}(\mathbf{x},t-\zeta) \Lambda_{3} \Big(T^{(2)}(\mathbf{x},\zeta) \Big) \, d\zeta dV + \\ & + \int_{V} \int_{0}^{t} Q^{(1)}(\mathbf{x},t-\zeta) \Lambda_{3} \Big(T^{(2)}(\mathbf{x},\zeta) \Big) \, d\zeta dV + \\ & + T_{0} \int_{V} \int_{0}^{t} \Lambda_{0}^{(1)}(\mathbf{x},t-\zeta) \Lambda_{3} \Big(T^{(2)}(\mathbf{x},\zeta) \Big) \, d\zeta dV + \\ & + \int_{V} \int_{0}^{t} Q^{(1)}(\mathbf{x},t-\zeta) \Lambda_{3} \Big(T^{(2)}(\mathbf{x},\zeta) \Big) \, d\zeta dV + \\ & + \int_{V} \int_{0}^{t} A_{0}^{(1)}(\mathbf{x},t-\zeta) \Lambda_{3} \Big(T^{(2)}(\mathbf{x},\zeta) \Big) \, d\zeta dV + \\ & + \int_{V} \int_{0}^{t} A_{0}^{(1)}(\mathbf{x},t-\zeta) \Lambda_{3} \Big(T^{(2)}(\mathbf{x},\zeta) \Big) \, d\zeta dV + \\ & + \int_{V} \int_{0}^{t} A_{0}^{(1)}(\mathbf{x},t-\zeta) \Lambda_{3} \Big(T^{(2)}(\mathbf{x},\zeta) \Big) \, d\zeta dV + \\ & + \int_{V} \int_{0}^{t} A_{0}^{(1)}(\mathbf{x},t-\zeta) \Lambda_{3} \Big(T^{(2)}(\mathbf{x},\zeta) \Big) \, d\zeta dV + \\ & + \int_$$

Here S_{21}^{12} indicates the same expression on left hand side except that the superscripts (1) and (2) interchanged. Hence the reciprocity theorem is proved.

Variational criterion

The criterion of virtual work with variations of displacement for deformable elastic body with thermal and chemical potential is given as

$$\int_{V} \rho(F_{i} - \ddot{u}_{i} + (\boldsymbol{\Omega} \times (\boldsymbol{\Omega} \times \boldsymbol{u}))_{i} + (2\boldsymbol{\Omega} \times \dot{\boldsymbol{u}})_{i})\delta u_{i}dV + \int_{A} h_{i}\delta u_{i}dA = \int_{V} t_{ij}\delta u_{i,j}dV.$$
 (103)

In Eq. (103) left hand side corresponds to virtual work of body forces F_i , inertial forces $\rho \ddot{u}_i$, surface force $h_i = t_{ji} n_i$ although the right hand side corresponds to the virtual work of internal forces. We denote by n_i the outward unit normal of A.

Equation (103) with the aid of symmetry of stress tensor and the definition of strain tensor can be written in another form as: substitute the value of t_{ij} from Eq. (1) in Eq. (103):

$$\int_{V} \rho \left(F_{i} - \ddot{u}_{i} + \left(\boldsymbol{\Omega} \times (\boldsymbol{\Omega} \times \boldsymbol{u}) \right)_{i} + (2\boldsymbol{\Omega} \times \dot{\boldsymbol{u}})_{i} \right) \delta u_{i} dV + \int_{A} L \delta u_{i} dA = \delta W - \int_{V} \alpha e_{kij} \chi_{lk,l} \delta u_{i,j} dV - \gamma_{1} \int_{V} T \delta e_{kk} dV - \gamma_{2} \int_{V} P \delta e_{kk} dV,$$

$$(104)$$

$$W = \mu \int_{V} e_{ij}e_{ij}dV + \frac{\lambda_0}{2} \int_{V} e_{kk}e_{kk}dV, \tag{105}$$

where W is strain density function.

Taking into consideration (60) and introducing heat source term Q_1 such that $Q=T_0\dot{Q}_1$. Then, the Eqs. (4) and (5) with the aid of (6) reduce to:

$$\delta\phi_{i,i} = -l_1\delta T - \gamma_1\delta e_{kk} - d\delta P + \delta Q_1,\tag{106}$$

$$\frac{T_0}{\kappa} J_i + T_{,i} = 0, {107}$$

where

$$J_i = \left(\delta^0 + \sum_{r=1}^{N^0} \frac{\tau_q^r}{r!} \frac{\partial^r}{\partial t^r}\right) \dot{\phi}_i + \frac{\kappa}{T_0} \sum_{r=1}^{M^0} \frac{\tau_T^r}{r!} \frac{\partial^r}{\partial t^r} T_{,i}. \tag{108}$$

Multiplying the Eq. (107) by $\delta \phi_i$ and integrating over the volume V, yields:

$$\int_{V} \left(\frac{T_0}{\kappa} J_i + T_{,i}\right) \delta \phi_i dV = 0. \tag{109}$$

Equation (109) with the aid of the relation $T_{,i}\delta N_i = (T\delta N_i)_{,i} - T\delta N_{i,i}$ and Gauss's divergence theorem can be written as:

$$\int_{A} T \delta \phi_{i} n_{i} dA - \int_{V} T \delta \phi_{i,i} dV + \frac{T_{0}}{V} \int_{V} J_{i} \delta \phi_{i} dV = 0.$$

$$\tag{110}$$

Using value of $\delta \phi_{i,i}$ in Eq. (110), we obtain:

$$\int_{A} T \delta \phi_{i} n_{i} dA + \delta P_{1} + \gamma_{1} \int_{V} T \delta e_{kk} dV + d \int_{V} T \delta P dV - \int_{V} T \delta Q_{1} dV + \delta D_{1} = 0,$$
 (111) where $\delta P_{1} = l_{1} \int_{V} T \delta T dV$, $\delta D_{1} = \frac{T_{0}}{V} \int_{V} J_{i} \delta \phi_{i} dV$.

Taking into consideration (66) and introducing chemical potential source term M_2 such that $A_0 = \dot{M}_2$. Then, Eqs. (7) and (8) with the aid of Eq. (9) reduce to:

$$\delta N_{i,i} = -n\delta P - \gamma_2 \delta e_{kk} - d\delta T + \delta M_2, \tag{112}$$

$$\frac{Y_i}{P_i} + P_{,i} = 0,$$
 (113)

where $Y_i = \left(\delta^0 + \sum_{r=1}^{N^0} \frac{\tau_{\eta}^r}{r!} \frac{\partial^r}{\partial t^r}\right) \dot{N}_i + D \sum_{r=1}^{M^0} \frac{\tau_r^r}{r!} \frac{\partial^r}{\partial t^r} P_{,i}$

Multiplying the Eq. (113) by δN_i and integrating over the volume V, yields:

$$\int_{V} \left(\frac{Y_i}{P} + P_{ii}\right) \, \delta N_i dV = 0. \tag{114}$$

Equation (114) with the aid of the relation $P_{,i}\delta N_i = (P\delta N_i)_{,i} - P\delta N_{i,i}$ and Gauss's divergence theorem can be written as:

$$\int_{V} \frac{Y_{i}}{D} \delta N_{i} dV + \int_{A} P \delta N_{i} n_{i} dA - \int_{V} P \delta N_{i,i} dV = 0.$$

$$\tag{115}$$

Using value of $\delta N_{i,i}$ from Eq. (112) in Eq. (115):

$$\delta D_2 + \delta P_2 + \int_A P \delta N_i n_i dA + \int_V \gamma_2 P \delta e_{kk} dV + \int_V P d\delta T dV - \int_V P \delta M_2 dV = 0.$$
 (116) where $D_2 = \frac{1}{D} \int_V Y_i \ \delta N_i dV$, $\delta P_2 = \int_V n P \delta P dV$.

Equation (104) with the aid of Eq. (111), and Eq. (116) can be written as:

$$\delta(W + D_1 + P_1 + D_2 + P_2 + d \int_V PT dV) = \int_V \rho \left(F_i - \ddot{u}_i + \left(\mathbf{\Omega} \times (\mathbf{\Omega} \times \mathbf{u}) \right)_i + \left(2\mathbf{\Omega} \dot{\mathbf{u}} \right)_i \right) \delta u_i dV + \int_A L \delta u_i dA + \int_V \alpha e_{kij} \chi_{lk,l} \delta u_{i,j} dV - \int_A T \delta \phi_i n_i dA - \int_A P \delta N_i n_i dA + \left(117 \right) + \int_V T \delta Q_1 dV + \int_V P \delta M_2 dV.$$
(117)

Equation (117) represents variational principle for thermoelastic diffusion body under multi-phase-lags. In Eq. (117), right hand side interpreted as the work done by the body force, surface traction, inertia forces, heating of the surface, heat source and mass diffusion source with the virtual deformation, whereas left hand side explores the variation of the sum of the dissipation function, heat potential, chemical potential and the work of deformation.

Applications

Consider an infinite isotropic thermoelastic medium in absence of rotation and couple stress parameters in which the surface integrals are removed in Eq. (94), the body forces, heat sources and chemical potential sources are acting in bounded region only.

Also considering $C_r = \{F_i^{(r)}(\mathbf{x},t), h_i^{(r)}(\mathbf{x},t), U_i^{(r)}(\mathbf{x},t), v^{(r)}(\mathbf{x},t), Q^{(r)}(\mathbf{x},t), \omega^{(r)}(\mathbf{x},t), A_0^{(r)}(\mathbf{x},t)\}$ and thus, we get relation:

$$s\rho T_0 \int_V \left(F_i^{(1)} u_i^{(2)} - F_i^{(2)} u_i^{(1)} \right) dV - \int_V \left(Q^{(1)} T^{(2)} - Q^{(2)} T^{(1)} \right) dV - -T_0 \int_V \left(A_0^{(1)} P^{(2)} - A_0^{(2)} P^{(1)} \right) dV = 0.$$
(118)

For implementation of the inverse Laplace transform defined by Eq. (44) in (118), determine:

$$\rho T_0 \int_V \int_0^t F_i^{(1)}(\mathbf{x}, t - \zeta) \frac{\partial}{\partial \zeta} u_i^{(2)}(\mathbf{x}, \zeta) d\zeta dV - \int_V \int_0^t Q^{(1)}(\mathbf{x}, t - \zeta) T^{(2)}(\mathbf{x}, \zeta) d\zeta - T_0 \int_V \int_0^t A_0^{(1)}(\mathbf{x}, t - \zeta) P^{(2)}(\mathbf{x}, \zeta) d\zeta dV = S_{21}^{12}.$$
(119)

Here S_{21}^{12} demonstrates the similar expression on left hand side barring the superscripts (1) and (2) can be reciprocated.

Assuming the point η_1 and η_2 , the instantaneous concentrated body forces $F_i^{(1)}$ and $F_i^{(2)}$ acting in the direction of x_j -axis and x_k -axis, respectively. Thus, we obtain:

$$C_{1} = \{F_{i}^{(1)}, 0, 0, 0, 0, 0, 0, 0\}, C_{2} = \{F_{i}^{(2)}, 0, 0, 0, 0, 0, 0, 0\}, F_{i}^{(1)} = \delta(\mathbf{x} - \eta_{1})\delta_{ij}\delta(t), F_{i}^{(2)} = \delta(\mathbf{x} - \eta_{2})\delta_{ij}\delta(t), u_{i}^{(1)} \equiv u_{i}^{(1)}(\mathbf{x}, \eta_{1}, t), u_{i}^{(2)} \equiv u_{i}^{(2)}(\mathbf{x}, \eta_{2}, t).$$

$$(120)$$

Incorporating Eq. (120) in (119), yield:

$$\dot{u}_k^{(1)}(\eta_2, \eta_1, t) = \dot{u}_i^{(2)}(\eta_1, \eta_2, t). \tag{121}$$

It means that the velocity of the displacement $u_j^{(2)}$ at the point η_1 due to the action of instantaneous concentrated forces acting at point η_2 in the direction x_k -axis is equal to the velocity of the displacement $u_k^{(1)}$ at the point η_2 produced by the action of a concentrated forces acting at the point η_1 in the direction of the x_j -axis.

Presuming the point η_1 and η_2 , there act instantaneous concentrated heat sources $Q^{(1)}$ and $Q^{(2)}$. Thus, we obtain:

$$C_{1} = \{0,0,0,0,Q^{(1)},0,0\}, C_{2} = \{0,0,0,0,Q^{(2)},0,0\}, Q^{(1)} = \delta(\mathbf{x} - \eta_{1})\delta(t),$$

$$Q^{(2)} = \delta(\mathbf{x} - \eta_{2})\delta(t), T^{(1)} \equiv T^{(1)}(\mathbf{x},\eta_{1},t), T^{(2)} \equiv T^{(2)}(\mathbf{x},\eta_{2},t).$$
(122)

Incorporating Eq. (122) in (119), yield:

$$T^{(1)}(\eta_2, \eta_1, t) = T^{(2)}(\eta_1, \eta_2, t). \tag{123}$$

It is concluded that the temperature $T^{(2)}$ at the point η_1 due to the action of heat sources at point η_2 is equal to the temperature $T^{(1)}$ at the point η_2 produced by the action of heat sources atthe point η_1 .

Considering the point η_1 and η_2 , there act instantaneous concentrated chemical potential sources $A_0^{(1)}$ and $A_0^{(2)}$. Thus, we obtain:

$$C_{1} = \{0,0,0,0,0,0,A_{0}^{(1)}\}, C_{2} = \{0,0,0,0,0,0,A_{0}^{(2)}\}, A_{0}^{(1)} = \delta(\mathbf{x} - \eta_{1})\delta(t),$$

$$A_{0}^{(2)} = \delta(\mathbf{x} - \eta_{2})\delta(t), P^{(1)} \equiv P^{(1)}(\mathbf{x}, \eta_{1}, t), P^{(2)} \equiv P^{(2)}(\mathbf{x}, \eta_{2}, t).$$
(124)

Incorporating Eq. (124) in (119), yield:

$$P^{(1)}(\eta_2, \eta_1, t) = P^{(2)}(\eta_1, \eta_2, t). \tag{125}$$

Thus, the chemical potential $P^{(2)}$ at the point η_1 due to the action of chemical potential sources at point η_2 is equal to the chemical potential $P^{(1)}$ at the point η_2 produced by the action of chemical potential sources at the point η_1 .

Taking the point η_1 and η_2 , there act instantaneous concentrated body forces $F_i^{(1)}$ acts in the direction x_i -axis and heat sources $Q^{(2)}$, respectively. Thus, we obtain:

$$C_{1} = \{F_{i}^{(1)}, 0, 0, 0, 0, 0, 0, 0\}, C_{2} = \{0, 0, 0, 0, Q^{(2)}, 0, 0\}, F_{i}^{(1)} = \delta(\mathbf{x} - \eta_{1})\delta_{ij}\delta(t),$$

$$Q^{(2)} = \delta(\mathbf{x} - \eta_{2})\delta(t), F_{i}^{(2)} = 0; Q^{(1)} = 0, u_{i}^{(1)} \equiv u_{i}^{(1)}(\mathbf{x}, \eta_{1}, t), T^{(2)} \equiv T^{(2)}(\mathbf{x}, \eta_{2}, t).$$
(126)

Incorporating Eq. (126) in (119), yield:

$$T^{(1)}(\eta_2, \eta_1, t) = -\rho T_0 \dot{u}_i^{(2)}(\eta_1, \eta_2, t), \tag{127}$$

where $T^{(1)}(\eta_2,\eta_1,t)$ is the temperature at η_2 due to $F_i^{(1)}$ acting at η_1 in the direction x_i -axis and $\dot{u}_i^{(2)}(\eta_1,\eta_2,t)$ is the velocity of particle at η_1 due to $Q^{(2)}$ located at η_2 .

Imaging the point η_1 and η_2 , there act instantaneous concentrated body forces $F_i^{(1)}$ acts in the direction x_j -axis and chemical potential sources $A_0^{(2)}$, respectively. Thus, we obtain:

$$C_{1} = \{F_{i}^{(1)}, 0, 0, 0, 0, 0, 0, 0\}, C_{2} = \{0, 0, 0, 0, 0, 0, A_{0}^{(2)}\}, F_{i}^{(1)} = \delta(x - \eta_{1})\delta_{ij}\delta(t),$$

$$A_{0}^{(2)} = \delta(x - \eta_{2})\delta(t), F_{i}^{(2)} = 0, A_{0}^{(1)} = 0, u_{i}^{(1)} \equiv u_{i}^{(1)}(x, \eta_{1}, t), P^{(2)} \equiv P^{(2)}(x, \eta_{2}, t).$$
(128)

Incorporating Eq. (128) in (119), yield:

$$P^{(1)}(\eta_2, \eta_1, t) = -\rho \dot{u}_i^{(2)}(\eta_1, \eta_2, t), \tag{129}$$

where $P^{(1)}(\eta_2, \eta_1, t)$ is the chemical potential at η_2 due to $F_i^{(1)}$ acting at η_1 in the direction x_j -axis and $\dot{u}_i^{(2)}(\eta_1, \eta_2, t)$ is the velocity of particle at η_1 due to $A_0^{(2)}$ located at η_2 .

Considering the point η_1 and η_2 , there act instantaneous concentrated heat sources $Q^{(1)}$ and instantaneous chemical potential $A_0^{(2)}$. Thus, we get:

$$C_{1} = \{0,0,0,0,Q^{(1)},0,0\}; C_{2} = \{0,0,0,0,0,0,A_{0}^{(2)}\}; Q^{(1)} = \delta(\mathbf{x} - \eta_{1}) \delta(t); A_{0}^{(2)} = \delta(\mathbf{x} - \eta_{2}) \delta(t); P^{(1)} \equiv P^{(1)}(\mathbf{x},\eta_{1},t); T^{(2)} \equiv T^{(2)}(\mathbf{x},\eta_{2},t); Q^{(2)} = A_{0}^{(1)} = 0.$$

$$(130)$$

Incorporating Eq. (130) in (119), yield:

$$T_0 P^{(1)}(\eta_2, \eta_1, t) = T^{(2)}(\eta_1, \eta_2, t). \tag{131}$$

It is concluded that the temperature $T^{(2)}$ at the point η_1 due to the action of chemical sources at point η_2 is equal to the chemical potential $P^{(1)}$ at the point η_2 produced by the action of heat sources at the point η_1 .

Consider heat source $Q^{(1)}$ moving with uniform speed v in an infinite thermoviscoelastic medium in the direction x_3 and an instantaneous concentrated heat source $Q^{(2)}$ located at η_2 , thus we have:

$$C_{1} = \{0,0,0,0,Q^{(1)},0,0\}, C_{2} = \{0,0,0,0,Q^{(2)},0,0\}, Q^{(1)} = \delta(x_{1})\delta(x_{2})\delta(x_{3} - vt), Q^{(2)} = \delta(x - \eta_{2})\delta(t), T^{(1)} \equiv T^{(1)}(x,t), T^{(2)} \equiv T^{(2)}(x,\eta_{2},t).$$

$$(132)$$

Incorporating Eq. (132) in (119), yield:

$$T^{(1)}(\eta_2, t) = \int_0^t T^{(2)}(\zeta, \eta_2, t - \tau) d\tau, \tag{133}$$

where $\zeta = (0,0,vt)$ also the temperature field $T^{(1)}$ due to the moving heat source $Q^{(1)}$ in the terms of the temperature $T^{(2)}$ due to the instantaneous concentrated heat source $Q^{(2)}$.

To evaluate the velocity field due to moving heat source $Q^{(1)}$ and the instantaneous concentrated body force $F_i^{(2)}$ acting at point η_2 in the direction of x_j -axis, consider:

$$C_{1} = \{0,0,0,0,Q^{(1)},0,0\}, C_{2} = \{F_{i}^{(2)},0,0,0,0,0,0\}, Q^{(1)} = \delta(x_{1})\delta(x_{2})\delta(x_{3} - vt),$$

$$F_{i}^{(2)} = \delta(x - \eta_{2})\delta_{ij}\delta(t), Q^{(2)} = F_{i}^{(1)} = 0; u_{i}^{(1)} \equiv u_{i}^{(1)}(x,t), T^{(2)} \equiv T^{(2)}(x,\eta_{2},t),$$

$$(134)$$

$$\dot{u}_{j}^{(2)}(\eta_{2},t) = -\frac{1}{\rho T_{0}} \int_{0}^{t} T^{(j)}(\zeta,\eta_{2},t-\tau) d\tau, \tag{135}$$

where $T^{(j)}(x, \eta_2, t)$ is the temperature at the point x due to the instantaneous concentrated body force $F_i^{(2)}$ acting at point η_2 in the direction of the x_i axis.

Consider chemical potential source $A_0^{(1)}$ moving with uniform speed v in an infinite thermoviscoelastic medium in the direction x_3 and an instantaneous concentrated chemical potential source $A_0^{(2)}$ located at η_2 , thus we have:

$$C_1 = \{0,0,0,0,0,0,A_0^{(1)}\}, C_2 = \{0,0,0,0,0,0,A_0^{(2)}\}, A_0^{(1)} = \delta(x_1)\delta(x_2)\delta(x_3 - vt),$$
(136)

$$A_0^{(2)} = \delta(\mathbf{x} - \eta_2)\delta(t), P^{(1)} \equiv P^{(1)}(\mathbf{x}, t), P^{(2)} \equiv P^{(2)}(\mathbf{x}, \eta_2, t).$$
Incorporating Eq. (136) in (119), yield:
$$P^{(1)}(\eta_2, t) = \int_0^t P^{(2)}(\zeta, \eta_2, t - \tau) d\tau,$$
(137)

where $\zeta = (0,0,vt)$ also the chemical potential field $P^{(1)}$ due to the moving chemical potential source $A_0^{(1)}$ in the terms of the chemical potential $P^{(2)}$ due to the instantaneous concentrated chemical potential source $A_0^{(2)}$.

To evaluate the velocity field due to moving chemical potential source $A_0^{(1)}$ and the instantaneous concentrated body force $F_i^{(2)}$ acting at point η_2 in the direction of x_j -axis, consider:

$$C_{1} = \{0,0,0,0,0,0,A_{0}^{(1)}\}, C_{2} = \{F_{i}^{(2)},0,0,0,0,0,0\}, A_{0}^{(1)} = \delta(x_{1})\delta(x_{2})\delta(x_{3} - vt),$$

$$F_{i}^{(2)} = \delta(x - \eta_{2})\delta_{ij}\delta(t), A_{0}^{(2)} = F_{i}^{(1)} = 0, u_{i}^{(1)} \equiv u_{i}^{(1)}(x,t), P^{(2)} \equiv P^{(2)}(x,\eta_{2},t),$$

$$(138)$$

$$\dot{u}_{j}^{(2)}(\eta_{2},t) = -\frac{1}{c} \int_{0}^{t} P^{(j)}(\zeta,\eta_{2},t-\tau)d\tau, \tag{139}$$

where $P^{(j)}(x, \eta_2, t)$ is the chemical potential at the point x due to the instantaneous concentrated body force $F_i^{(2)}$ acting at point η_2 in the direction of the x_i axis.

Unique cases

- 1.1. In absence of rotation impact in Eqs. (11), (72), (102) and (117), we determine the equivalent results for modified couple stress thermoelastic diffusion under multi-phase-lags model.
- 1.2. Taking $\delta^0=1$, $\tau_T=\tau_q=\tau_\eta=\tau_P=0$, $\alpha=0$ and independent of rotation impact in Eqs. (11), (72), (102) and (117) yields the corresponding results for coupled thermoelastic diffusion model and these results are similar as obtained by Kumar and Gupta [25] as a special case.
- 1.3. Taking $\delta^0=1$, $\tau_T=0$, $\tau_P=0$, $N^0=1$, $\alpha=0$ and independent of rotation impact in Eqs. (11), (72), (102) and (117) determine the resulting expressions for coupled thermoelastic diffusion under L-S model, these results are similar as obtained by Ezzat and Fayik [39] in a special case.
- 1.4. Letting $N^0 = 1$, $M^0 = 1$, $\delta^0 = 1$, $\alpha = 0$ and independent of rotation impact determine the resulting results for coupled thermoelastic diffusion with single-phase-lag model.
- 1.5. If $\delta^0 = 1, N^0 = 2, M^0 = 1$, $\alpha = 0$ and independent of rotation impact in Eqs. (11), (72), (102) and (117) yields the corresponding results for thermoelastic diffusion with dual-phase-lag model, these results are similar as obtain by Kumar and Gupta [25].
- 1.6. In the absence of diffusion parameter, couple stress parameter and independent of rotation impact, Eqs. (11), (72), (102) and (117) yields the results for thermoelastic with dual-phase-lag model, these results are similar as obtained by Kumar and Gupta [26] as a special case.

Conclusions

In this paper, a new establishment of modified couple stress thermoelastic diffusion under multi-phase-lags model in rotating frame of reference has been conferred. The fundamental theorems alike energy, uniqueness and reciprocity along with the variational criterion have been established in the simulated model. Laplace transform is

used to prove uniqueness theorem and reciprocity theorem. With the quide of energy theorem, we can examine the motion of the system under different sources (mechanical force, thermal source and mass-diffusion source). As an application of reciprocity theorem, instantaneous concentrated body forces, heat forces and chemical potential sources along with moving heat source, chemical potential sources are taken. Uniqueness theorem is important in establishing the existence and properties of mathematical objects. With the help of reciprocity theorem, different methods of integrating differential equation of thermoelasticity using the Green function can be analyzed. The variational criterion leads in deriving the differential equation of various systems like membranes and cells easy aspect and also prepares it possible to infer distinct approximation techniques for the solution of various problems (statics and dynamics). Although the problem is theoretical, but it helps for further investigation to examine wave phenomena and variational problems in the assume model. The results obtained in particular case of the model are verified from the well-known results. The proposed model is unique in its form and physical meaning is apparent. It is convenient and provides more approaches to estimate how a material behaves in the real world. It is concluded that all the field quantities are sufficiently restricted to thermal and couple stress parameters. We observe that phase-lag and rotation have significant effect on the all the field studied and the results supporting the definition of the classification of thermal conductivity of the material. It is concluded that modified couple stress and thermoelastic diffusion fields play valuable role in processing and characterization to improve material properties. The results obtained in this study should be useful for research working in thermodynamic engineering, material science and hyperbolic thermoelastic models. The mathematical model proposed in this work is a powerful, indispensable tool for studying various problems, scientific research, product, process development and manufacturing.

CRediT authorship contribution statement

Saurav Sharma SC: writing-review and editing, conceptualization, investigation, supervision, data curation; **Devi Sangeeta** SCC: writing-review and editing, writing-original draft, Investigation, data curation; **Rajneesh Kumar** SCC: writing-original draft, conceptualization, supervision, data curation.

Conflict of interest

The authors declare that they have no conflict of interest.

References

- 1. Lord HW, Shulman Y. A generalized dynamical theory of thermoelasticity. *Journal of the Mechanics and Physics of Solids*. 1967;15(5): 299–309.
- 2. Green AE, Lindsay KA. Thermoelasticity. *Journal of Elasticity*. 1972;2: 1–7.
- 3. Green AE, Naghdi PM. Thermoelasticity without energy dissipation. *Journal of Elasticity*. 1993;31: 189–208.
- 4. Hetnarski RB, Ignaczak J. Generalized thermoelasticity. *Journal of Thermal Stresses*. 1999;22(4): 451–476.
- 5. Tzou DY. Thermal shock phenomena under high rate response in solids. In: Tien CL. (eds.) *Annual Review of Heat and mass Treansfer*. Washington, D.C.: Hemisphere Publishing Inc.; 1992. p.111–185.

6. Cattaneo C. A form of heat equation which eliminate the paradox of instantaneous propagation. *C. R. Acad. Sci., Paris.* 1958;246: 431–433.

- 7. Vernotte P. The paradoxes of the continuous theory of heat equation. *C. R. Acad. Sci., Paris.* 1958; 246: 3154–3155.
- 8. Tzou DY. A unified approach for heat conduction from macro-to-micro-scales. *Journal of Heat Transfer-transactions of The Asme*. 1995;117: 8–16.
- 9. Tzou DY. The generalized lagging response in small scale and high-rate heating. *International Journal of Heat and Mass Transfer.* 1995;38(17): 3231–3240.
- 10. Roychouduri SK. On a thermoelastic three-phase-lags model. *Journal of Thermal stresses*. 2007;30(3): 231–238.
- 11. Tzou DY. Macro- to Microscale Heat Transfer: The Lagging Behavior. New York: Taylor and Francis; 1997.
- 12. Nowacki W. Dynamical problems of thermodiffusion in solids I. *Bulletin of the Polish Academy of Sciences: Technical Sciences.* 1974;22: 55–64.
- 13. Nowacki W. Dynamical problems of thermodiffusion in solids II. *Bulletin of the Polish Academy of Sciences: Technical Sciences.* 1974;22: 205–211.
- 14. Nowacki W. Dynamical problems of thermodiffusion in solids III. Bulletin of the Polish Academy of Sciences: Technical Sciences. 1974;22: 257 266.
- 15. Nowacki W. Dynamical problems of thermodiffusion in elastic solids. Proc. Vib. Prob. 1974;15: 105-128.
- 16. Sherief HH, Hamza FA, Saleh HA. The theory of generalized thermoelastic diffusion. *International Journal of Engineering Science*. 2004;42(5–6): 591–608.
- 17. Kumar R, Kansal T. Propagation of Lamb waves in transversely isotropic thermoelastic diffusive plate. *International Journal of Solids and Structures*. 2008;45(22–23): 5890–5913.
- 18. Mindlin RD, Tiersten HF. Effects of couple-stresses in linear elasticity. *Archive for Rational Mechanics and Analysis*. 1962; 11: 415 448.
- 19. Toupin RA. Elastic materials with couple-stresses. Archive for Rational Mechanics and Analysis. 1962;11: 385 414.
- 20. Koiter WT. Couple-stresses in the theory of elasticity, I & II. *Proceedings Series B, Koninklijke Nederlandse Akademie van Wetenschappen*. 1964;67: 17 44.
- 21. Yang F, Chong ACM, Lam DCC, Tong P. Couple stress based strain gradient theory for elasticity. *International Journal of solids and structures*. 2002;39(10): 2731–2743.
- 22. Park SK, Geo XL. Bernoulli-Euler beam model based on modified couple stress theory. *Journal of Micromechanics and Microengineering*. 2006;16(11), 2355–2359.
- 23. Aouadi M. Generalized Theory of thermoelastic diffusion for anisotropic media. *Journal of Thermal Stresses*. 2008;31(3): 270–285.
- 24. Kumar R, Kothari S, Mukhopadhyay S. Some theorems on generalized thermoelastic diffusion. *Acta Mechanica*. 2011;217: 287–296.
- 25. Kumar R, Gupta V. Uniqueness, reciprocity theorem and plane waves in thermoelastic diffusion with fractional order derivative. *Chinese Physics B.* 2013;22(7): 07601.
- 26. Kumar R, Gupta V. Uniqueness, reciprocity theorems and plane wave propagation in different theories of thermoelasticity. *International Journal of Applied Mechanics and Engineering*. 2013;18(4): 1067–1086.
- 27. Sarkar I, Mukhopadhyay B. On energy, uniqueness theorems and variational principle for generalized thermoelasticity with memory-dependent derivative. *International Journal of Heat and Mass Transfer*. 2020;149(5): 119112.
- 28. El-Karamany AS, Ezzat MA. On the Two-Temperature Green–Naghdi Thermoelasticity Theories. *Journal of Thermal Stresses*. 2011;34(12): 1207–1226.
- 29. El-Karamany AS, Ezzat MA. On the dual-phase-lag thermoelasticity theory. *Meccanica*. 2014;49: 79-89.
- 30. Bala S, Khurana A, Tomar SK. Uniqueness, continuous and dependence and reciprocity theorems in the thermoelastic relaxed micromorphic continuum. *Journal of thermal stresses*. 2021;44(6): 715–730.
- 31. Al-Lehaibi EAN. The variationally principle of two-temperature thermoelasticity in the absence of the energy dissipation theorem. *Journal of Umm Al-Qura University for Engineering and Architecture*. 2022;13: 81–85.
- 32. Paul K, Mukhopadhyay B. A novel mathematical model on generalized thermoelastic diffusion theory. *Journal of Thermal Stresses.* 2023;46(4): 253–275.
- 33. Abouelregal AE. Modified fractional thermoelasticity model with multi-relaxation times of higher order: application to spherical cavity exposed to a harmonic varying heat. *Waves in Random and Complex Media*. 2021;31(5): 812-232.
- 34. Abouelregal AE. Two-temperature thermoelastic model without energy dissipation including higher order time-derivatives and two phase-lags. *Material Research Express*. 2019;6(11): 116535.

- 35. Abouelregal AE. On Green and Naghdi thermoelasticity model without energy dissipation with higher order time differential and phase-lags. *Journal of Applied and Computational Mechanics*. 2020;6(3): 445–456. 36. Zenkour AM. Refined microtrmperatures multi-phase-lags theory for plane waves propagation in thermoelastic medium. *Results in Physics*. 2018;11: 929–937.
- 37. Zenkour AM. Refined multi-phase-lags theory for photothermal waves of a gravitational semiconducting half-space. *Composite Structures*. 2019;212: 346–364.
- 38. Zenkour AM. Wave propagation of a gravitated piezo-thermoelastic half-space via a refined multiphase-lags theory. *Mechanics of Advanced Materials and Structures*. 2019;27(22): 1923–1934.
- 39. Ezzat MA, Fayik M. Fractional order theory of thermoelastic diffusion. Journal of Thermal Stresses. 2011;34(8): 851–872.
- 40. Kumar R, Sharma P. Variational principle, uniqueness and reciprocity theorems in porous piezothermoelastic with mass diffusion. *Cogent Mathematics*. 2016;3(1): 1231947.
- 41. Sharma S, Devi S, Kumar R, Marin M. Examining basic theorems and plane waves in the context of thermoelastic diffusion using a multi-phase-lag model with temperature dependence. *Mechanics of Advanced Materials and Structures*. 2024: 1–18.
- 42. Roy Choudhuri SK. Electro-magneto-thermoelastic plane waves in rotating media with thermal relaxation. *International Journal of Engineering Science*. 1984;22(5): 519–530.
- 43. Kumar R, Devi S, Sharma V. Effects of Hall Current and Rotation in Modified Couple Stress Generalized Thermoelastic Half Space due to Ramp-Type Heating. *Journal of Solid Mechanics*. 2017;9(3): 527 542.
- 44. Ezzat MA. Fundamental solution in generalized magneto-thermoelasticity with two relaxation times for perfect conductor cylindrical region. *International Journal of Engineering Science*. 2004;42(13): 1503–1519.
- 45. Ezzat MA, Youssef HM. Stokes' first problem for an electro-conducting micropolar fluid with thermoelectric properties. *Canadian Journal of Physics*. 2010;88(1): 35–48.
- 46. Sharma S, Sharma K, Bhargava RR. Plane waves and fundamental solution in an electro-microstretch elastic solids. *Afrika Matematika*. 2014;25: 483–497.
- 47. Ezzat MA, El-Karamany AS, El-Bary AA. On Thermo-viscoelasticity with Variable Thermal Conductivity and Fractional-Order Heat Transfer. *International Journal of Thermophysics*. 2015;36: 1684–1697.
- 48. Sharma S, Khator S. Power generation planning with reserve dispatch and weather uncertainties including penetration of renewable sources. *International Journal of Smart Grid and Clean Energy*. 2021;10(4): 292–303.
- 49. Sharma S, Khator S. Micro-Grid planning with aggregator's role in the renewable inclusive prosumer market. *Journal of Power and Energy Engineering*. 2022;10(4): 47–62.
- 50. Panja SK, Lahiri A, Mandal SC. A thermoelastic model with higher order time derivatives for a crack in a rotating solid. *International Journal for Computational Methods in Engineering Science and Mechanics*. 2023;24(2): 107 –118.
- 51. Bibi F, Ali H, Azhar E, Jamal M, Ahmed I, Ragab AE. Propagation and reflection of thermoelastic waves in rotating nonlocal fractional order porous medium under Hall current influence. *Scientific Reports*. 2023;13: 17703.
- 52. El-Sapa S, El-Bary AA, Atef HM. The influence of rotation and viscosity on generalized conformable fractional micropolar thermoelasticity with two temperatures. *Frontiers in Physics*. 2023;11.
- 53. Biot MA. Thermoelasticity and irreversible thermodynamic. Journal of Applied Physics. 1956;27(3): 240–253.
- 54. Churchill RV. Operational mathematics. New-York: McGraw-Hill; 1972.

Submitted: September 24, 2024

Revised: February 12, 2025

Accepted: March 26, 2025

Modelling forced convection and magneto-elastic interactions in a downward conduit using ferrofluid

H. Derraz 🖾 🗓, M. Bouzit 🗓, A. Bencherif 🗓

Laboratory of Maritime Sciences and Engineering LSIM Faculty of Mechanical Engineering,

University of Science and Technology of Oran, Mohamed Boudiaf, El Mnaouar, Oran, Algeria

[™] hanaa.derraz@univ-usto.dz

ABSTRACT

An unsteady numerical investigation of fluid-structure interaction in forced magnetohydrodynamic convection of a ferrofluid within a downward step configuration, aiming to analyze its influence on flow dynamics and heat transfer mechanisms is presented. The research explicitly incorporates the deformation of an elastic top wall under the combined effects of hydrodynamic, magnetic, and thermal forces. This approach enhances the understanding of the interplay between wall deformation and forced convection under dynamic magnetic fields, an aspect rarely addressed in existing literature. The study examines the impact of key physical parameters, including the Reynolds number (100 ≤ Re ≤ 200), Hartmann number $(0 \le \text{Ha} \le 50)$, Cauchy number $(10^{-7} \le \text{Ca} \le 10^{-3})$, magnetic field inclination angle $(0^{\circ} \le 7 \le 60^{\circ})$, and nanoparticle volume fraction (0 % $\leq \varphi \leq$ 8 %) on flow structure, heat transfer, and wall deformation. The numerical modeling is based on the arbitrary Lagrangian-Eulerian formulation, solving the coupled Navier-Stokes, energy, and structural displacement equations using the finite element method. The results reveal that increasing the Reynolds number enhances thermal agitation and vortex formation, leading to improved heat transfer, while a decrease in the Cauchy number amplifies these effects. Conversely, a higher Hartmann number strengthens Lorentz forces, suppressing flow motion and stabilizing the thermal boundary layer. Furthermore, the inclination angle of the magnetic field significantly influences wall deformation, altering the interaction between the ferrofluid and the elastic boundary.

KEYWORDS

forced convection • magnetic fields • elasticity • heat transfer • Hartmann number • MHD • FSI

Citation: Derraz H, Bouzit M, Bencherif A. Modelling forced convection and magneto-elastic interactions in a downward conduit using ferrofluid. *Materials Physics and Mechanics*. 2025;53(2): 83–103. http://dx.doi.org/10.18149/MPM.5322025_8

Introduction

Convective heat transfer of fluids influenced by magnetic fields and nanoparticles has become an increasingly significant research area within the scientific community. The advent of nanofluids fluids containing nanometer-sized particles suspended in a base fluid has further heightened interest in this field due to their unique thermophysical properties. These nanofluids interact complexly with electromagnetic forces, making them a crucial subject of study for understanding the mechanisms governing fluid behavior under such conditions.

Researchers are actively exploring the wide range of potential benefits that this technology offers across various domains. For instance, in electronics, nanofluids subjected to magnetic fields are employed to cool electronic components, thereby enhancing both their performance and longevity. In the medical field, this technology



facilitates more effective and less invasive targeting and treatment of cancerous tumors. Furthermore, in industrial processes, particularly in heating, ventilation, and air conditioning (HVAC) systems, nanofluids improve energy efficiency, resulting in reduced costs and a smaller environmental footprint for buildings. Precise temperature control enabled by nanofluids also holds promise for more efficient manufacturing processes and higher-quality products.

Recent studies have placed increasing emphasis on the effects of magnetic fields on nanofluids, unveiling new possibilities for enhancing the performance of heat transfer systems in sectors such as microelectronics, cooling systems, industrial processes, and energy and biomedical technologies. These advancements have the potential to revolutionize thermal management in electronic devices, optimize manufacturing processes, and drive the development of innovative medical technologies.

In [1], it was studied forced convective flow within a backward step containing a fixed-diameter rotary cylinder using the ferrofluid Fe₃O₄-H₂O in the presence of an external magnetic field. Their findings demonstrated that while the average Nusselt number decreases as the Hartmann number increases, the nanoparticle concentration and the magnetic field's inclination led to an increase in the average Nusselt number. In [2], it was examined the effects of step height on flow and heat transfer properties, finding that both the average Nusselt number and the skin friction coefficient increase with step height. Several other studies have investigated the effects of nanoparticles on heat transfer in a backward-facing step configuration [3-6]. These studies consistently found that the volume fraction of nanoparticles increases along with the average Nusselt number. In [7], authors used the step length of the backward-facing step as a control parameter in their numerical study and revealed that an increase in step length leads to a higher Nusselt number. In [8], the impact of the ferrofluid Fe₃O₄-H₂O was examined on a backward-facing step in the presence of an inclined magnetic field using a forced convective current. They found that when the cylinder rotates counterclockwise, the rate of heat transfer increases. Additionally, it was studied forced convection ferrofluid flow in a backward-facing step with a pinched cylinder, discovering that adding a fin to the cylinder significantly enhances heat transfer [9]. In [10], it was identified that an oscillating fin mounted on a backward-facing step is the most effective method, as it results in a high average Nusselt number and low-pressure drop. In [11], it was investigated the impact of a baffle on flow and heat transfer distributions in a rectangular duct near a backward-facing step through numerical simulations. Their findings indicate that variations in the Reynolds number and aspect ratio influence heat transfer characteristics and fluid flow properties during separation and reattachment. The influence of the Reynolds number on heat transfer characteristics, showing a significant impact on heat transfer during flow over a backward-facing step, was numerically examined [12]. In [13], a numerical analysis was conducted to investigate the impact of the Reynolds number on the flow characteristics over a BFS. The findings showed that Reynolds number variation affects the diameters of recirculation districts. In [14], it was studied the impact of a baffle mounted on the upper wall of a conduit based on laminar and turbulent mixed convection. The results indicate that baffle height, position, and distance all have a significant impact on the properties of heat transfer and fluid flow.

Numerical studies have extensively explored the effects of adding nanoparticles to a base fluid on heat transfer performance. Research by [15–19] demonstrated that the incorporation of nanoparticles increases the average Nusselt number, enhances mass transfer, and improves flow characteristics as the volume fraction of nanoparticles rises [20]. Experiments were conducted comparing two nanofluids, CuO-EG and MgO-EG, and it was found that the CuO-EG nanofluid exhibited a higher heat transfer rate than the MgO-EG nanofluid. Similarly, through numerical simulations of mixed convection in laminar nanofluids, revealed that both the shape and type of nanoparticles significantly influence flow properties, with nanofluids generally providing superior heat transfer compared to water alone [21]. In [22], it was investigated the magnetohydrodynamic (MHD) boundary layer flow of three types of nanofluids, focusing on heat and mass transfer in porous media. More recently, it was examined the impact of magnetic nanoparticles on the thermophysical properties of nanofluids and forced convective heat transfer, concluding that increasing the magnetic field (MF) and nanoparticle (NP) concentrations leads to a corresponding increase in the Nusselt number of the nanofluids [23].

Several studies have examined the fluid flow characteristics and heat transfer quality in systems involving a rotating cylinder. In [24–26], it was found that high Reynolds number values significantly increase the average Nusselt number, and that flow instability positively impacts forced convection heat transfer, particularly on the cylinder's surface. Further, it was investigated ferrofluid flow-induced convection over a descending step using a spinning finned cylinder [27]. Their study revealed that the rotation of the finned cylinder enhanced heat transfer by 177.33 % compared to a cylinder without a fin.

Additionally, the influence of external magnetic fields on thermal transfer control and quality in systems with an inclined and rotated cylinder has been extensively studied by [28–30]. These studies concluded that an inclined magnetic field effectively eliminates recirculation zones, and that a higher Reynolds number further enhances heat transfer.

Numerous studies have investigated the impact of nanofluids on thermal and hydrodynamic properties in enclosures using magneto-hydrodynamic (MHD) forced convection. Research by [31–35] has shown that the temperature gradient increases with the Hartmann number, and the Nusselt number's growth is influenced by domain velocity and permeability. These studies also found that magnetic forces improve conduction, and the inclusion of nanofluids enhances overall heat transfer. Additionally, it was observed that the lowest wall of the cavity is sensitive to the elastic wall, while the top wall shows an increase in temperature gradient with the Hartmann number.

Further investigations into the forced convection of non-Newtonian nanofluids in wavy channels [36,37] revealed that the addition of nanoparticles and an increase in the Reynolds number significantly enhance heat transfer in such channels. In [38], it was studied magnetohydrodynamic mixed convection in a 3D lid-driven enclosure containing a Cu-water nanofluid, while in [39] it was focused on steady MHD mixed convective cooling in a vented, porous cavity with an intense elliptical inward cylinder containing MWCNT/CMC nanofluid. Their results demonstrated that Nusselt numbers increase with Richardson number and porosity ratio, although the Hartmann number tends to dominate at lower levels of fluidity within the cavity. Finally, it was investigated transient mixed convection in a vented square container with heated walls and a flexible baffle, finding

that the enhanced average Nusselt number is most prominent in cavities with flexible baffles [40]. The effect of a flexible fin on unsteady natural convection of a Bingham fluid in a laterally heated square cavity is analyzed in [41]. The results indicate that heat transfer reaches its peak at $Ra = 10^5$ when Bn = 0, while an increasing Bingham number gradually suppresses convection, ultimately leading to a conduction-dominated regime at Bn = 20. In contrast, the modulus of elasticity of the fin has a negligible impact on heat transfer.

In the present study, the coupling effects of forced magnetic field convection and elastic membrane deformation in a descending ferrofluid conduit. This work analyzed various levels of Reynolds number, elasticity, Hartmann number, and magnetic field tilt angle and nanoparticle volume fraction.

Modeling approach

A two-dimensional unsteady numerical study has been carried out to examine the flow of a nanofluid subjected to forced convection in the presence of an external magnetic field. This study focuses on a one-step backward-facing configuration with an elastic top wall incorporating a non-rotating cylinder. Figure 1 illustrates the physical configuration and associated boundary conditions. The length of the rearward-facing step is denoted H, and the height of the horizontal duct is 2H. The cylinder has a radius of D = H, with a central position at (4H, H). At the entrance to the duct, the velocity is $u = u_0$ and v = 0. At the outlet of the pipe, all the gradients of the variables in the x direction are zero. The associated temperatures are T_c for the low temperature of the ferrofluid and Th for the high temperature of the bottom wall. The Prandtl number of the base fluid is maintained at 6.2, and the constant thermophysical properties of H_2O and Fe_3O_4 are listed in Table 1.

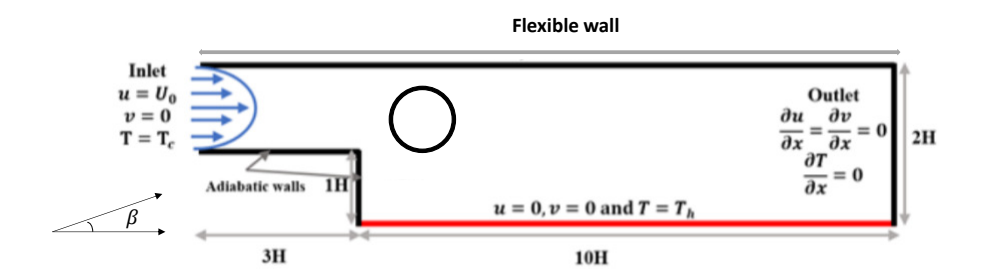


Fig. 1. Physical model

Table 1. Thermo-physical properties of Water and Iron Oxide

Thermophysical properties	<i>ρ,</i> kg/m³	<i>Cp</i> , J/kg·K)	<i>k</i> , W/m⋅K	<i>β</i> , 1/K	<i>σ,</i> 1/Ω·m
Water	997.1	4,179	0.613	21.10-5	0.05
Fe ₃ O ₄	5,200	670	6	1.18·10 ⁻⁵	25,000

Hence, the thermophysical properties were considered independent of temperature. Employing the assumptions revealed earlier and using the Arbitrary Lagrangian-Eulerian (ALE) method, the equations modelling the hydrodynamic and thermal characteristics of the problem are presented as follows [8,41].

For fluid domain:

$$\frac{\partial u}{\partial x} + \frac{\partial v}{\partial y} = 0. \tag{1}$$

Momentum equations:

$$\rho_{nf} \left[\frac{\partial u}{\partial t} + u \frac{\partial u}{\partial x} + v \frac{\partial u}{\partial y} \right] = -\frac{\partial p}{\partial x} + \mu_{nf} \left[\frac{\partial^2 u}{\partial x^2} + \frac{\partial^2 u}{\partial y^2} \right] + \sigma_{nf} B_0 \left(v \sin \gamma \cos \gamma - u \sin^2 \gamma \right); \tag{2}$$

$$\rho_{nf} \left[\frac{\partial v}{\partial t} + u \frac{\partial v}{\partial x} + v \frac{\partial v}{\partial y} \right] = -\frac{\partial p}{\partial y} + \mu_{nf} \left[\frac{\partial^2 v}{\partial x^2} + \frac{\partial^2 v}{\partial y^2} \right] + \sigma_{nf} B_0 \left(u \sin \gamma \cos \gamma - v \sin^2 \gamma \right). \tag{3}$$

The energy equation for the fluid:

$$\frac{\partial T}{\partial t} + u \frac{\partial T}{\partial x} + v \frac{\partial T}{\partial y} = \alpha_{nf} \left(\frac{\partial^2 T}{\partial x^2} + \frac{\partial^2 T}{\partial y^2} \right). \tag{4}$$

For elastic structure domain, the equations of the motion of flexible fins can be written as:

$$\rho_{s} \frac{\partial^{2} d_{x}}{\partial t^{2}} - \frac{\partial \sigma^{*}_{xx}}{\partial x} - \frac{\partial \sigma^{*}_{xy}}{\partial y} = 0;$$
(5)

$$\rho_{s} \frac{\partial^{2} d_{y}}{\partial t^{2}} - \frac{\partial \sigma^{*}_{xy}}{\partial x} - \frac{\partial \sigma^{*}_{yy}}{\partial y} = 0.$$
 (6)

The energy equation for the flexible fin:

$$\rho_s c_{ps} \frac{\partial^2 T_s}{\partial t^2} = k_s \left(\frac{\partial^2 T_s}{\partial x^2} - \frac{\partial^2 T_s}{\partial y^2} \right). \tag{7}$$

The Neo-Hookean solid model is applied to express the stress tensor of Eqs. (5) and (6). The tensor σ is given by:

$$\boldsymbol{\sigma}^* = J^{-1}FSF^{tr} | F = (I + \nabla^* \mathbf{d}_s^*), J = \det(F) \& S = \partial W_s / \partial \varepsilon;$$
(8)

$$W_s = \frac{1}{2}l(J^{-1}I_1 - 3) - lLn(J) + \frac{1}{2}\lambda(Ln(J))^2;$$

$$\begin{vmatrix} l = E / (2(1+\nu)) \\ \lambda = E\nu / ((1+\nu)(1-2\nu)) \end{cases};$$
(9)

$$\varepsilon = \frac{1}{2} \left(\nabla^* \mathbf{d}_s^* + \nabla^* \mathbf{d}_s^{*tr} + \nabla^* \mathbf{d}_s^{*tr} \nabla^* \mathbf{d}_s^* \right). \tag{10}$$

The boundary conditions pertinent to the external walls and the interface of the flexible upper wall can be formulated as follows:

- 1. the inlet: $u = u_0$, v = 0, $T = T_c$;
- 2. the downstream bottom wall: u = 0, v = 0, $T = T_h$;
- 3. the outlet: $\frac{\partial u}{\partial n} = \frac{\partial T}{\partial n} = 0$;
- 4. other walls are adiabatic and the velocity is no-slip: u = v = 0 and $\partial T/\partial n = 0$;
- 5. the adiabatic cylinder: $\partial T/\partial n = 0$;
- 6. the cylinder velocity components: u = v = 0.

The dimensionless form equations: $X = \frac{x}{H}$, $Y = \frac{y}{H}$, $\theta = \frac{T - T_c}{T_h - T_c}$, $P_r = \frac{v_f}{\alpha_f}$, $Ha = B_0 H \sqrt{\frac{\sigma_{nf}}{\mu_{nf}}}$, $Re = \frac{H\bar{u}}{v_f}$, $\tau = \frac{t\alpha}{H^2}$, $\sigma^* = \frac{\sigma}{E}$, $P = \frac{p}{\rho_n f \bar{u}^2}$, $U = \frac{u}{\bar{u}}$, $V = \frac{v}{\bar{u}}$.

The governing dimensionless equations are hence. Mass balance:

$$\frac{\partial U}{\partial X} + \frac{\partial V}{\partial Y} = 0. \tag{11}$$

Momentum balance:

$$\frac{\partial U}{\partial \tau} + U \frac{\partial U}{\partial X} + V \frac{\partial U}{\partial Y} = -\frac{\partial P}{\partial X} + \frac{1}{\text{Re}} \frac{\rho_f}{\rho_{nf}} \frac{\mu_{nf}}{\mu_{nf}} \left(\frac{\partial^2 U}{\partial X^2} + \frac{\partial^2 U}{\partial Y^2} \right) + \frac{\rho_f}{\rho_{nf}} \frac{\sigma_{nf}}{\sigma_f} \frac{\text{Ha}^2}{\text{Re}} \left(V \sin \gamma \cos \gamma - U \sin^2 \gamma \right); \quad (12)$$

$$\frac{\partial V}{\partial \tau} + U \frac{\partial V}{\partial X} + V \frac{\partial V}{\partial Y} = -\frac{\partial P}{\partial Y} + \frac{1}{\text{Re}} \frac{\rho_f}{\rho_{nf}} \frac{\mu_{nf}}{\mu_{nf}} \left(\frac{\partial^2 V}{\partial X^2} + \frac{\partial^2 V}{\partial Y^2} \right) + \frac{\rho_f}{\rho_{nf}} \frac{\sigma_{nf}}{\sigma_f} \frac{\text{Ha}^2}{\text{Re}} \left(U \sin \gamma \cos \gamma - V \sin^2 \gamma \right). \tag{13}$$

The energy equation for the fluid:

$$\frac{\partial \theta_f}{\partial \tau} + U \frac{\partial \theta_f}{\partial X} + V \frac{\partial \theta_f}{\partial Y} = \frac{1}{\text{Re} \times \text{Pr}} \frac{\alpha_{nf}}{\alpha_f} \left(\frac{\partial^2 \theta_f}{\partial X^2} + \frac{\partial^2 \theta_f}{\partial Y^2} \right). \tag{14}$$

Structural displacement of the flexible fin:

$$\frac{\rho_s}{\text{Ca}} \frac{\partial^2 D_X}{\partial \tau^2} - \frac{\partial \Gamma_{XX}}{\partial X} - \frac{\partial \Gamma_{XY}}{\partial Y} = 0 ;$$
(15)

$$\frac{\rho_s}{\text{Ca}} \frac{\partial^2 D_Y}{\partial \tau^2} - \frac{\partial \Gamma_{XY}}{\partial X} - \frac{\partial \Gamma_{YY}}{\partial Y} = 0.$$
 (16)

The energy equation for the fin:

$$\frac{\partial^2 \theta_s}{\partial \tau^2} = k_s \left(\frac{\partial^2 \theta_s}{\partial X^2} - \frac{\partial^2 \theta_s}{\partial Y^2} \right). \tag{17}$$

Nusselt number:

$$Nu = \frac{\kappa_{nt}}{\kappa_{nf}} \left(\frac{\partial \theta}{\partial Y} \right). \tag{18}$$

The average Nusselt number:

$$Nu_{avg} = \frac{1}{L} \int_{S}^{L} Nu dX.$$
 (19)

Thermo-physical properties of ferrofluid are presented below.

Density:

$$\rho_{nf} = (1 - \phi)\rho_f + \phi\rho_p. \tag{20}$$

Thermal diffusivity:

$$\alpha_{nf} = \frac{k_{nf}}{(\rho c_p)_{nf}}.$$
 (21)

Electrical conductivity:

$$\delta_{nf} = \delta_f \left[1 + \frac{3(\delta - 1)\phi}{(\delta + 2) - (\delta - 1)\phi} \right]; \ \delta = \frac{\delta_p}{\delta_f}.$$
 (22)

Specific heat:

$$(\rho c_p)_{nf} = (1 - \phi)(\rho c_p)_f + \phi(\rho c_p)_p. \tag{23}$$

Thermal expansion coefficient:

$$(\rho\beta)_{nf} = (1-\phi)(\rho\beta)_f + \phi(\rho\beta)_p. \tag{24}$$

Thermal conductivity:

$$\frac{k_{nf}}{k_f} = \frac{k_p + 2k_f - 2\phi(k_f - k_p)}{k_p + 2k_f + \phi(k_f - k_p)}.$$
 (25)

Dynamic viscosity:

$$\mu_{nf} = \frac{\mu_f}{(1-\phi)^{2.5}} \,. \tag{26}$$

Dimensionless Boundary conditions:

- 1. the inlet: $U = U_0$, V = 0; $\theta = 0$;
- 2. the downstream bottom wall: U = 0, V = 0, $\theta = 1$;
- 3. the outlet: $\partial U/\partial X = \partial V/\partial Y = 0$, $\partial \theta/\partial X = 0$;
- 4. Other walls are adiabatic and the velocity is no-slip: $U = V = \partial \theta / \partial n = 0$;
- 5. the adiabatic cylinder: $\partial \theta / \partial n = 0$;
- 6. the cylinder velocity components: U = V = 0.

Numerical solution method: Grid independency test and Validation

Numerical solution method

Numerical methods are utilized to tackle the governing equations and boundary conditions for unsteady Forced convection of a magneto-elastic interactions in a downward conduit using ferrofluid. The equations are first reformulated for simplicity, then solved using the Galerkin Method of Weighted Residuals, a variant of the Finite Element Method (FEM). The fluid-structure interface, including the dynamic motion of the flexible wall, is captured using the Arbitrary Lagrangian-Eulerian (ALE) method. The computational domain is finely discretized into non-uniform triangular elements, ensuring precise flow field representation. To address the nonlinear momentum equations, a Newton iteration algorithm is applied.

Grid independency test

To validate that the results obtained are not influenced by the size of the mesh used, a mesh independence test was carried out. This test consists of analysing the evolution of the average Nusselt number as a function of dimensionless time on the hot wall for different levels of mesh refinement. The parameters used are Re = 150; Ha = 25, $Ca = 10^{-4}$, $\gamma = 0^{\circ}$ and $\varphi = 5$ %. The results are shown in Table 2, where it can be seen that variations in the average Nusselt number as a function of time become negligible from a mesh size greater than 80283. Consequently, this mesh size (Fig. 2) was chosen to present the results in the rest of the study.

Table 2. Grid independence test at Re = 150; Ha = 25, Ca = 10^{-4} , γ = 0° and φ = 5 %

Elements Number	19846	27721	42512	80283	136134
Time	2640 s	4830 s	7167 s	14820 s	17635 s
Nu _{avg}	4.680953	4.669642	4.667470	4.667216	4.667101

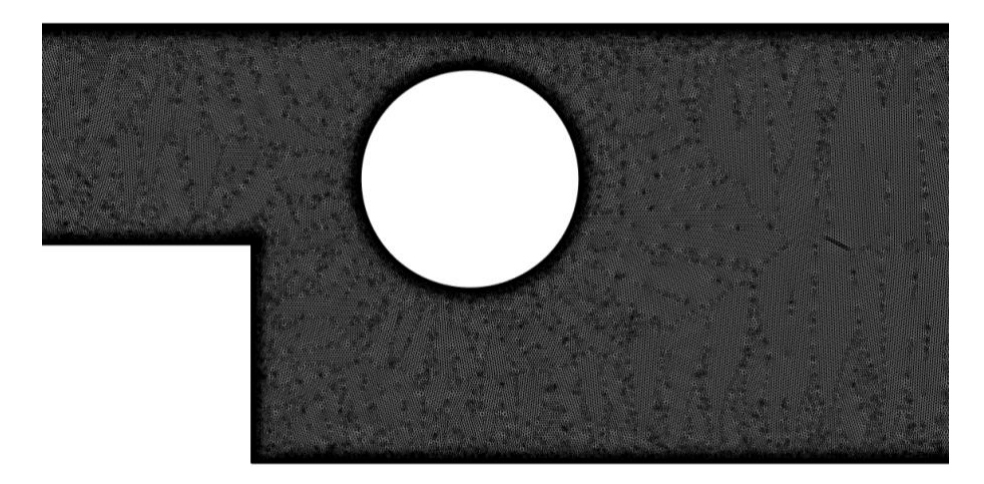


Fig. 2. The physical configuration with the best mesh size

Validation

To further validate the calculation code used in this study, we compared our results with the numerical data reported by [8] for the case of forced convection over a downward step, with *Re* set at 100 and *Pr* at 5. Figure 3 illustrates this comparison, demonstrating good agreement between the two sets of results. Further validation was conducted by comparing the mean Nusselt number as a function of the Hartmann number (*Ha*) reported by [8] with the results obtained in the present work.

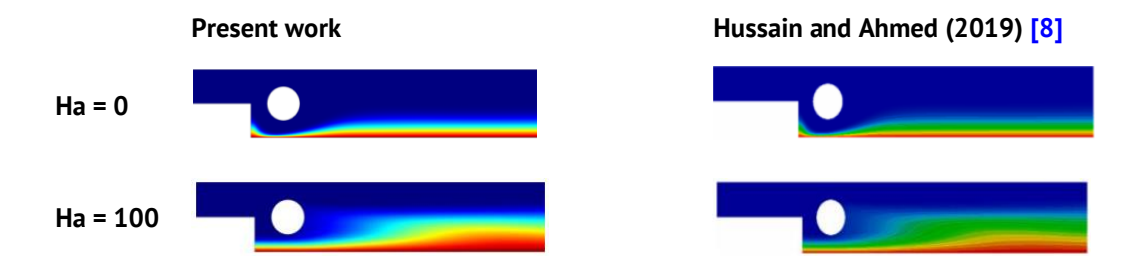


Fig. 3. Comparing the results of the present study and reported by [8]

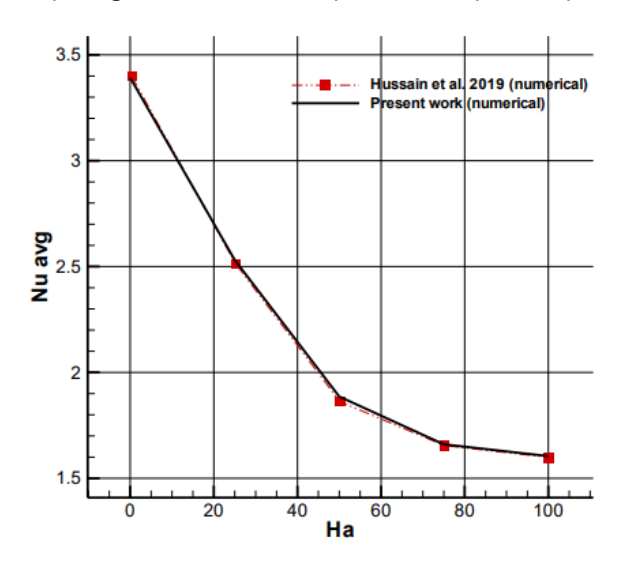


Fig. 4. Comparing the results of the present study and Nusselt number reported by [8]

As shown in Fig. 4, excellent agreement is observed between the present study and the previously reported data. These comparisons bolster the accuracy and reliability of the calculation code used in this research, demonstrating its effectiveness in simulating and predicting the complex interactions and phenomena within the system. The alignment between the results reinforces confidence in the underlying mathematical models and numerical methods employed in the code.

Results and Discussion

This section delves into the analysis of how changing key control parameters, specifically the dimensionless Reynolds $100 \le Re \le 200$, Hartmann $0 \le Ha \le 50$, and Cauchy $10^{-7} \le Ca \le 10^{-3}$ numbers, nanoparticles concentration $0\% \le \varphi \le 8\%$, magnetic field inclination $0\% \le \gamma \le 60\%$, affects various aspects. We explore how these parameters shape flow characteristics, like streamlines, and thermal fields, as indicated by isotherm contours. Moreover, we meticulously investigate the consequences of these parameter shifts on overall heat transfer performance and structural deformation. This examination involves scrutinizing curves that chart the progression of both the mean Nusselt number, local Nusselt number and the displacement field.

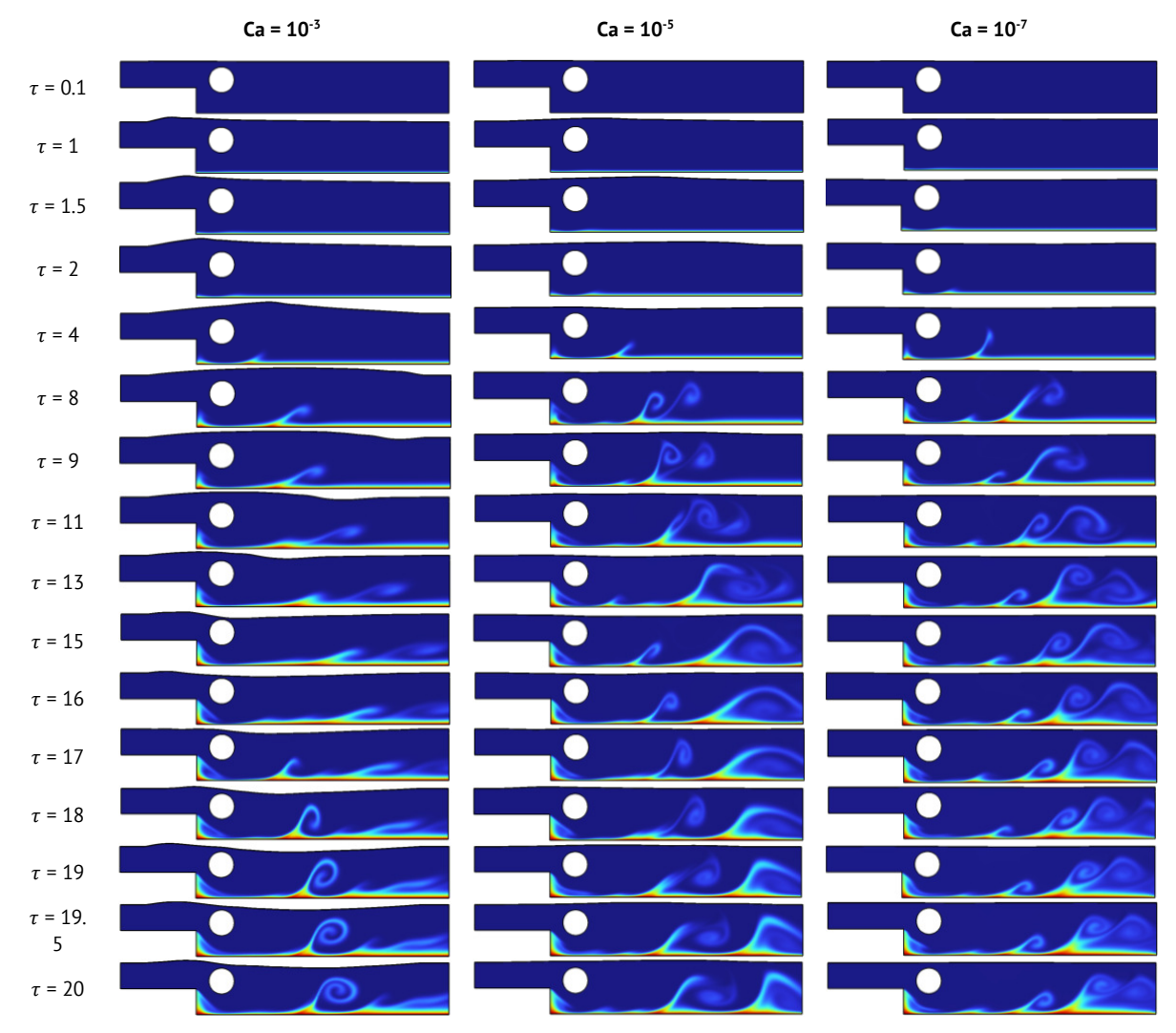


Fig. 5. Development of isotherms with time for Re = 150, Ha = 0, $\gamma = 0^{\circ}$ at $\varphi = 5\%$

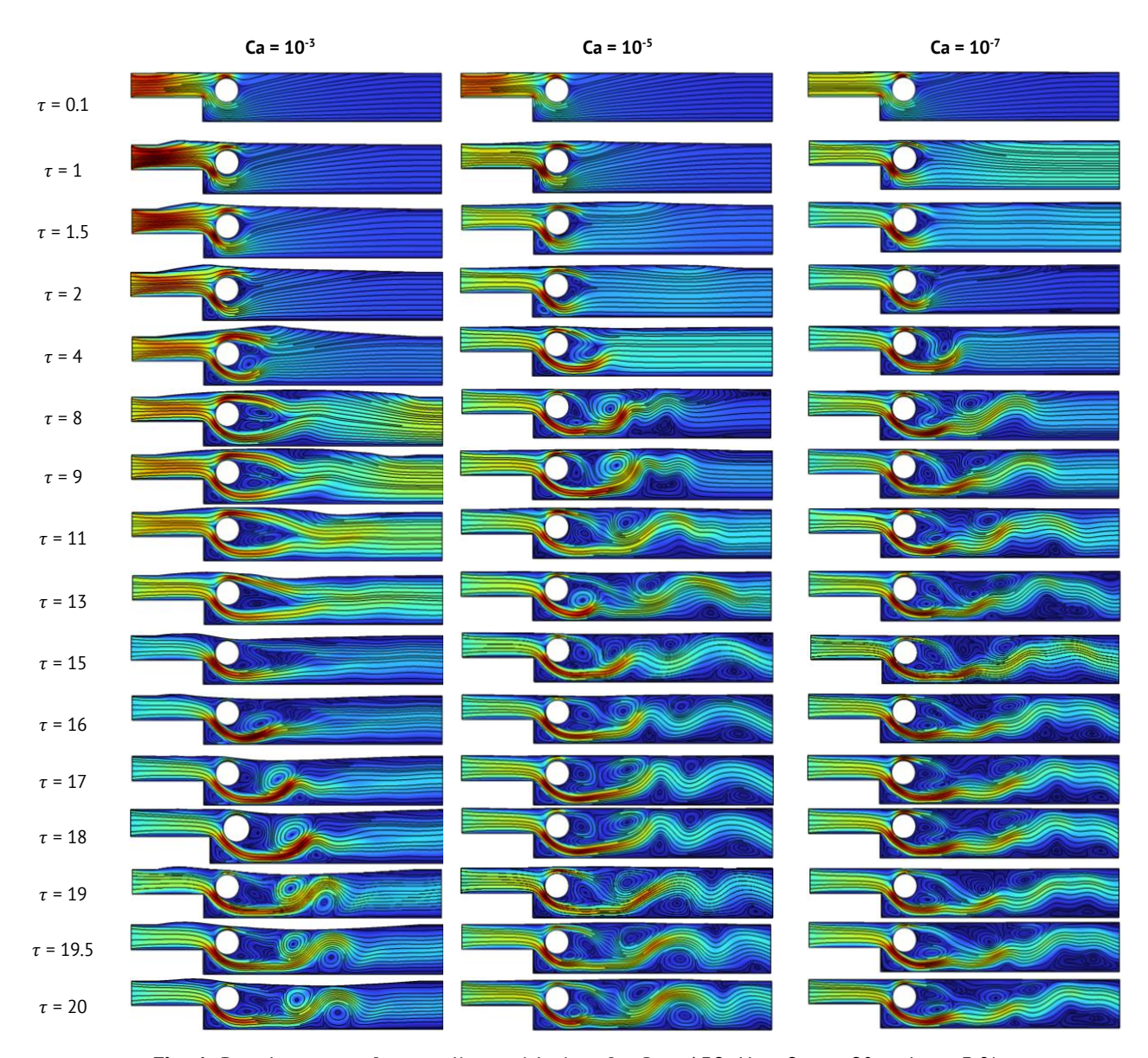


Fig. 6. Development of streamlines with time for Re = 150, Ha = 0, $\gamma = 0^{\circ}$ and $\varphi = 5\%$

Figures 5 and 6 illustrate the variation of isotherms and streamlines as a function of time for distinct values of the Cauchy number, with Re set at 150, Ha = 0, $\gamma = 0^{\circ}$, $\varphi = 5\%$ and Pr at 6.2. During the initial phases (beginning from $\tau = 0$ to 2), the analysis of isotherms unveiled an initial deformation of the elastic top wall, a phenomenon that exhibits a proportional decrease in response to the reduction in the Cauchy number. Concurrently, the streamlines indicated a notable acceleration of flow at the channel entrance, followed by a gradual attenuation as the Cauchy number diminished. These observations can be attributed to variations in viscosity and temperature distribution induced by changes in the Cauchy number. In the subsequent time interval (extending from $\tau = 4$ to 11), a substantial increase in the perturbation of the thermal boundary layer was observed. This disturbance exhibited an amplifying trend in tandem with the decrease in the Cauchy number, resulting in enhanced wall stiffening. Simultaneously, an increase in the deformation of the upper wall was recorded, presenting an inverse proportional relationship with the Cauchy number. These observations collectively suggest a significant correlation between fluid

thermodynamics, wall deformation, and the Cauchy number, underscoring the importance of Multiphysics interactions in this experimental setup. During this same period, the streamlines revealed an increasing formation of vortices downstream of the channel, specifically behind the cylinder. This rise in vortex occurrence appears intrinsically linked to the decrease in the Cauchy number, emphasizing the major influence of this parameter on flow dynamics. In the subsequent time range (commencing from $\tau = 13$ to 16), a significant intensification was observed in both vortex formation and thermal boundary layer perturbation. Notably, a distinct deviation of the elastic upper wall was detected specifically for Cauchy $Ca = 10^{-3}$. This deviation can be attributed to complex forces resulting from magnetohydrodynamic interactions and thermal variations induced by the magnetic field and the Cauchy number. Finally, from $\tau = 17$ onwards, stability emerged in both the isotherms and streamlines, suggesting that the system has reached a state of equilibrium or is converging towards a steady-state. These comprehensive observations highlight the richness of physical phenomena involving fluid-thermal-magnetic interactions and emphasize the need for a profound understanding of the parameters for a complete interpretation of the system's dynamic behavior.

Figures 7 and 8 show the isotherms and streamline contours for various Reynolds and Cauchy numbers, with Ha=0, Pr=10, $\varphi=5$ % and $\gamma=0$ °. As shown in the figures, an increase in the Reynolds number leads to significant agitation within the thermal boundary layer, along with a rise in the number of vortices. Conversely, a decrease in the Cauchy number results in increased disturbance in the thermal boundary layer and a corresponding increase in vortex formation. The relationship between the Reynolds number and the dominance of velocity-related inertial forces over viscous forces is apparent. This dominance leads to faster flow and, consequently, enhanced heat transfer rates. Furthermore, the intensification of vortices with increasing Reynolds number contributes to the augmentation of forced convection within the thermal boundary layer.

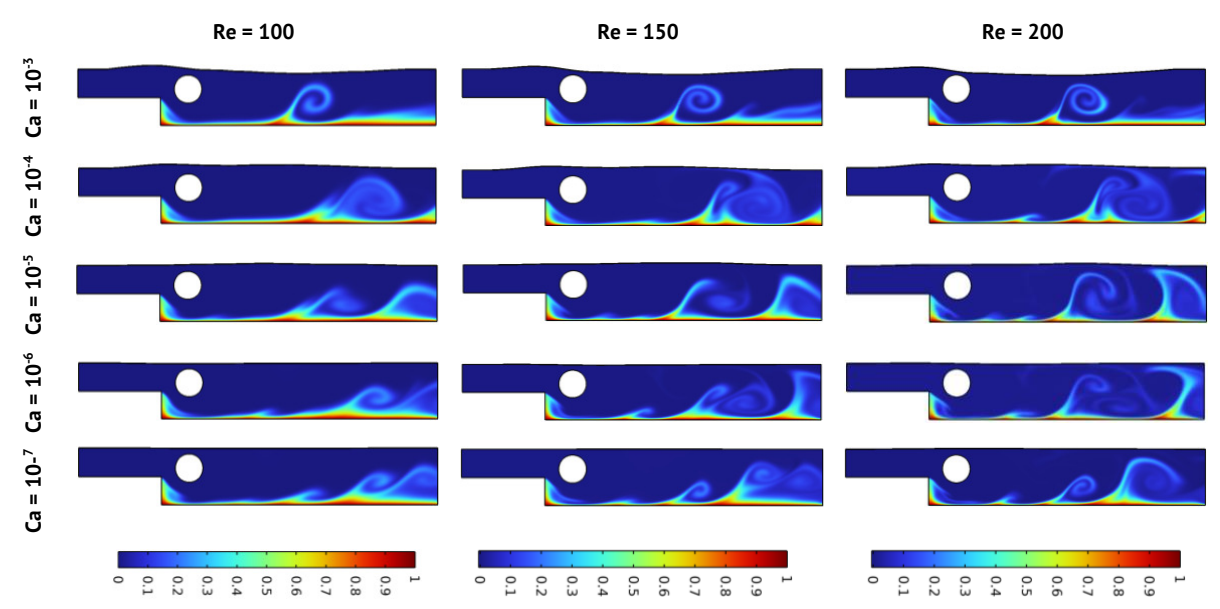


Fig. 7. Effect of Reynolds number *Re* with different values of Cauchy number one isotherms with Ha = 0, Pr = 6.2, $\varphi = 5$ % and $\gamma = 0$ °

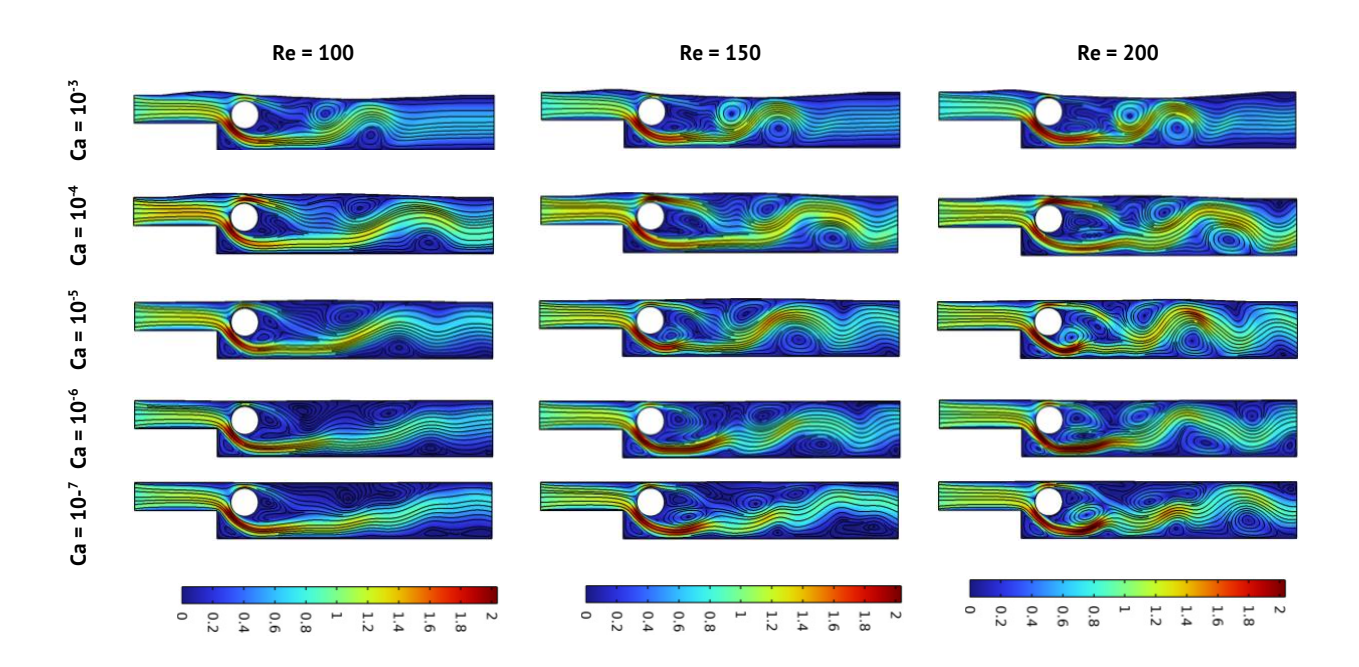


Fig. 8. Effect of Reynolds number *Re* with different values of Cauchy number one Streamlines with Ha = 0, Pr = 6.2, $\varphi = 5$ % and $\gamma = 0$ °

Figure 9 illustrates the variation of the average Nusselt number as a function of Ha for different values of Reynolds number and Cauchy number, with Pr = 6.2, $\varphi = 5$ % and $\gamma = 0$ °. It should be noted that increasing the Reynolds number has a favorable impact on improving the average Nusselt number, as does decreasing the Cauchy number. The increase in Reynolds number results in an intensification of the inertial forces associated with velocity, leading to an acceleration of fluid motion. Consequently, it can be concluded that, as the Reynolds number increases, heat transfer improves, manifested by an increase in the Nusselt number.

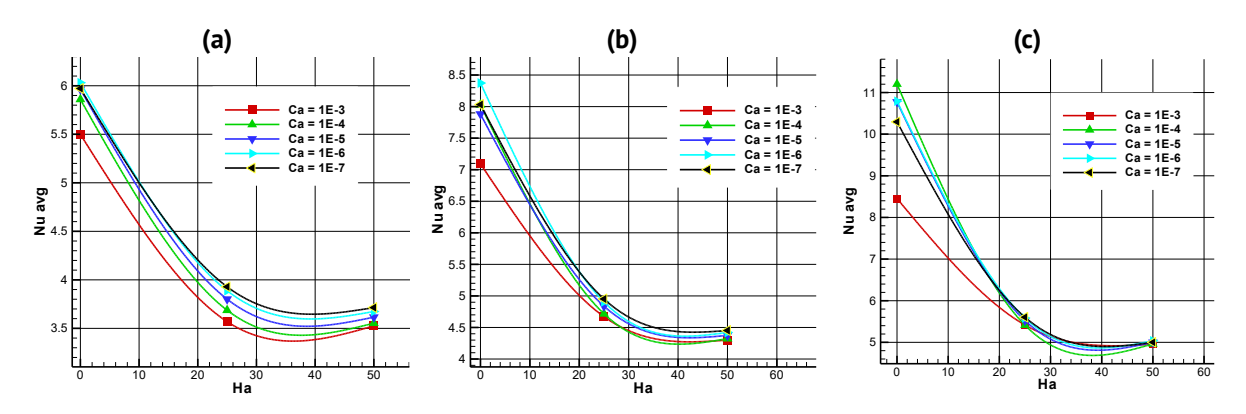


Fig. 9. Effect of Reynolds number Re with different values of Cauchy number one average Nusselt number with Pr = 6.2, $\varphi = 5$ % and $\gamma = 0^{\circ}$: (a) Re = 100; (b) Re = 150, (c) Re = 200

Figure 10 presents the variation of local Nusselt number with Reynolds number along the hot wall for $\gamma = 0^{\circ}$, $\varphi = 5$ %, $Ca = 10^{-4}$ and Ha = 25. By observing the graphs, it is noted that the increase in Reynolds number leads to an increase in the local Nusselt number. The distribution of the local Nusselt number is maximum near the area between X = 3 and X = 5, close to the adiabatic cylinder. Moving away from this area, that is, towards X = 5 and

beyond, the Nusselt number starts to gradually decrease towards the outlet. This distribution is due to the increase in Reynolds number, and thus the inertial forces relative to the viscous forces favor convection phenomena, which are particularly intense in this region where the temperature gradients are most significant. This results in an increase in the local Nusselt number, especially near the adiabatic cylinder.

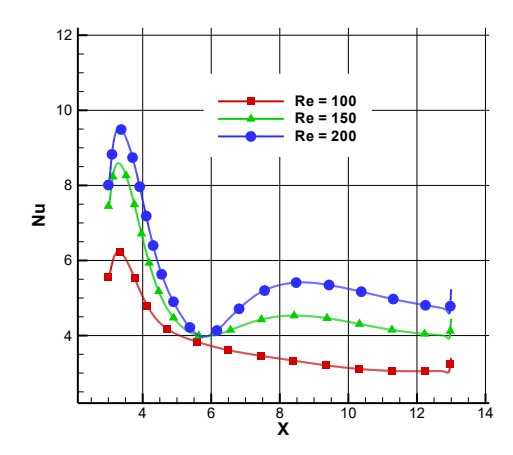


Fig. 10. Effect of Reynolds number on local Nusselt number along the heated wall for $\gamma = 0^{\circ}$, Ha = 25, $Ca = 10^{-4}$ and $\varphi = 5 \%$

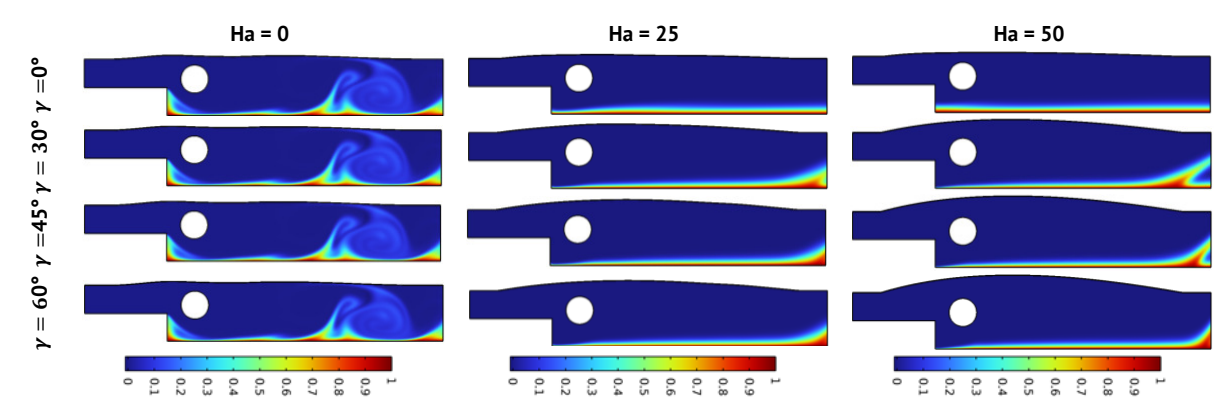


Fig. 11. Effect of Hartmann number Ha with different values of angle of magnetic field inclination one isotherms at Re = 150, $\varphi = 5$ %, $Ca = 10^{-4}$ and Pr = 6.2

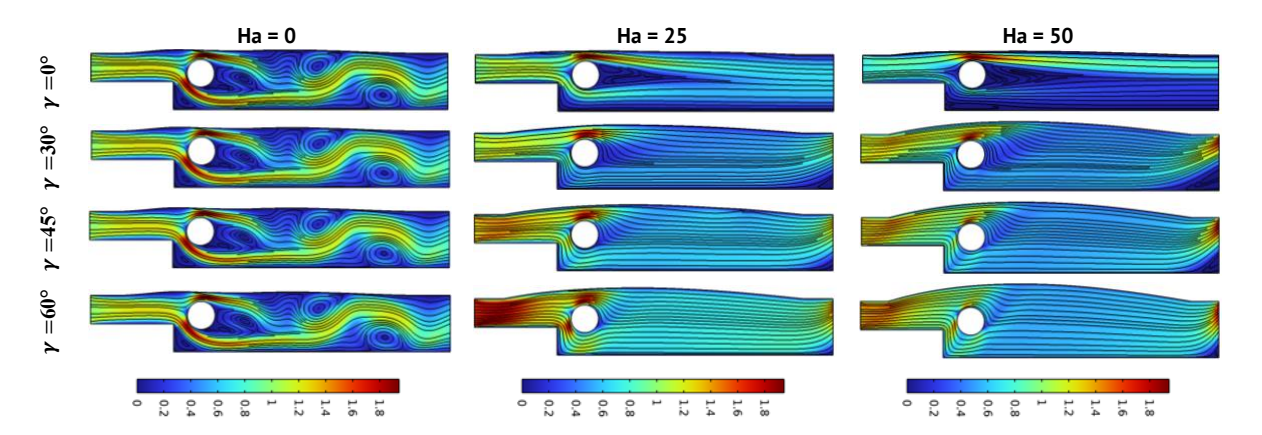


Fig. 12. Effect of Hartmann number Ha with different values of angle of magnetic field inclination one Streamlines at Re = 150, $\varphi = 5$ %, $Ca = 10^{-4}$ and Pr = 6.2

Figures 11 and 12 illustrate the effect of varying the angle of magnetic field inclination on the configuration of isotherms and streamlines for different values of Hartmann number at Re = 150, $\varphi = 5$ %, $Ca = 10^{-4}$ and Pr = 6.2. As mentioned previously, an increase in the Hartmann number leads to a reinforcement of the Lorentz forces, resulting in a slowing down of the fluid motion and increased thermal boundary layer stabilisation near the heated bottom wall.

Concerning the angle of inclination of the magnetic field, variations in this angle had a significant effect on the increase in deformation of the elastic upper wall, with a maximum deformation noted for $\gamma = 60^{\circ}$ and Ha = 50. For the isotherms, an increase in the thickness of the thermal boundary layer is observed as the angle of inclination increases. Regarding the streamlines, an acceleration of the flow at channel entry is noted as the y number increases.

These behaviours can be explained by the positive impact of the inclination of the magnetic field on the enhancement of forced convection, leading to a gain in heat transfer rate and an overall improvement in the process.

Figure 13 illustrates the impact of varying the angle of magnetic field inclination on the average Nusselt number as a function of the Hartmann number, under specific conditions Re set at 150, Ca at 10^{-4} , Pr at 10, and at φ = 5 %. Upon analyzing the average Nusselt curves, a progressive improvement in this parameter is evident as the angle of inclination increases, signifying an enhancement in heat transfer efficiency. This improvement can be attributed to the favorable influence of the inclination angle on the promotion of convective heat transfer within the fluid domain. The inclined magnetic field disrupts stagnant fluid regions, enhancing the overall heat transfer process and resulting in the observed increase in the average Nusselt number.

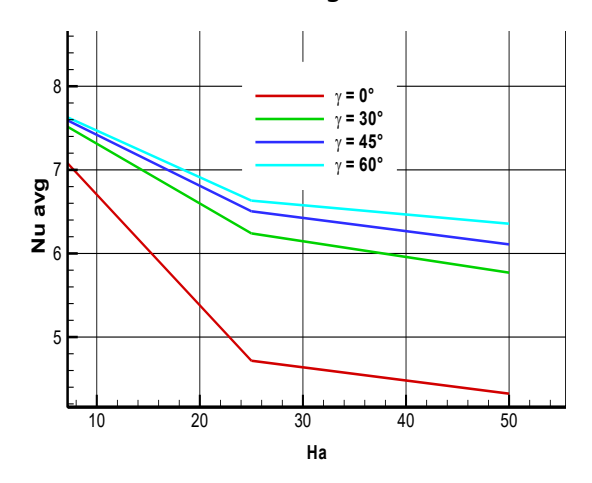
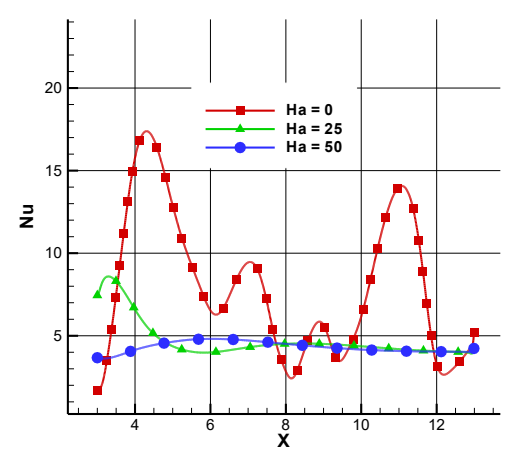


Fig. 13. Effect of Hartmann number Ha with different values of angle of magnetic field inclination one average Nusselt number for Re = 150, Ha = 25, $Ca = 10^{-4}$ and $\varphi = 5\%$

Figure 14 illustrates the impact of a growing magnetic field (reflected by the increasing Hartmann number) on heat transfers at the hot wall for a flow characterized by a Reynolds number of 150. A clear trend of decreasing local Nusselt number is observed. This evolution is attributable to the intensification of Lorentz forces, which act as a resistive force opposing the fluid's motion. This braking action induces a reduction in velocity and temperature fluctuations within the fluid, resulting in a stabilized thermal

boundary layer. A more stable thermal boundary layer is less conducive to intense heat exchanges, hence the decrease in the local Nusselt number.

Figure 15 shows the evolution of the local thermal transfer coefficient (Nusselt number) along the hot wall for a flow characterized by a Reynolds number of 150 and a Hartmann number of 25, depending on the inclination of the magnetic field. We observe an increasing trend in the local Nusselt number as the inclination angle of the magnetic field increases. This increase can be explained by the fact that a greater inclination of the magnetic field intensifies the Lorentz forces induced in the fluid, stimulating fluid movements and enhancing heat exchanges at the wall.



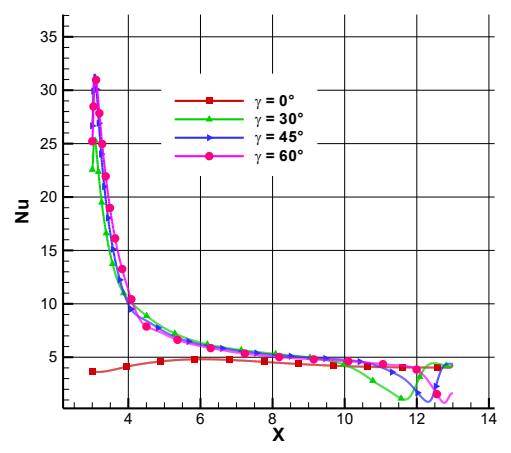


Fig. 14. Effect of Hartmann number on local Nusselt number along the heated wall for Re = 150, Ha = 25, $Ca = 10^{-4}$ and $\varphi = 5\%$

Fig. 15. Effect of magnetic field inclination on local Nusselt number along the heated wall for Re = 150, Ha = 25, $Ca = 10^{-4}$ and $\varphi = 5$ %

Figures 16 and 17 demonstrate the influence of varying the concentration of nanoparticles of Fe₃O₄ on the flow configuration as a function of the Hartmann number, for given parameters such as Re = 150, $Ca = 10^{-4}$, Pr = 6.2 and $\gamma = 0^{\circ}$. The observation shows that the variation in the Hartmann number has a significant influence on the configuration of the isotherms and streamlines compared with the variation in the concentration of the ferrofluid.

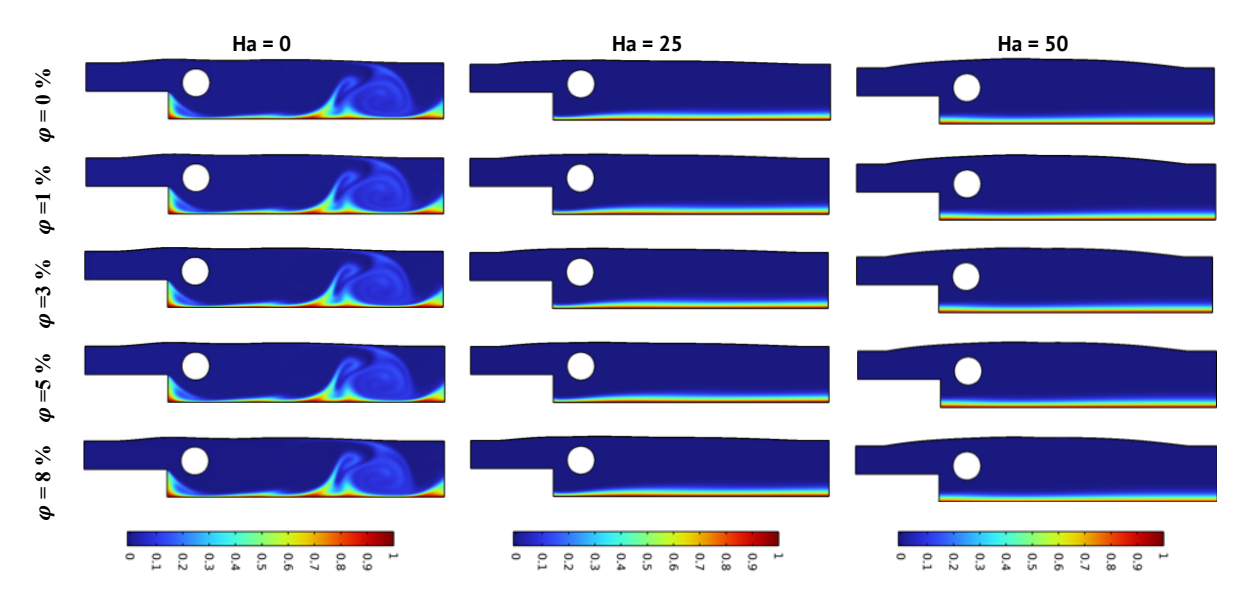


Fig. 16. Effect of nanoparticles concentration φ with different values of Hartmann number at Re = 150, $Ca = 10^{-4}$, Pr = 6.2 and $\gamma = 0^{\circ}$

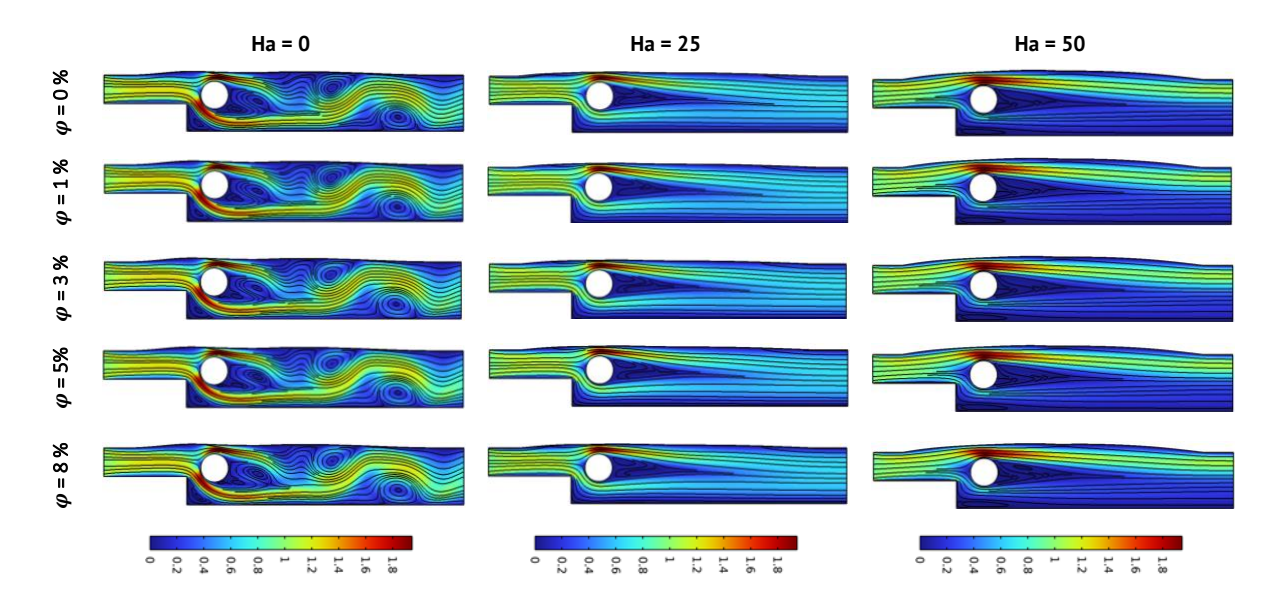


Fig. 17. Effect of nanoparticles concentration φ with different values of Hartmann number at Re = 150, $Ca = 10^{-4}$, Pr = 6.2 and $\gamma = 0^{\circ}$

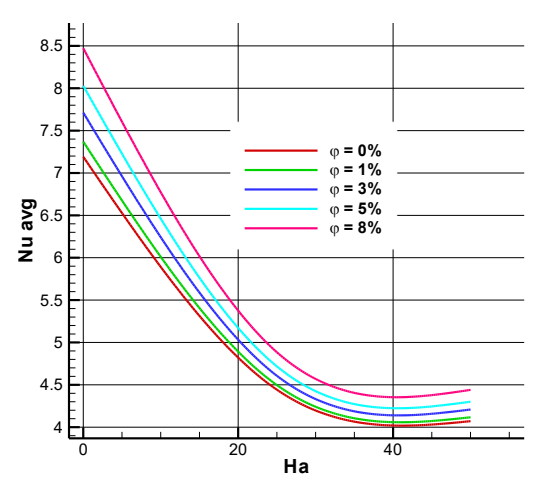


Fig. 18. Effect of ferrofluid concentrations on average Nusselt number along the heated wall for Re = 150, Ha = 25, $Ca = 10^{-4}$ and $\gamma = 0^{\circ}$

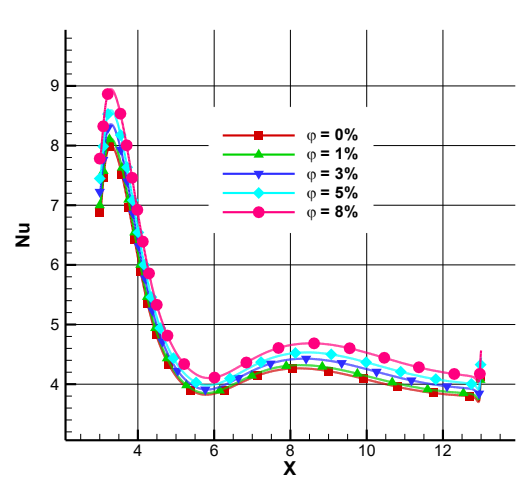


Fig. 19. Effect of ferrofluid concentrations on local Nusselt number along the heated wall for Re = 150, Ha = 25, $Ca = 10^{-4}$ and $\gamma = 0^{\circ}$

Figure 18 shows the variation of the average Nusselt number as a function of Hartmann number for different ferrofluid concentrations, with defined parameters such as Re = 150, $Ca = 10^{-4}$, Pr = 6.2, and $\gamma = 0^{\circ}$. Examining the average Nusselt curves, it is observed that increasing the ferrofluid concentration has a positive effect on the improvement of the average Nusselt number. This can be attributed to the increase in conductive heat transfer, because incorporating nanoparticles into a base fluid increases the thermal conductivity of the fluid, leading to an improvement in heat transfer compared to the pure fluid.

Figure 19 displays the evolution of the local thermal transfer coefficient along the hot wall for a flow characterized by a Reynolds number of 150, γ =0°, Ca = 10⁻⁴ and a Hartmann number of 25, depending on the nanoparticle concentration. A positive correlation is observed between the nanoparticle concentration and the local Nusselt

number. Increasing the nanoparticle concentration enhances the fluid's effective thermal conductivity, resulting in an increased local thermal transfer coefficient.

Figure 20 shows the variation in elastic top wall deformation as a function of Cauchy number, for different Reynolds number values at Ha = 0, $\varphi = 5$ %, $\gamma = 0$ ° and Pr = 6.2. The observations reveal an inverse relationship between the deformation of the elastic top wall and the two parameters considered. An increase in Reynolds number is associated with an increase in deformation, suggesting enhanced forced convection and flow acceleration. On the other hand, a decrease in Cauchy number leads to a reduction in deformation, which can be attributed to the increase in wall resistance to deformation resulting from the decrease in this parameter.

Figure 21 shows the impact of varying the Hartmann number (Ha) on the deformation of the elastic top wall, for different values of the Cauchy number at Re = 150, γ =0°, φ = 5 % and Pr = 6.2. It should be noted that the rise in magnetic force, reflected by the increase in Ha number, exerts a favorable influence on the increase in deformation. Corresponding to previous observations, the reduction in the Cauchy number indicates a strengthening of the wall's resistance to deformation, resulting in a reduction in said deformation.

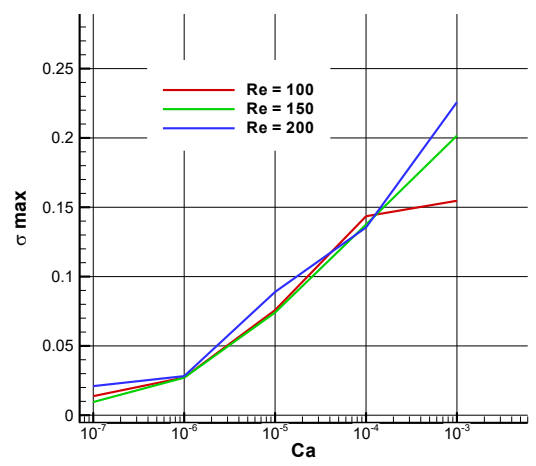


Fig. 20. Variation in elastic top wall deformation as a function of Cauchy number, for different Reynolds number at Ha = 0, $\varphi = 5$ %, $\gamma = 0$ ° and Pr = 10

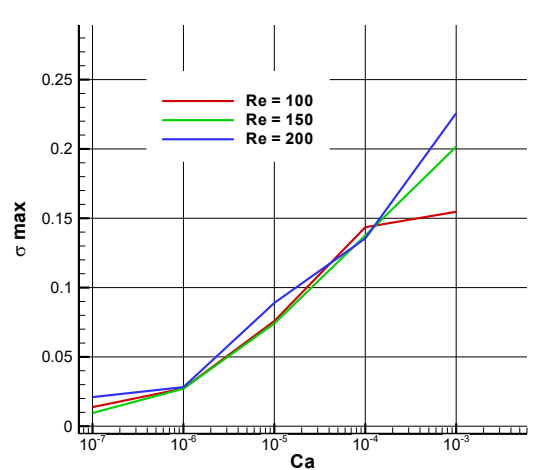


Fig. 21. Variation in elastic top wall deformation as a function of Cauchy number, for different Hartmann number at Re = 150, $\gamma = 0^{\circ}$, $\varphi = 5 \%$

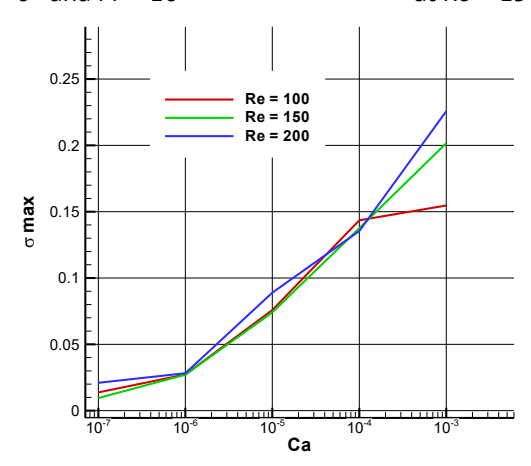


Fig. 22. Variation of elastic top wall deformation as a function of magnetic field inclination angle for various values of Hartmann number at Re = 150, $\varphi = 8$ %, $Ca = 10^{-4}$ and Pr = 6.2

Figure 22 shows the variation in elastic top wall deformation as a function of magnetic field inclination angle, for various values of Hartmann number (Ha), with defined parameters such as Re = 150, $\varphi = 8$ %, $Ca = 10^{-4}$ and Pr = 6.2. It should be noted that increasing Ha and γ parameters influence elastic wall deformation positively. Specifically, maximum deformation is observed at an angle of inclination of 60 % degrees and a Hartmann number of 50.

Conclusions

We have conducted a numerical investigation of forced convective laminar flow over a two-dimensional downward step, involving an elastic upper wall interacting with a stationary cylinder of fixed diameter. To unravel this complex phenomenon, we employed the Galerkin finite element method, enhanced by a multigrid technique, and explored a wide range of parameters. Our findings, when compared to previous studies, provide novel insights into these fluid-structure interactions.

An increase in the Reynolds number and a decrease in the Cauchy number intensify vortex formation and disrupt the thermal boundary layer, thereby enhancing forced convective heat transfer. An increase in the Hartmann number decelerates the flow and stabilizes the thermal boundary layer, while a magnetic field inclination angle of 60° intensifies the deformation of the elastic wall and improves forced convective heat transfer.

Increasing the magnetic field inclination angle and the concentration of nanoparticles enhances heat transfer, as evidenced by an increase in the average Nusselt number, promoting convection and fluid thermal conductivity.

A decrease in the local Nusselt number is attributed to the intensification of Lorentz forces, which inhibit fluid flow and stabilize the thermal boundary layer, whereas an increase in the magnetic field inclination and nanoparticle concentration stimulates fluid motion and improves heat transfer.

CRediT authorship contribution statement

Hanaa Derraz (writing – review & editing, writing – original draft; Mohamed Bouzit (supervision; Atika Bencherif (data curation.

Conflict of interest

The authors declare that they have no conflict of interest.

References

- 1. Hussain S, Öztop HF. Impact of inclined magnetic field and power law fluid on double diffusive mixed convection in lid-driven curvilinear cavity. *International Communications in Heat and Mass Transfer*. 2021;127(11): 105549.
- 2. Kherbeet ASh, Mohammed HA, Munisamy KM, Salman BH. The effect of step height of microscale backward-facing step on mixed convection nanofluid flow and heat transfer characteristics. *International Journal of Heat and Mass Transfer*. 2014;68: 554–566.
- 3. Mobadersani F, Rezavand Hesari A .Magneto Hydrodynamic Effect on Nanofluid Flow and Heat Transfer in Backward-Facing Step Using Two-Phase Model. *AUT Journal of Mechanical Engineering*. 2020;4(1): 51–66.
- 4. Al-Aswadi AA, Mohammed H, AShuaib NH, Campo A. Laminar forced convection flow over a backward-facing step using nanofluids. *International Communications in Heat and Mass Transfer*. 2010;37(8): 950–957.

- 5. Turkyilmazoglu M. Nanofluid flow and heat transfer due to a rotating disk. *Computers & Fluids*. 2014;94: 139–146. 6. Selimefendigil F, Öztop HF. Identification of forced convection in pulsating flow at a backward facing step with a stationary cylinder subjected to nanofluid. *International Communications in Heat and Mass Transfer*. 2013;45: 111–121.
- 7. Moosavi R, Moltafet R, Lin CX, Chuang PYA. Numerical modeling of fractional viscoelastic non-Newtonian fluids over a backward facing step Buoyancy driven flow and heat transfer. *Thermal Science and Engineering Progress*. 2021;21:100767.
- 8. Hussain S, Ahmed SE. Unsteady MHD forced convection over a backward facing step including a rotating cylinder utilizing Fe₃O₄-water ferrofluid. *Journal of Magnetism and Magnetic Materials*. 2019;484: 356–366.
- 9. Toumi M, Bouzit M, Bouzit F, Mokhefi A. MHD forced convection using ferrofluid over a backward facing step containing a finned cylinder. *Acta Mechanica et Automatica*. 2022;16(1): 70–81.
- 10. Kumar S, Vengadesan S. The effect of fin oscillation in heat transfer enhancement in separated flow over a backward facing step. *International Journal of Heat and Mass Transfer*. 2019;128: 954–963.
- 11. Nie JH, Chen YT, Hsieh HT. Effects of a baffle on separated convection flow adjacent to backward-facing step. *International Journal of Thermal Sciences*. 2009;48(3): 618–625.
- 12. Lan H, Armaly BF, Drallmeier JA. Three-dimensional simulation of turbulent forced convection in a duct with backward-facing step. *International Journal of Heat and Mass Transfer*. 2009;52(7–8): 1690–1700.
- 13. Erturk E. Numerical solutions of 2-D steady incompressible flow over a backward-facing step, Part I: High Reynolds number solutions. *Computers & Fluids*. 2008;37(6): 633–655.
- 14. Mohammed HA, Fathinia F, Vuthaluru HB, Liu S. CFD-based investigations on the effects of blockage shapes on transient mixed convective nanofluid flow over a backward facing step. *Powder Technology*. 2019;346: 441–451.
- 15. Abu-Nada E. Application of nanofluids for heat transfer enhancement of separated flows encountered in a backward facing step. *International Journal of Heat and Fluid Flow.* 2008;29(1): 242–249.
- 16. Kherbeet ASh, Mohammed HA, Salman BH. The effect of nanofluids flow on mixed convection heat transfer over microscale backward-facing step. *International Journal of Heat and Mass Transfer*. 2012;55(21–22): 5870–5881.
- 17. Nath R, Krishnan M. Numerical study of double-diffusive mixed convection in a backward-facing step channel filled with Cu-water nanofluid. *International Journal of Mechanical Sciences*. 2019;153–154: 48–63.
- 18. Lv J, Hu C, Bai M, Li L, Shi L, Gao D. Visualization of SiO₂-water nanofluid flow characteristics in backward-facing step using PIV. *Experimental Thermal and Fluid Science*. 2019;101: 151–159.
- 19. Xie WA, Xi GN, Zhong MB. Effect of the vortical structure on heat transfer in the transitional flow over a backward-facing step. *International Journal of Refrigeration*. 2017;74: 465–474.
- 20. Hilo A K, Iborra A A, Sultan M T H and Hamid M F A. Experimental study of nanofluids flow and heat transfer over a backward-facing step channel. *Powder Technology*. 2020;372: 497–505.
- 21. Selimefendigil F, Öztop HF. Influence of inclination angle of magnetic field on mixed convection of nanofluid flow over a backward facing step and entropy generation. *Advanced Powder Technology*. 2015;26(6): 1663–1675.
- 22. Hussain S, Ahmed SE, Akbar T. Entropy generation analysis in MHD mixed convection of hybrid nanofluid in an open cavity with a hori zontal channel containing an adiabatic obstacle. *International Journal of Heat and Mass Transfer*. 2017;114: 1054–1066.
- 23. Yagoub M, Saeed Z H. Thermophysical characteristics and forced convective heat transfer of ternary doped magnetic nanofluids in a circular tube: An experimental study. *Case Studies in Thermal Engineering*. 2023;52: 103748. 24. Yoon HS, Seo JH, Kim JH. Laminar forced convection heat transfer around two rotating side-by-side
- circular cylinder. *International Journal of Heat and Mass Transfer*. 2010;53(21–22): 4525–4535.
- 25. Sarkar S, Ganguly S, Biswas G, Saha P. Effect of cylinder rotation during mixed convective flow of nanofluids past a circular cylinder. *Computers & Fluids*. 2016;127: 47–64.
- 26. Xie WA, Xi GN. Flow instability and heat transfer enhancement of unsteady convection in a step channel. *Alexandria Engineering Journal*. 2022;61(9): 7377–7391.
- 27. Toumi M, Bouzit M, Mokhefi A, Derbal D. Unsteady numerical investigation of ferrofluid forced convection over a downward step containing a rotating finned cylinder. *Journal of the Serbian Society for Computational Mechanics*. 2022;16(2): 67–86.
- 28. Hussein AK, Bakier MA, Ben Hamida MB, Sivasankaran S. Magneto hydrodynamic natural convection in an inclined T-shaped enclosure for different nanofluids and subjected to a uniform heat source. *Alexandria Engineering Journal*. 2016;55(3): 2157–2169.
- 29. Selimefendigil F, Öztop HF. Effect of a rotating cylinder in forced convection of ferrofluid over a backward facing step. *International Journal of Heat and Mass Transfer*. 2014;71: 142–148.

- 30. Geridönmez BP, Öztop HF. Effects of inlet velocity profiles of hybrid nanofluid flow on mixed convection through a backward facing step channel under partial magnetic field. *Chemical Physics*. 2021;540: 111010.
- 31. Sheikholeslamia M, Hayatb T, Alsaedi A. Numerical simulation for forced convection flow of MHD CuO-H2O nanofluid inside a cavity by means of LBM. *Journal of Molecular Liquids*. 2018;249: 941–948.
- 32. Selimefendigil F, Öztop HF. Forced convection of nanofluid in double vented cavity system separated by perforated conductive plate under magnetic field. *Engineering Analysis with Boundary Elements*. 2023;149: 18–26.
- 33. Al-Amir QR, Hamzah HK, Ali FH, Bayraktar S, Arici M, Hatami M. Comparison study of vertical and horizontal elastic wall on vented square enclosure filled by nanofluid and hexagonal shape with MHD effect. *The European Physical Journal Special Topics*. 2022;231: 2623–2643.
- 34. Selimefendigil F, Öztop HF, Abu-Hamdeh N. Impacts of conductive inner L shaped obstacle and elastic bottom wall on MHD forced convection of a nanofluid in vented cavity. *Journal of Thermal Analysis and Calorimetry*. 2020;141: 465–482.
- 35. Sheikholeslami M, Keramati H, Shafeed A, Li Zh, Alawad OA, Tlili I. Nanofluid MHD forced convection heat transfer around the elliptic obstacle inside a permeable lid drive 3D enclosure considering lattice Boltzmann method. *Physica A: Statistical Mechanics and its Applications*. 2019;523; 87–104.
- 36. Ahmed Sh, Hossain A, Zahangir Hossain Md, Mamun Molla Md. Forced convection of non-Newtonian nanofluid in a sinusoidal wavy channel with response surface analysis and sensitivity test. *Results in Engineering*. 2023;19: 101360.
- 37. Derikvand M, Solari MSh, Toghraie D. Entropy generation and forced convection analysis of ethylene glycol/MWCNTs-Fe₃O₄ non-Newtonian nanofluid in a wavy microchannel with hydrophobic surfaces. *Journal of the Taiwan Institute of Chemical Engineers*. 2023;143: 104707.
- 38. Ghasemi K, Siavashi M. Three-dimensional analysis of magnetohydrodynamic transverse mixed convection of nanofluid inside a lid-driven enclosure using MRT-LBM. *International Journal of Mechanical Sciences*. 2022;165: 105199.
- 39. Jamshed W, Eid MR, Hussain SM, Abderrahmane A, Safdar R, Younis O, Pasha AA. Physical specifications of MHD mixed convective of Ostwald-de Waele nanofluids in a vented-cavity with inner elliptic cylinder. *International Communications in Heat and Mass Transfer.* 2022;134: 106038.
- 40. Hamzah HK, Al-Amir QR, Abdulkadhim A, Ahmed SY, Ali FH, Abed AM, Abed IM. In a Vented Square Enclosure, the Effect of a Flexible Baffle Attached to a Solid Cylinder on Mixed Convection. *Arabian Journal for Science and Engineering*. 2022;47: 15489–15504.
- 41. Derraz H, Bouzit M, Mokhfi A, Bencherif A, Toumi M. Numerical study of natural convection of Bingham fluid using a flexible fin. *International Journal of Thermofluid Science and Technology*. 2024;11(2): 110202.

Appendix A. Nomenclature

B ₀ D _s	Magnetic field strength, Tesla dimensionless displacement vector	Greek symbols $oldsymbol{\phi}$ nanoparticle concentratio					
Н	heat transfer coefficient, W/m ² K	α	thermal diffusivity, m ² /s				
На	Hartmann number, $B_0 H \sqrt{rac{\sigma_{nf}}{\mu_{nf}}}$	β	expansion coefficient, 1/K				
K	thermal conductivity, W/m K	γ	inclination angle of magnetic field				
Н	inlet step height, m	θ	dimensionless temperature, $\frac{T-T_c}{T_h-T_c}$				
n	normal coordinate	ν	kinematic viscosity, m2/s				
Nu	Local Nusselt number	ρ	density of the fluid, kg/m ³				
Nu _{avg}	averaged Nusselt number	$oldsymbol{\sigma}^*$	the solid stress tensor				
p	pressure, Pa	μ	dynamic viscosity, N s/m ²				
P	non-dimensional pressure	τ	dimensionless time				
Pr	Prandtl number, $\frac{v_f}{\alpha_f}$		Subscripts				
Re	Reynolds number, $\frac{H\overline{u}}{v_f}$	C	cold				
Т	temperature, K	h	hot				
C p	thermal specific heat, J/Kg K	avg	average				
Ca	Cauchy number	nf	nanofluid				
u, v	x-y velocity components, m/s	f	fluid				
U, V	dimensionless velocity components	S	solid				
x, y	Cartesian coordinates, m						
X, Y	dimensionless coordinates						
t	time						
\overline{u}	average velocity, m s ⁻¹						

Submitted: November 24, 2024 Revised: April 4, 2025 Accepted: May 12, 2025

Effect of loading on tribotechnical characteristics of antifriction diamond-bearing mineral ceramics

A.N. Bolotov , O.O. Novikova [™], V.V. Novikov

Tver State Technical University, Tver, Russia

[™] onvk@mail.ru

ABSTRACT

A calculation and experimental analysis of tribotechnical properties of a pair of materials diamond-bearing mineral ceramics – ceramics in a wide range of loads are shown. The molecular-mechanical theory of friction was used for the analysis. It also accepted a linear-elastic nature of microroughness contact after running in in a steady-state mode. A criterion that determines the change in deformation behavior is the load which creates an average elastic pressure on a contact spot equal to material microstrength. Using both theoretical and experimental approaches, we determined the critical nominal pressure and friction coefficient depending on physical and mechanical constants of materials and friction surface profile parameters.

KEYWORDS

diamond-bearing ceramics • antifriction properties • contact interaction model • microstrength • friction • wear

Citation: Bolotov AN, Novikova OO, Novikov VV. Effect of loading on tribotechnical characteristics of antifriction diamond-bearing mineral ceramics. *Materials Physics and Mechanics*. 2025;53(2): 104–112. http://dx.doi.org/10.18149/MPM.5322025_9

Introduction

One of the directions for creating innovative tribounits is using ceramic elements as parts involved in direct friction contact. In addition to high tribotechnical properties of ceramics, there are unique temperature, anticorrosion, and electrical characteristics. Ceramic composite materials with high-strength, wear-resistant properties of the matrix supplemented by abrasive or antifriction fillers' characteristics are especially promising [1,2].

Graphite, molybdenum disulfide or polymeric materials are typically used as fillers with low shear resistance for composite materials of friction units that operate under conditions of lubricant deficiency. Recent scientific studies pay special attention to another allotropic form of graphite - diamond as an antifriction component of a ceramic matrix [3–7]. Most authors emphasize the complexity of forming oxide mineral ceramic diamond-containing materials. This is due to the sensitivity of diamond to oxidation at relatively high temperatures. However, the controlled degree of diamond graphitization during composite preparation and friction process leads to a synergetic effect of creating a highly solid and wear-resistant tribo-surface with a given gradient of friction properties [3,5].

During the research, we obtained a mineral ceramic material, which is a matrix of aluminum oxides of α -, β -, and γ -modifications with incorporated dispersed diamond grains [8,9]. We have developed a technology which assumes that the first stage of material production involves sintering of a dispersed aluminum and diamond billet. Then billet's surface layer is modified by microplasma electrolytic oxidation. The formed part combines physical and mechanical properties of an aluminum matrix, i.e. the base and



tribotechnical properties of a ceramic hardened layer with partially graphitized dispersed diamonds. Preliminary results show that when a ceramic base is alloyed with diamonds with a grit < 20/14, mineral ceramic material has good antifriction properties while lubricant is in short supply or even absent [8].

Some results show that the obtained diamond-bearing mineral ceramic material (DBMC) has consistently low values of triboparameters in a sufficiently large pressure range. However, the wear intensity increases sharply with further increase of contact pressure. We obtained similar conclusions for composite coatings hardened with synthetic diamonds and electrocorundum [10] and diamond-like coatings [11]. We can assume that certain loads cause a change in the wear type of such materials. If we establish the rational load area for mineral ceramic materials of dry friction units, the trouble-free period of tribounit operation might be significantly extended.

A lot of research has analyzed wear of ceramic materials [12-15]. The most widely accepted theoretical models are based on linear elastic fracture mechanics and Weibull statistics [12,13,16,17]. The nature of wear of ceramic diamond-bearing materials has been studied to a much lesser extent [18-21]. This is due to the innovativeness of the technologies for obtaining diamond mineral ceramics; the friction characteristics of the composite material are determined by the emergent nature of its constituent structural components. The results presented in [18] show the linear-elastic nature of wear of diamond-bearing ceramic tools. They also show the adequacy and correctness of the fatique failure and wear mechanisms for the working layer of such materials. Elastic interaction is the most typical mechanism, even in calculating diamond-abrasion parameters [18,21]. Depending on matrix and counter-surface material properties, we propose applying mathematical models for elastic, brittle or elastic-plastic contact, as well as using criteria for transition from one interaction type to another. The analysis of the tribosurface morphology of mineral-ceramic material (ceramic control sample) after tests did not reveal plastic deformation in a steady-state mode and in the subcritical loading area [8,22]. We can assume that the elastic behavior of material deformation during friction is replaced by its brittle destruction while diamond grains are simultaneously removed with a part of the surrounding ceramic matrix.

In case of brittle fracture materials (including diamond-bearing composite materials with ceramic matrix), critical stress is bending strength, microhardness, microstrength, etc. [12,18,23,24]. For composite materials, it is necessary to consider the influence of the dimensional effect of discrete components on micromechanical properties. In [23], it is shown the validity of applying strength characteristics obtained by indentation using a microhardness tester to describe the properties of materials with particle discreteness from 250 to 400 μ m. It also notes how informative the microstrength index for evaluating a brittle fracture area.

Earlier in [22], we proposed a model of elastic contact interaction between surfaces of mineral ceramics and ceramics. However, we have not yet investigated deformation processes in the case of brittle fracture. It is also necessary to conduct additional tribotechnical tests to confirm the validity of the selected models and assumptions made. The purpose of the present work is to evaluate tribocontact properties in a wide range of loads based on the model of contact interaction between a pair of materials: diamond-bearing mineral ceramics and ceramics.

Problem statement

The molecular-mechanical theory of friction was used for calculating the friction parameters [25–27]. The model should take into account the physical and mechanical properties of materials diamond-bearing mineral ceramics – ceramics, their microgeometry and loading conditions. Let us assume that the microroughness contact after running-in in the steady-state mode has linear-elastic nature. At critical overloading, brittle fracture of mineral ceramic material prevails.

We take a load that creates an average elastic pressure on the contact spot as a criterion determining the change in deformation behavior. The average elastic pressure on the contact spot is equal to the material microstrength σ [23]. Microstrength corresponds to the stress required to form a brittle fracture unit area.

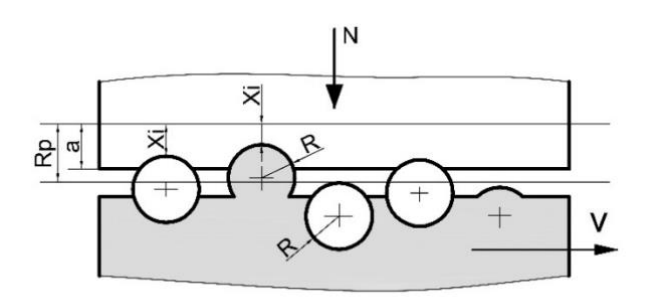


Fig. 1. Contact of a rough half-space made of a ceramic matrix with distributed diamond grains

We consider the contact interaction between a rough half-space made of a ceramic matrix with distributed diamond grains with volume density τ and a rough half-space of a control sample (Fig. 1). The size of diamond grains correlates with matrix microroughnesses. This fact allows modeling the composite material surface as spherical segments of the same radius R [25,28]. Let us introduce the concepts of an equivalent surface and a bearing curve. Due to the thickness of the diamond-bearing ceramic layer, we can ignore the substrate material influence and use Hertz's formulas [29] to determine single microroughness contact characteristics. We assume that the mutual influence of microroughnesses is negligible [25,26].

Solution method

The load in the contact zone consists of normal forces perceived by matrix irregularities and protruding diamond grains:

$$N = \tau \int_0^a N_{i \text{ aK}}(a_i) \, n'(x) dx + (1 - \tau) \int_0^a N_{i \text{ cK}}(a_i) \, n'(x) dx,$$

$$n(x) = \frac{t_m v A_a}{2p_R R_p^y} x^{y-1},$$
(1)

where $N_{i\,\mathrm{ak}}(a_i)$ and $N_{i\,\mathrm{ck}}(a_i)$ are the load acting on a diamond grain and matrix microroughness, respectively, n(x) is a protrusion distribution function that shows the number of protrusions with tops located above the level x, v, R_p , t_m are roughness parameters of the interacting surfaces [25,28], A_a is a nominal contact area.

We consider that $a_i = a - x$ and apply Hertz formulas to determine the characteristics of elastic contact of unit spherical irregularities. Thus, we obtain an equation for calculating the nominal pressure in the elastic contact area:

$$q_{ay} = \frac{N}{A_a} = \frac{t_m \nu (\nu - 1) a^{\nu + 0.5} K_3}{1.5 p R_p^{\nu}} \left(\frac{\tau}{I_a} + \frac{(1 - \tau)}{I_c} \right), \tag{2}$$

where K_3 is a coefficient that characterizes the bearing curve [28], $I_{\rm a}=\frac{1-\mu_{\rm a}^2}{E_{\rm a}}+\frac{1-\mu_{\rm k}^2}{E_{\rm k}}$ and $I_{\rm c}=\frac{1-\mu_{\rm c}^2}{E_{\rm c}}+\frac{1-\mu_{\rm k}^2}{E_{\rm k}}$ are the elastic constants of a diamond–counter sample and a bond–counter sample contact, respectively; $E_{\rm a}$, $E_{\rm c}$, $E_{\rm k}$ are the elastic moduli of diamond, matrix and counter sample materials, μ_a , μ_c , μ_k are Poisson's coefficients of diamond, ceramic matrix (bond) and counter sample materials. We express the elastic convergence of the contacting surfaces from Eq. (2):

$$a_{y} = R_{p} \left[\frac{1.5\pi q_{a} I_{e}}{t_{m} \nu (\nu - 1) K_{3}} \left(\frac{R}{R_{p}} \right)^{0.5} \right]^{\frac{1}{\nu + 0.5}}, \tag{3}$$

where $I_e = \left(\frac{I_a I_c}{\tau I_c + (1 - \tau)I_a}\right)$ is an equivalent elastic constant.

According to Hertz's relations, the load on a unit microroughness at pressure equal to the microstrength is the following: $N_i = a_i R \sigma \pi$. Then, we extend the solution to the multiple contact of rough surfaces and conduct an analysis similar to the above one in order to find a critical nominal pressure value as a convergence function: $q_{ax} = \frac{tm v \sigma a_x^v}{2Rn^v}$.

Therefore, for the critical convergence we obtain the following:

$$a_{x} = Rp \left(\frac{2q_{\rm ax}}{tm\nu\sigma}\right)^{1/\nu}.$$
 (4)

After equating the proximity of the contacting surfaces for an elastic (3) and brittle (4) contact, we obtain the following:

$$q_{\rm ax} = \left(\frac{t_m \nu \sigma}{2}\right)^{2\nu + 1} \times \left[\frac{1.5\pi I_e}{t_m \nu (\nu - 1)K_3} \left(\frac{R}{R_p}\right)^{0.5}\right]^{2\nu}.\tag{5}$$

Equation (5) allows calculating critical nominal pressure depending on physical and mechanical constants of materials and friction surface profile parameters. The change in the deformation type implies a change in tribocontact friction characteristics. We estimate the friction coefficient and force based on I.V. Kragelsky's molecular-mechanical theory of friction [25]. We also use the relations obtained above. Let us represent the rough surface friction force $F_{\rm fr}$ as following:

$$F_{\rm fr} = \tau_0 A_r + \beta N + K_{\rm x} \int_0^{n_r} N_i \sqrt{\frac{a_i}{R}} dn_{\rm x}, \tag{6}$$

where A_r is an actual contact area, τ_0 and β is shear resistance of the molecular bond when there is no normal load and the molecular bond hardening coefficient. Since plastic deformation is not significant in frictional wear of brittle and high-strength materials, we assume $K_{\rm x}=0.19\alpha_{\rm r}$, $\alpha_{\rm r}=0.02$ as a hysteresis loss coefficient [26]. Assuming that $\int_0^{n_r} N_i \sqrt{\frac{a_i}{R}} dn_x = \frac{1}{0.75 I_e} \int_0^{n_r} a_i^2 dn_x$ for the friction force at elastic contact we obtain the following:

$$F_{\text{fr y}} = \frac{\tau_0 t m A_a}{2} \left(\frac{a_y}{Rp}\right)^{\nu} + \beta N + 0.19 \alpha_{\Gamma} \frac{A_a t m a_y^{\nu+1}}{\pi R R p^{\nu} (\nu+1) I_o}.$$
 (7)

For the subcritical pressure in a tribounit at $q>q_{\rm ax}$, we find the friction force as following:

$$F_{\text{fr x}} = \frac{\tau_0 t m A_a}{2} \left(\frac{a_x}{Rp}\right)^{\nu} + \beta N + 0.19 \alpha_{\Gamma} \frac{A_a t m \nu (\nu - 1) \sigma \pi^2 a_x^{\nu + 0.5} K_3}{2R^{0.5} Rp^{\nu}}.$$
 (8)

In practice, it is convenient to obtain calculation relations for estimating friction coefficients in a wide range of loads. In addition, Eqs. (7) and (8) are convergence functions, therefore calculations are complicated. Using the definition $f_{\rm fr}=\frac{F_{\rm fr}}{N}$, as well as Eqs. (3) and (4) we obtain the following for friction coefficients:

$$f_{y} = \frac{\tau_{0}\sqrt{tm} \left(\pi\delta I_{e}\right)^{\frac{2\nu}{2\nu+1}}}{\frac{\nu}{2\Delta^{2\nu+1}}q_{a}^{\frac{1}{2\nu+1}}} + \beta + 0.19\alpha_{\Gamma} \frac{tm\Delta^{\frac{\nu}{2\nu+1}}\delta^{\frac{\nu+1}{\nu+0.5}}}{0.75(\nu+1)} \left(\frac{q_{a}I_{e}}{\pi}\right)^{\frac{1}{2\nu+1}},\tag{9}$$

$$f_{\rm X} = \frac{\tau_0}{v\sigma} + \beta + 0.19\alpha_{\rm r} \frac{1.5\sqrt{\Delta}}{\delta v} \left(\frac{2q_a}{tm\sigma v}\right)^{\frac{1}{2\nu}},\tag{10}$$

where
$$\Delta = \frac{R_p}{R}$$
, $\delta = \frac{1.5}{\nu(\nu-1)K_3}$.

Analysis of modeling results

According to the technology [8], we obtained composite material samples from aluminum powder and synthetic diamonds of AC6 grade with grit 20/14, 14/10. The volume density of diamonds τ was 25 and 12.5 %, which corresponds to 100 and 50 % of diamond concentration K (100 % diamond concentration in material is the diamond powder value 4.39 carats in 1 cm³). We compared the results with D16 alloy samples, which have the surface modified by microarc oxidation (MAO), until obtaining a ceramic-like coating.

We carried out tribotechnical tests on the MT-2 friction machine [6]. We used fingerring friction scheme and the following materials of control samples: ceramics $BaO-SiO_2-AI_2O_3$. The tests were carried out under conditions of dry friction and with water. The linear sliding velocity was 0.75 m/s.

We determined the coefficients τ_0 and β according to the methodology and using the equipment proposed in the patent [30]. Evaluation of microgeometry parameters of friction surfaces involved using standard methods of profilometry GOST 19300-86 [21], microstructure analysis involved using a metallographic microscope. We evaluated microstrength using a PMT-3 microhardness tester with a Vickers pyramid indenter.



Fig. 2. Diamond-bearing material sample

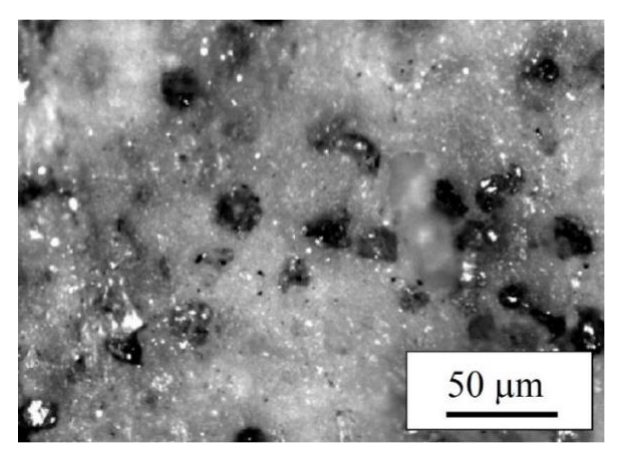


Fig. 3. Surface microstructure of diamond-bearing material (d = 20/14, K = 100%)

The typical appearance of their diamond-bearing material sample after testing is shown in Fig. 2. The tribo-surface is smoothed to gloss, there are no scratches and displayed crumble. Figure 3 shows the sample surface microstructure before testing: dark grains of graphitized diamond are distributed in the volume of an aluminum oxide matrix.

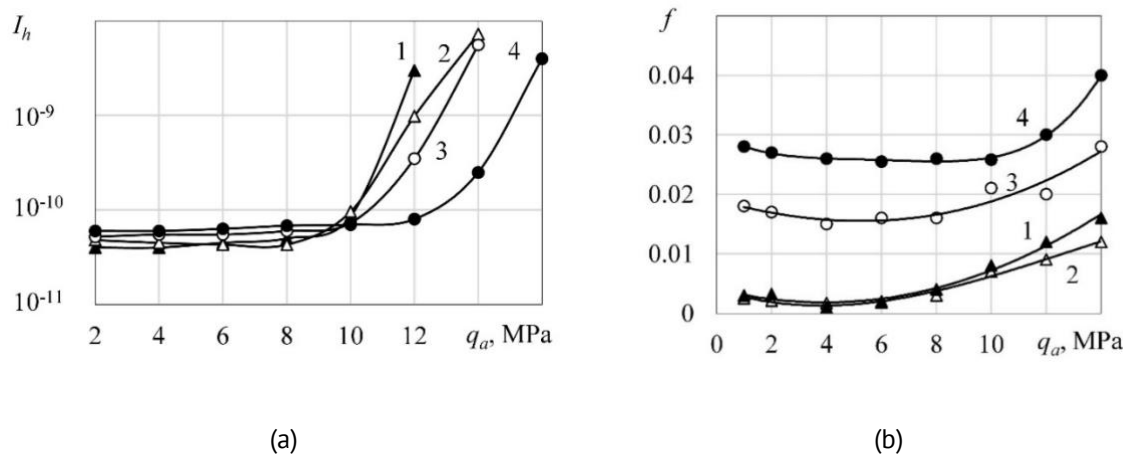


Fig. 4. Critical pressure estimation: by wear intensity (a), by a friction coefficient (b) under boundary friction conditions. 1 - DBMC: d = 20/14, K = 100; 2 - DBMC: d = 14/10, K = 100; 3 - DBMC: d = 20/14, K = 50; 4 - MAO D16

The test results (Figs. 4 and 5) confirm the nonlinear behavior of triboparameter change depending on pressure in the friction zone: regardless of friction conditions it is possible to identify a characteristic inflection point that corresponds to a change in the deformation type of friction surfaces. Table 1 shows the critical pressure obtained experimentally and calculated by Eq. (5).

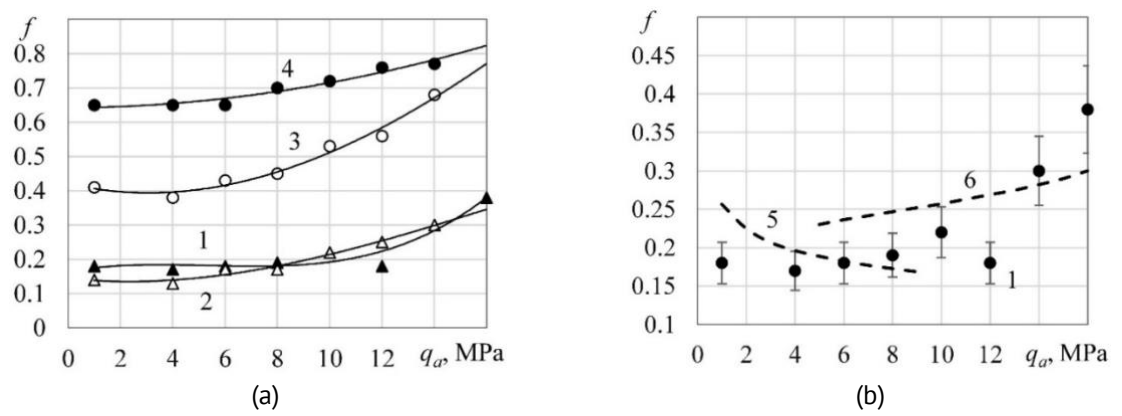


Fig. 5. Dry friction coefficient estimation: experimental results (a); comparing experimental results and calculations by Eqs. (9) and (10) (b). 1 - DBMC: d = 20/14, K = 100; 2 - DBMC: d = 14/10, K = 100; 3 - DBMC: d = 20/14, K = 50; 4 - MAO D16; 5 - calculation by Eq. (9); <math>6 - calculation by Eq. (10)

Table 1. Tribotechnical properties of tested materials

No	Friction pair material	Micro strength (σ), GPa	Microhardness	Critical pressure, MPa		
			(HV), GPa	Test results	Calculation	
				Test Tesuits	by Eq. (5)	
1	DBMC $d = 20/14$, $K = 100$	1.78	6.71	6.4	5.71	
2	DBMC $d = 14/10$, $K = 100$	1.96	6.62	6.2	5.65	
3	DBMC $d = 20/14$, $K = 50$	2.25	5.83	7.5	6.47	
4	MAO D16	2.68	16.48	11.0	10.16	

Critical pressures calculated by Eq. (5) within up to 15 % coincide with the values obtained experimentally, however there is a tendency of understating theoretical values. We can assume that at the calculated values of $q_{\rm ax}$ the cracking process just starts to form; it becomes significant at higher pressures, at $q_{\rm x}$ = 1.1 ÷ 1.5 $q_{\rm ax}$. As diamond grit increases, the right coefficient in Eq. (5) increases too, but microstrength decreases, which reduces the effect of grit change. The increase in diamond concentration decreases material microstrength. This is due to the growth of internal stress concentrators and the decrease in the volume of matrix bonding material. The diamond concentration included in I_e operator significantly affects the tribocontact elastic properties if friction countersurface material is close to ceramic matrix and diamond material in mechanical properties, as in our case. We can state that increasing diamond concentration reduces critical pressure.

According to the experimental results, the friction coefficient of a pair of materials diamond-bearing ceramics – ceramics during elastic deformation depends weakly on pressure (Fig. 4). The analysis of Eq. (9) shows that the pressure influence in the first and the last summand should compensate each other. Usually, it happens to metals and polymers. In our case, materials with high elasticity moduli are in contact, therefore pressure influence is more significant according to theoretical calculations. Experimental results and calculation by Eq. (9) showed that the friction coefficient does not change significantly with decreasing diamond grit. Diamond concentration affects the friction coefficient through the operator I_e . Moreover, the coefficients τ_0 and β change significantly with increasing diamond concentration (especially in dry friction conditions) due to the increase of free graphite in the friction zone. In general, when diamond concentration increases, the friction coefficient decreases.

When the contact pressure is above the critical one, the friction coefficient increases with increasing load (Eq. (10), Fig. 4). The molecular component of the friction coefficient (Eq. (10)) does not depend on pressure; the mechanical component increases to the degree $\frac{1}{2\nu}$, where $\nu \approx 1.5 \div 3$. Therefore, surface roughness (and grit indirectly) affects the friction coefficient increase rate. Diamond grit and concentration affect the brittle friction coefficient indirectly through material microstrength.

The rate of dependence curves f on load for dry and boundary friction is very similar. The shift along the vertical axis is due to the change of coefficients τ_0 , β and $\alpha_{\rm r}$ depending on the type of lubricant and contact pressure. The friction coefficient for diamond-bearing ceramics with d=20/14, $\tau=10$, K=100 during dry friction and in water differ by ten folds. Considering the fact that the theoretical evaluation of tribotechnical test results is sensitive to experimental conditions, it is difficult to expect high accuracy. An example of calculation by Eqs. (9) and (10) is shown in Fig. 5(b). Mathematical curves describe the behavior of friction coefficient change with increasing contact pressure adequately. Friction coefficient dependence behavior and the critical pressure value, which were obtained theoretically and experimentally, correlate with the data obtained by the authors [10] for gas-thermal coatings hardened with synthetic diamonds and electrocorundum.

We can note good antifriction properties of diamond-bearing material in comparison with the basic ceramic coating without diamonds, which was obtained through modification of aluminum by micro-arc oxidation. DBMC friction coefficient is lower than the one for oxidized coating by $1.4 \div 9.3$ times at boundary friction and by $1.6 \div 4$ times at dry friction. Graphite, which was formed during diamond oxidation, is not removed from the friction zone. It fills the pores of the ceramic matrix, reduces the shear resistance of material surface layers.

Conclusions

Theoretical and experimental studies detected the influence of load in a tribocontact zone on the change in the contact interaction type, wear nature and friction coefficient of antifriction diamond-bearing mineral ceramics. We showed the validity of the classical approach to describing frictional properties of triboconjugation involved diamond-bearing mineral ceramics and ceramics in a wide range of loads.

It is confirmed that microstrength can be a criterion that determines the change of deformation nature at the contact spot for ceramic composite materials. The microstrength decreases with increasing diamond grit and concentration. The critical pressure depends on microgeometry parameters, mechanical properties of friction pair materials, diamond grit and concentration.

We have established theoretically and experimentally the influence of microparameters of interacting half-spaces on the friction coefficient in the case of elastic deformation and brittle fracture. The friction coefficient decreases when pressure increases in the elastic region and increases in the subcritical region. The rate of curves of friction coefficient dependence on load for dry and boundary friction is similar but differs by an order of magnitude.

Diamond-bearing ceramic material has satisfactory antifriction properties when there is no lubrication. The friction coefficient of diamond-bearing material is $1.6 \div 4$ times lower than the one for oxidized coating without diamonds at dry friction. A ceramic matrix structure enables diamond grain retention and distribution of solid-lubricating graphite films in the friction zone. The obtained regularities allow optimizing the composition of diamond-bearing mineral ceramics and choosing a range of loading modes for operation of tribounits from this class materials.

CRediT authorship contribution statement

Aleksandr N. Bolotov Sc: writing – review & editing, supervision; Olga O. Novikova Sc: conceptualization, investigation, writing – original draft; Vladislav V. Novikov Sc: investigation, data curation.

Conflict of interest

The authors declare that they have no conflict of interest.

References

- 1. Drozdov YN. Generalized factors to characterize technical ceramics wear. Vestnik RGUPS. 2004;3: 13-22. (In Russian)
- 2. Li W, Gao J, Ma Y, Zheng K, Zhi J, Xin Y, Xie S, Yu S. Undoped and diamond-doped MAO coatings prepared on Ti6Al4V: Microstructure, wear, corrosion, and biocompatibility properties. *Surface and Coatings Technology*. 2023;458: 129340.

- 3. Liu B, Zhuge Z, Zhao S, Zou Y, Tong K, Sun L, Wang X, Liang Z, Li B, Jin T, Chen J, Zhao Z. Effects of diamond on microstructure, fracture toughness, and tribological properties of TiO2-diamond composites. *Nanomaterials*. 2022;12(21): 3733. 4. Xia Y, Lu Y, Yang G, Chen C, Hu X, Song H, Deng L, Wang Y, Yi J, Wang B. Application of nano-crystalline diamond in tribology. *Materials*. 2023;16(7): 2710.
- 5. Jin L, Li Y, Liu C, Fan X, Zhu M. Friction mechanism of DLC/MAO wear-resistant coatings with porous surface texture constructed in-situ by micro-arc oxidation. *Surface and Coatings Technology*. 2023;473: 130010.
- 6. Bolotov AN, Novikov VV, Novikova OO. Dependence of wear of friction pair composite diamond-containing material ceramics. In: *Mechanics and physics of processes on the surface and in contact of solids, parts of technological and power equipment*. 2017. p.153-157. (In Russian)
- 7. Gusakov GA, Gasenkova IV, Mukhurov NI, Sharonov GV. Research of effect of heat treatment on microhardness and wearing resistance of anodic oxide aluminum coatings modified by nano diamonds. *Proc. of the National Academy of Sciences of Belarus. Physical-Technical Series*. 2019;64(2): 157-165. (In Russian)
- 8. Bolotov AN, Novikov VV, Novikova OO. Mineral ceramic composite material: Synthesis and friction behavior. *Metal Working and Material Science*. 2020;22(3): 59-68. (In Russian)
- 9. Bolotov AN, Novikov VV, Novikova OO. Synthesis of abrasive tools with diamond ceramic coating for precision micromachining of superhard materials. *All Materials: Encyclopedic Reference Book.* 2020;4: 30-37. (In Russian)
- 10. Kobyakov OS, Spiridonov NV. Research on formation processes and tribotechnical properties of wear-resistant composite gas-thermal coatings that are disperse-hardened with synthetic diamonds and electrocorundum. *Bulletin of the Belarusian National Tech. Univ.* 2011;2: 17-23. (In Russian)
- 11. Vysotina EA, Kazakov VA, Polyansky MN, Savushkina SV, Sivtsov KI, Sigalaev SK, Lyakhovetsky MA, Mironova SA, Zilova OS. Investigation of the structure and functional properties of diamond-like coatings obtained by physical vapor deposition. *J. Surf. Investig.* 2017;11: 1177-1184.
- 12. Drozdov UN, Nadein VA, Savinova TM. Summarized characteristics for determination of the service life by the wear of industrial ceramicss. *J. Frict. Wear.* 2008;29: 15–20.
- 13. Kim JH, Choi SG, Kim SS. A fracture mechanics approach to wear mechanism of ceramics under non-conformal rolling friction. *Int. J. Precis. Eng. Manuf.* 2019;20(6): 983-991.
- 14. Krasnitckii SA, Sheinerman AG, Gutkin MYu. Brittle vs ductile fracture behavior in ceramic materials at elevated temperature. *Materials Physics and Mechanics*. 2024;52(2): 82-89.
- 15. Agarwal S, Angra S, Singh S. A review on the mechanical behaviour of of aluminium matrix composites under high strain rate loading. *Materials Physics and Mechanics*. 2023; 51(6): 1-13.
- 16. Morozov EM, Zernin MV. Contact Problems of Fracture Mechanics. Moscow: LIBROCOM Book House; 2017. (In Russian)
- 17. Aizikovich SM, Aleksandrov VM, Argatov AI. Mechanics of Contact Interactions. Moscow: Fizmatlit Publ.; 2001. (In Russian)
- 18. Sudnik LV, Vityaz PA, Ilyushchenko AF. Diamond-Bearing Abrasive Nanocomposites. Minsk: Belaruskaya navuka Publ.; 2012. (In Russian)
- 19. Vityaz PA, Zhornik VI, Kukareko VA, Komarov AI, Senyut VT. *Modification of Materials and Coatings by Nanoscale Diamond-Bearing Additives*. Minsk: Belaruskaya navuka Publ.; 2011. (In Russian)
- 20. Fedorenko DO, Fedorovich VA, Fedorenko EY, Daineko KB. Ceramic-matrix composite materials for the diamond abrasive tools manufacture. *Scientific Research on Refractories and Technical Ceramics*. 2017;117: 212-224.
- 21. Chepovetsky IH. Contact Interaction Mechanics in Diamond Machining. Kiev: Nauk. Dumka Publ.; 1978. (In Russian)
- 22. Novikova OO, Bolotov AN, Novikov VV. Modeling of wear of a friction pair diamond-bearing mineral ceramics ceramics. *Bulletin of Mechanical Engineering*. 2024;103(4): 299-304.
- 23. Pushkarev OI, Kulik OG, Nikuiko LA. Size effects and their impact on micromechanical properties of abrasives. *Industrial Laboratory. Diagnostics of Materials*. 2017;83(2): 49-52. (In Russian)
- 24. Mitlina LA, Vinogradova MR, Yankovskaya TV. Basic regularities of elastoplastic and brittle fracture of epitaxial ferrospinels. *J. of Samara State Tech. Univ., Ser. Physical and Math. Sci.* 2004;26: 141-150. (In Russian)
- 25. Kragelsky IV, Dobychin MN. Fundamentals of Calculations on Friction and Wear. Moscow: Mashinostroenie Publ.; 1977. (In Russian)
- 26. Chichinadze AV, Berliner EM, Brown ED. *Friction, Wear and Lubrication (Tribology and Tribotechnics)*. Moscow: Mashinostroenie Publ.; 2003. (In Russian)
- 27. Goryacheva IG, Dobychin, MN. Some results concerning the development of the molecular-mechanical theory of friction. *Friction and Wear*. 2008;29(4): 243-250.
- 28. Demkin NB, Ryzhov EV. *Surface Quality and Contact of Machine Parts*. Moscow: Mashinostroenie Publ.; 1981. (In Russian) 29. Johnson KL. *Contact Mechanics*. Cambridge: Cambridge University Press; 1989.
- 30. Izmailov VV, Gusev AF, Gusev DA, Nesterova IN, Novoselova MV. *Method for determining the rest friction coefficient of the surface layer of electrically conductive material*. RU 2525585 C1 (Patent), 2014.

Submitted: March 10, 2025 Revised: October 18, 2024 Accepted: April 17, 2025

Elastic-plastic deformation when bending rotating workpieces

T.V. Brovman [□]

Tver State Technical University, Tver, Russia

[™] brovman@mail.ru

ABSTRACT

A method of calculating plastic deformation during bending a rotating circular beam is presented. Rotating blank loading is examined in the two cases: plastic deformation occurs over the thickness of the blank and plastic deformation is absent in the blank. When the pipe being bent rotates, the symmetry with respect to the force plane is broken. The nature of bending deformation of a rotating blank differs from that of a fixed one. Since the beam axis is not a plane but a space curve, there is a lateral displacement and deviation of the deflection from the force plane.

KEYWORDS

plastic deformation • acceleration limits • strain rate tensor

Citation: Brovman TV. Elastic-plastic deformation when bending rotating workpieces. *Materials Physics and Mechanics*. 2025;53(2): 113–122.

 $http:\!//dx.doi.org/10.18149/MPM.5322025_10$

Introduction

The methods used for bending circular blanks, such as bending by rotational pulling, compression, pressure, and rolling, must provide the product of high quality. The commonly used methods of bending beams on rollers ensure their bending in one plane. Bending occurs due to compressive stresses above the neutral axis and due to tensile stresses below it. The basic theory of plastic deformation of sheets and shells developed by A.A. Ilyushin, N.N. Malinin, R. Hill, etc. does not apply to the bending of rotating circular blanks as their bending belongs to the problems that are more complex. The lack of analytical solutions to these problems hinders the creation of engineering methods to calculate the deformed bending of rotating blanks, which negatively affects the quality of technological processes of pipe bending production. In addition, there is no information on theoretical and experimental research on the issue in the literature. Though S. Clifford, K. Pan, K.A. Stelson, W.C. Whang as well as V.S. Yusupov, R.L. Shatalov [1–5] et al. published their findings on displacement and deformation fields of plastic bending of a pipe under the action of torque or transverse force, their solutions cannot serve as a theoretical basis for pipe bending processes due to the simplified blank loading scheme.

PAO TMK (Pipe Metallurgical Co., OJSC), Seversky Pipe Plant, Taganrog Metallurgical Works, SMS Meer, Danieli, and Multistand Pipe Mill use the tools for alignment and bending where circular blanks move non-rotating through a cage that follows a closed trajectory. The problem of fixed pipe deformation has been well studied. The rotation of a pipe being deformed during bending is not believed to affect its deformation significantly.



114 T.V. Brovman

The novelty of this research lies in the determination of the direction of maximum deflection during the elastic-plastic bending of rotating circular beams. The purpose and objectives of the research are to develop methods of calculating deformations and stresses during this process, with rotation during bending taken into account. The purpose is achieved by solving differential equations for bending under concentrated loads. The research also aims to determine the functional dependence of the deflection direction on the bending moment value.

Object of research

This research examines the elastic-plastic deformation of circular beams that undergo small deformations and rotations. It does not take into account the curvature of beam sections, tangential stresses, or the effects of hardening as well as the Bauschinger effect.

The example of a thin-walled pipe in Fig. 1 shows the difference in bending deformation between fixed and rotating beams. A pipe with radius r and wall thickness h is bent by force P in the middle of the l-long span. If force P is directed along the z-axis (opposite to the axis), then the y-axis is the neutral one, and the bending deformation in section A'A at angle φ to the y-axis is equal to $\varepsilon = w''(x)r\sin\varphi$, where w'' is the second derivative of deflection w(x) which coincides with the direction of z-axis, i.e. with the direction of P.

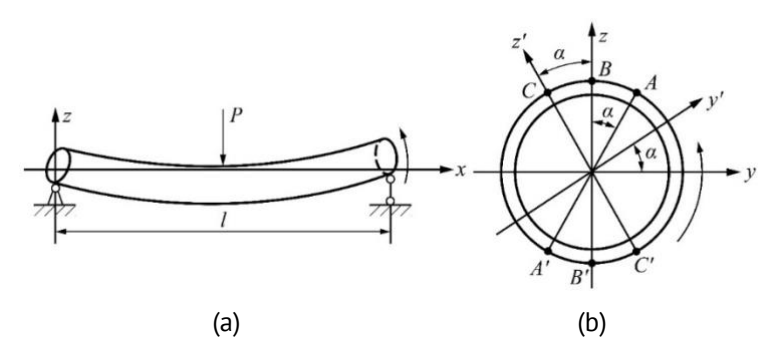


Fig. 1. Bending deformation: (a) a fixed beam; (b) a rotating beam

The bending moment for the diagram shown in Fig. 1 (for $0 \le x \le 0.5l$) is $M_y = 0.5P_x$, and the moment of the z-axis is zero (since there are no forces in the direction of the y-axis). We used an approximate expression for curvature here, assuming that the first derivative is |w'(x)| << 1 [6–8]. Plastic deformation begins in sections B and B' and as we approach the section x = 0.5l there are two zones of plastic deformation: those of compression ABC and tension A'B'C' where the stresses are $\sigma = -\sigma_m$ and $\sigma = +\sigma_m$ (where σ_m is the yield point). In zones C'A and A'C, elastic deformation occurs, and it is equal to $\sigma = E \cdot \varepsilon$ (where E is the elastic modulus).

Exploratory procedure

The resisting moment about the y-axis for fixed pipes in elastic-plastic deformation is equal to $M_y=0.5~P_x=\int_0^{2\pi}\sigma r^2h\sin\varphi d\varphi$, the moment about the z-axis is $M_z=0$. For some φ_1

characterizing the position of point A and A' $\sigma = Ew''r\sin\varphi = \pm\sigma_m$, and for $|\varphi| < \varphi_1$ deformations are elastic, and it are plastic for $\varphi_1 < \varphi < \pi - \varphi$ and $\pi - \varphi_1 < \varphi < 2\pi - \varphi_1$.

If the load acts in the xz-plane, Fig. 1(a), then for a fixed beam, the plastic zones ABC and A'B'C' are symmetrical with respect to the z-axis. When the pipe rotates and is under constant loads (the direction of rotation is shown in Fig. 1(b)), plastic deformations are possible only along arcs AB and A'B', and after reaching the maximum (at point B) and the minimum (at point B') deformations, unloading occurs in sections BC and B'C'.

However, if plastic deformations occur only under load along AB and A'B', then the bending moment is $M_z \neq 0$, since the plastic zones are not symmetrical with respect to the z-axis. This contradicts the statement of the problem, since external loads act only in the xz-plane [9-11]. For a rotating pipe, the condition $M_z = 0$ can be fulfilled only if bending occurs not in the xz-plane, but in the xz'-plane, i.e. the deflection direction is parallel to the z'-axis (Fig. 1(b)) and forms the angle α with the z-axis. Then the maximum deformation is achieved at point C, the minimum one is at C' and unloading begins at these points. The neutral axis is also rotated by an angle α with respect to the y-axis.

Denoting the variable angle by φ , we define the bending stresses: $\sigma = \sigma_m$ for $\frac{\pi}{2} - \alpha < \varphi \leq \frac{\pi}{2} + \alpha$ (in ABC); $\sigma = \sigma_m - Ew''r[1 - \sin(\varphi - \alpha)]$ for $\frac{\pi}{2} + \alpha < \varphi \leq \frac{3}{2}\pi - \alpha$ (in the zone CA'); $\sigma = -\sigma_m$ for $\frac{3}{2}\pi - \alpha < \varphi \leq \frac{3}{2}\pi + \alpha$ (in the zone A'B'C'); $\sigma = -\sigma_m + Ew''r[1 + \sin(\varphi - \alpha)]$ for $\frac{3}{2}\pi + \alpha < \varphi \leq 0$, and for $0 < \varphi \leq \frac{\pi}{2} - \alpha$ (in the zone C'A). For $\varphi = \frac{\pi}{2} - \alpha$ the stresses are $\sigma_m = -\sigma_m + Ew''r[1 + \sin(\frac{\pi}{2} - 2\alpha)]$ or $\frac{2\sigma_m}{\epsilon_r} = w''(1 + \cos 2\alpha)$. Therefore, we get: $\frac{w''l}{a} = 1/\cos^2 \alpha, a = \frac{\sigma_m l}{Er}.$ (1)

The bending moment of the y-axis is $M_y(x) = \int_0^{2\pi} \sigma(\varphi) r^2 h \sin \varphi \, d\varphi$. With the calculations taken into account (1), we obtain a nonlinear bending equation:

$$M_{y}(x) = \pi \sigma_{m} r^{2} h f(\alpha),$$

$$f(\alpha) = \frac{\pi - 2\alpha + \sin 2\alpha}{\pi \cos \alpha}.$$
(2)

 $f(\alpha) = \frac{\pi - 2\alpha + \sin 2\alpha}{\pi \cos \alpha}$. For a pipe of length l loaded with concentrated force P (Fig. 1), the moment is $M_y(x) = 0.5Px$. Denoting $m = \frac{Pl}{4\pi\sigma_m r^2 h}$, we obtain in the zone of elastic-plastic deformation $(x_1 = \frac{0.5l}{m})$:

$$\frac{2mx}{l} = f(\alpha) \text{ for } x_1 < x \le 0.5l, \tag{3}$$

and in the elastic zone:

$$w''(x) = \frac{2amx}{t^2}$$
 for $0 \le x \le x_1$. (4)

If $m \le 1.0$, then the deformations are elastic and $\alpha = 0$.

Since it follows from Eq. (1) that $\lg \alpha = \left(\frac{w''l}{a} - 1\right)^{0.5}$, then substituting α by w'' into Eq. (2), we obtain, instead of Eq. (3), the following equation:

$$x = lm^{-1}\varphi\left(\frac{w''l}{a}\right),$$

$$\varphi\left(\frac{w''l}{a}\right) = \frac{1}{\pi}\sqrt{\frac{w''l}{a}}\left[\pi + 2\sqrt{\frac{a}{w''l}}\left(1 - \frac{a}{w''l}\right) - 2\arctan\sqrt{\frac{w''l}{a} - 1}\right],$$
(5)

where φ is a differentiable function of w''. The greater is the load, the wider is the angle between the directions of force and deflection. As the load approaches it maximum, this angle tends to 90°. The value of w'(x) in a parametric form in t function is:

116 T.V. Brovman

$$x = \frac{l\varphi(t)}{2m}, x_{1} < x \le 0.5l,$$

$$w'(x) = C_{1} + \frac{a}{2m} \int_{1}^{t} t \frac{d\varphi}{dt} dt,$$

$$W(x) = C_{2} + C_{1}x + \frac{al}{4m^{2}} \int_{1}^{t} \frac{d\varphi(t)}{dt} \left[\int_{1}^{t} t \frac{d\varphi}{dt} dt \right] dt,$$
(6)

where C_1 and C_2 are the constants of integration.

The parameter t is then substituted into the function φ instead of the value $\frac{w''l}{a}$. The choice of the value t=1 as the lower limit in the integrals of Eq. (6) corresponds to the boundary of the elastic-plastic and elastic zones ($\frac{w''l}{a} = 1.0$ when $x = x_1$). In the elastic zone, the solution of linear equation (4) under the condition w=0 for x=0 has the form:

$$w(x) = C_3 x + \frac{\frac{1}{3}amx^3}{l^2}, \ 0 \le x \le x_1.$$
 (7)

Based on the variability w(x) and w'(x) as well as w'=0 for x=0.5l we define the constants $C_1=-\frac{a}{2m}\int_1^{t_m}t\frac{d\varphi(t)}{dt}dt$, $C_2=-\frac{al}{12m^2}$, $C_3=C_1-\frac{a}{4m}$, where t_m is the largest value of parameter t for x=0.5l.

According to the first of Eqs. (6), we obtain $\varphi(t_m) = m$. Substituting constants into Eqs. (6) and integrating the double integral in parts, taking into account $\varphi(t_m) = m$, we define the maximum deflection w_m for x = 0.5l:

$$w_{m} = \frac{al}{12m^{2}} \left[1 + 3 \int_{1}^{t_{m}} t \, \varphi(t) \frac{d\varphi(t)}{dt} dt \right],$$

$$\varphi(t) = \sqrt{t} + \frac{2}{\pi} \sqrt{t - \frac{1}{t}} - \frac{2\sqrt{t}}{\pi} \operatorname{arctg} \sqrt{t - 1}.$$
(8)

By replacing variable t with v(t), where v is a parameter similar to α and equal to $v=\arctan(t-1)^{\frac{1}{2}}$, we obtain $w_m=\frac{al}{12m^2}\Big\{1+\frac{3}{\pi^2}\int_0^{\alpha_m}\frac{1}{\cos^5 v}[(\pi-2v)^2+\sin^2 v]\sin v\,dv\Big\}$, where α_m is the maximum value of angle α when x=0.5l.

Having calculated the integral, we can define the maximum deflection as $w_m = \frac{al}{12m^2} \left[\frac{1}{4} + \frac{3(\pi - 2\alpha_m)^2}{4\pi^3 \cos \alpha_m} + \frac{3}{\pi^2} (\pi - 2\alpha_m) \left(\operatorname{tg} \alpha_m + \frac{1}{3} \operatorname{tg}^3 \alpha_m - \frac{5}{\pi^2} \operatorname{tg}^2 \alpha_m - \frac{16}{\pi^2} \ln \cos \alpha_m \right) \right]$, where value α_m is defined from the following equation:

$$f(\alpha_m) = \pi - 2\alpha_m + \sin\frac{2\alpha_m}{\pi\cos\alpha_m} = m, (9)$$

where the parameter α_m is equal to the maximum angle between the directions of force and deflection (in the middle of the beam length).

Curves $\alpha_m(m)$ obtained by the numerical solution of Eq. (9) are shown in Fig. 2. With increasing m, parameter α_m increases and, when m approaches the limit value $m_0 = 1.275$, parameter $\alpha_m = 90^\circ$, i.e., the direction of deflection when plastic deformation spreads over the entire section, deviates more and more from the direction of an external force and approaches the direction that makes up a right angle with the force.

Figure 3 shows the change in the value $\frac{w_m}{al} = w^\circ$ (curve 1) and its projections on the z-axis (curve 2) and the y-axis (curve 3). The component of deflection in the direction of force P (along the z-axis) is not seen to increase with the onset of plastic deformation and the force increase, but to decrease. At m = 1.16, the parameter $\alpha_m = 45^\circ$ and the deflection projections on the z- and y-axes are equal. In elastic deformation, when the stresses are completely specified by deformations, rotation does not affect the beam bending. However, in elastic-plastic deformation, when the stresses depend on the loading history, the beam rotation significantly changes the bending process and leads to the lateral displacement and deviation of the deflection from the force plane [5,9,12]. Since angle α

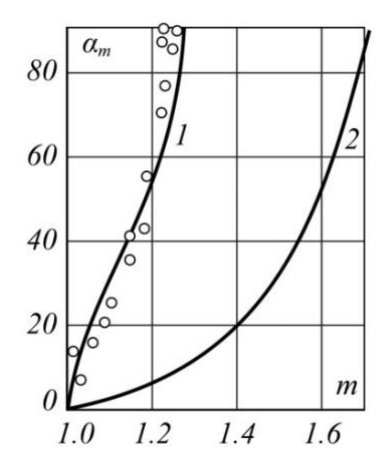


Fig. 2. Curve $\alpha_m(m)$ obtained by numerical solution of Eq. (9), (curve 1)

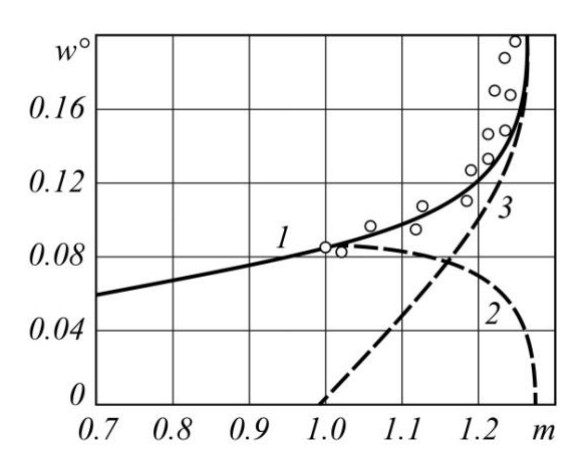


Fig. 3. Graphs of the value $\frac{w_m}{al} = w^{\circ}$ (curve 1) and its projections on the *z*-axis (curve 2) and the *y*-axis (curve 3)

depends on the bending moment and the x coordinate, the beam axis is not flat, but a space curve.

Results and Discussion

The problem is considered for the case where the bending moment vector rotates around the pipe axis, and the deflection direction rotates at the same speed, with a phase shift of angle α .

To estimate the range of bending parameters, we can neglect tangential torsional stresses τ . If we assume that for each revolution of the pipe, the work equal to $4\sigma_m^2\left(\frac{w''l}{a-1}\right)/E$ contributes to plastic deformation of a unit volume, and the entire volume of the pipe with length $(l-2x_1)$ undergoes plastic deformation, then we obtain an upper bound of the plastic work as follows $A=\frac{8\sigma_m^2}{E}\pi r l h\left(1-\frac{1}{m}\right)\left(\frac{w''l}{a}-1\right)=4\pi\tau r^2 h$. Therefore, we have $\frac{\tau}{\sigma_m}=\frac{2a}{\pi}\left(1-\frac{1}{m}\right)\left(\frac{w''l}{a}-1\right)$. Assuming the maximum value of $m_0=1.275$, we find that $\frac{\tau}{\sigma_T}=0.137a\left(\frac{w''l}{a}-1\right)=0.137a\,tg^2\,\alpha_m$.

Assuming that the condition $\frac{\tau}{\sigma_m} < 0.05$ must be met, then, if x = 0.5l, it is sufficient that w''l < 0.362 - a, $\lg \alpha_m < \left(\frac{0.362}{a}\right)^{0.5}$. For example, for $\sigma_m = 240$ MPa, $E = 2\cdot10^5$ MPa, $\frac{l}{r} = 10$, $a = 1.2\cdot10^2$, $\lg \alpha_m < 5.5$, $\alpha_m < 79.5$ °, i.e., the formulas are applicable for large values of α_m [11,13–16]. Note that the influence of tangential stresses on a pipe can be approximately accounted for by substituting $\sigma_1 = (\sigma_m^2 - 3\tau^2)^{0.5}$ into the equations instead of σ_m .

For other loading schemes, Eq. (2) is solved for x, and Eqs. (6) and (7), $\varphi(t_m)=m$ is true if the corresponding $\varphi(t)$ function is defined. For example, for a cantilevered pipe of length l, loaded with force P we have $\varphi(t)=2\left[m-\sqrt{t}-\frac{2}{\pi}\sqrt{1-\frac{1}{t}}-\frac{2}{\pi}\mathrm{arctg}\sqrt{t-1}\right], \ m=\frac{Pl}{\pi\sigma_m r^2h}.$ For a pipe supported on two points, loaded with a uniform distributed load of intensity p, we have, for $m=\frac{pl^2}{8\pi\sigma_m r^2h}$: $\varphi(t)=m+\left\{m\left[m-\sqrt{t}-\frac{2}{\pi}\sqrt{1-\frac{1}{t}}-\frac{2}{\pi}\mathrm{arctg}\sqrt{t-1}\right]\right\}^{\frac{1}{2}}.$

118 T.V. Brovman

Many problems that are important for practical applications lead to the equations similar to Eq. (2), which, with a complex dependence on the variable w'', are solved with respect to the variable x in a form similar to Eq. (3). Equations (6) then determine the solution for known values m and $\varphi(t)$, showing the advantage of the parametric method to solve problems of elastic-plastic bending [17–22].

The deformation of a free pipe is discussed above. If the deflection plane is fixed in the xz-plane, $\alpha=0$ can be ensured by using rigid, smooth rulers that hold the beam along its entire length to prevent lateral displacement. In this case, $M_y(x)=\frac{\sigma_m r^2 h(2\pi-2\alpha_1+\sin 2\alpha_1)}{1+\cos \alpha_1}, M_z(x)=4\pi\sigma_m r^2 h\left(1-\frac{a}{w''l}\right), \ \alpha_1=\arccos(2a-1).$

The rulers apply pressure to the pipe, creating this value $M_z(x)$. As force P increases, moment M_y reaches its maximum at the angle of $\alpha_1 = 57^\circ$, $m_0 = 1.075$. After that, it decreases, while the moment M_z continues to increase. Therefore, the maximum load limit is not defined by $m_0 = 1.275$, as it would be with a free beam, but by $m_0 = 1.075$, which is 18 % less.

Let's consider the bending of thick-walled circular beams with outer and inner radii r and r_1 . There can be two cases (Fig. 4): in the first one, plastic deformation does not penetrate the entire thickness of the beam and deformations are elastic for $\rho \leq \rho_0$, Fig. 4(a). In this case, stresses are $\sigma = Ew''\rho\sin(\varphi-\alpha)$. Bending occurs on the z'-axis, and the neutral axis y' has zero deformation. Plastic zones ABC and A'B'C' are shown shaded in Fig. 4. The equation of the line AC has the form $\rho_1 = \frac{2ar}{[w''l[1+\sin(\varphi-\alpha)]]}$, and the equation of the line A'C' is $\rho_2 = \frac{2ar}{[w''l[1-\sin(\varphi-\alpha)]]}$. For $\varphi = \frac{\pi}{2} + \alpha$ (point C) and $\varphi = \frac{3\pi}{2} + \alpha$ (point C') $\rho_1 = \rho_2 = \rho_0 = ur$; $u = \frac{a}{w''l}$.

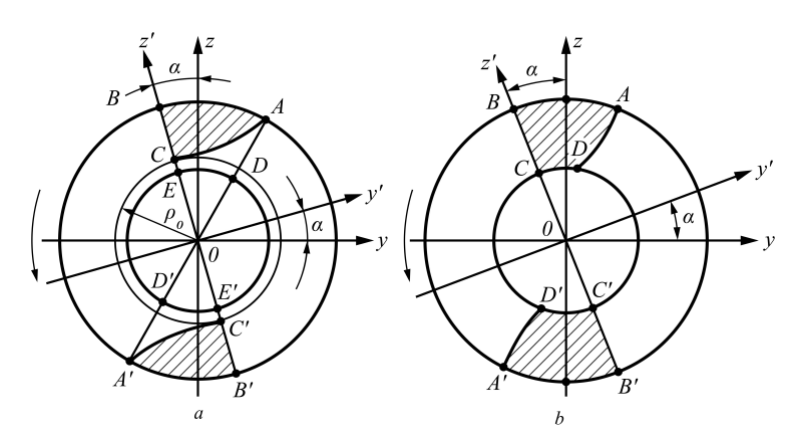


Fig. 4. Bending schemes of thick-walled circular beams with external and internal radii r and r_1 : (a) plastic deformation does not penetrate the entire thickness of the beam; (b) plastic deformation penetrates the entire thickness of the beam

The scheme shown in Fig. 4(a), can be used for $\rho_0 \ge r_1$ or $u \ge 2u_1$, $u_1 = \frac{0.5r}{r_1}$. Unloading happens in zones BCA'C' and B'C'CA. The bending moments about the y- and z-axes are equal to $M_y(x) = \iint \sigma(\rho, \varphi) \, \rho^2 \sin \varphi \, d\rho d\varphi$; $M_z(x) = \iint \sigma(\rho, \varphi) \, \rho^2 \cos \varphi \, d\rho d\varphi$, where integrals are calculated over the entire contour of the section. According to the calculations, we obtain:

$$\begin{split} M_{y}(x) &= \sigma_{m} r^{3} [f_{1}(u) \sin \alpha + f_{2}(u) \cos \alpha], \\ M_{z}(x) &= \sigma_{m} r^{3} [f_{3}(u) \sin \alpha + f_{4}(u) \cos \alpha], \\ f_{1}(u) &= f_{4}(u) = \frac{4}{3} - 2u + \frac{2}{3}u^{3}, \\ f_{2}(u) &= -f_{3}(u) = \frac{\pi}{8u} + \frac{1}{4u} \arcsin(2u - 1) - \frac{4\pi u_{1}^{4}}{u} + \sqrt{u(1 - u)} \left(\frac{9}{5} - \frac{1}{2u} - \frac{4}{15}u - \frac{8}{15}u^{2}\right). \end{split} \tag{11}$$

If $M_z(x) = 0$, then $\operatorname{tg} \alpha = \frac{f_1(u)}{f_2(u)}$; excluding value α from Eq. (10), we obtain the bending

$$\frac{M_{\mathcal{Y}}(x)}{\sigma_m r^3} = \sqrt{f_1^2(u) + f_2^2(u)}. (12)$$

For a beam loaded with concentrated force P, Eq. (6) can be applied by taking function $\varphi(t)$ as:

$$\varphi(t) = c \sqrt{f_1^2 \left(\frac{1}{t}\right) + f_2^2 \left(\frac{1}{t}\right)},$$

$$c = \frac{4}{[\pi(1-16u_1^4)]},$$
(13)

and constant $m = \frac{Pl}{[\pi \sigma_m r^3(1-16u_1^4)]}$. In the special case, when $u_1 = 0$ we have a solid circular shaft.

The linear equation (4) works in the elastic zone. The maximum deflection is defined by Eq. (8), into which function $\varphi(t)$ should be substituted according to Eq. (13). If $u_m = \frac{1}{t_m} < 2u_1$, then the scheme shown in Fig. 4(b), takes place, i.e. plastic deformation will spread along the entire section of the beam. Plastic deformation occurs in shaded areas ABCD and A'B'C'D', and unloading occurs in zones BCD'A' and B'C'DA. According to the calculations similar to Eqs. (10), we obtain:

$$\begin{split} M_{y}(x) &= \sigma_{m} r^{3} [f_{5}(u) \sin \alpha + f_{6}(u) \cos \alpha], \\ M_{z}(x) &= \sigma_{m} r^{3} [f_{7}(u) \sin \alpha + f_{8}(u) \cos \alpha], \\ f_{5}(u) &= f_{8}(u) = \frac{4}{3} - 2u + 8uu_{1}^{2} - \frac{32}{3}u_{1}^{3}, \\ f_{6}(u) &= -f_{7}(u) = \frac{\pi}{8u} + \frac{1}{4u} \arcsin(2u - 1) - \frac{4u_{1}^{4}}{u} \arcsin\left(\frac{u}{u_{1}} - 1\right) - 2\pi u_{1}^{4} + \\ &+ \sqrt{u(1 - u)} \left(\frac{9}{5} - \frac{1}{2u} - \frac{4}{15}u - \frac{8}{15}u^{2}\right) + \sqrt{\frac{u}{u_{1}} \left(2 - \frac{u}{u_{1}}\right)} \left(4\frac{u_{1}^{4}}{u} - \frac{36}{5}u_{1}^{3} + \frac{8}{15}uu_{1}^{2}\right). \end{split}$$
(14)

For $u = u_1$ from Eqs. (11) and (14) we have $f_1(u_1) = f_5(u_1)$, $f_2(u_1) = f_6(u_1)$. In the special case, if $M_z = 0$, then $\operatorname{tg} \alpha = \frac{f_5(u)}{f_6(u)}$. In Eqs. (8), instead of $\varphi(t)$ for $0 \le u \le 2u_1$, we substitute: $\varphi_1(t) = c \left[f_5^2 \left(\frac{1}{t} \right) + f_6^2 \left(\frac{1}{t} \right) \right]^{0.5}$.

$$\varphi_1(t) = c \left[f_5^2 \left(\frac{1}{t} \right) + f_6^2 \left(\frac{1}{t} \right) \right]^{0.5}. \tag{15}$$

When considering the bending of a beam in the elastic zone for $0 \le x \le x_1$, we have Eq. (4), then for $x_1 < x \le x_2$ there will be a zone of elastic-plastic deformation in which there is an elastic core in the beam section (Fig. 4(a)) and Eq. (11) $x_2 = \frac{0.5l\varphi(\frac{1}{u_1})}{m}$ is valid.

For $x_2 < x \le 0.5l$ there is a zone of elastic-plastic deformation where the plastic flow spreads over the entire thickness (Fig. 4(b)) and Eq. (14) is valid. Solving the bending equations, we find the maximum deflection:

$$w_m = \frac{al}{12m^2} \left[1 + 3 \int_1^{2t_1} f \, \varphi(t) \frac{d\varphi(t)}{dt} dt + 3 \int_{2t_1}^{t_m} f \, \varphi_1(t) \frac{d\varphi_1(t)}{dt} dt \right], \ t_1 = \frac{1}{u_1}, \tag{16}$$

where value t_m is defined by equation $\varphi_1(t_m) = m$. The equations obtained should be applied if $0 \le u_m < 2u_1$; in the case of $2u_1 \le u_m \le 1.0$, the equation $\varphi(t_m) = m$ and Eq. (8) are valid, where $\varphi(t)$ is defined by Eq. (13).

Based on numerical calculations performed with these equations, values $\alpha_m(m)$ and $w^{\circ}(m)$ shown in Fig. 2 (curve 2) and Fig. 5 [16-21,23-30] were determined. Note that the dependencies $w_m(m)$ are satisfactorily defined by equation $w_m = \frac{1}{12} a l \left[\frac{m_0 - 1}{m_0 - m} \right]^{\frac{1}{3}}$, where the limiting moment is $m_0 = \frac{16(1-8u_1^3)}{3\pi(1-16u_1^4)}$

120 T.V. Brovman

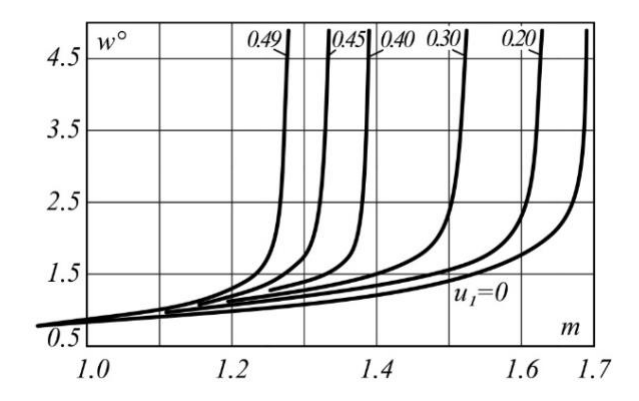


Fig. 5. Graphs of values $\alpha_m(m)$, $w^{\circ}(m)$

The experimental study was performed in bending copper and aluminum pipes with radius 0.6 and 1.0 cm and thickness 0.1 and 0.2 cm. The installation was mounted on a lathe. The pipes were rotated with a lathe chuck, and the force was applied by a clip with gaskets that reduce the crumpling of the hollow blank through a lathe caliper with an elastic dynamometer. Deflection angle α_m was determined by the deflection components.

The experimental points are shown in Figs. 2 and 3. For $1.0 \le m \le 1.20$, the experimental data are in satisfactory agreement with the calculated ones; the discrepancies do not exceed 20 % for both angle α_m and deflection value. For m > 1.20, the discrepancy between the calculated and experimental values increases.

In all cases when rotating pipes are bent and plastic deformation happens, lateral displacement occurs. When bearing capacity is lost and deformation decreases, the deflection of pipes occurs not in the direction of force action, as for fixed beams, but at angle 90° to the force action line.

Conclusions

- 1. The elastic-plastic deformation of rotating circular blanks differs from that of fixed pipes significantly. In this case, the direction of maximum deflection does not coincide with the direction of the bending force.
- 2. Graphs and analytical dependences of deflection on load with respect to bending force are given. It is shown that the deflection of a rotating blank (pipe) can exceed that of a stationary one by 20-25 %. As the maximum load approaches, deflection occurs at an angle of $\sim 90^{\circ}$ to the force direction.
- 3. At the stage of unloading, or deformation reduction, it is necessary to carry out symmetrical tension-compression cycles, which ensures the quality of straightening.
- 4. The design of proper machine tools must take into account the movement of the blank.

CRediT authorship contribution statement

Tatyana V. Brovman (DSC): writing - original draft.

Conflict of interest

The author declares that she has no conflict of interest.

References

- 1. Shelest AE, Yusupov VS, Rogachev SO, Andreev VA, Karelin RD, Perkas MM. Study of the additional possibility of the effect of elastic-plastic alternating deformation on the properties of metal materials during their processing on a roller straightening machine. *Metally*. 2023;1:75–83. (In Russian)
- 2. Shelest AE, Yusupov VS, Perkas MM, Sheftel' EN, Akopyan KE, Prosvirnin VV. Formation of the Mechanical Properties of Copper Strips during Alternating Elastoplastic Bending. *Russian Metallurgy (Metally)*. 2018;2018:500–506.
- 3. Shatalov RL, Genkin AL. Sheet mill control in steel strip hot rolling. *Journal of Chemical Technology and Metallurgy*. 2015;50(6): 624–628.
- 4. Ivlev DD. *Theory of ideal plasticity*. Moscow: Nauka; 1966. (In Russian)
- 5. Rudskoi AI, Kodzhaspirov GE, Kamelin EI Simulation of dynamic recrystallization of austenitic corrosion-resistant steel during the formation of a complex section by high-temperature thermomechanical treatment. *Russian Metallurgy (Metally)*. 2022;2022:1181–1185.
- 6. Brovman TV. Elastic-plastic bending deformation during profiling. *Ferrous metallurgy. Izvestiya VUZov.* 2000;9: 36–39. (In Russian)
- 7. Shapiro GS. On the limiting and elastic-plastic state of structures. *Izv. of the USSR Academy of Sciences. Mechanics and Mechanical Engineering*. 1963;4: 138–144. (In Russian)
- 8. Klyushnikov VD. Mathematical theory of plasticity. Moscow: Publishing House of Moscow State University; 1979. (In Russian)
- 9. Brovman TV. Forces in case of local deformation of tubular billets. *Technology of Metals*. 2015;6: 9–13. (In Russian) 10. Savikovskii AV, Semenov AS. Influence of material anisotropy on the interaction between cracks under tension and shear. *Materials Physics and Mechanics*. 2023;51(5): 24–37.
- 11. Gulin AE, Korchunov AG, Konstantinov DV, Sheksheev MA, Polyakova M. Features of the properties of steel with the trip effect under various types of deformation loading. *Materials Physics and Mechanics*. 2023;51(5): 152–164.
- 12. Fomin SV, Rostovtsev VS, Meltsov VU, Shirokova ES. Prediction of mechanical properties of elastomeric materials using neural networks. *Materials Physics and Mechanics*. 2023;51(5): 66–78.
- 13. Brovman TV, Kutuzov AA. Improving accuracy in the manufacture of curved metal workpieces by bending deformation. *Russian Metallurgy (Metally)*. 2016;2016: 477–484.
- 14. Andrianov IK, Feoktistov SI. Integral equations of deformation of cylindrical workpieces in axisymmetric matrices of complex shape. *Materials Physics and Mechanics*. 2023;51(2): 112–121.
- 15. Brovman TV. Nonstationary process plastic deformation in bending of workpieces. *The Scientific Heritage*. 2019;36: 55–59. (In Russian)
- 16. Babeshko VA, Evdokimova OV, Babeshko OM. On the exact solution of mixed problems for multicomponent multilayer materials. *Materials Physics and Mechanics*. 2023;51(5): 1–8.
- 17. Rudskoy Al Kojaspirov GE, Kliber Ch, Apostolopoulos A, Kitaeva DA. Physical fundamentals of thermomechanical processing in ultrafine-grained metallic materials manufacturing. *Materials Physics and Mechanics*. 2020;43(1): 51–58.
- 18. Prokofieva OV, Beigelzimer YaE, Usov VV, Shkatulyak NM, Savkova TS, Sapronov AN, Prilepo DV, Varyukhin VN. Formation of a Gradient Structure in a Material by Twist Extrusion. *Russian Metallurgy (Metally)*. 2020;2020: 573–578.
- 19. Khvan AD, Khvan DV, Voropaev AA. Bauschinger Effect during the Plastic Forming of Ferrous Metals. *Russian Metallurgy (Metally)*. 2021;3: 81–84.
- 20. Bakulin VN. Block based finite element model for layer analysis of stress strain state of three-layered shells with irregular structure. *Mechanics of Solids*. 2018;53: 411–417.

122 T.V. Brovman

21. Maksimov EA, Shatalov RL, Shalamov VG. Calculation of Residual Stress and Parameters of Sheet Springing on a Roller Leveler. *Steel in Translation*. 2021;51: 1–6.

- 22. Brovman TV. Analysis of Plastic Deformation by the Method of Inverse Problems. *Inorganic Materials: Applied Research.* 2025;16(3): 724-729.
- 23. Brovman TV. Obtaining accurate parts in non-stationary processes of bending deformation. *Physics and Chemistry of Materials Treatment*. 2020;2: 80–84. (In Russian)
- 24. Maximov EA, Ustinovsky EP. Method for calculating force in the machine applied for correcting the "ski formation" defect of plates. *Mechanical Equipment of Metallurgical Plants*. 2019;2(13):45–48. (In Russian)
- 25. Zaides SA, Hai NH. Influence of tool geometry on the stress-strain state of cylindrical parts during reversible surface plastic deformation. *Russian Engineering Research*. 2023;43: 1088–1094.
- 26. Shalaevsky DL. Investigation of thermal mode of hot-rolling mill working rolls in order to improve the accuracy of calculating the thermal profile of their barrels' surface. *Izvestiya Ferrous Metallurgy*. 2023;66(3): 283–289.
- 27. Nikolaev VA, Roberov IG. Calculation of roll deflection, taking into account nonuninformity of linear contact forces. *Proizvodstvo Prokata*. 2019;12: 9–14. (In Russian)
- 28. Pimenov VA, Lagman AI, Kovalev DA. Analysis and Mathematical Simulation of Formation Regularities of Strip Transversal Profile during Hot Rolling. *Steel in Translation*. 2020;50: 107–111.
- 29. Kukhar VD, Korotkov VA, Yakovlev SS, Shishkina AA. Formation of a mesh of spiral wedge rotrusions on the inner surface of a steel shell by local plastic deformation. *Chernye Metally.* 2021;65: 65–68.
- 30. Zakarlyuka SV, Rudenko EA, Goncharov VE. Elastic tension of non-planar strips with asymmetric out-of-flatness for the biquadratic law of stress distribution over the width. *Metallurgist*. 2024;68: 239–247.

Submitted: April 29, 2024 Revised: February 17, 2025 Accepted: April 28, 2025

Al-driven modeling and prediction of mechanical properties of additively manufactured Al-6061/B₄C composite

D. Kumar ¹ (10), S. Singh ², P.K. Karsh ³ (10), A. Chauhan ⁴ (10), G. Saini ⁴ (10), A. Chouksey ⁵ (10),

- ¹ Maharishi Markandeshwar (Deemed to be University), Mullana, Ambala, India
- ² Chandigarh Engineering College, Punjab, India
- ³ Parul Institute of Engineering and Technology, Parul University, Vadodara, India
- ⁴ Panjab University SSG Regional Centre Hoshiarpur, Punjab, India
- ⁵ Deenbandhu Chhotu Ram University of Science and Technology, Haryana, India
- [™] kumar.d041789@gmail.com

ABSTRACT

This study investigates the effects of friction stir processing on the mechanical and damping properties of Al-6061 aluminum alloy, reinforced with boron carbide (B₄C) nanoparticles. A CNC milling machine was used to conduct friction stir processing, varying key processing parameters such as rotational speed, feed rate, and the number of passes. The mechanical properties analyzed include ultimate tensile strength, yield strength, natural frequency, and damping ratio. An advanced machine learning approach was implemented using a long short-term memory model optimized with the sine cosine algorithm to predict the processed material's attributes. The experimental findings demonstrate that friction stir processing significantly enhances damping characteristics due to grain refinement, with the highest damping efficiency observed at 1400 rpm. Higher rotational speeds resulted in a notable increase in yield strength, attributed to finer grain structures. The introduction of B₄C nanoparticles further improved damping properties. Additionally, the study found that an increased number of friction stir processing passes decreased shear modulus and natural frequency while increasing the loss factor and damping ratio. The developed machine learning model achieved high predictive accuracy, with R^2 values of 0.981 for the ultimate tensile strength, 0.991 for YS, 0.973 for natural frequency, and 0.995 for damping ratio. The special relativity search-optimized long short-term memory model outperformed other approaches, attaining R^2 values ranging from 0.961 to 0.998 during training and 0.919 to 0.992 during testing. These findings highlight the effectiveness of friction stir processing in enhancing material properties and the superior predictive capability of machine learning models in capturing the effects of processing parameters.

KEYWORDS

FSP • CNC • Al-6061 • microstructural evolution • material toughness • deformation desistance • LSTME optimization techniques • SRS

Citation: Kumar D, Singh S, Karsh P K, Chauhan A, Saini G, Chouksey A, Kumar P. Al-driven modeling and prediction of mechanical properties of additively manufactured Al-6061/B₄C composite. *Materials Physics and Mechanics*. 2025;53(2): 123–141.

http://dx.doi.org/10.18149/MPM.5322025_11

Introduction

Friction stir processing (FSP) is a material processing technology that operates without melting and is based on the principles of friction stir welding (FSW) [1]. It is utilized to modify the microstructure and properties of materials, specifically metals and alloys. In the FSP procedure, a specially designed rotating tool is introduced into the material



and maneuverer along the designated trajectory [2]. The rotating tool generates heat via friction, resulting in the material softening without beyond its melting point. As the instrument advances, it mechanically stirs the substance, resulting in the disintegration and redistribution of the microstructure [3]. Upon completion of the stirring process, the material is allowed to cool and undergo recrystallization, resulting in a more refined microstructure with improved mechanical properties. Friction stir processing (FSP) is a commonly employed method for objectives including grain structure refinement, alloy component homogenization, microstructural modification, surface enhancement, and defect rectification in castings and welds [4]. The method is versatile and can be used to a wide range of metallic materials, including aluminum, magnesium, titanium, steel, and their alloys. FSP offers numerous advantages over traditional processing techniques, including reduced operating temperatures, minimized distortion, and improved mechanical properties [5].

Friction stir processing (FSP) significantly improves specific mechanical properties of materials [6]. FSP does this by enhancing the microstructure of materials, resulting in a more uniform grain distribution and a reduction in grain size [7]. This refinement frequently enhances the material's tensile strength, becoming it more resilient and less susceptible to deformation. Similar to tensile strength, FSP improves the yield strength of materials by refining the grain structure and promoting a more uniform distribution of alloying elements [8]. As a result, the material demonstrates enhanced resistance to deformation and can endure greater levels of stress prior to yielding. FSP can alter the microstructure and texture of materials, hence affecting their intrinsic frequency. Friction stir processing (FSP) enhances the natural frequency of materials by refining the grain structure and introducing compressive residual stresses, hence increasing their applicability for applications requiring high vibration resistance [9]. FSP may improve the damping characteristics of materials by generating fine, equiaxed grains and promoting a more uniform distribution of alloying elements. Microstructural refinement enhances the material's ability to absorb mechanical energy, resulting in an increased damping ratio and improved vibration-damping properties [10]. Friction stir processing (FSP) offers a versatile and cost-effective approach to improving the mechanical properties of materials, rendering it applicable across several sectors. The capacity to manufacture lightweight, robust components with enhanced durability and performance makes it an attractive option for industries that emphasize material properties [11]. The improvements make FSP-processed materials highly desirable for various applications, including aerospace, automotive, marine, and structural engineering [12]. Traditional mathematical modeling techniques and machine learning (ML) present both advantages and limitations in accurately simulating friction stir processing (FSP) [13]. The finite element method (FEM) is commonly utilized for simulating FSP. The procedure involves dividing the substance into small components and employing mathematical formulas to analyze each component [14]. The finite element method (FEM) can deliver accurate estimates regarding temperature distribution, material flow, and residual stresses during friction stir processing (FSP) [15]. Nonetheless, the finite element method (FEM) requires simplifications and assumptions, potentially leading to an inadequate depiction of the complex physical processes occurring during the finite element analysis. Analytical models, such as heat conduction and flow models, provide more straightforward

mathematical representations of FSP [16]. These models exhibit remarkable efficiency regarding computational resources and can swiftly provide estimations of essential process parameters. Nonetheless, analytical models may simplify the physics of FSP and may not adequately capture all the complexities of the process. Machine learning (ML) techniques extract complex patterns and relationships from data and can be trained to predict several aspects of FSP, including temperature distribution, material flow, and microstructure evolution. This technique can successfully capture non-linear correlations and complex interactions among process components, perhaps resulting in greater accuracy than traditional models. Nonetheless, these models require significant amounts of data for training and may overfit the training data if not sufficiently regularized [17]. Machine learning methods can achieve more accuracy than conventional mathematical modeling techniques, especially when addressing complex, non-linear interactions. Machine learning techniques typically require a significant amount of data for training, while conventional modeling approaches tend to prioritize theoretical equations and assumptions [18]. Traditional modeling methodologies are frequently more intelligible because of their dependence on physical equations and principles [19]. Conversely, machine learning models are often perceived as opaque, creating difficulties in comprehending the underlying relationships. Machine learning optimization can significantly reduce processing costs relative to traditional optimization techniques [20]. Machine learning models can learn from current data and effectively ascertain optimal parameter values, hence obviating the necessity for expensive simulations or experiments. Upon completion of training, machine learning models may be seamlessly transferred to new datasets or FSP applications with minimal further work [21]. This facilitates the effective fine-tuning of FSP parameters for diverse materials, geometries, or processing conditions. Machine learning algorithms can autonomously identify and ascertain significant attributes and correlations within the data, hence reducing the necessity for manual feature engineering. This is particularly beneficial for FSP, as the relationships between process parameters and output variables can be complex and difficult to delineate using traditional methods [22].

This work employed aluminium alloy 6061 (Al-6061) as the matrix material in metal matrix composites (MMCs), with boron carbide (B₄C) acting as the reinforcement. Al-6061/boron carbide MMCs exhibit a combination of lightweight, remarkable strength, and wear resistance, making them suitable for various applications across multiple industries [23]. The Al-6061/boron carbide metal matrix composites possess the capability to improve mechanical properties such as strength, stiffness, wear resistance, and corrosion resistance [24]. The characteristics of boron carbide reinforcement particles can be tailored according to their volume percent and dimensions, leading to a lower density in comparison to steel [25]. This renders them ideal for lightweight applications. Advanced machine learning techniques provide a novel approach for forecasting optimal processing parameters in friction stir processing (FSP) of Al-6061 alloy augmented with boron carbide nanoparticles [26]. Our objective is to employ machine learning to efficiently optimize the FSP parameters to enhance the mechanical properties and performance of the composite material [27]. This innovative method offers a data-driven strategy to enhance the efficiency and effectiveness of the FSP process, yielding superior Al-6061/boron carbide nanocomposites tailored for high-performance applications [28].

The mechanical properties and dynamic features of the materials were evaluated under different processing circumstances. The research employed cutting-edge machine learning methods to predict the sample's attributes. This approach enhances a comprehensive model of a long short-term memory (LSTME) with the application of a sine cosine algorithm (SRS) technique. The created model was assessed in a performance evaluation with three other machine-learning methods.

Materials and Method

Matrix and Reinforcement

A sheet of aluminum alloy consisting of Al-6061 and having a thickness of 4 mm served as the foundation of the construction. For the purpose of reinforcing, the B₄C nanoparticle was utilized. The results of the chemical analysis that was carried out on the FSP tool and the aluminum alloy with the use of a spectroscopic analyzer are shown in Table 1.

Table 1. Composition of Al-6061 alloy

Elements	Si	Mg	Cu	Fe	Mn	Cr	Al
Wt. %	0.510	0.797	0.219	0.257	0.043	0.157	98.000

According to the results of the transmission electron microscopy (TEM) study, the reinforcing particles displayed a distinguished degree of purity, with a measurement of 99.9 %. Furthermore, the average size of these particles was determined to be 16 ± 5.6 nm, as seen in Fig. 1.

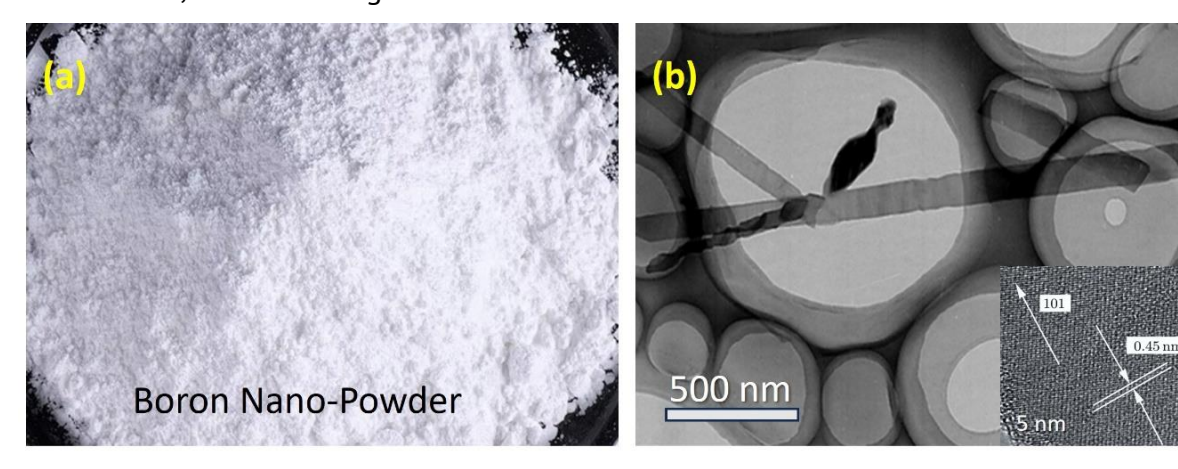


Fig. 1. (a) B₄C powder in typical form and (b) TEM Analysis of B₄C nanoparticles

Processing method

In order to change the microstructure and characteristics of a material, a solid-state joining technique known as friction stir processing (FSP) is utilized. This process makes use of frictional heat and mechanical deformation [29]. In order to form longitudinal grooves in which reinforcing particles will be included, an aluminum sheet is given the preparation necessary for milling. During the FSP process, a tool that has a taper square shape is chosen. With the tool that was chosen, the CNC milling machine is prepared for use. It is then that the tool comes into touch with the aluminum sheet that has been

prepared. As it moves down the sheet, the tool creates grooves that run in a longitudinal direction. The tool rotates at a variety of rates during this operation, including 900, 1150, 1400, and 1650 revolutions per minute, and it travels at a variety of traverse speeds, including 10, 15, and 20 mm/min throughout the procedure [30].



Fig. 2. (a) FSP processing and (b) tool dimensioning

After the FSP technique has been completed, the samples are subjected to grinding using silicon carbide paper that has grit sizes ranging from 220 to 2500. This is done in order to remove any surface flaws that may now exist. A water wash is subsequently performed on the ground samples in order to remove any abrasive residue or metal particles that may have been present. We use a solution that consists of three milliliters of hydrofluoric acid with a concentration of fifty percent, eight milliliters of a solution of nitric acid, and seventy milliliters of filtered water as the solvent. This solution is used to etch the samples. For the purpose of revealing both the microstructure and the macrostructure of the materials that have been treated, this etching method is carried out at room temperature. Until the required degree of surface quality is attained, the etched samples are examined in great detail in order to investigate the microstructure and macrostructure of the materials that have been treated. Etching is used to clean samples before they are then subjected to analysis.

In order to determine the magnitude of the treated region, we extracted dog bone-shaped samples from the central portion of the treated zone and sliced them into flat pieces. According to the criteria established by ASTM, these samples were sliced. To carry out the tensile testing, a universal testing machine (UTM) with a maximum load capacity of one hundred kilonewtons was deployed. Specific dimensions were required for the samples in accordance with the standards of ASTM B557: The width is 13 mm, the thickness of the sheet is 6 mm, the gauge length is 50 mm, the parallel length is 100 mm, the grab section length is 70 mm, and the shoulder radius is 5 mm. Through an examination of the composite surface's free vibration, the scientists were also able to determine the natural frequency and damping factor of the surface materials. The authors decided to connect accelerometers to the cut samples and monitor the vibration response of the material in order to gain a better understanding of how the material deteriorates over time.

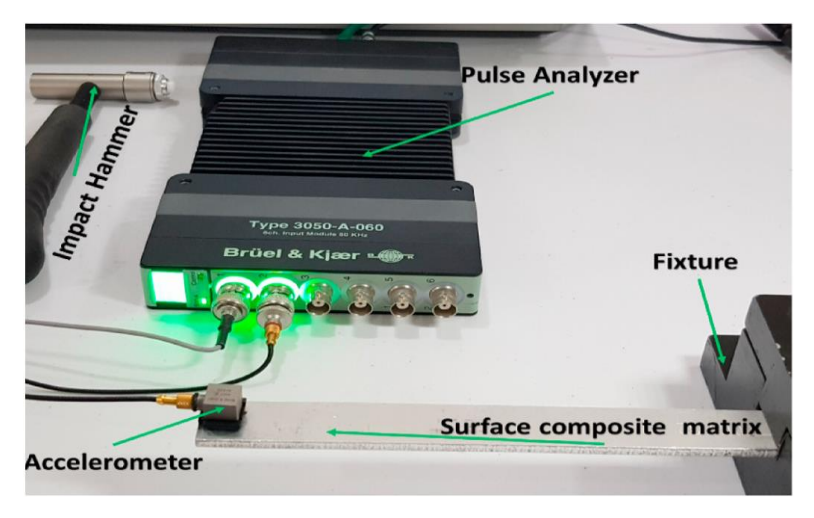


Fig. 3. 3050 Pulse analyzer to evaluate free impact vibration

A pulse data analyzer (3050 K&B vibration analyzer, Denmark) and an impact hammer (8206 K&B vibration analyzer, Denmark) were utilized in order to accomplish this task. The free vibration experiment was carried out five times as part of the procedure to guarantee the accuracy of the findings. The frequency response function (FRF), damping ratio, and fundamental frequencies of the material were all estimated via a modal analysis application known as I Scope.

Special Relativity Search Modeling Approach

One of the innovative approaches to modeling is known as the special relativity search (SRS) technique. SRS provides a fresh viewpoint on the optimization of machine learning models, and it is influenced by ideas from theoretical physics, in particular special relativity.

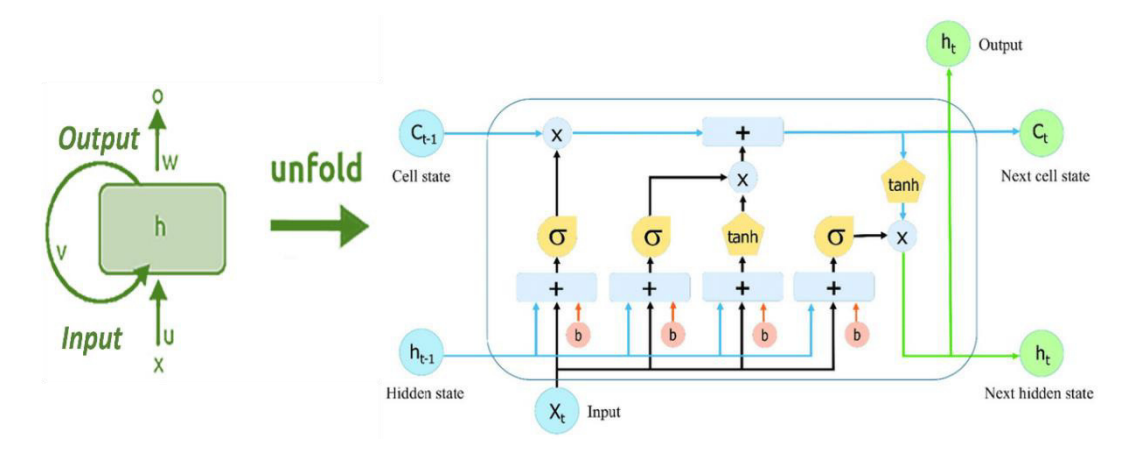


Fig. 4. Systematic view of LSTME network

The concept of relativistic transformations is the fundamental idea behind SRS. In this kind of transformation, variables are dynamically altered according to the relative significance they hold and the contribution they make to the overall performance of the model. SRS takes into consideration the inherent linkages and dependencies among variables, which is analogous to the relativistic effects that are observed in high-speed

motion. This is in contrast to typical optimization approaches, which handle variables in a uniform manner. The following are important elements that make up the SRS.

The variable transformation: variables undergo a transformation that is comparable to the relativistic effects, in which their values are modified according to the relevance of the variables in relation to other variables and the overall purpose of the model.

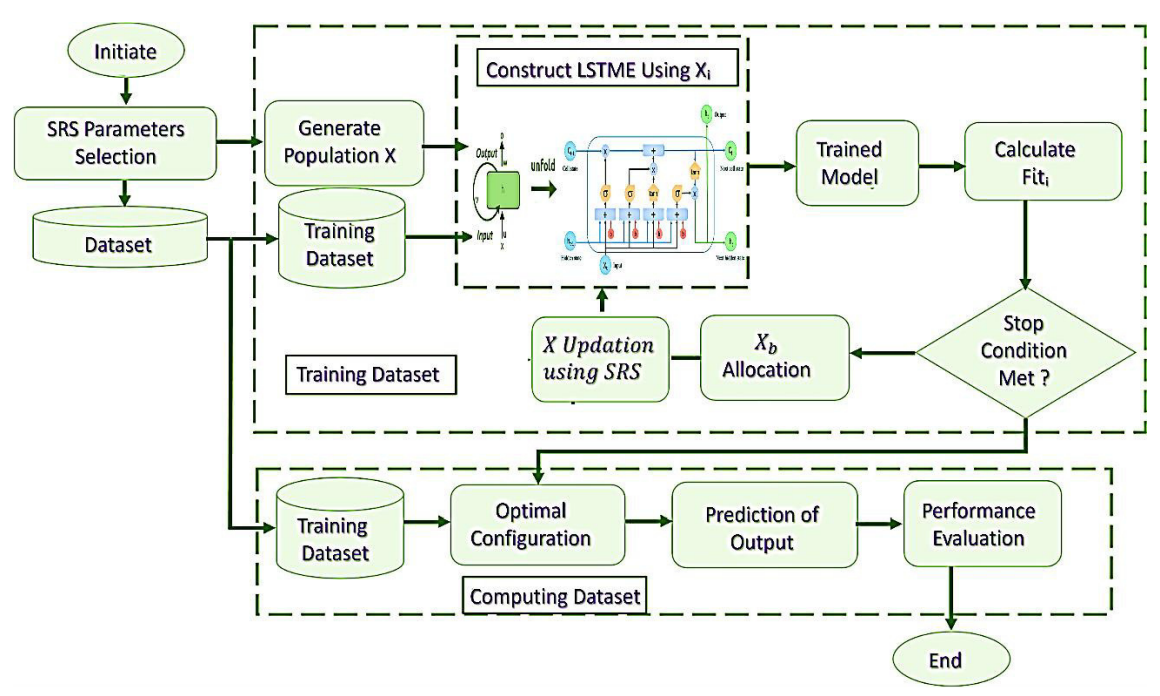


Fig. 5. Special relativity search-based LSTME network model

The concept of dynamic scaling is analogous to the concept of time dilation in special relativity. It is possible for variables to undergo dynamic scaling dependent on the relative significance of the variables. To guarantee that the model remains balanced while giving essential variables a larger weightage, this ensures that the model meets the requirements.

Velocity-based optimization: special relativistic systems (SRS) use velocity-based optimization approaches to iteratively tune variable transformations. These techniques are inspired by the idea of velocity in special relativity. The model is able to dynamically adapt to changing data dynamics and optimization goals as a result of this.

Not only does SRS take into account the spatial correlations between variables, but it also takes into account the temporal dynamics of those variables. Because of this, the model is able to recognize complex patterns and relationships across time, which greatly improves its ability to make accurate predictions.

Nonlinear transformations: SRS makes use of nonlinear transformations in order to capture both complicated relationships and interactions among variables. This helps to improve the expressiveness of the model as well as its ability to accurately predict future outcomes.

Results and Discussions

Dynamic characteristics

The results of the research investigation, which are presented in Figs. 6-8, unequivocally demonstrate that there is a direct connection between the FSP Parameters and the damping ratio. However, the capacity to reduce vibrations may be enhanced at a specific ideal rotational velocity. This is something that can be done.

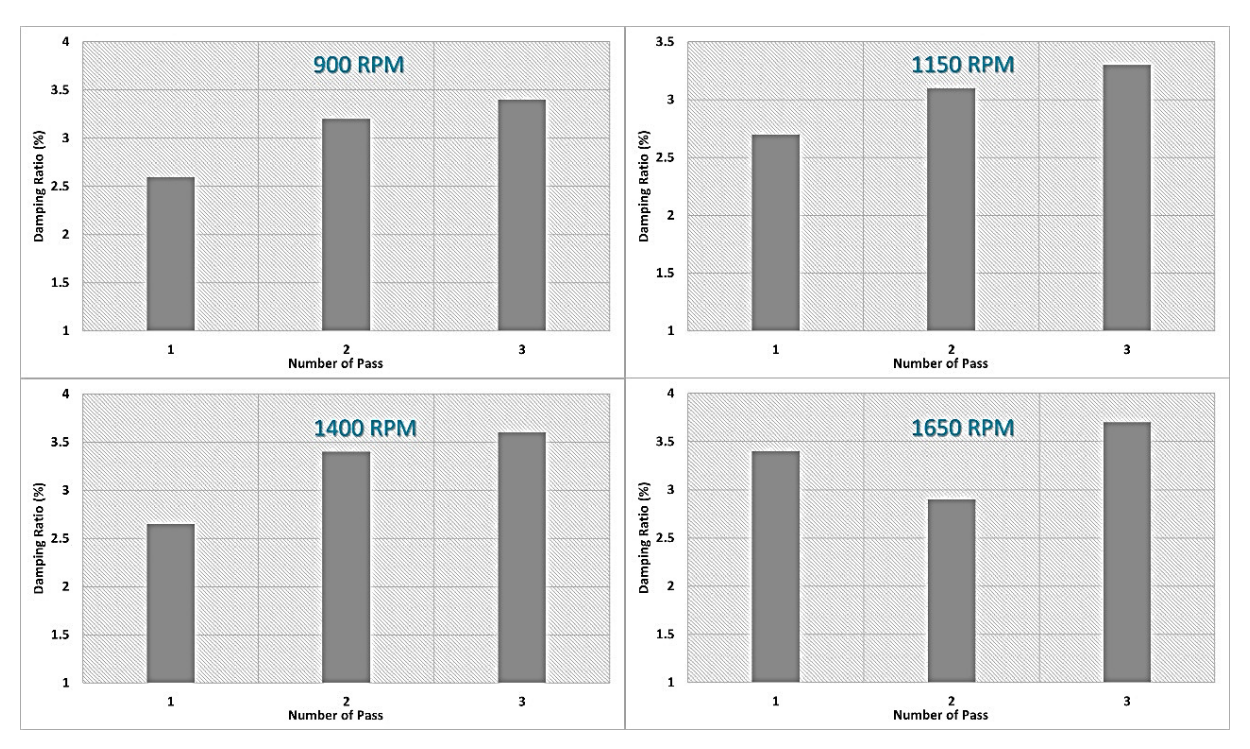


Fig. 6. Damping capacity of the samples at a traverse speed of 10 mm/min

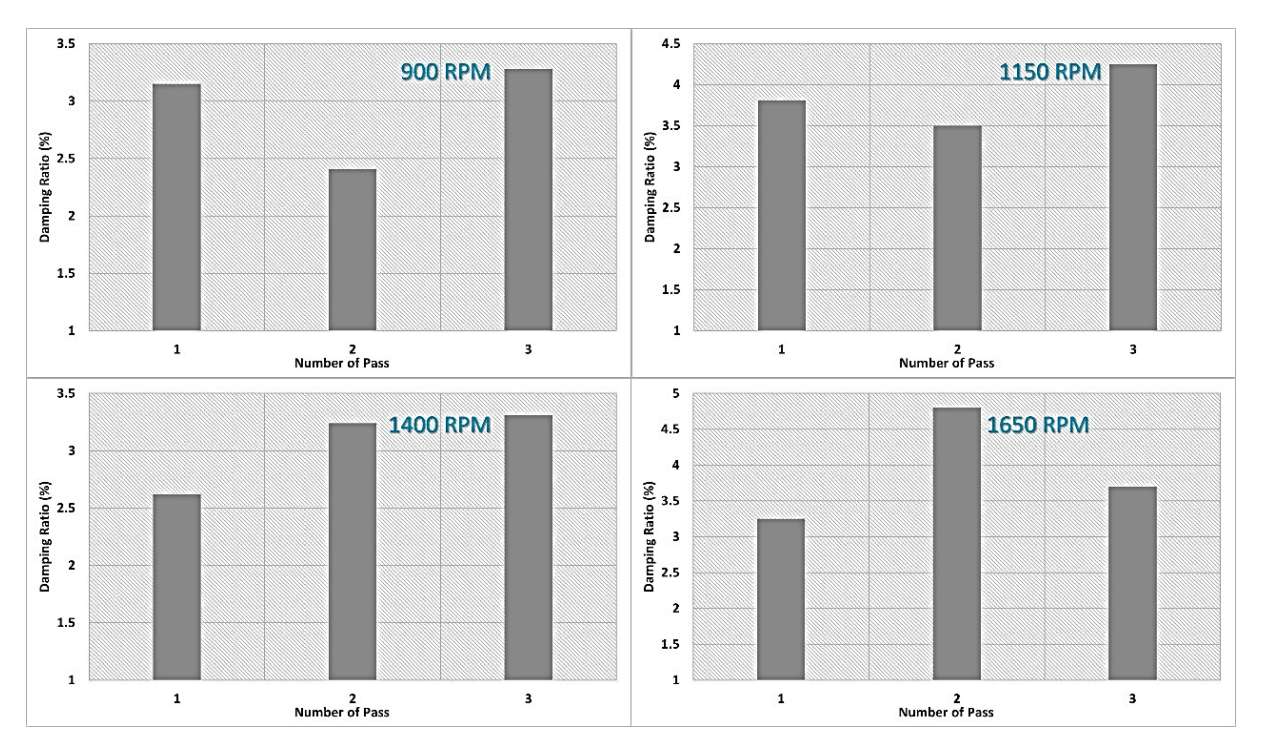


Fig. 7. Sample's damping ratio at 15 mm/min traverse speed

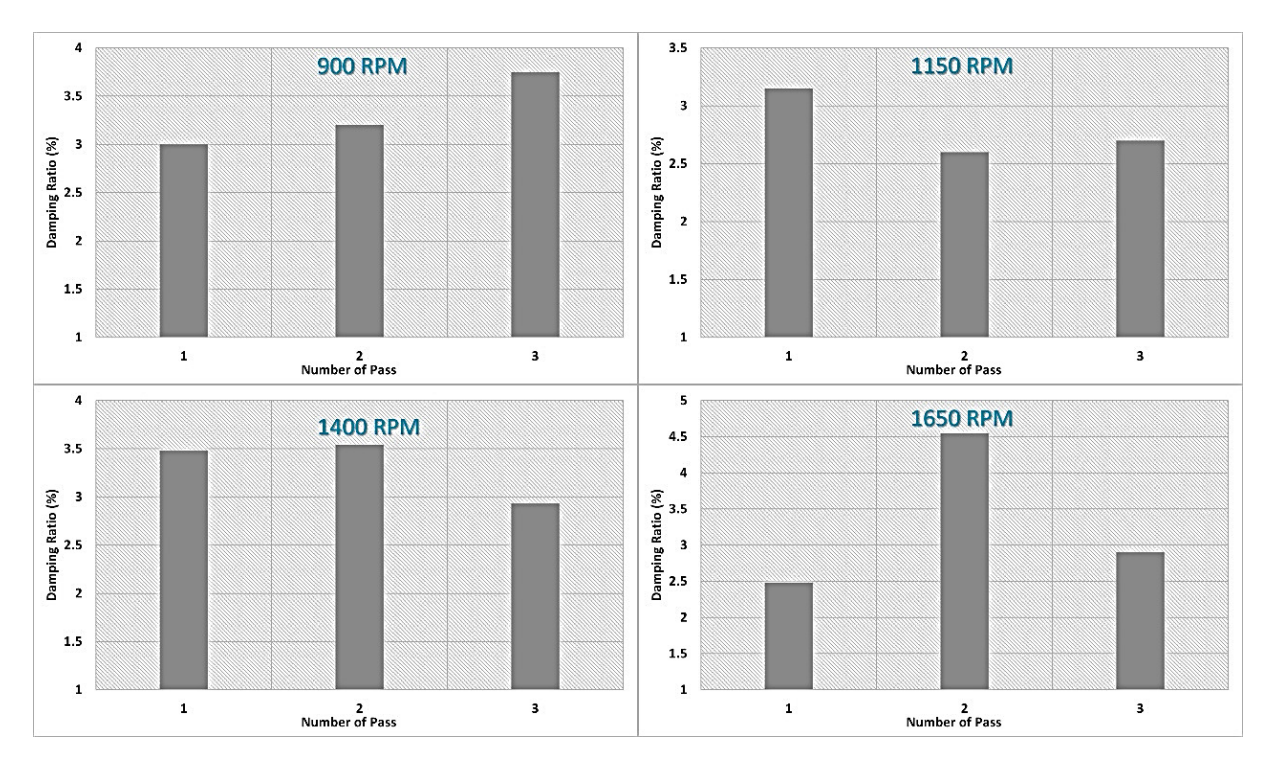


Fig. 8. Damping capacity of the samples at a traverse speed of 20 mm/min

According to the technical point of view, the rotational speed was set at 900 revolutions per minute, which resulted in the highest degree of damping capabilities being attained in all of the testing scenarios. One may have a better understanding of the events by examining the link that exists between the rate of thermal energy creation and the rotational velocity. The microstructure becomes more uniform and finely distributed as a result of the breakdown of the constituent grains of the material, which is induced by the excessive heat. There is an improvement in its capacity to absorb and reduce vibrations as a result of the increased density of its streamlined shape.

Based on the statistical study, it was determined that the damping capacity did not change regardless of the pace of travel. Specifically, this can be related with two primary variables: There is a possibility that the experiment's travel speed range was too limited to find any obvious change in damping capacity. This is something that may be considered at first appearance.

There is a possibility that the oscillations in damping capacity numbers are responsible for concealing the actual impact of transit speed. By incorporating boron carbide nanoparticles into the metal matrix, the vibration dampening capabilities of the material were significantly improved. In order to achieve this improvement, it was established that the concentration of nanoparticles in the matrix was the most important parameter. As the ratio of nanoparticles was raised, there was a corresponding rise in the improvement of damping capacity that was observed.

When the number of passes is increased, the natural frequency of the samples decreases in proportion to the increase. Repetitive agitation of the instrument results in the breakdown of material particles, which in turn leads to a reduction in stiffness and the subsequent production of this phenomena. However, increasing the number of passes results in samples that have a higher damping ratio. This is the opposite of what you

would expect. As a result of the agitating action, the grain structure is improved, which in turn increases the presence of flaws and improves the grain's ability to collect and absorb vibrations. In a similar vein, the sample loss factor will increase in proportion to the growing number of different passes. Because of the presence of a grain structure that is more accurate, there has been an increase in the amount of frictional losses recorded. During vibration, the amount of energy that is transformed into heat is quantified by the loss factor, which is the opposite of the energy conversion factor. Increasing the number of passes also results in a decrease in the retained modulus of the samples. There is a high probability that the reason is the deterioration of the grain structure, which leads to a decreasing elasticity. Increasing the number of passes results in a loss modulus trend that is comparable to the one we saw in the samples. The main justification for this occurrence is supplied by the loss modulus, which quantifies the energy dissipation that happens during vibration; materials with finer grain patterns show higher levels of frictional losses. This is the core rationale for this occurrence.

Table 2. Significant Process Parameters of FSP Process

Rotational speed, rpm	Number of passes	Transverse speed, mm/min	Damping ratio (ζ)	Loss factor	Shear modulus, MPa
1650	3	20	2.98	0.058	26.12
900	3	15	3.57	0.072	25.91

The differences in the dynamic properties of the samples at different RPMs are summarized in Table 2, which gives a short summary of the subject matter. The natural frequency of each specimen decreases as the revolutions per minute (RPM) rises. This occurs as a result of the increased heat generated by the greater spinning speed, which leads to the grain structure being more disorganized and the material becoming less rigid. In spite of the fact that the samples indicate a decrease in stiffness, the damping ratio demonstrates an increase as the RPMs climb. The reason for this is because the grain structure has been polished much further, which makes it possible for imperfections to absorb and attenuate vibrations more effectively. Increasing the rotational speed also results in a rise in the loss factor, which is a measurement of the amount of energy that is lost during vibration. At faster speeds, the grain structure becomes finer, which results in larger frictional losses. This is the reason why this is the case. The shear modulus of the samples falls as the revolutions per minute (RPM) increases. The frequent agitation of the tool is responsible for this phenomenon. This agitation causes the particles of the material to break down, which ultimately leads to a reduction in the material's flexibility. The loss modulus of the sample, which is a measure of the amount of energy that is lost during vibration, likewise increases as the speed at which the sample is spinning increases. When rotational velocities are raised, a finer grain structure is formed, which results in increased frictional losses. This is the reason why this circumstance occurs. A direct association exists between the rise in the complex moduli of the samples and the increase in rotational speed. This correlation also exists between the two variables. The complex modulus is a mathematical representation of the overall stiffness and damping qualities of the material. Shear modulus of the samples decreases as the revolutions per minute (RPM) increases. The rationale for this is because increasing the RPMs makes it more difficult to shear the grain structure that is smaller, which ultimately results in a reduction in the shear strength. The results of this study demonstrate that the dynamic characteristics of the samples are altered when the rotational speed of the samples increases during the processing phase.

The results of the study indicate that there is a clear connection between the rate of rotation and a number of dynamic properties of the specimens. As the revolutions per minute (RPM) increases, the natural frequency and shear modulus drop. This is because the increase in dampening ratio and loss factor was observed to be the reason for the decline. According to the findings of the study, friction stir processing has the potential to significantly improve the damping capabilities of materials by producing a grain structure composition that is more refined. This more finely structured grain structure makes it possible to inject a greater number of faults into the material, which in turn helps the material to more effectively catch and absorb vibrations. As an additional point of interest, the findings provide light on the connection that exists between the speed at which an object is moving and its capacity to dampen vibrations. The dampening effect is also enhanced by traverse speed, which is similar to the impact of rotational speed. The greater thermal energy that is created during the process assists in dissolving granules, which in turn reduces the stiffness of the encapsulated particles. Additionally, the creation of a finer grain structure at greater traversal speeds increases the presence of defects in the material, which in turn enhances the material's capacity to catch and absorb vibrations.

Mechanical properties

The grain structure is refined using the friction stir surface processing, which has a major impact on the mechanical properties of the materials through its use. A highly prominent average grain size of around 142 μ m is observed in the earliest stages of the Al-6061 base alloy, which exhibits an aspect ratio of approximately 32.3 % within the initial stages. As a result of three rounds of FSP, the average grain size falls to 12.92 μ m, while the aspect ratio increases to 91.8 %.

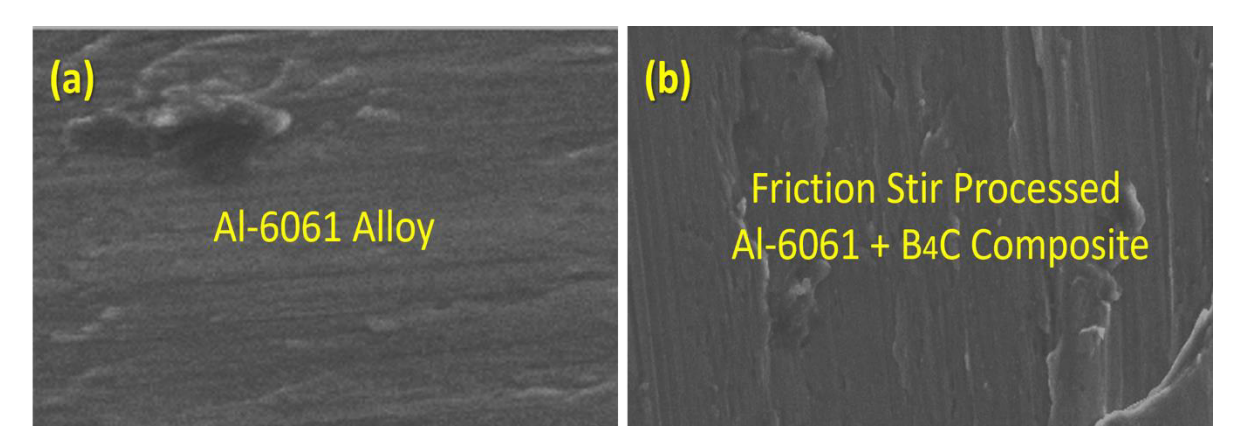


Fig. 9. Optical microscope (a) Al-6061 alloy and (b) Al-6061/B₄C FSP-ed composite

The microstructure picture shown in Fig. 9 illustrates that a reduction in grain size is a strong indicator that the grain structure has been successfully refined by FSP. The

results of the investigation suggest that there is a connection between the mechanical characteristics and the rotating speed of the instrument.

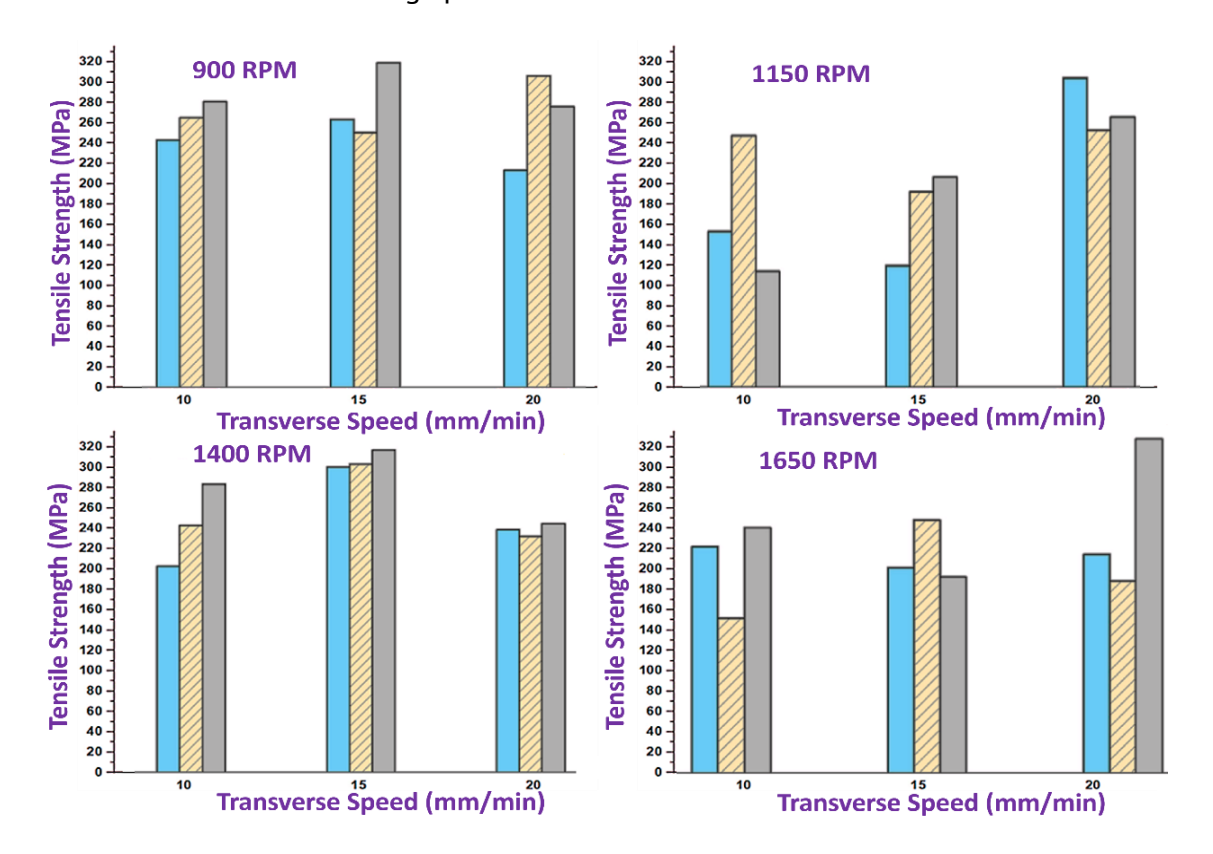


Fig. 10. Tensile strength of the specimens at different RPM (a) 900 RPM, (b) 1150 RPM, (c) 1650 RPM and (d) 1400 RPM

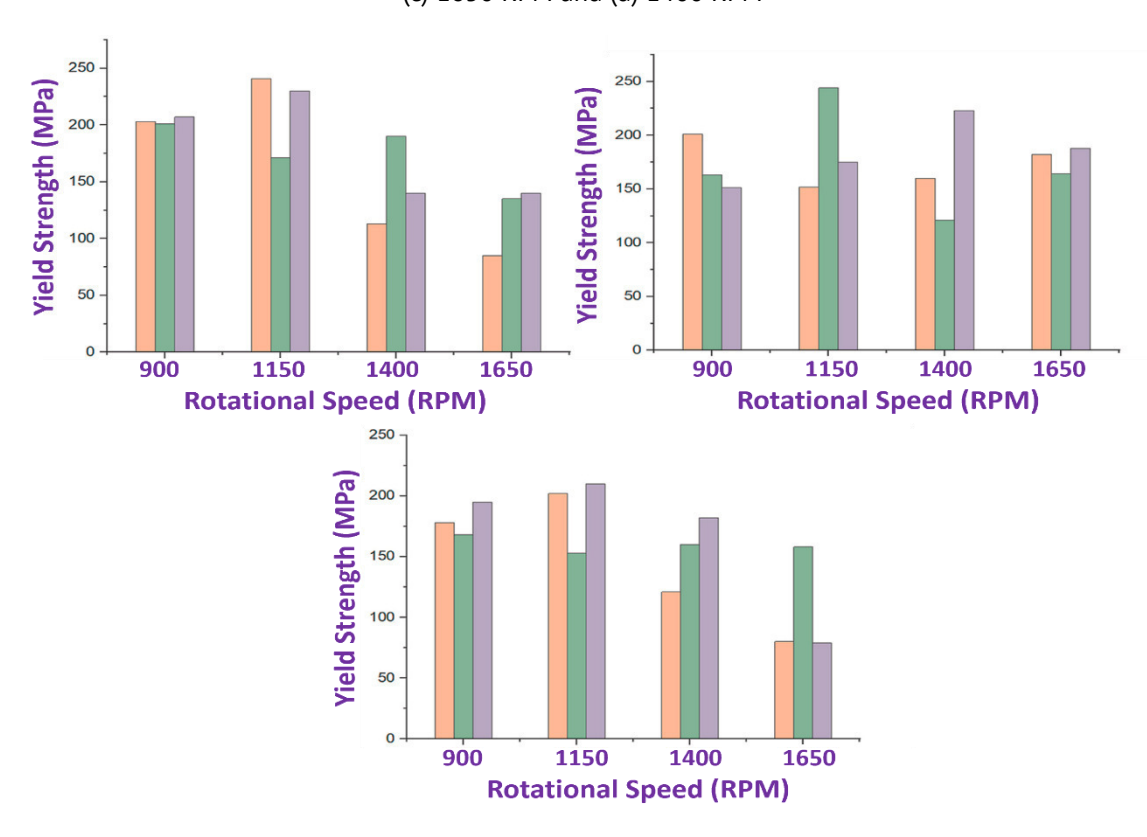


Fig. 11. Yield strength of the specimens at different RPM

It has been observed that the rotating speeds have a beneficial impact on the ultimate tensile strength (UTS) and yield strength (YS) of the samples, which ultimately results in the increase of these properties (Figs. 10 and 11). There is a clear correlation between the higher speeds, which creates more heat, and the disintegration of grains, which is a direct result of the stronger material. The more finely organized microstructure that results from higher rotational velocities is responsible for the increased yield strength of the material. Additionally, the material's capacity to tolerate deformation is enhanced, which leads to an increase in the material's yield strength. Increasing the number of FSP passes results in a drop in both the yield and ultimate tensile strengths (UTS and UTS, respectively). As a result of the frequent agitation of the instrument, the grains gradually get fragmented, which ultimately compromises the structural integrity of the material. In a similar vein, decreasing the feed rate causes a slower dissipation of heat, which in turn leads to a drop in mechanical properties as a result of less grain disintegration.

Predicted results

In order to make predictions about the characteristics of the processed data, this research endeavor makes use of four different machine-learning models. The UTS, YS, natural frequency, and damping ratio are all included in the models respectively (Fig. 12–15). In contrast to the subsequent three models, which combine LSTME with optimization strategies, the first model is an independent LSTME. The LSTME-FHO, the LSMTE-SRS, and the LSTME-DMOA are some of the optimization strategies that are discussed in this article. Both the training and testing of the models are carried out with the use of empirical data.

The remaining thirty percent of the data is reserved for testing, while seventy percent of the data is given up to training. In order to evaluate the effectiveness of each model, three different indicators of accuracy are utilized. The root mean square error (RMSE), the coefficient of determination (R^2), and the mean absolute error (MAE) are the metrics that are utilized in this study.

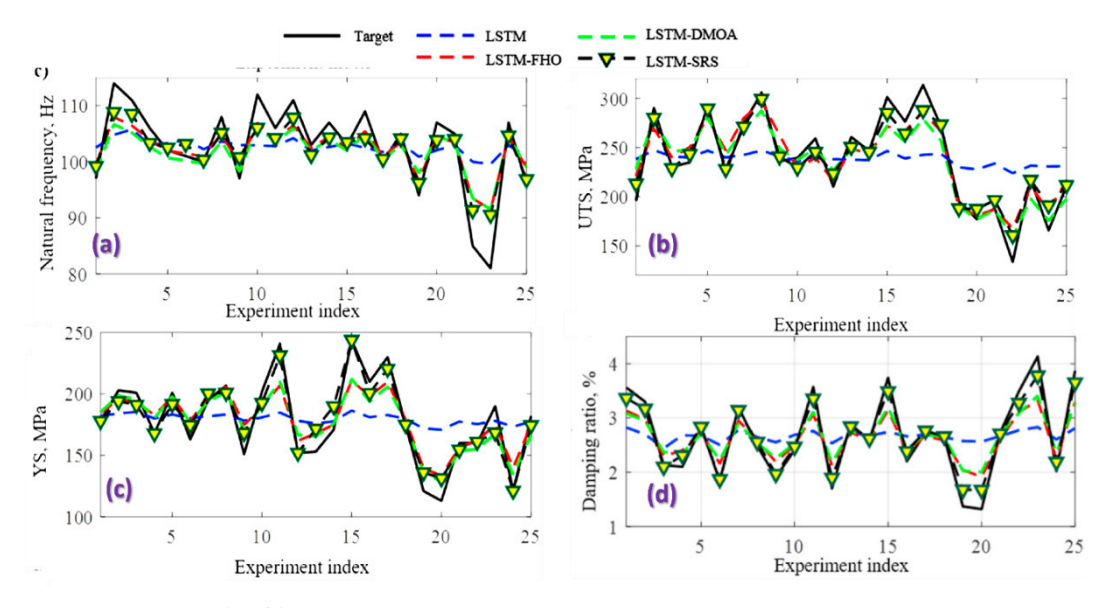


Fig. 12. Training process of experimental and predicted data

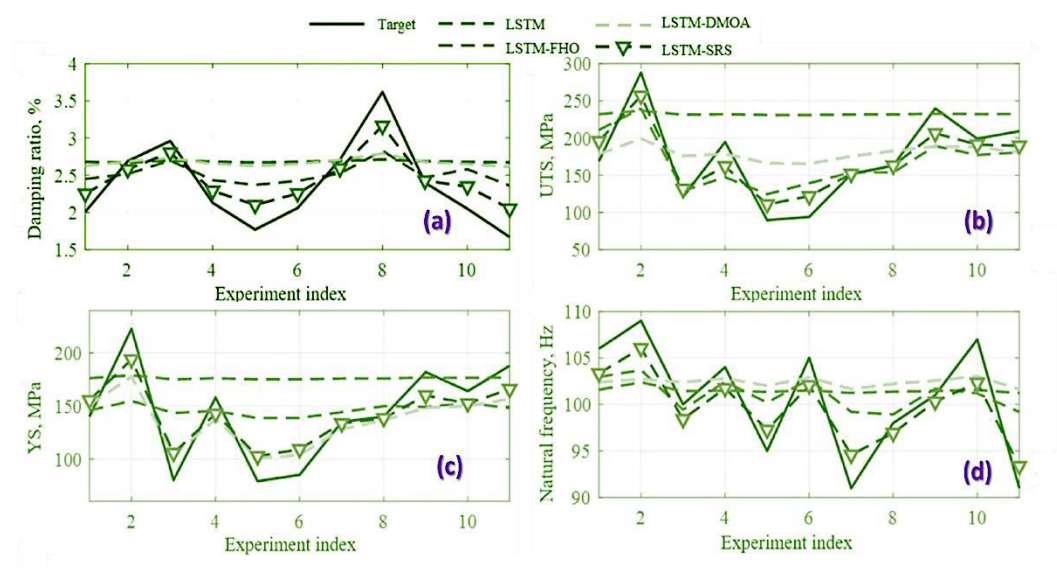


Fig. 13. Testing process of experimental and predicted data

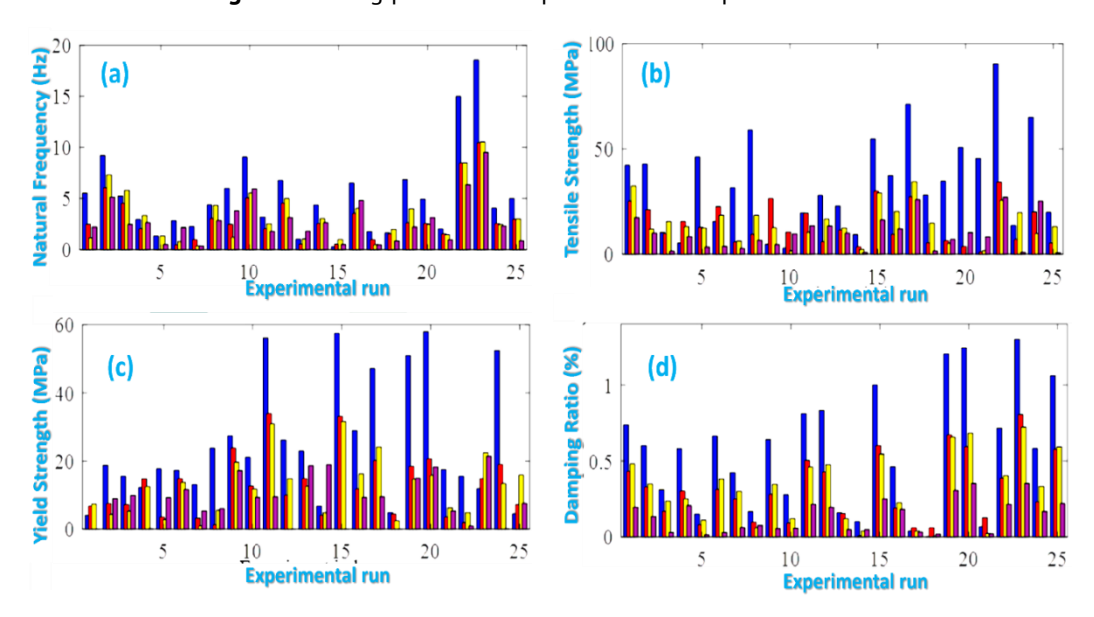


Fig. 14. Training processing error of experimental and predicted data

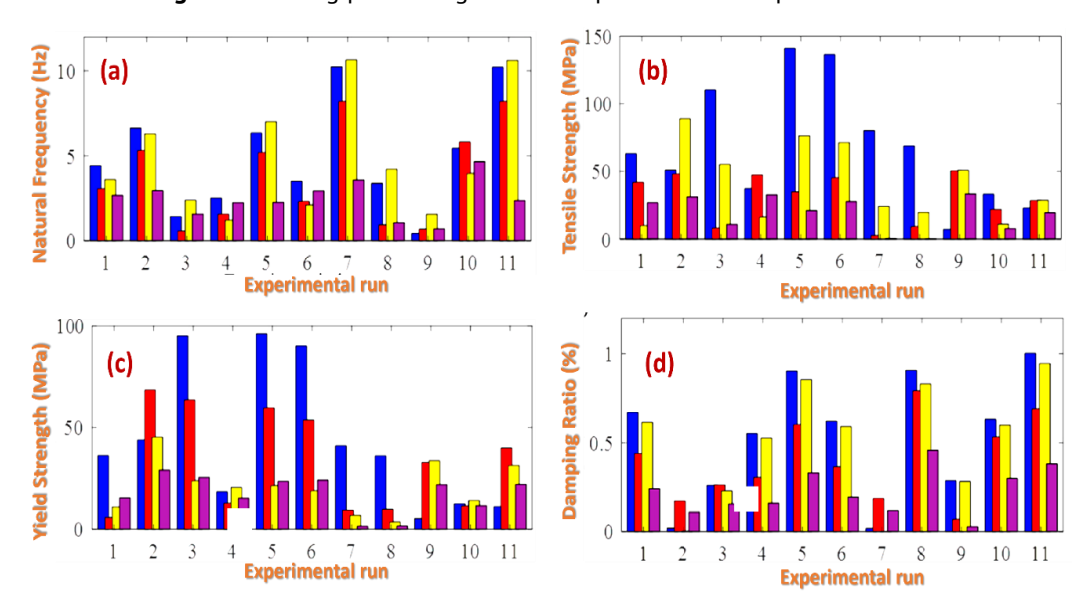


Fig. 15. Testing processing error of experimental and predicted data

According to the findings, there is a significant connection between the data that was obtained through experimentation and the data that was projected. When compared to the performance of all of the other models that were used, the LSTME-SRS model demonstrated higher performance, with the LSTME-DMOA and LSTME-FHO models following closely behind a close second. Throughout the entirety of the training and testing stages, the independent LSTME model demonstrates the least level of agreement with the experimental data.

A further demonstration of the agreement is provided by the absolute error research, which demonstrates that the LSTME-SRS consistently has the lowest error across all features. This demonstrates that it has a stronger predictive potential. The absolute errors that are exhibited by LSTME-DMOA and LSTME-FHO are relatively low when compared to the errors that are created by LSTME-SRS and the solo LSTME model.

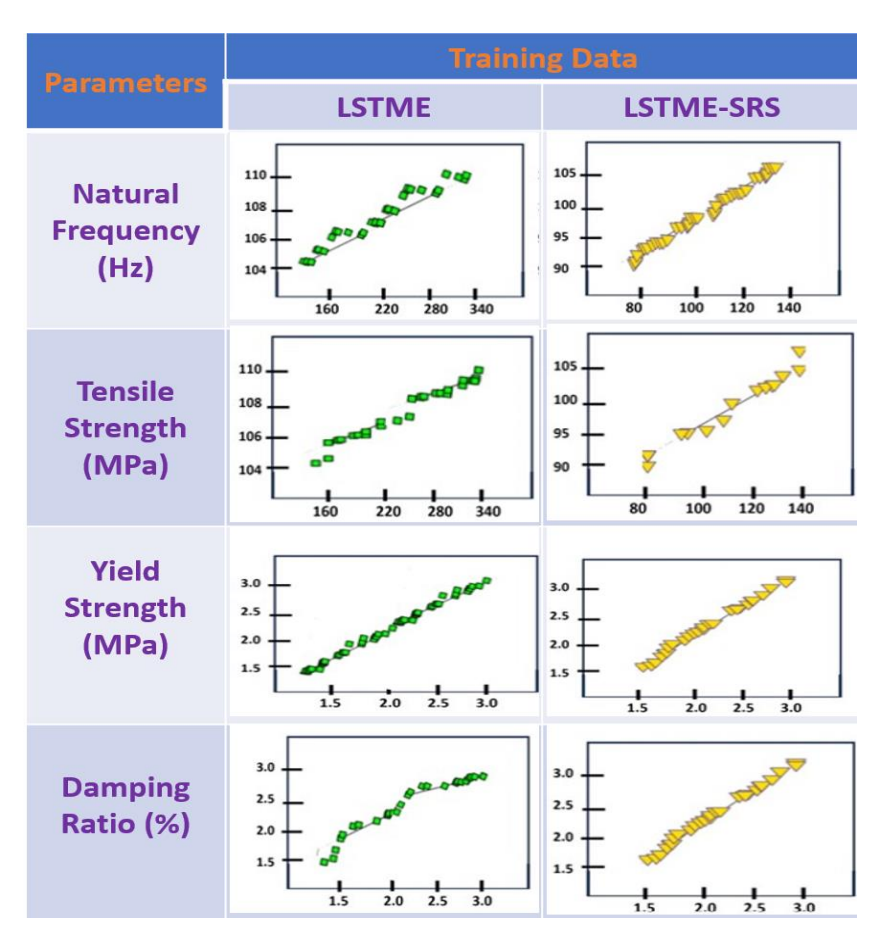


Fig. 16. QQ plots during training and testing of data

Considering the extraordinary capacity of the LSTME-SRS algorithm to generate the least amount of absolute error, it is clear that the algorithm is highly effective in accurately predicting a wide variety of characteristics of the processed data. In terms of prediction accuracy, our findings indicate that LSTME-SRS performs better than other models, which suggests that it is able to successfully anticipate the characteristics of processed data. When LSTME-DMOA and LSTME-FHO are compared to LSTME-SRS in the QQ graphs shown in Fig. 16, there is a stronger link between the anticipated data and the actual data.

The statement is made in respect to the other two ideas that have been proposed. In comparison to the other models that were examined, the single LSTME model demonstrates the least amount of connection with the available experimental data. The close connection or proximity of the yellow outcomes to the diagonal lines is evidence that the predictions produced by LSTME-SRS are accurate. This proximity can be observed in the yellow results. The projected data that was created by the independent LSTME model, which is represented by a light blue color, on the other hand, displays a higher distance from the diagonal lines. The fact that this gap exists is more evidence that LSTME-SRS performs better than LSTME, LSTME-FHO, and LSTME-DMOA in terms of performance in terms of accuracy. In order to evaluate the correctness of the models, a number of performance metrics were utilized. These metrics included R^2 , MAE, and RMSE measures.

Table 3. Machine-learning model and performance measures

Droportics	Models	Training data			Testing data		
Properties		R ²	RMSE	MAE	R ²	RMSE	MAE
11142	LSTME-SRS	0.969	12.446	9.735	0.916	22.820	19.373
Ultimate	LSTME-FHO	0.903	16.867	1.399	0.708	65.429	30.877
tensile	LSTME-DMOA	0.899	17.088	14.439	0.889	49.553	41.315
strength, MPa	LSTME	0.792	40.970	34.291	0.725	81.095	68.701
	LSTME-SRS	0.971	10.878	8.539	0.958	19.681	17.526
Yield strength,	LSTME-FHO	0.907	15.444	12.581	0.760	40.988	33.503
MPa	LSTME-DMOA	0.948	15.137	12.636	0.939	24.136	21.052
	LSTME	0.886	30.813	25.397	0.865	55.295	44.406
	LSTME-SRS	0.982	2.817	2.232	0.957	2.697	2.475
Natural	LSTME-FHO	0.969	5.785	4.478	0.714	4.715	3.824
frequency, Hz	LSTME-DMOA	0.928	5.610	4.435	0.849	5.875	4.900
	LSTME	0.671	6.707	5.260	0.544	5.866	4.984
	LSTME-SRS	0.997	0.173	0.139	0.990	0.259	0.228
Damping ratio (ζ)	LSTME-FHO	0.993	0.376	0.309	0.827	0.461	0.407
	LSTME-DMOA	1.004	0.389	0.318	0.982	0.592	0.501
	LSTME	0.750	0.691	0.567	0.728	0.632	0.536

To make things easier for you, the findings are presented in a condensed version in Table 3. The prediction efficacy of diverse LSTM-based models for ultimate tensile strength (UTS), yield strength (YS), natural frequency, and damping ratio (ζ) is assessed utilizing statistical measures including R^2 (coefficient of determination), RMSE (root mean square error), and MAE (mean absolute error). A superior R^2 value denotes enhanced predictive accuracy, and diminished RMSE and MAE values imply decreased prediction mistakes. The LSTME-SRS model routinely surpasses others in all attributes, exhibiting exceptional predictive performance. For UTS, LSTME-SRS attains the maximum accuracy, evidenced by R^2 of 0.969 in training and 0.916 in testing, alongside the lowest RMSE (12.446 and 22.820 MPa) and MAE (9.735 and 19.373 MPa). The LSTME-FHO and LSTME-DMOA models exhibit modest accuracy, however the standard LSTME model has worse performance, achieving R^2 of just 0.725 during testing and considerably elevated error values. Likewise, for yield strength, LSTME-SRS demonstrates enhanced accuracy with R^2 of 0.971 during training and 0.958 during testing, resulting in minimum RMSE (10.878

and 19.681 MPa) and MAE (8.539 and 17.526 MPa). The foundational LSTME model is the least successful, exhibiting R^2 of 0.865 and elevated error metrics. The LSTME-SRS model yields optimal predictions for Natural Frequency, achieving R^2 of 0.982 during training and 0.957 during testing, while exhibiting minimal RMSE and MAE values. Conversely, the base LSTME model demonstrates the worst performance, achieving a testing R^2 of just 0.544. Ultimately, for the damping ratio (ζ), LSTME-SRS achieves exceptional accuracy with R^2 of 0.997 during training and 0.990 during testing, accompanied by negligible RMSE (0.173 and 0.259) and MAE (0.139 and 0.228), establishing it as the most dependable model. The LSTME-DMOA and LSTME-FHO models exhibit satisfactory performance; however, the standard LSTME model is the least successful, demonstrating R^2 of just 0.728 during testing, accompanied by considerably greater error rates. The results underscore the exceptional predictive capability of LSTME-SRS, establishing it as the most efficacious model for predicting material properties, hence providing enhanced accuracy and dependability in forecasting mechanical and vibrational characteristics.

Conclusions

The study utilized a CNC milling machine to perform FSP on Al-6061 aluminum alloy, incorporating boron carbide nanoparticles as reinforcements. The primary objective was to examine the influence of key processing parameters—feed rate, number of passes, and rotational speed—on the mechanical properties of the processed samples. Specifically, the study focused on UTS, YS, natural frequency, and damping ratio. To enhance predictive accuracy, an advanced machine learning approach was employed using LSTME model optimized with SRS. The following conclusions were mentioned follows:

- 1. Friction stir processing significantly improves the damping properties of Al-6061 alloy by refining the grain structure, with maximum damping efficiency observed at 1400 rpm.
- 2. Increasing rotational and traverse speeds enhances both mechanical properties and damping performance, while additional FSP passes improve the damping ratio but reduce the shear modulus and natural frequency.
- 3. The incorporation of boron carbide nanoparticles further improves damping capabilities, contributing to better material performance.
- 4. Higher rotational speeds generate increased thermal energy, promoting grain breakdown and finer grain structures, which enhance yield strength and overall material toughness.
- 5. The SRS-optimized LSTME model demonstrated high predictive accuracy, achieving R² values of 0.981 for UTS, 0.991 for YS, 0.973 for natural frequency, and 0.995 for damping ratio, outperforming other machine learning models.

CRediT authorship contribution statement

Dinesh Kumar Screen: writing – original draft, writing – review & editing; **Sarabjeet** Singh: writing – review & editing; **Pardeep Kumar Karsh** Screen: writing – original draft; **Abhishek Chauhan**: writing – review & editing; **Gaurav Saini**: writing – review & editing; **Arti Chouksey** Screen: writing – original draft; **Pardeep Kumar** Screen: writing – review, editing & supervision.

Conflict of interest

The authors declare that they have no conflict of interest.

References

- 1. Nikhil B, Govindan P. Effect of tool probe geometry on the material flow and mechanical behaviour of dissimilar AA2024 / AA7075 friction stir welded joints. *International Journal on Interactive Design and Manufacturing (IJIDeM)*. 2024;18(3): 1645–1664.
- 2. Paul RC, Joseph R, Nadana Kumar V, Booma Devi P, Manigandan S. Experimental analysis of hybrid metal matrix composite reinforced with Al2O3 and graphite. *International Journal of Ambient Energy*. 2022;43(1): 648–652.
- 3. Kumar D, Singh S, Angra S. Dry sliding wear and microstructural behavior of stir-cast Al6061-based composite reinforced with cerium oxide and graphene nanoplatelets. *Wear.* 2023;204615: 516–517.
- 4. Kumar D, Singh S. Enhancing friction and wear performance in hybrid aluminum composites through grey relational analysis. *Res. Eng. Struct. Mater.* 2024;10(3): 943–956.
- 5. Subburaj A, Antony Joseph Decruz AMM, Chandra Moorthy VA, Durairaj R. Mechanical Characterization and Micro-structural Analysis on AA2024 Hybrid Composites Reinforced with WC and Graphene Nanoparticles. *Trans Indian Inst Met.* 2022;75: 1721–1730.
- 6. Khiyavi BA, Aghchai AJ, Arbabtafti M, Givi MKB, Jafari J. Effect of friction stir processing on mechanical properties of surface composite of Cu reinforced with Cr particles. *Advanced Materials Research*. 2014;829: 851–856.
- 7. Li X, Das H, Pole M, Li L, Soulami A, Grant GJ, Herling DR, Efe M. Exceptional strength and wear resistance in an AA7075 / TiB 2 composite fabricated via friction consolidation. *Materials & Design*. 2024;242:113006. 8. Vasu C, Durga KJAN, Srinivas I, Dariyavali S, Venkateswarlu B, Sunil BR. Developing composite of ZE41 magnesium alloy- calcium by friction stir processing for biodegradable implant applications. *Materials Today: Proceedings*. 2019;18: 270–277.
- 9. Molla Ramezani N, Davoodi B. Evaluating the influence of various friction stir processing strategies on surface integrity of hybrid nanocomposite Al6061. *Scientific Reports*. 2024;14: 8056.
- 10. Rajak DK, Pagar DD, Menezes PL, Linul E. Fiber-reinforced polymer composites: Manufacturing, properties, and applications. *Polymers*. 2019;11(10): 1667.
- 11. Kumar D, Angra S, Singh S. Mechanical Properties and Wear Behaviour of Stir Cast Aluminum Metal Matrix Composite: A Review. *International Journal of Engineering, Transactions A: Basics*. 2022;35(4): 794–801.
- 12. Kumar D, Angra S, Singh S. Synthesis and characterization of DOE-based stir-cast hybrid aluminum composite reinforced with graphene nanoplatelets and cerium oxide. *Aircraft Engineering and Aerospace Technology*. 2023;95(10): 1604–1613.
- 13. Kumar J, Singh D, Kalsi NS, Sharma S, Mia M, Singh J, Rahman MA, Khan AM, Rao KV. Investigation on the mechanical, tribological, morphological and machinability behavior of stir-casted Al/SiC/Mo reinforced MMCs. *Journal of Materials Research and Technology*. 2021;12: 930–946.
- 14. Maurya MC, Ali Jawaid SM, Chakrabarti A. Flexural Behaviour of Nanocomposite Plate with CNT Distribution and Agglomeration Effect. *Mechanics of Advanced Composite Structures*. 2023;10(1): 123–136.
- 15. Kumar P, Kumar N, Agarwal S. Microstructural, microhardness and electrical conductivity analysis of AD31T alloy processed by friction stir processing. *Multidiscipline Modeling in Materials and Structures*. 2024;20(6): 937–951.
- 16. Yadav A, Jain A, Verma R. Effect of rotational speed on various performance measures in friction stir lap weld of aluminium alloy 6061 using numerical simulation approach. *Materials Physics and Mechanics*. 2024;52(6): 114–125.
- 17. Kilimtzidis S, Kotzakolios A, Kostopoulos V. Efficient structural optimisation of composite materials aircraft wings. *Composite Structures*. 2023;303(5): 116268.
- 18. Hasan MS, Kordijazi A, Rohatgi PK, Nosonovsky M. Application of Triboinformatics Approach in Tribological Studies of Aluminum Alloys and Aluminum-Graphite Metal Matrix Composites. In: Srivatsan TS, Rohatgi PK, Hunyadi Murph S. (eds) *Metal-Matrix Composites. The Minerals, Metals & Materials Series.* Cham: Springer; 2022. p.41–51.
- 19. Agarwal S, Singh S. Production techniques and properties of particulate reinforced metal matrix composites: a review. *Materials Physics and Mechanics*. 2024;52(6): 136–153.
- 20. Wang Y, Wang H, Razzaghi R, Jalili M, Liebman A. Multi-objective coordinated EV charging strategy in distribution networks using an improved augmented epsilon-constrained method. *Applied Energy*. 2024;369: 123547.

- 21. Rao TB, Ponugoti GR. Characterization, Prediction, and Optimization of Dry Sliding Wear Behaviour of Al6061/WC Composites. *Transactions of the Indian Institute of Metals*. 2021;74(1): 159–178.
- 22. Jeon CH, Jeong YH, Seo JJ, Tien HN, Hong ST, Yum YJ, Hur SH, Lee KJ. Material properties of graphene/aluminum metal matrix composites fabricated by friction stir processing. *Int. J. Precis. Eng. Manuf.* 2014;15: 1235–1239.
- 23. Gangadharappa M, Geetha HR, Manjunath NK, Umesh GL, Shivakumar MM. Study on n-TiB2 particulates reinforced Al7075 nano composite for soil nail applications: mechanical, wear, and fracture characterizations. *Materials Physics and Mechanics*. 2024;52(6): 101–113.
- 24. Kumar N, Bharti A, Chauhan AK. Effect of Ti reinforcement on the wear behaviour of AZ91/Ti composites fabricated by powder metallurgy. *Materials Physics and Mechanics*. 2021;47(4): 600–607.
- 25. Kumar D, Singh S, Angra S. Qualitative and quantitative interdependence of physical and mechanical properties of stir-casted hybrid aluminum composites. *Materials Physics and Mechanics*. 2023;51(6): 14–23. 26. Sharath BN, Madhu KS, Pradeep DG, Madhu P, Premkumar BG, Karthik S. Effects of tertiary ceramic additives on the micro hardness and wear characteristics of Al2618 + Si3N4-B4C-Gr hybrid composites for automotive applications. *Journal of Alloys and Metallurgical Systems*. 2023;3(1): 100014.
- 27. Kumar D, Angra S, Singh S. High-temperature dry sliding wear behavior of hybrid aluminum composite reinforced with ceria and graphene nanoparticles. *Engineering Failure Analysis*. 2023;151(3): 107426.
- 28. Nirala A, Soren S, Kumar N, Kaushal DR. A comprehensive review on mechanical properties of Al-B4C stir casting fabricated composite. *Materials Today: Proceedings*. 2020;21(4): 1432–1435.
- 29. Raja R, Shanmugam R, Jannet S, Kumar GBV, Venkateshwaran N, Naresh K, Ramoni M. Development of Al-Mg2Si Alloy Hybrid Surface Composites by Friction Stir Processing: Mechanical, Wear, and Microstructure Evaluation. *Materials*. 2023;16(11): 4131.
- 30. Sharma S, Handa A, Singh SS, Verma D. Influence of tool rotation speeds on mechanical and morphological properties of friction stir processed nano hybrid composite of MWCNT-Graphene-AZ31 magnesium. *Journal of Magnesium and Alloys*. 2019;7(3): 487–500.

Accepted: February 4, 2025

Submitted: November 22, 2024

Revised: December 19, 2024

Electrochemical crystallization and functional properties of nickel-based composite coatings

V.N. Tseluikin [™] (10), A.S. Dzhumieva (10), A.I. Tribis (10), D.A. Tikhonov (10)

Yuri Gagarin State Technical University or Saratov, Saratov, Russian Federation

[™]tseluikin@mail.ru

ABSTRACT

The electrochemical crystallization of nickel/graphene oxide composite electrochemical coatings was researched by the chronovoltamperometry method. The microstructure of the composite electrochemical coatings was studied by scanning electron microscopy and X-ray diffraction analysis. The microhardness and corrosion rate of nickel/graphene oxide composite electrochemical coatings obtained at different cathode current densities were measured. It was revealed that in the presence of a dispersed phase of multilayer graphene oxide, the rate of the cathode process increases. Based on scanning electron microscopy and X-ray diffraction data, it was found that the dispersed phase affects the crystal structure of the nickel matrix. In the presence of graphene oxide, the nickel deposit is formed uniform and fine-grained. It was found that the microhardness of the nickel/graphene oxide composite electrochemical coatings increases ~ 1.20 times compared with pure nickel. This is a consequence of the formation of fine crystalline deposits with long grain boundaries, which prevents the movement of dislocations and plastic deformation of the crystal lattice. Tests in 3.5% NaCl showed that the inclusion of graphene oxide particles in the composition of electrolytic nickel deposits leads to a decrease in their corrosion rate by 1.35-1.60 times. This effect is due to the fact that graphene oxide particles ensure a uniform distribution of corrosion currents over the coating surface, and in the structure of composite electrochemical coatings, the dispersed phase forms compounds that are more corrosion resistant than the metal matrix.

KEYWORDS

electrochemical composition coatings • nickel • graphene oxide • microhardness • corrosion

Citation: Tseluikin VN, Dzhumieva AS, Tribis AI, Tikhonov DA. Electrochemical crystallization and functional properties of nickel-based composite coatings. *Materials Physics and Mechanics*. 2025;53(2): 142–148. http://dx.doi.org/10.18149/MPM.5322025_12

Introduction

Electrochemical deposition of coatings based on nickel and its alloys is one of the most effective methods for surface modification of steel products to protect them against wear and corrosion [1]. Significant improvement in the characteristics of electrolytic nickel can be achieved through its co-deposition with various dispersed particles. Electrochemical deposits modified with a dispersed phase are called composite electrochemical coatings (CECs). In particular, nickel-based CECs, due to their excellent adhesion, high hardness and abrasion resistance, find applications in mechanical engineering, chemical and oil/gas industries, medical equipment etc. [2–4].

The performance characteristics of composite coatings are largely determined by the dispersed phase. Among the wide variety of dispersed materials, carbon derivatives have attracted considerable attention from researchers. Specifically, nickel CECs modified with carbon nanotubes [5–7], fullerenes [8,9], nanodiamonds [10,11], graphene and its oxide [12–16] have been obtained. The latter occupies a special place among carbon



compounds. Graphene is a two-dimensional material with a high specific surface area. Its interaction with strong mineral acids leads to the formation of graphene oxide (GO). In the structure of GO, carbon atoms are bonded to oxide functional groups (carbonyl, carboxyl, epoxy etc.), which make it hydrophilic and enable the formation of stable aqueous dispersions. These compounds are inert in many aggressive environments, making them suitable for corrosion protection [17-19]. Additionally, the high physical and mechanical properties of GO are of particular interest [20].

The aim of the present work is to obtain, under stationary electrolysis conditions (galvanostatic mode), composite coatings based on nickel modified with multilayer GO, and to study their structure, physical and mechanical and corrosion properties.

Materials and Methods

The Ni-GO composite coatings were deposited on a steel substrate (Steel 45) from a sulfate-chloride electrolyte (Table 1) with constant stirring using a magnetic stirrer. Pure nickel electrochemical deposits were obtained from a similar solution without the GO dispersed phase. The coating thickness was 20 μ m. Preliminary preparation of the electrode surface prior to coating deposition included mechanical polishing with microngrade sandpaper, anodic treatment in 48 % H_3PO_4 at a current density of 50 A/dm² for 5 sec and rinsing with distilled water.

Table 1. Electrol	yte composition	n and electrochemical	deposition parameters

No.	Electrolyte composition	Concentration, g/l	Deposition parameters
1	NiSO₄·7H₂O	220	
2	$NiCl_2 \cdot 6H_2O$	40	Temperature $T = 45 ^{\circ}\text{C}$
3	CH₃COONa	30	Cathode current density i_k = 7, 8, 9, 10 A/dm ²
4	graphene oxide	10	

Multilayer GO was synthesized through electrochemical oxidation of natural graphite powder GB/T 3518-95 (China) in galvanostatic mode. A detailed description of the synthesis method and the structure of the formed GO is provided in [21]. Phase composition studies were conducted using an ARL X'TRA device (Thermo Scientific, Ecublens, Switzerland) with Cu K α radiation (λ = 0.15412 nm). The surface morphology of nickel coatings was examined using an ASPEX Explorer scanning electron microscope (ASPEX, Framingham, MA, USA). Electrochemical measurements were performed using a P-30J potentiostat (Elins LLC, Russia). Potentials were set relative to a saturated silver/chloride reference electrode and recalculated according to the hydrogen scale.

The Vickers microhardness (*HV*) of the deposits was measured using a PMT-3 instrument (LOMO JSC, Russia) by static indentation of a diamond pyramid under a 100 g load. *HV* values were calculated based on seven parallel tests, with a measurement error of 3 %. The surface roughness parameter (Ra) of nickel coatings was determined using a TR 220 profilograph-profilometer (TIME GROUP Inc., China). The average roughness value was calculated from five parallel measurements. To evaluate the corrosion rate of nickel coatings, studies were conducted in a 3.5 % NaCl solution.

Results and Discussion

During electrochemical co-deposition with metals, dispersed phase particles influence the kinetics of electrode (cathodic) processes. As chronovoltamperometry results show (Fig. 1), nickel electrodeposition in the presence of GO exhibits a potential shift toward more positive values compared to pure nickel. Consequently, the cathodic reduction rate increases for Ni-GO CECs. Morphological analysis of GO revealed [21] that this compound has an ordered layered structure with individual layer thickness below 0.1 µm. The Brunauer–Emmett–Teller method determined GO's specific surface area as 46.78 m²/g [21]. The developed surface of GO may adsorb cations from the solution, leading to positive charging of dispersed phase particles. Therefore, GO transfer to the cathode occurs not only through convection, but also via electrophoretic forces [14–16].

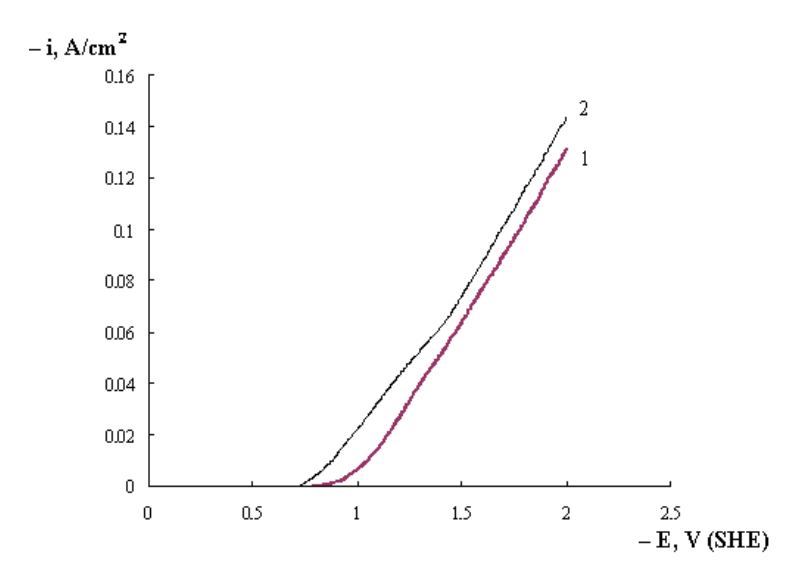


Fig. 1. Potentiodynamic polarization curves of electrochemical deposition of nickel (1) and CEC Ni-GO (2) (potential sweep rate $V_o = 8$ mV/s)

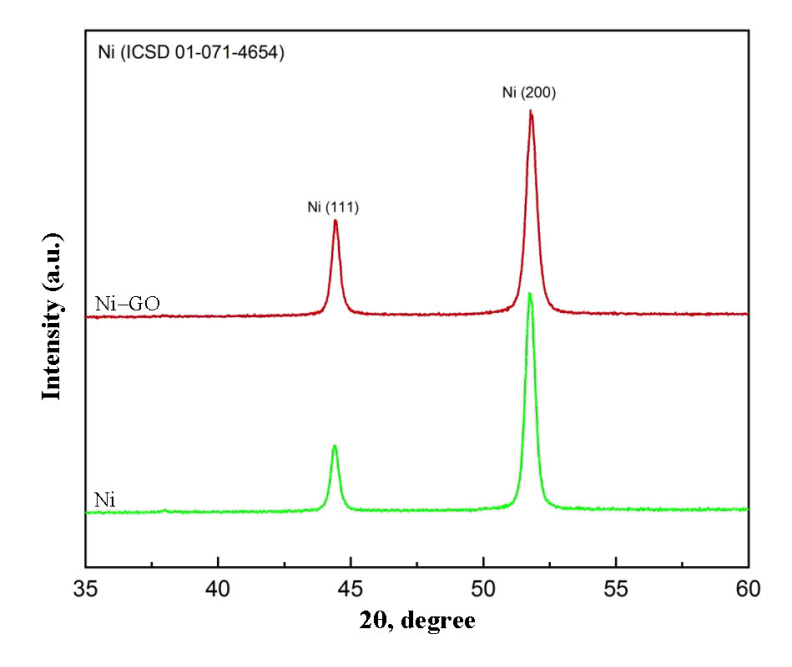
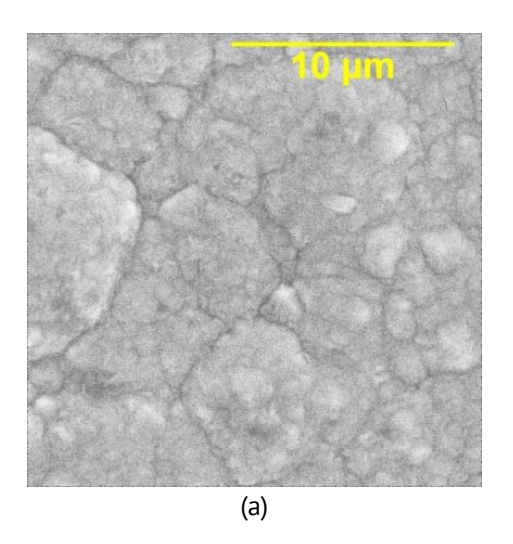


Fig. 2. XRD pattern of nickel and Ni-GO CEC obtained at a current density of $i_k = 10 \text{ A/dm}^2$

X-ray diffraction analysis (XRD) of the obtained coatings revealed changes in nickel's crystal structure under GO influence. X-ray diffraction peaks at 44.5° and 52.2° (Fig. 2) correspond to nickel's (111) and (200) crystal planes, respectively [11]. According to the X-ray diffraction, the main orientation for nickel crystals is the (200) direction. While peak intensities at 52.2° remain unchanged for nickel without dispersed phase and Ni-GO CECs, GO presence increases the 44.5° peak intensity, indicating enhanced crystal growth along the (111) plane. Clearly, the dispersed phase affects the nickel matrix's crystalline structure. GO layers may serve as nucleation sites for metal deposits, restricting grain growth and making them more compact.

Scanning electron microscopy (SEM) analysis of nickel coatings' surface morphology demonstrated GO's structural influence. Electrolytic nickel without dispersed phase (Fig. 3(a)) shows disordered, coarse-grained structure approaching X-ray amorphous state. With GO present, ordered, fine-grained and uniform nickel deposits form (Fig. 3(b)). SEM analysis of the composite coatings confirmed carbon presence, proving GO incorporation into the nickel matrix.



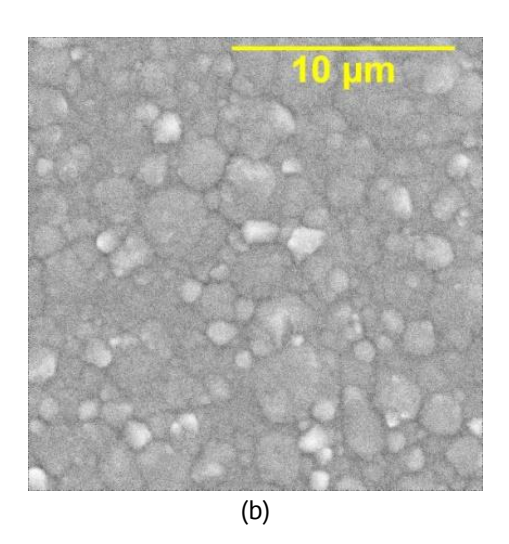


Fig. 3. SEM images of the nickel surface (a) and the Ni-GO composite coating (b) obtained at a cathode current density of $i_k = 10 \text{ A/dm}^2$. Magnification x10000

Grain size calculations based on XPA data (Fig. 2) at the intensity of the crystal lattice (111) using Scherrer's equation [22]: $d = \frac{0.9\lambda}{b\cos\theta}$, where λ is the wave length and equals 0.15412 nm, b is the peak width at half maximum, θ is the diffraction angle. The calculations revealed grain size reduction from 69.0 nm (nickel without dispersed phase) to 21.5 nm (Ni-GO CEC), i.e., over threefold decrease.

Table 2. Parameter R_a	values, um	of surface rough	iness of nickel-base	d coatings

Cathode current density i_k ,	Roughness parameter R_a , μ m		
A/dm ²	Nickel	Ni-GO	
7	1.395	0.673	
8	1.017	0.420	
9	0.771	0.401	
10	0.596	0.369	

To characterize the electrolytic nickel deposits condition, its surface roughness was measured, i.e., arithmetic mean of absolute values of profile deviations within the base length (R_a). The R_a parameter values decrease for composite coatings across studied current densities compared with pure nickel (Table 2). Evidently, GO particles promote uniform metal deposit distribution across the cathode surface without causing agglomeration in the nickel matrix volume.

The reduction in grain size of nickel deposits and the associated change in surface morphology should affect their physical and mechanical properties. The GO layers within the coating volume act as vacancy sites and inhibit metal grain growth. This process leads to an increased nucleation rate. The crystallites become finer, and the extended grain boundaries impede dislocation movement and plastic deformation of the crystal lattice [11]. Notably, GO possesses high mechanical properties. When an external load is applied to the composite coating, the GO layers absorb part of the load through shear stress transfer. Dislocation motion in the nickel matrix is constrained by the GO particle layers, resulting in deformation resistance and increased lattice distortion energy [23,24]. These factors enhance microhardness from 1938–2459 MPa (nickel without dispersed phase) to 2200–3076 MPa (Ni-GO CEC), i.e., by ~ 20 % (Table 3). The microhardness of the Steel 45 substrate was 894 MPa.

Table 3. Microhardness values HV_{100} of nickel-based coatings

Cathodo surrent density i A/dm²	Microhardness HV ₁₀₀ , MPa		
Cathode current density i_k , A/dm ²	Nickel	Ni-GO	
7	1938	2200	
8	2150	2520	
9	2350	2938	
10	2459	3076	

Another critical operational property of composite coatings is corrosion resistance. The corrosion rate (CR) of nickel deposits was determined by mass loss after 24-hour immersion in 3.5 % NaCl (weighing before/after testing) using the following equation [25,26]: $CR = \frac{KW}{AtD}$, where K is the constant (8.76·10⁴), W is the mass loss (g), A is the coating area (1 cm²), t is the testing time (h) and D is the nickel density, which equals 8.9 g/sm³. Corrosion tests in 3.5 % NaCl revealed a decrease in corrosion rate from 0.328–0.656 mm/year (nickel without dispersed phase) to 0.205–0.492 mm/year (Ni-GO CEC), i.e., ~40% reduction (Table 4). The Steel 45 substrate exhibited a corrosion rate of 0.881 mm/year.

Table 4. Corrosion rate of nickel-based coatings

Cathodo surrent density i A/dm²	Corrosion rate, mm/year		
Cathode current density i _k , A/dm ²	Nickel	Ni-GO	
7	0.656	0.492	
8	0.574	0.410	
9	0.451	0.328	
10	0.328	0.205	

The primary factors governing corrosion behavior of the electrolytic nickel deposits are its composition and structure. Nickel's electrochemical corrosion susceptibility depends on crystallographic orientation, which determines surface free energy per unit area [25]. The ordered fine-crystalline structure of CECs (Fig. 3(b)), unlike nickel without dispersed phase (Fig. 3(a)), promotes uniform corrosion current distribution [27,28]. Dispersed phase agglomeration in the metal matrix worsens corrosion properties by forming microgalvanic elements [29]. Thus, GO inclusions are uniformly distributed throughout the coating volume and surface. Moreover, GO's stability and impermeability elongates the diffusion path for aggressive media [30], preventing nickel ion penetration through GO particle cross-sections. It is worth noting that the dispersed phase enhances corrosion resistance only if it forms compounds more stable than the metal matrix at phase boundaries or throughout the whole volume. Otherwise, corrosion won't stop, bypassing the particles (with possible minor rate reduction). Such stable compounds evidently form in the studied Ni-GO CEC structure. All the factors listed above improve the corrosion resistance of Ni-GO CECs compared to pure nickel deposits.

Conclusions

The conducted studies allow to conclude that in the galvanostatic electrolysis mode from a sulfate-chloride nickel-plating electrolyte containing a dispersion of multilayer GO, composite coatings are formed. The incorporation of the GO phase into the matrix of electrolytic nickel deposits leads to changes in their surface microtopography and a reduction in grain size from 69 to 21.5 nm. GO contributes to the improvement of physical and mechanical and corrosion properties of the studied CECs. Modification of the electrochemical coating with dispersed particles results in an increase of microhardness from 1938–2459 to 2200–3076 MPa, as well as a decrease in corrosion rate from 0.328–0.656 mm/year for nickel without dispersed phase to 0.205–0.492 mm/year for Ni-GO CECs.

CRediT authorship contribution statement

Vitaly N. Tseluikin Science supervision, conceptualization, writing – review & editing, writing – original draft; **Asel S. Dzhumieva** Science investigation, data curation, writing – review & editing; **Alena I. Tribis** Science investigation, data curation; **Denis A. Tikhonov** Science investigation, data curation.

Conflict of interest

The authors declare that they have no conflict of interest.

References

- 1. Orinakova R, Turonova A, Kladekova D, Galova M, Smith RM. Recent developments in the electrodeposition of nickel and some nickel-based alloys. *J. Appl. Electrochem.* 2006;36: 957–972.
- 2. Low CTJ, Wills RGA, Walsh FC. Electrodeposition of composite coatings containing nanoparticles in a metal deposit. *Surf. Coat. Technol.* 2006;201: 371–383.
- 3. Walsh FC. A review of the electrodeposition of metal matrix composite coatings by inclusion of particles in a metal layer: An established and diversifying technology. *Trans. IMF*. 2014;92: 83–98.
- 4. Tseluikin V, Dzhumieva A, Tribis A, Brudnik S, Tikhonov D, Yakovlev A, Mostovoy A, Lopukhova M. Electrochemical Deposition and Properties of Ni Coatings with Nitrogen-Modified Graphene Oxide. *J. Compos. Sci.* 2024;8: 147.

- 5. Giannopoulos F, Chronopoulou N, Bai J, Zhao H, Pantelis D, Pavlatou EAI, Karatonis A. Nickel/MWCNT-Al2O3 electrochemical co-deposition: Structural properties and mechanistics aspects. *Electrochim. Acta.* 2016;207:76–86. 6. Jyotheender K. S., Gupta A., Srivastava C. Grain boundary engineering in Ni-carbon nanotube composite coatings and its effect on the corrosion behaviour of the coatings. *Materialia.* 2020;9: 100617.
- 7. Yang P, Wang N, Zhang J, Lei Y, Shu B. Investigation of the microstructure and tribological properties of CNTs/Ni composites prepared by electrodeposition. *Mater. Res. Express.* 2022;9: 036404.
- 8. Antihovich IV, Ablazhey NM, Chernik AA, Zharsky IM. Electrodeposition of nickel and composite nickel-fullerenol coatings from low-temperature sulphate-chloride-isobutyrate electrolyte. *Procedia Chem.* 2014;10: 373–377.
- 9. Tseluikin VN. Electrodeposition and properties of composite coatings modified by fullerene C60. *Prot. Met. Phys. Chem. Surf.* 2017;53: 433–436.
- 10. Chayeuski VV, Zhylinski VV, Rudak PV, Rusalsky DP, Visniakov N, Cernasejus O. Characteristics of ZrC/Ni-UDD coatings for a tungsten carbide cutting tool. *Appl. Surf. Sci.* 2018;446: 18–26.
- 11. Makarova I, Dobryden I, Kharitonov D, Kasach A, Ryl J, Repo E, Vuorinen E. Nickel-nanodiamond coatings electrodeposited from tartrate electrolyte at ambient temperature. *Surf. Coat. Technol.* 2019;380: 125063.
- 12. Algul H, Tokur M, Ozcan S, Uysal M, Cetinkaya T, Akbulut H, Alp A. The effect of graphene content and sliding speed on the wearmechanism of nickel–graphene nanocomposites. *Appl. Surf. Sci.* 2015;359: 340–348.
- 13. Yasin G, Arif M, Nizam NM, Shakeel M, Khan MA, Khan WQ, Hassan TM, Abbas Z, Farahbakhsh I, Zuo Y. Effect of surfactant concentration in electrolyte on the fabrication and properties of nickel-graphene nanocomposite coating synthesized by electrochemical co-deposition. *RSC Adv.* 2018;8: 20039–20047.
- 14. Ambrosi A, Pumera M. The structural stability of graphene anticorrosion coating materials is compromised at low potentials. *Chem.-A Eur. J.* 2015;21: 7896–7901.
- 15. Jyotheender KS, Srivastava C. Ni-graphene oxide composite coatings: Optimum graphene oxide for enhanced corrosion resistance. *Compos. Part B.* 2019;175: 107145.
- 16. Tseluikin V, Dzhumieva A, Tikhonov D, Yakovlev A, Strilets A, Tribis A, Lopukhova M. Pulsed electrodeposition and properties of nickel-based composite coatings modified with graphene oxide. *Coatings*. 2022;12: 656.
- 17. Tseluikin V, Dzhumieva A, Yakovlev A, Tikhonov D, Tribis A, Strilets A, Lopukhova M. Electrodeposition and Properties of Composite Ni Coatings Modified with Multilayer Graphene Oxide. *Micromachines*. 2023;14: 1747.
- 18. Korkmaz S, Kariper IA. Graphene and graphene oxide based aerogels: Synthesis, characteristics and supercapacitor applications. *J. Energy Storage*. 2020;27: 101038.
- 19. Arvas MB, Gürsu H, Gencten M, Sahin Y. Preparation of different heteroatom doped graphene oxide based electrodes by electrochemical method and their supercapacitor applications. *J. Energy Storage*. 2021;35: 102328. 20. Ropalekar AR, Ghadge RR, Anekar NA. Experimental investigation on flexural fatigue strength of graphene oxide modified E-glass epoxy composite beam. *Materials Physics and Mechanics*. 2024;52(1): 132–141.
- 21. Yakovlev AV, Yakovleva EV, Vikulova MA, Frolov IN, Rakhmetulina LA, Tseluikin VN, Krasnov VV, Mostovoy AS. Synthesis of multilayer graphene oxide in electrochemical graphite dispersion in H2SO4. *Russ. J. Appl. Chem.* 2020;93: 219–224.
- 22. Zhang H, Zhang N, Fang F. Fabrication of high-performance nickel/graphene oxide composite coatings using ultrasonicassisted. *Ultrason. Sonochem.* 2020;62: 104858.
- 23. Lai R, Shi P, Yi Z, Li H, Yi Y. Triple-band surface plasmon resonance metamaterial absorber based on open-ended prohibited sign type monolayer graphene. *Micromachines*. 2023;14: 953.
- 24. Hong Q, Wang D, Yin S. The microstructure, wear and electrochemical properties of electrodeposited Ni-diamond composite coatings: Effect of diamond concentration. *Mat. Tod. Comm.* 2023;34: 105476.
- 25. Yang F, Kang H, Guo E, Li R, Chen Z, Zeng Y. The role of nickel in mechanical performance and corrosion behaviour of nickel-aluminium bronze in 3.5 wt.% NaCl solution. *Corros. Sci.* 2018; 139: 333–345.
- 26. Rekha MY, Srivastava C. Microstructural evolution and corrosion behavior of Zn-Ni-graphene oxide composite coatings. *Metall. Mater. Trans. A.* 2019;50: 5896–5913.
- 27. Wang Y, Tay SL, Wei S, Xiong C, Gao W, Shakoor RA, Kahraman R. Microstructure and properties of solenhanced Ni-Co-TiO2 nano-composite coatings on mild steel. *J. Alloys Compd.* 2015;649: 222–228.
- 28. Lou G, Shen L, Qian Y, Chen Y, Bai H, Cheng H, Xu J, Yang Y. Study on the antibacterial and anti-corrosion properties of Ni-GO/Ni-rGO composite coating on manganese steel. *Surf. Coat. Technol.* 2021; 424: 127681. 29. Vodopyanova S, Mingazova G, Fomina R, Sayfullin R. Physical and mechanical properties of modified chrome coatings. *Materials Physics and Mechanics*. 2023;51(7): 123–136.
- 30. Carboni N, Mazzapioda L, Capr A, Gatto I, Carbone A, Baglio V, Navarra MA. Composite Anion Exchange Membranes based on Graphene Oxide for Water Electrolyzer Applications. *Electrochim. Acta.* 2024;486: 144090.

Submitted: August 1, 2024

Revised: September 5, 2024

Accepted: September 30, 2024

The effect of the magnetron discharge power on the deposition rate of chrome coating obtained by spattering an uncooled extended target

G.V. Kachalin 📵, K.S. Medvedev 📵, A.B. Tkhabisimov 🖾 📵, D.I. Iliukhin 📵

National Research University "Moscow Power Engineering Institute", Moscow, Russia

[™] abt-bkt@mail.ru

ABSTRACT

The effect of the magnetron discharge power in the range from 2.2 to 8.2 kW on the deposition rate of chrome coatings obtained by spraying an uncooled and cooled planar extended target is studied. The coatings were applied to 12Cr18Ni10Ti stainless steel samples with temperature control using a chromel-copel thermocouple. It is shown that the deposition rate of coatings for an uncooled chrome target increases non-linearly with an increase in power of more than 6.5 kW, and at a power of 8.2 kW reaches $45~\mu\text{m/h}$, which is more than 2 times higher than for a cooled target. The results obtained indicate the prospects of using such extended magnetron systems to solve a number of applied problems in the energy sector, in particular, the formation of thermal barrier coatings on the domestic gas turbine blades.

KEYWORDS

magnetron sputtering • cooled target • uncooled target • deposition rate • chrome coating • discharge power

Acknowledgements. The research was supported by the Ministry of Science and Higher Education of the Russian Federation within the framework of the state assignment "Development of physical and chemical foundations for the formation and prediction of properties of promising materials and coatings for energy conversion and storage systems" (FSWF-2023-0016).

Citation: Kachalin GV, Medvedev KS, Tkhabisimov AB, Iliukhin DI. The effect of the magnetron discharge power on the deposition rate of chrome coating obtained by spattering an uncooled extended target. *Materials Physics and Mechanics*. 2025;53(2): 149–156.

http://dx.doi.org/10.18149/MPM.5322025_13

Introduction

Coatings of chromium and its compounds are widely used in industry. A chromium layer can be applied to provide corrosion protection or to increase surface hardness and wear resistance. The widely used galvanic chromium plating (electroplating) processes now face several restrictions due to the recognition of hexavalent chromium as a carcinogen in the 1990s. As a result, many countries have actively begun to develop and implement alternative chromium plating processes, among which physical vapor deposition (PVD) methods were the most widespread. However, all PVD processes developed to date still fall short of electroplating in three key criteria: productivity, cost and the ability to process large and elongated products. While recent years have seen the emergence of technological setups capable of handling products of varying dimensions [1,2], the challenge of improving PVD process efficiency remains unresolved.

One of the most widely used PVD processes is magnetron sputtering of a target by inert gas ions at reduced pressure. The devices implementing this process are called magnetron sputtering systems (MSS) [3-5].



Today, MSS are employed for depositing thin films and protective coatings in many industries due to their undeniable advantages: drop-free atomic flow, compatibility with any conductive materials and semiconductors and relative ease of scaling for large and elongated products [6-8]. The drawbacks of MSS include low deposition rates, target material utilization coefficient not exceeding 30 ÷ 40 % and a low percentage of ionization of sputtered atoms. The vast majority of industrial MSS use cooled ("cold") targets, where cooling is primarily necessary to prevent overheating of the magnetic system [9,10] rather than the processed products. In magnetron sputtering processes for coating formation in engineering applications, such as depositing erosion-resistant coatings on steam turbine blades or heat-resistant coatings on gas turbine blades, the temperature of the products can reach 400 °C or higher. For such tasks, cooled targets are not strictly necessary. Target heating occurs mainly due to the kinetic energy transferred to the target by accelerated ions generated in the magnetron discharge plasma burning region, leading to sublimation of material from the target surface. Sublimation significantly increases the deposition rate. The target material must have sufficient sublimation rates at its heating temperature, which is determined by the Hertz-Knudsen equation [11] (e.g., chromium or titanium). The target mounting design should minimize heat transfer to the magnetron's cooled parts, for example, by using thermal insulation gaskets. This positively affects the growing film's structure and enhances the productivity and cost-efficiency of the coating process.

Recently, several studies [12–28] have been published on uncooled chromium target sputtering, but these are research-oriented, as they used small planar round targets. In contrast, engineering applications require elongated planar targets comparable in size to the products. Elongated target sputtering (circa over 500 mm) presents technical challenges, particularly in ensuring uniform heating along the target's length, since the sublimation rate is a power function of temperature.

This study investigates the effect of discharge power on the deposition rate of chromium coatings formed by magnetron sputtering of an elongated uncooled target for industrial protective coating applications.

Materials and Methods

The coatings were formed using a vacuum system developed at National Research University "Moscow Power Engineering Institute" [29,30], equipped with four elongated magnetrons arranged in opposing pairs ("face-to-face") at a distance of 300 mm. The magnetic fields of the magnetrons were synchronized to form a closed magnetic field in the space between them.

Thanks to the specialized planetary mechanism of the system's carousel, various processing and coating deposition modes could be implemented. In particular, it was possible to perform ion cleaning (etching) of samples using one pair of magnetrons while depositing coatings with the other pair, which was utilized in the present study.

Coating deposition was performed using a planar elongated magnetron with both cooled and uncooled targets made of chromium (99.9 %). The target dimensions were $710 \times 65 \times 6 \text{ mm}^3$, with the uncooled target assembled from separate plates. A key feature

of the uncooled target's cathode assembly was its attachment to the magnetron through a thermal insulation gasket, ensuring low heat transfer and consequent target heating.

Coatings were deposited on polished 12Cr18Ni10Ti stainless steel samples measuring $30 \times 40 \times 1$ mm 3 . During the technological process, samples were mounted on a rotating fixture positioned in front of the magnetron. The target-to-fixture rotation axis distance was 150 mm. Experiments were conducted in high-purity argon atmosphere, with argon supplied to the vacuum chamber using an RRG-10 gas flow controller.

Target temperature was measured during the experiment using a chromel-alumel thermocouple with its tip installed at the target's side edge, allowing placement near the magnetron discharge zone. Sample temperature was monitored with a chromel-copel thermocouple with sample potential.

The coating process involved chamber preheating and high-vacuum pumping to 5×10^{-3} Pa using a diffusion pump. Argon was supplied to the chamber with 15.3 NL/h (normal liters per hour) consumption during all experiments. Ion cleaning of sample surfaces was carried out in glow discharge with magnetron discharge support on cooled targets for 10 min across all power ranges. During cleaning the heating of uncooled targets was carried out. Temperature measurements showed the uncooled target reached steady-state conditions within 10 min across the entire applied power range from 2.2 to 10 kW. The sample fixture was then moved to the uncooled target's deposition zone and after that the coating was deposited. During coating, samples rotated directly in front of the target. For cooled target experiments, samples remained stationary and after cleaning the coating was deposited. Coating deposition time was 20 min for all experiments with -100 V bias voltage applied to samples. During transfer between cleaning and deposition zones for uncooled targets, samples temporarily assumed floating potential. Coating thickness was measured with Calotest Compact measuring device using ball cratering in accordance with ISO 1071-2, with deposition rates calculated from thickness data. For some experiments, metallographic microsections were manufactured, which were examined using a TESCAN MIRA 3 LMU scanning electron microscope.

Results and Discussion

Figure 1 shows photographs of (a) an uncooled chromium target with an installed thermocouple in its lower part, (b) magnetron discharge on the surface of the uncooled target in argon plasma, (c) glow of the uncooled target immediately after turning off the magnetron discharge. Figure 1(b,c) demonstrates that target heating is uniform along its entire length. Table 1 presents the measured coating thickness and growth rate, as well as target and sample temperatures for the uncooled target.

Figure 2 shows the dependence of target temperature (curve 1) and sample temperature (curve 2) on discharge power in the range from 2.2 to 8.2 kW. Target temperature measurements were taken during brief turning offs of the discharge to avoid electromagnetic interference with the thermocouple.

Target temperature is a critical technological parameter that allows monitoring the onset of target material sublimation. The obtained dependencies of power influence on temperature (Fig. 2) and deposition rate (Fig. 3) are necessary for correlating target

temperature values with the beginning of its sublimation process, characterized by nonlinear growth in deposition rate.

Sample temperature is determined by the balance of power fluxes reaching its surface – the flow of sputtered atoms, crystallization heat, radiation from the heated target surface – and radiation from the sample surface [30]. The dependence of sample temperature on magnetron discharge power allows selecting a coating deposition mode that prevents changes in the sample's (product's) microstructure. Figure 3 shows the dependencies of chromium coating deposition rates obtained from the data in Table 1.

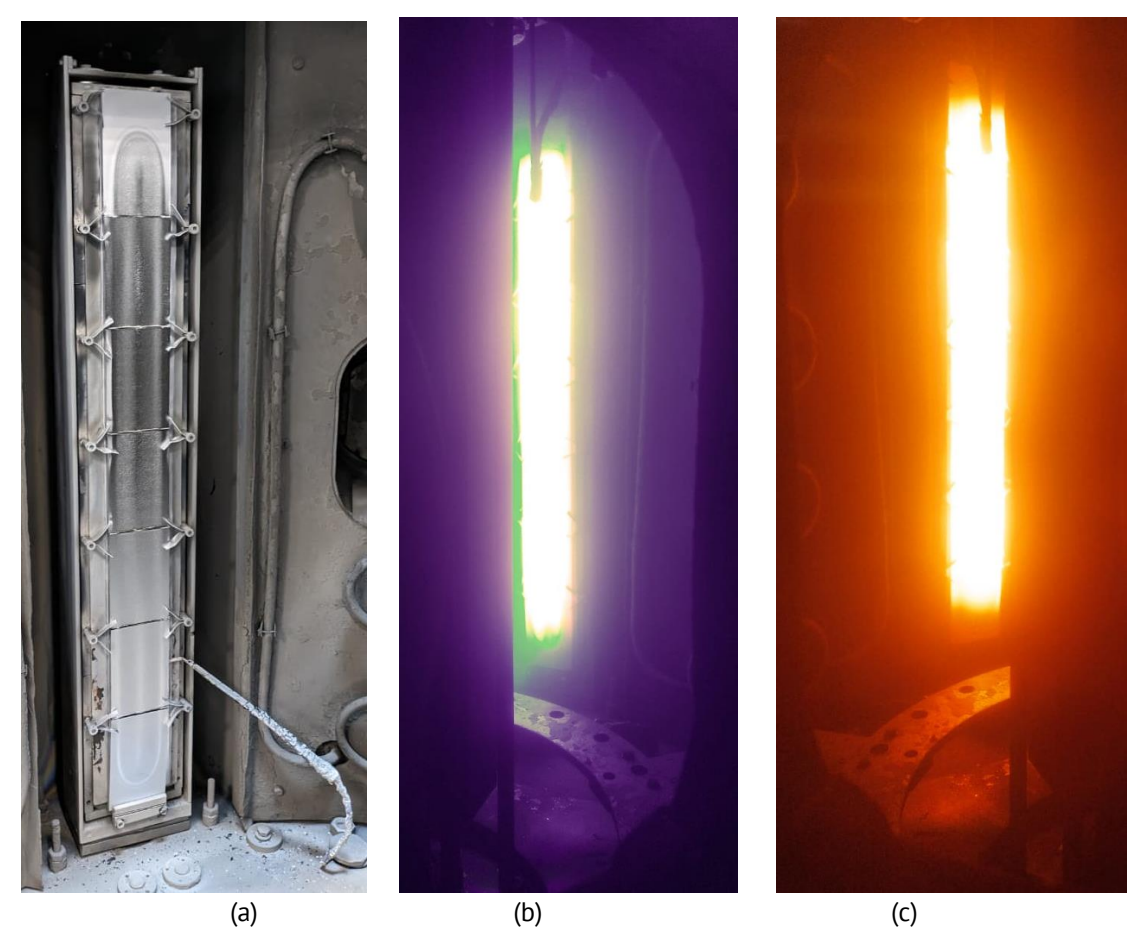


Fig. 1. Uncooled chromium target: (a) the thermocouple place of installation; (b) magnetron discharge in argon plasma; (c) the view immediately after turning off the discharge

Table 1. Coating thickness and growth rate and target and sample temperatures

Dower	Coole	d target	Uncooled target			
Power, kW	Coating	Coating growth	Coating	Coating growth	Target	Sample
t	thickness, µm	rate, µm/hour	thickness, µm	rate, µm/hour	temperature, °C	temperature, °C
2.2	1.74	5.22	1.76	5.3	679	335
3.2	2.6	7.8	3.2	9.6	876	374
4.1	3.2	9.6	4.3	12.9	993	400
5	4.0	12.0	5.0	15.0	1060	431
5.9	4.6	13.8	6.0	18.0	1114	446
6.5	5.0	15.0	6.6	19.8	1123	480
7.3	5.8	17.4	8.2	24.6	1158	498
8.2	6.5	19.5	15.0	45.0	1176	543

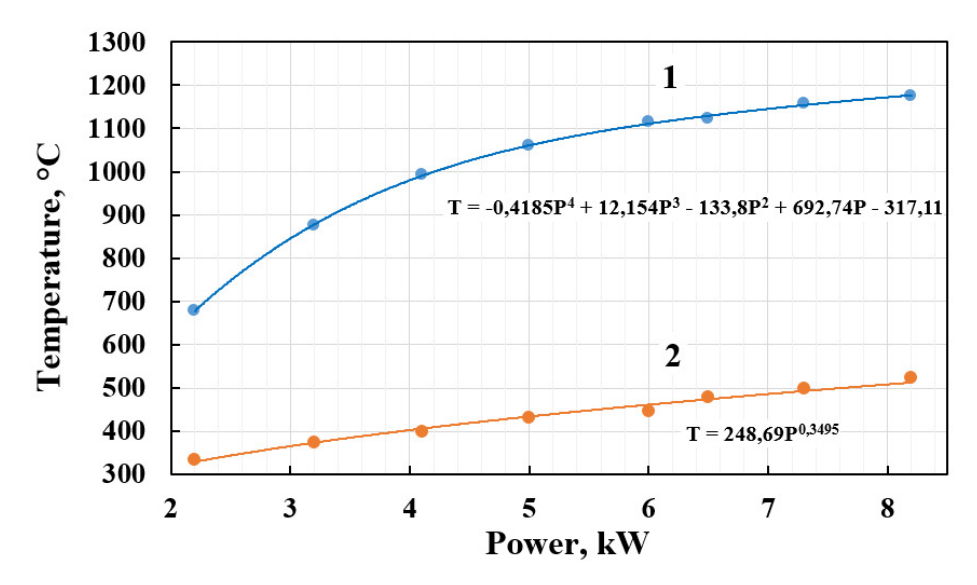


Fig. 2. Dependences of the temperature of the uncooled target (1) and sample (2) on the magnetron discharge power

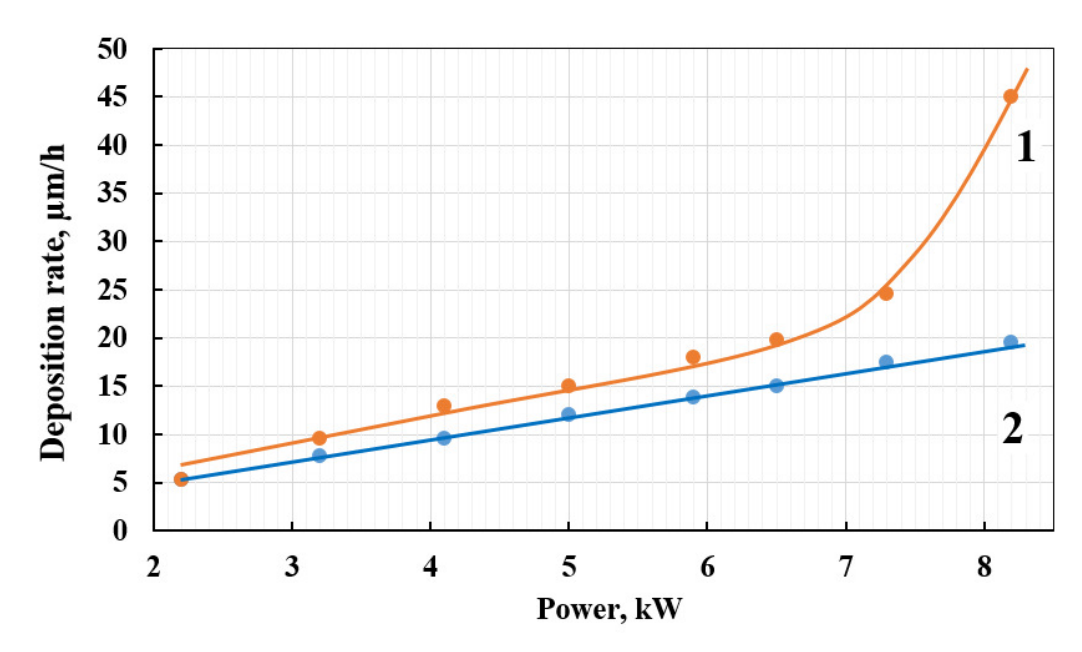


Fig. 3. Dependences of chromium coating growth rates on the magnetron discharge power for uncooled (1) and cooled (2) targets

Figure 3 demonstrates that at powers exceeding 6.5 kW, a nonlinear increase in coating growth rate is observed, caused by the addition of atoms evaporated from the target surface to the flow of sputtered atoms. At 8.2 kW power, the growth rate more than doubles, indicating equal flows of sputtered and evaporated chromium atoms from the target surface. Similar results were obtained for a magnetron with a small round uncooled target [17,31].

The obtained results demonstrate that increasing target temperature can significantly enhance chromium coating growth rates, which has substantial economic importance for industrial applications. Moreover, the sublimation process of target atoms

generally occurs from the entire heated target surface, which can improve target utilization efficiency.

Figure 4 shows that coatings in both cases (sputtering from cooled and uncooled targets) have dense columnar structures without visible pores or defects. However, in the case of the uncooled target (Fig. 4(b)), the chromium coating structure is finer-grained, with column widths ranging from 0.2 to 1.2 μ m, while sputtering from a cooled target (Fig. 4(a)) produces columns up to 3 μ m wide.

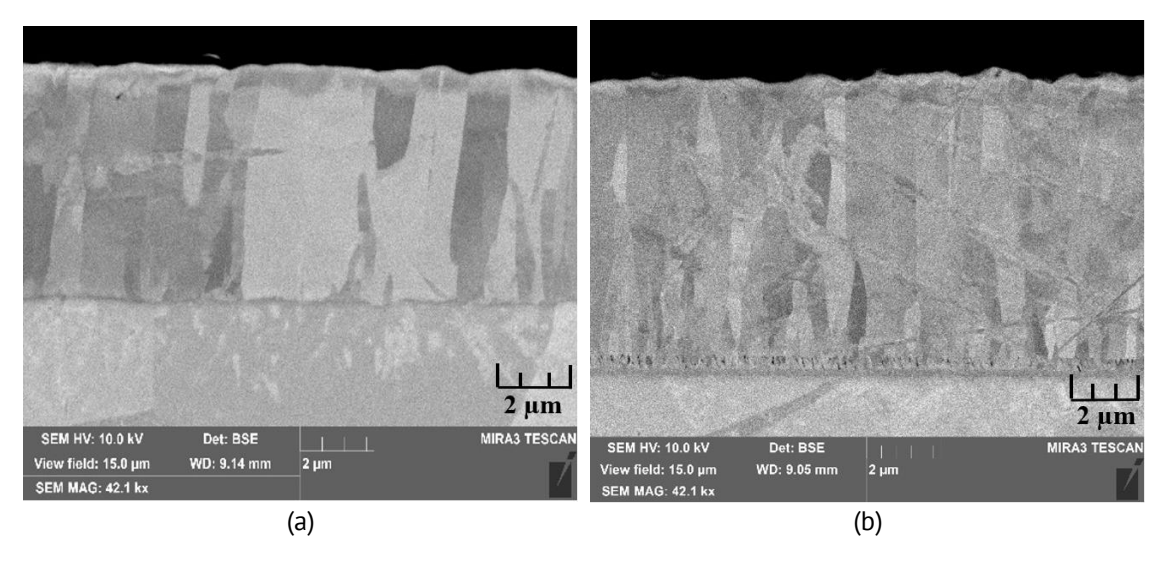


Fig. 4. Transverse sections of chromium coatings obtained by sputtering from a cooled (a) and uncooled (b) targets at a power range of 7.3 kW

Although the differences in coating structure may be insignificant in this particular case, they will inevitably affect coating properties. Furthermore, it should be expected that increasing coating growth rate through sublimation may reduce mechanical properties while increasing porosity and structural defects, due to the significant difference in energy between sputtered and evaporated atoms.

In [32], we investigated characteristics of chromium coatings obtained from an elongated uncooled target, which showed high adhesion and low roughness at high growth rates. However, we believe that optimal coating formation parameters will need to be determined for each specific application.

Conclusions

As a result of a series of experiments on chromium coating formation using elongated cooled and uncooled targets, it was established that when increasing the magnetron discharge power above 6.5 kW (which in our experimental conditions corresponds to an uncooled target temperature exceeding 1100 °C), a significant nonlinear increase in coating growth rate is observed.

At a magnetron discharge power of 8.2 kW, the growth rate of chromium coatings from an uncooled target more than doubles compared to the growth rate from a cooled target. This growth rate enhancement is associated with material sublimation from the target surface.

The results of this study were obtained for the first time and demonstrate the promising potential of using magnetrons with uncooled elongated targets to improve the efficiency and competitiveness of modern magnetron sputtering systems for industrial-scale protective coating formation.

CRediT authorship contribution statement

Gennadiy V. Kachalin Sceneroscoptualization, writing – original draft; **Konstantin S. Medvedev**: conceptualization, supervision; **Alexander B. Tkhabisimov** Sceneroscoptualization, attaining – review & editing, data curation; **Dmitriy I. Iliukhin**: investigation, data curation.

Conflict of interest

The authors declare that they have no conflict of interest.

References

- 1. Kachalin GV, Ryzhenkov AV, Medvedev KS, Bychkov AI, Parfenenok MA. Modern technological solutions for the formation of ion-plasma coatings on elements of fuel and energy complex equipment. *Safety and Reliability of Power Industry*. 2014;2: 8–12. (In Russian)
- 2. Li Y, Chen Y, Xu Z, Xia H, Natuski T, Xi Y, Ni Q. Effect of surface modification of carbon fiber based on magnetron sputtering technology on tensile properties. *Carbon*. 2023;204: 377 386.
- 3. Karlsson S, Eklund P, Österlund L, Birch J, Ali S. Effects of deposition temperature on the mechanical and structural properties of amorphous Al–Si–O thin films prepared by radio frequency magnetron sputtering. *Thin Solid Films*. 2023;787: 140135.
- 4. Yang Y, Zhang Y, Yan M. A review on the preparation of thin-film YSZ electrolyte of SOFCs by magnetron sputtering technology. *Separation and Purification Technology*. 2022;298: 121627.
- 5. Strzelecki GW, Nowakowska-Langier K, Mulewska K, Zieliński M, Kosińska A, Okrasa S, Wilczopolska M, Chodun R, Wicher B, Mirowski R, Zdunek K. Multi-component low and high entropy metallic coatings synthesized by pulsed magnetron sputtering. *Surface and Coatings Technology*. 2022;446: 128802.
- 6. Gudmundsson JT. Physics and technology of magnetron sputtering discharges. *Plasma Sources Science and Technology*. 2020;29: 113001.
- 7. Chodun R., Dypa M., Wicher B., Nowakowska-Langier K., Okrasa S., Minikayev R., Zdunek K. The sputtering of titanium magnetron target with increased temperature in reactive atmosphere by gas injection magnetron sputtering technique. *Applied Surface Science*. 2022;574: 151597.
- 8. Varavka VN, Kudryakov OV, Ryzhenkov AV, Kachalin GV, Zilova OS. Application of nanocomposite coatings to protect power equipment from droplet impact erosion. *Teploenergetika*. 2014;11: 29–35. (In Russian).
- 9. Graillot-Vuillecot R, Thomann A-L, Lecas T, Cachoncinlle C, Millon E, Caillard A. Hot target magnetron sputtering process: Effect of infrared radiation on the deposition of titanium and titanium oxide thin films. *Vacuum.* 2020;181: 109734.
- 10. Hovsepian PE, Ehiasarian AP. Six strategies to produce application tailored nanoscale multilayer structured PVD coatings by conventional and High Power Impulse Magnetron Sputtering (HIPIMS). *Thin Solid Films*. 2019;688: 137409.
- 11. Kupershtokh AL, Alyanov AV. Evaporation and condensation of pure vapor at the liquid surface in the method of lattice Boltzmann equations. *Numerical Methods and Programming*. 2022;23(4): 311–327. (In Russian).
- 12. Wang D, Zhong R, Zhang Y, Chen P, Lan Y, Yu J, Su GH, Qiu S, Tian W. Isothermal experiments on steam oxidation of magnetron-sputtered chromium-coated zirconium alloy cladding at 1200°C. *Corrosion Science*. 2022;206: 110544.
- 13. Kashkarov EB, Sidelev DV, Rombaeva M, Syrtanov MS, Bleykher GA. Chromium coatings deposited by cooled and hot target magnetron sputtering for accident tolerant nuclear fuel claddings. *Surface and Coatings Technology*. 2020;389: 125618.

- 14. Grudinin VA, Bleykher GA, Sidelev DV, Yuriev YuN, Lomygin AD. Magnetron deposition of chromium nitride coatings using a hot chromium target: Influence of magnetron power on the deposition rate and elemental composition. *Surface and Coatings Technology*. 2022;433: 128120.
- 15. Shapovalov VI, Ahmedov H, Kozin AA, Demir A, Korutlu B. Simulation of the effect of argon pressure on thermal processes in the sputtering unit of a magnetron with a hot target. *Vacuum.* 2021;192: 110421.
- 16. Graillot-Vuillecot R, Thomann A-L, Lecas T, Cachoncinlle C, Millon E, Caillard A. Properties of Ti-oxide thin films grown in reactive magnetron sputtering with self-heating target. *Vacuum.* 2022;197: 110813.
- 17. Kaziev AV, Kolodko DV, Tumarkin AV, Kharkov MM, Lisenkov VYu, Sergeev NS. Comparison of thermal properties of a hot target magnetron operated in DC and long HIPIMS modes. *Surface and Coatings Technology*. 2021;409: 126889.
- 18. Bleykher GA, Borduleva AO, Krivobokov VP, Sidelev DV. Evaporation factor in productivity increase of hot target magnetron sputtering systems. *Vacuum*. 2016;132: 62–69.
- 19. Bleykher GA, Sidelev DV, Grudinin VA, Krivobokov VP, Bestetti M. Surface erosion of hot Cr target and deposition rates of Cr coatings in high power pulsed magnetron sputtering. *Surface and Coatings Technology*. 2018;354: 161–168.
- 20. Sidelev DV, Bleykher GA, Bestetti M, Krivobokov VP, Vicenzo A, Franz S, Brunella MF. A comparative study on the properties of chromium coatings deposited by magnetron sputtering with hot and cooled target. *Vacuum.* 2017;143: 479–485.
- 21. Tang K, Li X, Wang C, Shen Y, Xu Y, Wen M. The application of NiCrPt alloy targets for magnetron sputter deposition: Characterization of targets and deposited thin films. *Thin Solid Films*. 2024;805: 140501.
- 22. Haneef M, Evaristo M, Morina A, Yang L, Trindade B. New nanoscale multilayer magnetron sputtered Ti-DLC/DLC coatings with improved mechanical properties. *Surface and Coatings Technology.* 2024;480: 130595. 23. Lee Y-C, Yen VC, Pithan C, Jan J-H. Study of Ni-Cr / CrN bilayer thin films resistor prepared by magnetron sputtering. *Vacuum.* 2023;213: 112085.
- 24. Grudinin VA, Sidelev DV, Bleykher GA, Yuriev YuN, Krivobokov VP, Berlin EV, Grigoriev VYu, Obrosov A, Weiß S. Hot target magnetron sputtering enhanced by RF-ICP source for CrN_x coatings deposition. *Vacuum*. 2021;191: 110400.
- 25. Xu Y, Li Y, Meng F, Huang F. Microstructure and multifunctionality of a 10-μm-thick dense yet smooth Cr(C) coating prepared by low-temperature magnetron sputtering. *Surface and Coatings Technology*. 2022;435:128255. 26. Larhlimi H, Ghailane A, Makha M, Alami J. Magnetron sputtered titanium carbide-based coatings: A review of science and technology. *Vacuum*. 2022;197: 110853.
- 27. Sun Q, Wang J, Xie Y, Hu Y, Jiang Q, Zhang F, Wu T, Si Y, Qiao Z, Yigit K, Li Z, Li H, Wang S. Preparation and properties of chromium protective coatings on lithium targets for accelerator-based neutron sources. *Vacuum.* 2024;224: 113151.
- 28. Lin J, Stinnett TC. Development of thermal barrier coatings using reactive pulsed dc magnetron sputtering for thermal protection of titanium alloys. *Surface and Coatings Technology*. 2020;403: 126377.
- 29. Ryzhenkov VA, Sidorov SV, Tkhabisimov AB, Kachalin GV, Mednikov AF. Technological installation with high-power pulsed magnetron discharge for forming wear-resistant coatings on the surface of elements of thermal power equipment. *Natural and Technical Sciences*. 2013;1(63): 171-177. (In Russian)
- 30. Ryzhenkov AV, Volkov AV, Mednikov AF, Tkhabisimov AB, Zilova OS, Sidorov SV. Results of measurements of substrate deformation and determination by bending of internal stresses in Ti-TiC-DLC coating obtained by using HIPIMS technology. *Materials Physics and Mechanics*. 2021;47(2): 285–292.
- 31. Tretyakov RS, Krivobokov VP, Yanin SN. Technological capabilities of the magnetron diode with an evaporating target. *Izvestiya vuzov. Fizika.* 2011;54(1/3): 288–293. (In Russian)
- 32. Kachalin GV, Medvedev KS, Kasyanenko VA, Mednikov AF, Tkhabisimov AB. Study of the growth rate and structure of chrome coating obtained by magnetron sputtering from uncooled turget. *Current Issues in Energy.* 2024;1(6): 25–29. (In Russian)

Submitted: May 15, 2024 Revised: August 21, 2024 Accepted: August 28, 2024

Gradient energy-absorbing nature-inspired metamaterial based on the "Schwarz Primitive" geometry

S.V. Balabanov 10, A.M. Kuropiatnik 1,2, M.M. Sychov 1,20, E.A. Pavlova 2, S.V. Diachenko 1,2 100

ABSTRACT

Gradient energy-absorbing nature-inspired cellular metamaterial with high energy-absorbing properties has been developed, made from polyamide-12 using selective laser sintering technology. It is shown that the gradient structure provides the effect of "pseudo-plastic failure" due to layer-by-layer deformation of the metamaterial with a significant increase in the energy absorption value, which was 1.88 MJ/m³ for the plastic series, and 1.45 MJ/m³ for the brittle series.

KEYWORDS

cellular materials • triply periodic minimal surfaces • additive technologies • 3D printing • strength deformation • selective laser sintering • pseudo-plastic failure • gradient cellular structures

Acknowledgements: The work on modeling, manufacturing and research of metamaterials was carried out within the framework of the Russian Science Foundation project "New generation energy-absorbing materials based on gradient cellular structures". (Agreement No. 20-73-10171; available online: https://www.rscf.ru/project/20-73-10171). The work on testing and analysis of metamaterials was carried out with financial support within the framework of the State Task No. 1024030700040-3-1.4.3 "Chemistry, physics and biology of nanostates".

Citation: Balabanov SV, Kuropiatnik AM, Sychov MM, Pavlova EA, Diachenko SV. Gradient energy absorbing nature-inspired metamaterial based on the "Schwarz primitive" geometry. *Materials Physics and Mechanics*. 2025;53(2): 157–167.

http://dx.doi.org/10.18149/MPM.5322025_14

Introduction

Materials with repeating cells of varying shapes and sizes are one of the types of modern metamaterials [1]. Currently, cellular materials find extensive applications across multiple scientific and technical domains: mechanical engineering (energy absorbers, thermal and acoustic insulation substrates [2]), medicine (implants and prostheses), chemical industry (functional reactor and catalyst bases) etc. In nature, cellular materials exist as bionic structures – honeycomb formations of highly organized insects (bees, wasps, hornets), lipid bilayer membranes, marine coral formations, beetle exoskeletons, mammalian bones etc. However, most such structures are either doubly periodic (exhibiting structural periodicity along two directions), like honeycombs, or spatially stochastic (irregular) – e.g., polymer and metal foams.

The works of Academician V.Ya. Shevchenko's team [3–9] have demonstrated that to enhance physical and mechanical properties of cellular materials in technical applications, triply periodic minimal surfaces (TPMS) show particular promise. TPMS are



¹ National Research Center "Kurchatov Institute", Konstantinov Petersburg Nuclear Physics Institute – Grebenshchikov Institute of Silicate Chemistry, St. Petersburg, Russia

² St. Petersburg State Institute of Technology, St. Petersburg, Russia

[™]svdiachenko@technolog.edu.ru

regular triply periodic structures (periodic along three directions) with zero mean curvature. A surface is considered minimal, when its mean curvature equals zero at any point [10]. It was the German mathematician Karl Schwarz who introduced the TPMS geometry based on mathematical calculations in 1865 [11]. Due to its isotropic cellular structure, large specific surface area, smoothness and controlled geometric parameters (due to the change in the parameters of the mathematical equation describing their geometry), TPMS-based materials offer promising solutions for various physical applications [12–15].

It is known that TPMS-based materials efficiently dissipate various energy types, including mechanical energy [16], and serve as structural materials due to their high specific strength and high isotropy of physical properties [17,18]. It is worth noting that materials with a similar structure are also found in nature – in cuticular structures in butterfly wing scales [19], chloroplast membranes [20], armadillo armor [21], fish scales [22] – qualifying TPMS as nature-inspired structures.

However, their structural complexity long hindered manufacturing TPMS-based materials [23]. Widespread research and practical implementation only became feasible with additive manufacturing (AM) rapid development. Today, AM is a pivotal tool for developing novel promising materials and products for high-tech industries [24]. 3D printing significantly expands production capabilities and is integral to "digital materials science" concept [25]. AM enable creating complex geometries unattainable via traditional subtractive methods of manufacturing [26], particularly TPMS-based cellular materials. Nevertheless, despite active research and popularization, precise methods and approaches to design and prediction of mechanical and other physical properties of TPMS-based cellular materials and similar ones remain underdeveloped due to their topological complexity.

This study aims to develop a gradient cellular material with high energy-absorption capacity and controlled deformation mechanisms. Gradient materials here denote macroporous structures with directional mechanical property variations via geometric modulation. The work comprehensively investigates the physical and mechanical properties of a gradient cellular material with Schwarz Primitive (Schwarz P) geometry, comparing results with similar non-gradient macroporous structures.

Materials and Methods

Manufacturing technology

For the research purposes, 3D models of specimens with Schwarz P surface geometry were developed, described by an implicit function with a varying unit cell size parameter t [16] according to the equation:

$$a \cdot \cos(x) + b \cdot \cos(y) + c \cdot \cos(z) = t$$
. (1) where a , b , c are the numerical coefficients in the equation; t is a geometric parameter (indicator).

The isosurface level parameter t took the following values: -0.9, -0.6, -0.3, 0, 0.3, 0.6. In this case, the numerical coefficients a, b, c were equal to 1. It should be noted that as parameter t increased, the unit cell size in the TPMS structure decreased while maintaining equal values along all three directions (Fig. 1). To study the influence of

structural heterogeneity on the physical and mechanical properties of the specimens, a gradient sample was developed with height-dependent geometric parameter t, where t = z/24, with z being the height coordinate.

Modeling was performed using parametric methods in Rhinoceros 6 software with Grasshopper plugin, and the models were saved in STL format for 3D printing. Autodesk Netfabb software was used to correct errors in STL files; structure renders are shown in Fig. 1.

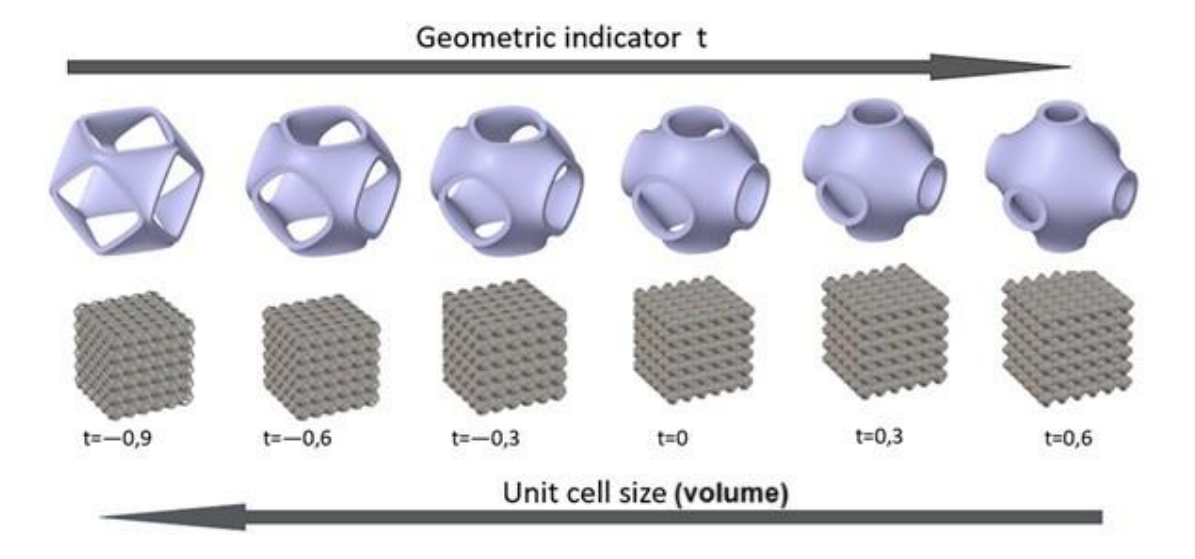


Fig. 1. Renders of the Schwartz P structure with different parameters (geometric indicator t)

The selective laser sintering (SLS) technology was chosen as the 3D printing method, implemented on an FORMIGA P100 3D printer by Electro Optical Systems. In this method, a laser sinters polymer powder particles layer by layer, fusing them together to create the structure [27]. The key advantages of this technology include high printing accuracy and absence of support structures [28]. EOS Parameter Editor software was used to prepare models for printing. Two series of specimens were printed from polyamide-12 (PA-12, $\rho \approx 1$ g/cm³) with dimensions of $60 \times 60 \times 60$ mm³ ($6 \times 6 \times 6$ unit cells) with different t parameter values under varying manufacturing conditions (Table 1).

Table 1.	3D	printing	modes	for	PA-12	samples
I UDIC I.	20	printing	111000	101	1 / \ T Z	Janpies

No.	Parameter	Mode 1	Mode 2	
1	Layer thickness <i>h</i> , µm	100.0		
2	Table temperature T_1 , °C	169.5	173.0	
3	Chamber temperature T_2 , °C	C 150.0 173.0		
4	Laser power P, W	22.0		
5	Filling distance s, µm	250.0		
6	Laser scanning speed V, m/s	25.0		
7	Energy density <i>E</i> , J/cm ³	35.2		

To introduce a gradient of physical and mechanical properties into the base structure, a gradient was applied along one direction (height) by linking it to the TPMS equation. Thus, the equation of the gradient Schwarz P surface, considering Eq. (1), took the form:

$$\cos(x) + \cos(y) + \cos(z) = \frac{z}{24}.$$
 (2)

It is assumed that the strength of each layer in the gradient structure corresponded to the strength of an isotropic specimen with the same t value. The general appearance of the gradient cellular structure is shown in Fig. 2.

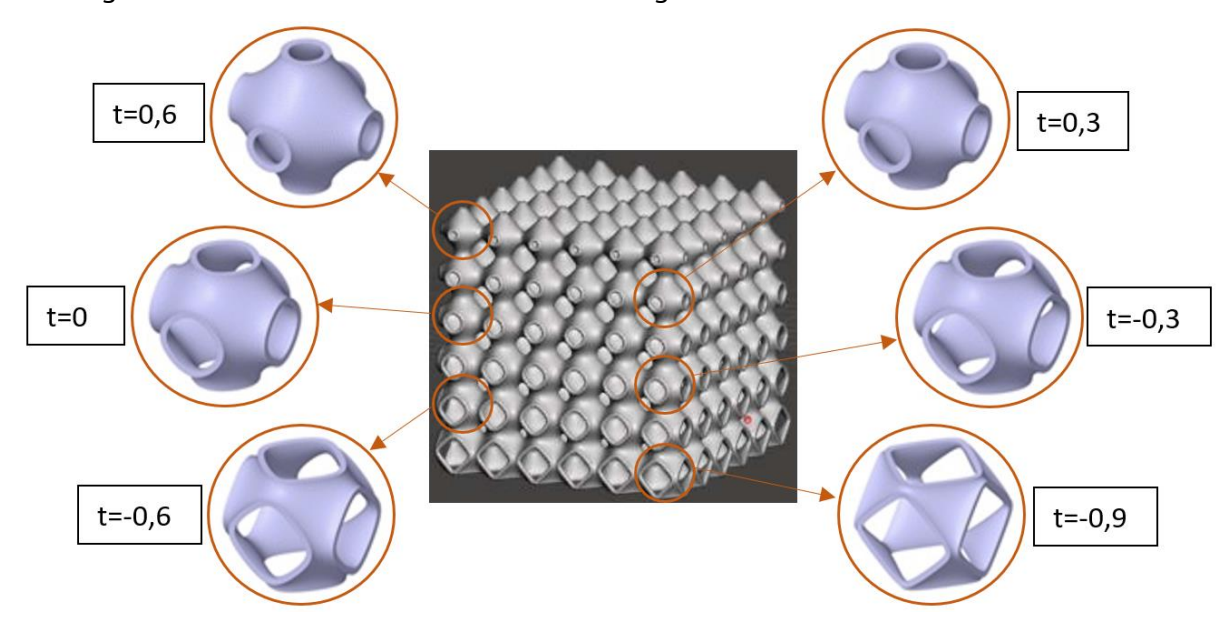


Fig. 2. The general appearance of the gradient cellular structure

Testing

The specimens were subjected to compression testing according to GOST 4651-2014 (ISO 604:2002)¹ standards on a REM-50-A-1-1 tensile testing machine with maximum load capacity of 50 kN and loading rate of 5 mm/min. Given that 3D-printed products exhibit mechanical property anisotropy, compression strength tests were conducted along the specimen's build direction [8]. In addition to TPMS compression tests, tensile tests of witness samples were performed in accordance with GOST 11262-2017 (ISO 527-2:2012)² at 5 mm/min rate to investigate the material's physical and mechanical properties.

Results and Discussion

Non-gradient specimens

The test results yielded stress σ versus relative strain ε curves for series 1 and 2 specimens (Figs. 3 and 4). The deformation curves differed significantly: specimens printed at lower temperature (series 1, mode 1) exhibited dominant elastic-plastic deformation up to $\varepsilon \approx 70$ % (Fig. 3(a)), whereas series 2 specimens (Fig. 3(b)) manufactured under mode 2 failed brittlely at 15–20 % strain.

¹ Interstate Council for Standardization, Metrology and Certification (ISC). *Plastics. Compression test method.* GOST 4651-2014. 2014. 16 p.

² Interstate Council for Standardization, Metrology and Certification (ISC). Plastics – Determination of tensile properties – Part 2: Test conditions for moulding and extrusion plastics, MOD. GOST 11262-2017. 2018. 24 p.

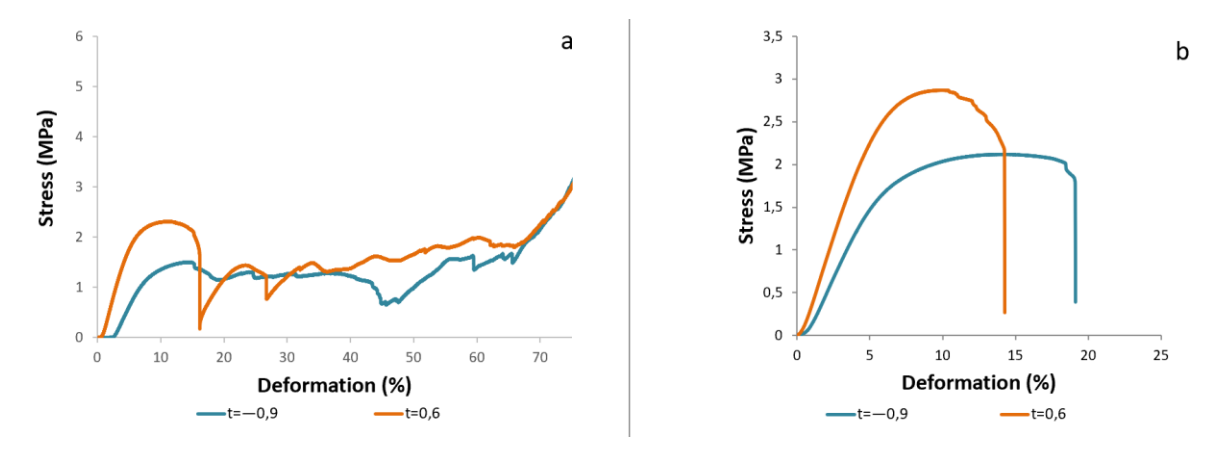


Fig. 3. Deformation curves for both series at different *t* parameter: (a) series 1; (b) series 2

To evaluate physical and mechanical properties of the samples under study, compression curves were analyzed and witness samples underwent tensile testing. Stress calculation was performed according to the following equation:

$$\sigma = \frac{N}{S},\tag{3}$$

where N is the applied load and S is the specimen base area (calculated via outer dimensions).

As shown in Fig. 4, the series 1 specimens demonstrate eight distinct characteristic regions. During specimen deformation in region I, stress increases sharply while maintaining proportionality law (Hooke's law), therefore this region can be classified as elastic deformation zone. At the end of region I, the Hooke's law no longer applies. Six subsequent regions (regions II–VII) exhibit elastic-plastic deformation with mutually similar patterns – regions of cellular structure layers deformation. Region II reaches the maximum (ultimate tensile strength) where rapid deformation of the first cellular layer occurs. Stress then decreases with continuing deformation accumulation. At the end of region II and at the beginning of region III, complete "collapse" of the first cellular layer occurs. Regions III–VII qualitatively replicate region II. At the end of region VIII and at the beginning of region VIII, the sixth (final) cellular layer "collapse". Region VIII is characterized by exponential load increase, marking the onset of plastic deformation.

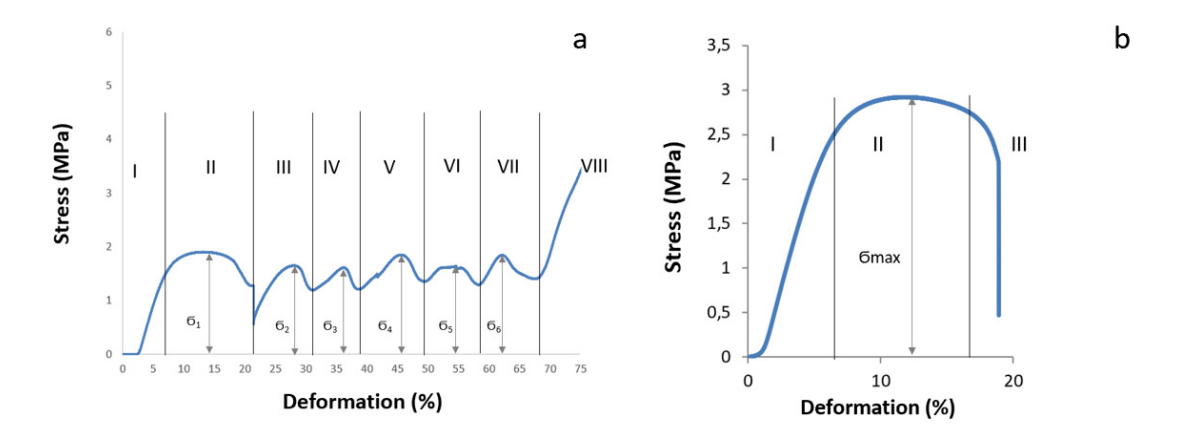


Fig. 4. Deformation curves for both series at t = 0: a) series 1; b) series 2

The deformation curve characteristics differ for series 2 specimens. Region I represents the elastic deformation zone, obeying Hooke's law as in Series 1. Region II is the transitional zone where compressive ultimate tensile strength is achieved. Region III shows crack propagation leading to brittle failure of the sample.

Unlike series 1, series 2 specimens exhibit brittle failure – upon reaching ultimate strength, they fracture rather than undergoing progressive layer-by-layer deformation. Comparing Figs. 5(b) and 5(c) one can observe that series 2 specimens fracture similarly to brittle ceramic materials. This behavior is characteristic of brittle materials where failure occurs along planes of maximum shear stress, typically oriented at 45° angles [29].

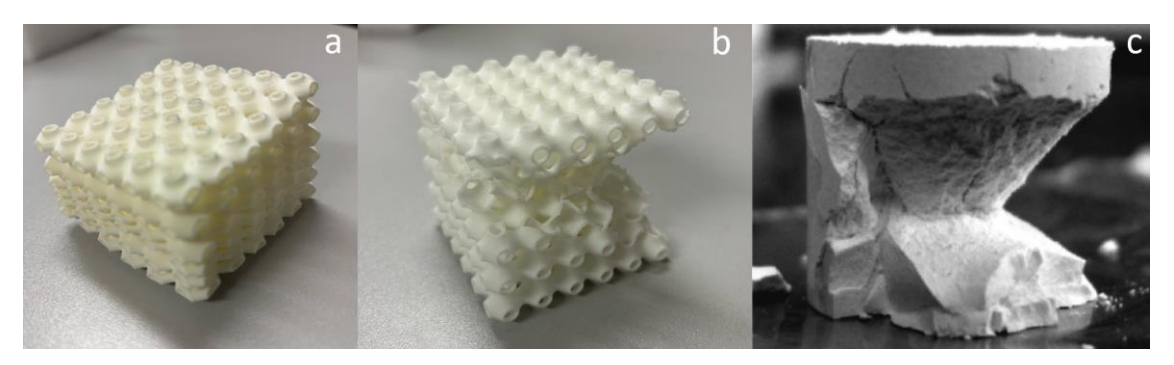


Fig. 5. Post-test specimens: (a) t = 0.3, series 1; (b) t = 0.3, series 2; (c) ceramic sample

Plasticity of the materials was assessed via indirect metrics: residual relative elongation at rupture δ and residual relative contraction (cross-section reduction) ψ at rupture [9]. Results are summarized in Table 2.

No.	Parameter	Series 1	Series 2	
1	$\sigma_{\sf max}$, MPa	50.0	49.0	
2	$\varepsilon(\sigma_{max})$, %	12.9	14.6	
3	$oldsymbol{arepsilon}_{\sf max}$, $\%$	13.1	21.1	
4	δ, %	12.9	9.8	
5	ψ, %	9.3	3.0	
6	F MPa	8.3	9.5	

 Table 2. PA-12 mechanical properties under tension

From Table 2, it follows that the change in cross-sectional area ψ and elongation δ for series 1 specimens printed at lower temperature T are higher than for series 2 specimens with increased T. This indicates that series 2 specimens exhibit reduced plastic properties compared to series 1 under equal conditions and identical printing energy density. It is possible that at high sintering temperatures, PA-12 crystallizes, consequently making the printed product more brittle [30]. This leads to the conclusion that to achieve high energy absorption characteristics, it is necessary to consider the polymer's crystallization temperature value, particularly for polyamide, when adjusting printing temperature, as it directly affects the final product's properties.

It is known that energy-absorbing materials should possess high plasticity. Maximum energy absorption A of the specimens was evaluated from the obtained deformation curves using the equation:

$$A = \int_0^{\varepsilon} \sigma d\varepsilon. \tag{4}$$

The test results demonstrate that increasing sintering temperature leads to embrittlement and altered deformation behavior of the specimens (Fig. 3). Consequently, these specimens are unsuitable for mechanical energy absorption applications. Table 3 shows that brittle specimens' energy absorption decreases several-fold compared to the plastic series – for instance, plastic specimens with t = 0.6 reach energy absorption of 1.13 MJ/m³, while brittle specimens under equal conditions show three times lower values. However, higher sintering temperatures increase specimens' strength and Young's modulus by 1.5 and 2 times, respectively, which is advantageous for their use as structural components.

Table 3 further reveals that increasing t parameter enhances the cellular structure's strength. Additionally, these structures exhibit layer-by-layer deformation and failure. This suggests that creating a gradient structure with varying t parameter between layers would correspondingly increase $\sigma_{\rm max}$ progressively from layer to layer.

	A, MJ/m ³		σ_{\max}	σ_{max} , MPa		<i>E</i> , MPa	
t	Series 1	Series 2	Series 1	Series 2	Series 1	Series 2	
-0.9	0.87	0.23	1.50	2.11	25.9	23.9	
-0.6	0.77	0.32	1.64	2.83	31.8	51.6	
-0.3	0.95	0.30	1.81	2.59	38.1	50.3	
0.0	1.03	0.32	1.90	2.92	34.8	53.4	
0.3	0.99	0.39	1.94	2.83	35.5	50.2	
0.6	1.13	0.32	2.31	2.87	46.3	52.5	

Table 3. Mechanical properties of two TPMS specimen series

Gradient specimen

To improve brittle material's energy absorption, a structure was developed that is capable of sequential layer failure through variation of layers' physical and mechanical properties, achieved by implementing geometric gradient via parameter t modulation. This gradient geometry may compensate for material brittle properties during deformation. Compression tests confirmed that despite inherent brittleness of series 2 specimen, the gradient specimen failed layer-by-layer (Fig. 6), progressing from least robust to most robust layers. During the testing the specimen demonstrated brittle, but local fracture – inside every layer, which led to the effect of "pseudo-plastic behavior" of the specimen.

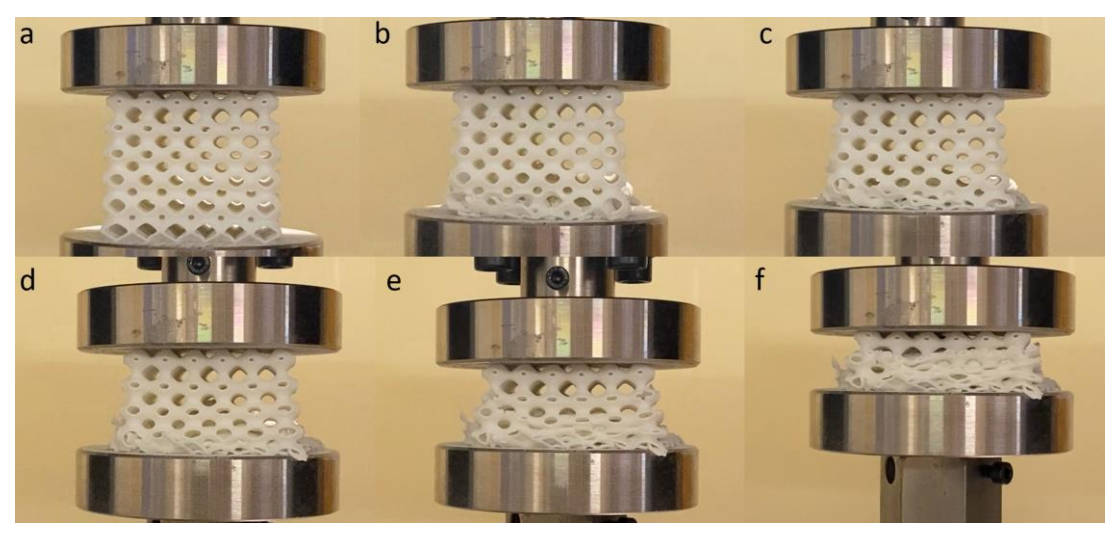


Fig. 6. Sequential layer-by-layer failure of gradient structure (series 2)

For comparison, Fig. 7 presents deformation curves of gradient and isotropic (non-gradient) series 2 specimens with constant t. It is obvious, that the curve characteristics vary, resembling plastic material's deformation curve. Besides, according to the curve characteristics, each layer's strength of gradient structure progressively increases with increasing t value, i.e., the material exhibits spring-like behavior until reaching $\sigma_{\rm max}$, followed by plastic deformation. These results confirm that parameter t variation effectively controls TPMS cellular materials' operational properties.

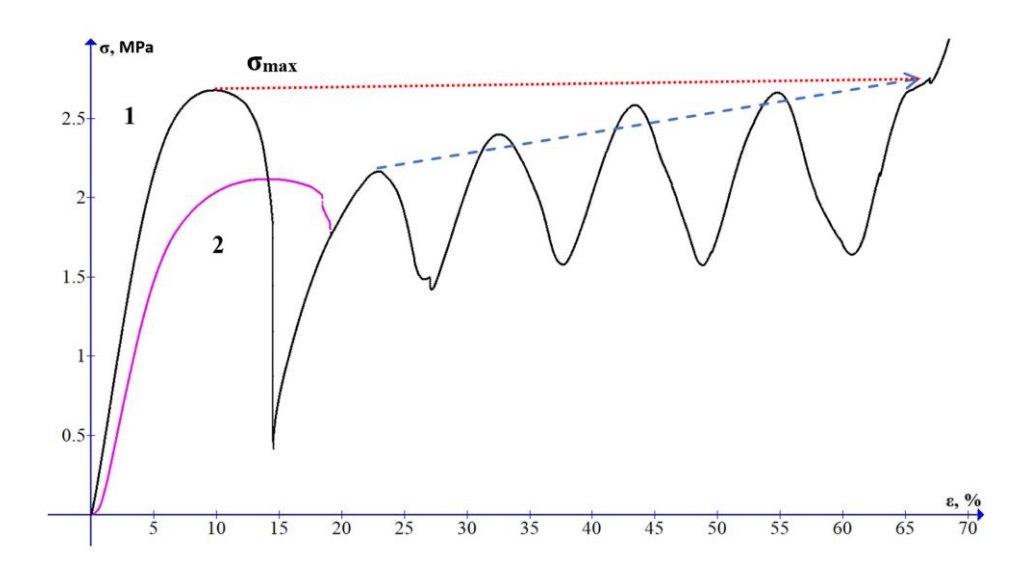


Fig. 7. Deformation curves of cellular structures (series 2, t = -0.9): (1) gradient specimen, (2) isotropic specimen

Figure 8 shows ultimate tensile strength $\sigma_{\rm max}$ dependency from the parameter t for both series' gradient specimens. Both series show monotonic ultimate tensile strength increase with increasing t, though brittle series maintains higher absolute values, consistent with non-gradient structures.

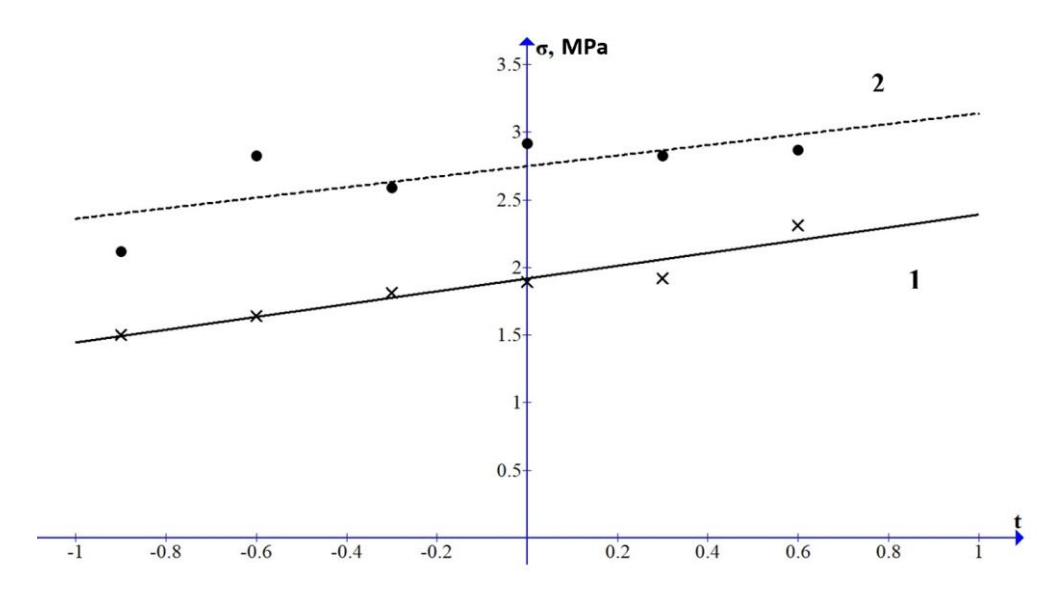


Fig. 8. Ultimate tensile strength σ_{max} dependency from t parameter for gradient specimens: (1) series 1; (2) series 2

To use these structures as energy absorbers, energy absorption A_g calculations were carried out for plastic and brittle series, yielding A_{g1} = 1.88 MJ/m³ and A_{g2} =1.45 MJ/m³, respectively. According to the results, gradient structures enhanced energy absorption significantly heterogeneity of physical and mechanical properties of the cellular structure layers. When comparing the values of A between gradient and isotropic structures, it can be noted that for the plastic series (1 series) the increase was ≈ 60%, while for the brittle series (2 series) the increase was ≈ 270%.

Conclusion

Gradient cellular nature-inspired metamaterial samples based on the TPMS "Schwarz Primitive" geometry were developed, fabricated from polyamide-12 using selective laser sintering (SLS) and investigated.

The following tasks were completed:

- 1. Modeling and manufacturing of a cellular nature-inspired metamaterial with gradient structure.
- 2. Investigation of mechanical properties of TPMS-based cellular material (Schwarz Primitive) with varying parameter *t* (cell size).
- 3. Analysis of mechanical properties of cellular material depending on specimen sintering conditions.
- 4. Identification of mechanical anisotropy in the gradient structure, mitigating the properties of isotropic TPMS (Schwarz Primitive) made from brittle polyamide.

It was concluded, that increasing t parameter enhances strength and energy absorption, while elastic modulus changes nonlinearly. When changing 3D printing parameters: chamber temperature ($\Delta T_1 = +23.0\,^{\circ}\text{C}$) and table temperature ($\Delta T_2 = +3.5\,^{\circ}\text{C}$) during sintering, induce brittleness in plastic specimens, likely due to increased crystallinity. Tensile tests revealed reductions in δ (–3.1%) and ψ (–6.3 %). For compressed TPMS specimens of two different series with various t values, higher sintering temperatures improve mechanical indicators, such as strength and elastic modulus, but reduce energy absorption.

Gradient structures with varying t parameter along height, printed via mode 2 exhibited a shift in compression failure mechanism: from brittle fracture (t = const) to "pseudo-plastic behavior" (t = -0.9...0.6). They also demonstrated simultaneous improvements in strength and energy absorption. Therefore, it can be concluded, that macrostructural and mechanical property gradient of such specimens effectively counteracts the brittleness of isotropic TPMS, regardless of the base material's plasticity, which is crucial for energy-absorbing applications.

Therefore, it can be said that the study proposes a method for designing macroporous structures that combine high strength and Young's modulus with enhanced energy absorption. High mechanical properties are achieved by optimizing 3D printing parameters to control polymer crystallization during manufacturing process. Decreasing plasticity is compensated by gradient geometry of cellular structure, and energy absorption value is higher that that of non-gradient specimens irrespective of polymer crystallinity.

CRediT authorship contribution statement

Sergey V. Balabanov (DSCR): writing – review & editing, writing – original draft; **Artur M. Kuropiatnik:** writing – original draft, investigation; **Maksim M. Sychov** (DSCR): supervision, conceptualization; **Emiliya A. Pavlova:** data curation; **Semen V. Diachenko** (DSCR): writing – review & editing, data curation.

Conflict of interest

The authors declare that they have no conflict of interest.

References

- 1. Borovkov AI, Maslov LB, Zhmaylo MA, Tarasenko FD, Nezhinskaya LS. Finite element analysis of elastic properties of metamaterials based on triply periodic minimal surfaces. *Materials Physics and Mechanics*. 2024;52(2): 11–29.
- 2. Sysoev EI, Sychov MM, Shafigullin LN, Dyachenko SV Design of Sound Absorbing Honeycomb Materials with a Geometry of Triply Periodic Minimal Surfaces (TPMS). *Acoustical Physics*. 2024;70(5): 887–898.
- 3. Shevchenko V, Balabanov S, Sychov M, Karimova L. Prediction of cellular structures mechanical properties with the geometry of triply periodic minimal surfaces (TPMS). *ACS Omega*. 2023;8(30): 26895–26905.
- 4. Shevchenko VYa, Sychev MM, Lapshin AE, Lebedev LA, Gruzdkov AA, Glezer AM. Polymer structures with the topology of triply periodic minimal surfaces. *Glass Physics and Chemistry*. 2017;43: 608–610.
- 5. Arsentev MYu, Sysoev EI, Vorobyov SA, Balabanov SV, Diachenko SV, Sychov MM, Skorb EV Crystal-inspired cellular metamaterials with reduced Poisson's ratio as analogues of TPMS. *Composite Structures*. 2025;363:119097.
- 6. Diachenko SV, Dolgin AS, Khristyuk NA, Lebedev LA, Nefedova LA, Pavlov SB, Merenkov KF, Ivkov VI, Dmitrieva AN 3D Printing of Ceramic Elements with Q-Surface Geometry for the Fabrication of Protective Barrier. *Ceramics*. 2023;6(2): 912–921.
- 7. Dolgin AS, Sychev MM, Bogdanov SP, Khristyuk NA, Kozlov VV Comparative Analysis of Triply Periodic Minimal Surface Corundum Products Obtained by 3D Printing. *Glass Physics and Chemistry*. 2019;45(6): 545–550.
- 8. Arsentev MYu, Balabanov SV, Makogon AI, Sychev MM. Experimental and theoretical studies of the mechanical properties of 3D printed polyamide products of the Schwarz Primitive topology. *Glass Physics and Chemistry*. 2019;45: 599–602.
- 9. Arsentev MYu, Sysoev EI, Makogon AI, Balabanov SV, Sychev MM, Hammouri MH, Moshnikov VA. High-throughput screening of 3D-printed architected materials inspired by crystal lattices: Procedure, challenges, and mechanical properties. *ACS Omega.* 2023;8(28): 24865–24874.
- 10. Lord EA, Mackay AL, Ranganathan S. *New geometries for new materials*. Cambridge, UK: Cambridge University Press: 2006.
- 11. Yan K, Wang J, Li L, Deng H. Numerical investigation into thermo-hydraulic characteristics and mixing performance of triply periodic minimal surface-structured heat exchangers. *Applied Thermal Engineering*. 2023;230(B): 120748.
- 12. Fu J, Sun P, Du Y, Li H, Zhou X, Tian Q. Isotropic design and mechanical characterization of TPMS-based hollow cellular structures. *Composite Structures*. 2021;279: 114818.
- 13. Gado MG, Al-Ketan O, Aziz M, Al-Rub RA, Ookawara S. Triply periodic minimal surface structures: Design, fabrication, 3D printing techniques, state-of-the-art studies, and prospective thermal applications for efficient energy utilization. *Energy Technology*. 2024;12(5): 2301287.
- 14. Zhang D, Yang Y, Lv X, Rao W-F. Fabrication of piezoelectric structures with high porosity by digital light processing. *3D Printing and Additive Manufacturing*. 2024;11(5): e1877–e1886.
- 15. Hu Y, Guo Z, Ragonese A. A 3D-printed molecular ferroelectric metamaterial. *Proceedings of the National Academy of Sciences USA*. 2020;117(44): 27204–27210.
- 16. Feng J, Fu J, Yao X, He Y. Triply periodic minimal surface (TPMS) porous structures: from multi-scale design, precise additive manufacturing to multidisciplinary applications. *International Journal of Extreme Manufacturing*. 2022;4: 022001.
- 17. Balabanov S, Sychov M, Koshevaya K, Makogon A, Gravit M. Study of isotropy of mechanical properties of the TPMS-based cellular structures. *E3S Web of Conferences*. 2022;363: 04053.

- 18. Balabanov SV, Makogon AI, Sychov MM, Gravit MV, Kurakin MK. Mechanical properties of 3D printed cellular structures with topology of triply periodic minimal surfaces. *Materials Today: Proceedings*. 2020;30(3): 439–442.
- 19. Michielsen K, Stavenga DG. Gyroid cuticular structures in butterfly wing scales: biological photonic crystals. *Journal of the Royal Society Interface*. 2007;5(18): 85–94.
- 20. Zhan T, Lv W, Deng Y. Multilayer gyroid cubic membrane organization in green alga Zygnema. *Protoplasma*. 2017;254: 1923–1930.
- 21. Chen I, Kiang JH, Correa V, Lopez MI, Chen P-Y, McKittrick J, Meyers MA. Armadillo armor: Mechanical testing and micro-structural evaluation. *Journal of the Mechanical Behavior of Biomedical Materials*. 2011;4(5): 713–722.
- 22. Rawat P, Zhu D, Rahman MZ, Barthelat F. Structural and mechanical properties of fish scales for the bio-inspired design of flexible body armors: A review. *Acta Biomaterialia*. 2021;121: 41–67.
- 23. Jones A, Leary M, Bateman S, Easton M. Parametric design and evaluation of TPMS-like cellular solids. *Materials & Design*. 2022;221(2): 110908.
- 24. Jandyal A, Chaturvedi I, Wazir I, Raina A, Ul Haq MI. 3D printing A review of processes, materials and applications in industry 4.0. *Sustainable Operations and Computers*. 2022;3: 33–42.
- 25. Bolmaro RE, Brokmeier H-G, Ferrante M, Fourty A, Lins JFC, Malarria J, Martino R, Sandim HRZ, Signorelli JW, Sobrero C, Sordi V. Digital materials science: Why do we need more images and numbers? *Acta Microscopica*. 2009;18(C): 23–24.
- 26. Gardan J. Additive manufacturing technologies: State of the art and trends. *International Journal of Production Research*. 2016;54: 3118–3132.
- 27. Fina F, Goyanes A, Gaisford S, Basit AW. Selective laser sintering (SLS) 3D printing of medicines. *International Journal of Pharmaceutics*. 2017;529(1–2): 285–293.
- 28. Matuš M, Bechný V, Joch R, Drbúl M, Holubják J, Czán A, Novák M, Šajgalík M. Geometric accuracy of components manufactured by SLS technology regarding the orientation of the model during 3D printing. *Manufacturing Technology*. 2023;23(2): 233–240.
- 29. Savchenko NL, Sevostyanova IN, Sablina TYu, Molnár L, Géber R, Gömze LA, Kulkov SN, Gömze LN. The influence of porosity on the elasticity and strength of alumina ceramics. *Journal of Silicate Based and Composite Materials*. 2014;66(2): 44–47.
- 30. Dupin S, Lame O, Barrès C, Charmeau J-Y. Microstructural origin of physical and mechanical properties of polyamide 12 processed by laser sintering. *European Polymer Journal*. 2012;48(9): 1611–1621.

MATERIALS PHYSICS AND MECHANICS

53 (2) 2025

УЧРЕДИТЕЛИ

Санкт-Петербургский политехнический университет Петра Великого **Адрес:** 195251, Санкт-Петербург, Политехническая ул., д. 29 Институт проблем Машиноведения Российской академии наук **Адрес:** 199178, Санкт-Петербург, Большой пр-кт В.О., д. 61

ИЗДАТЕЛЬ

Санкт-Петербургский политехнический университет Петра Великого **Адрес:** 195251, Санкт-Петербург, Политехническая ул., д. 29

Журнал зарегистрирован в Федеральной службе по надзору в сфере связи, информационных технологий и массовых коммуникаций (РОСКОМНАДЗОР), свидетельство ПИ №ФС77-69287 от 6 апреля 2017 года.

РЕДАКЦИЯ ЖУРНАЛА

Профессор, д.т.н., академик РАН, **А.И. Рудской** – главный редактор
Профессор, д.ф.-м.н., член-корр. РАН, **А.К. Беляев** – главный научный редактор
Профессор, д.ф.-м.н. **И.А. Овидько** (1961 - 2017) – основатель и почетный редактор
Профессор, д.ф.-м.н. **А.Л. Колесникова** – ответственный редактор
Профессор, д.ф.-м.н. **А.С. Семенов** – ответственный редактор
К.ф.-м.н. **Л.И. Гузилова** – выпускающий редактор
К.ф.-м.н. **Д.А. Китаева** – редактор, корректор

АДРЕС И ТЕЛЕФОН РЕДАКЦИИ

199178, Санкт-Петербург, Большой пр-кт В.О., д. 61

Тел. редакции: +7(812)552 77 78, доб. 224

E-mail редакции: mpmjournal@spbstu.ru Компьютерная верстка Л.И. Гузилова

Подписано в печать 30.09.2025 г. Выход в издания в свет: 31.10.2025 г. Формат 60х84/8. Печать цифровая Усл. печ. л. 10,0. Тираж 100. Заказ____. Цена: Бесплатно

Отпечатано в Издательско-полиграфическом центре Политехнического университета Петра Великого

Адрес: 195251, Санкт-Петербург, Политехническая ул., 29 Тел.: +7(812)552 77 17

United model for low-cycle, high and giga-cycle fatigue life prediction N.S. Selyutina, Yu.V. Petrov	1-12
Influence of grain size of nanocrystalline titanium on its dissolution intensity in aluminum G.M. Poletaev, Y.V. Bebikhov, A.S. Semenov	13-24
Electromagnetically cast Al-0.5 wt. % Fe alloy as a core material for the co-extruded copper-clad aluminium wire A.E. Medvedev, O.O. Zhukova, A.F. Shaikhulova, E.B. Medvedev, M.M. Motkov, M.Yu. Murashkin	25-39
S ₁₁ and S ₂₁ characteristics of carbon fiber fabric fixed in the polyurethane based matrixes O.V. Boiprav, E.S. Belousova, V.S. Mokerov	40-47
Conductive and mechanical properties of graphene-filled polymer composites D.N. Tonkov, M.I. Kobylyatskaya, E.S. Vasilyeva, V.E. Gasumyants	48-54
Effects of post-annealing duration on the properties of β-Ga ₂ O ₃ thin films prepared by spray pyrolysis	55-63
X. Zhang, D.I. Panov, V.A. Spiridonov, N.K. Kuzmenko, N.D. Prasolov, A.Yu. Ivanov, M.V. Dorogov, H.M. Wei, D.Y. Jiang, D.A. Bauman, A.E. Romanov	
Fundamental theorems and variational criterion in modified couple stress under multi-phase-lags and rotation S. Sharma, S. Devi, R. Kumar	64-82
Modelling forced convection and magneto-elastic interactions in a downward conduit using ferrofluid H. Derraz, M. Bouzit, A. Bencherif	83-103
Effect of loading on tribotechnical characteristics of antifriction diamond-bearing mineral ceramics A.N. Bolotov, O.O. Novikova, V.V. Novikov	104-112
Elastic-plastic deformation when bending rotating workpieces T.V. Brovman	113-122
Al-driven modeling and prediction of mechanical properties of additively manufactured Al-6061/B ₄ C composite D. Kumar, S. Singh, P.K. Karsh, A. Chauhan, G. Saini, A. Chouksey, P. Kumar	123-141
Electrochemical crystallization and functional properties of nickel-based composite coatings	142-148
V.N. Tseluikin, A.S. Dzhumieva, A.I. Tribis, D.A. Tikhonov The effect of the magnetron discharge power on the deposition rate of chrome coating obtained by spattering an uncooled extended target	149-156
G.V. Kachalin, K.S. Medvedev, A.B. Tkhabisimov, D.I. Iliukhin	
Gradient energy-absorbing nature-like metamaterial based on the "Schwarz Primitive" S.V. Balabanov, A.M. Kuropiatnik, M.M. Sychov, E.A. Pavlova, S.V. Diachenko	157-167

